

TECHNISCHE UNIVERSITÄT MÜNCHEN

Lehrstuhl für Biologische Bildgebung

Optoacoustic handheld imaging for clinical screening and intervention

Alexander Dima

Vollständiger Abdruck der von der Fakultät für Elektrotechnik und Informationstechnik der Technischen Universität München zur Erlangung des akademischen Grades eines

Doktor-Ingenieur (Dr. Ing.)

genehmigten Dissertation.

Vorsitzender: Univ. - Prof. Dr.-Ing. Martin Buss

Prüfer der Dissertation:

1. Univ. - Prof. Vasilis Ntziachristos, Ph. D.

2. Univ. - Prof. Dr.-Ing. Klaus Diepold

Die Dissertation wurde am 22.06.2015 bei der Technischen Universität München eingereicht und durch die Fakultät für Elektrotechnik und Informationstechnik am 17.12.2015 angenommen.

Abstract

Optoacoustic, also known as photoacoustic, imaging is a hybrid imaging modality that combines optical contrast with ultrasound resolution. The method has been studied since the 1990s, yet really took off only in the early 2000s, helped by the sufficient availability of technology components such as nanosecond pulsed lasers in the near-infrared, parallel data acquisition hardware and inversion algorithms. The foremost area of interest during these years has been pre-clinical biomedical imaging of small animals. In mice, reaching tissue diameters of up to 25mm, a number of disease models has been studied ranging from cancers and arthritis to Alzheimer's. To achieve ever better results a variety of contrast agents has also been applied or newly developed in order to visualize functional and molecular parameters relating to the disease studied. At the same time a desire to increase sensitivity to these agents led to the development of multi-spectral approaches, such as Multi-Spectral Optoacoustic Tomography (MSOT). These techniques also imposed additional requirements in terms of image quality and frame rate that could only be covered by introducing detector arrays and parallel acquisition hardware. As technology improved so did requirements, which at the time of writing reached a peak of 512-element arrays and 512-channel parallel sampling hardware at repetition rates of 10Hz. On the other hand numerous image reconstruction algorithms were developed spanning ultra-fast, yet less accurate, implementations of analytical inversion methods to more demanding methods based on numerical forward models offering higher accuracy and flexibility.

Optoacoustic technology has evolved to a stage where translation to clinical problems is not just feasible but highly desirable to bring the benefit of optical contrast at tissue depths and resolutions beyond the scope of purely optical modalities. Therefore in this work we approached clinical translation from the two most common imaging scenarios in patient care. First, we developed a handheld optoacoustic probe for non-invasive diagnostic imaging used in screening and therapy monitoring. Thereby we carefully compared previous illumination and detection patterns and studied achievable imaging depth and quality. To ensure a minimal footprint we devised optimal water coupling for the chosen cylindrically focused curved array and implemented flexible rectangular fiber bundle illumination. Using this handheld probe we were able to perform scans of various body parts. To enable live video feedback we furthermore optimized a simple inversion algorithm in C and parallelized it using first a multi-core CPU and later a consumer graphics card (GPU). Using this prototypical probe we were able to achieve the first ever optoacoustic images of the human carotids and thyroid.

In our second approach we targeted a common question posed in every surgical procedure: is this tissue viable? Every cut may disrupt the supply of blood to some tissue part and, if left undetected, can cause severe consequences to the patient.

When blood perfusion is too weak for visual and haptic assessment by the surgeon, robust and quantitative assistance is necessary. Optoacoustic imaging is ideally suited to provide such assistance, as it is highly sensitive to vasculature and by means of MSOT can also resolve molecular parameters such as oxygen concentration. In this context we chose to apply optoacoustic imaging to the resection of cancer and subsequent placement of the anastomosis (a suture connecting two tissue parts) in the lower colon. Using excised parts of the porcine lower colon we were able to identify the most suitable and flexible arrangement of detection and illumination. Additionally we devised a method for direct optoacoustic imaging of blood perfusion based on local arterial injection of medical saline. The method allows visual tracking of perfusion pathways and provides sufficient image quality for quantitative assessment of the perfusion rate. Moreover the procedure is clinically approved, highly robust and repeatable as well as risk free to the patient. We demonstrate the achievable contrast cycle on samples of excised porcine colon and on mouse tails in-vivo.

Finally, in preparation for future clinical deployment we studied achievable improvements of model-based image reconstruction algorithms in terms of memory consumption and execution speed. While GPU implementations of direct inversion algorithms are sufficient to enable live image feedback, more precise reconstructions can be obtained with model-based methods. Thus, in this work we also propose a paradigm change in numerical modeling. Instead of mixing physical wave propagation and geometric detector positioning, we treat each problem separately and are able to show a proof-of-concept implementation of accurate model-based optoacoustic inversion using only the numerical characteristics of a single detector position. The ultimate goal thereby is to enable inversion on consumer graphics cards that offer faster hardware compared to CPU/mainboard architecture as well as massive parallelization potential. Hence, the algorithm described herein is founded on image transformations – a cornerstone of computer graphics.

Contents

Abstract	3
1 Introduction	7
1.1 Modern clinical imaging	7
X-ray/XCT	7
PET/SPECT	8
MRI	9
Ultrasound imaging	9
1.2 Novel imaging requirements	10
1.3 Non-invasive clinical optoacoustic imaging	12
1.4 Objectives and outline	14
2 Optoacoustic imaging: instrumentation and theory	15
2.1 Propagation of light and sound in tissue	17
2.1.1 Light and tissue	17
2.1.2 Sound and tissue	21
2.2 The Photoacoustic effect	24
2.3 Laser excitation and illumination	29
2.4 Ultrasound detection	32
2.5 Array-based optoacoustic detection geometries	37
2.6 Image reconstruction	40
2.7 Multi-spectral unmixing	44
3 Imaging systems	47
3.1 Data acquisition electronics	48
3.2 Performance of linear versus curved array	54
3.3 Non-invasive handheld probe	62
3.4 Intraoperative setup and methodology	66
4 Optimizations for clinical deployability	70

4.1	Improving image reconstruction speed	70
4.2	Transformation-based Optoacoustic Modeling (TOM)	73
4.2.1	Proposed algorithm	75
4.2.2	Fast inversion	78
4.2.3	Evaluation using simulated data	79
4.2.4	Evaluation using handheld measurement data.	83
4.3	Array density – practical considerations	87
4.3.1	Characterization of arrays.	87
4.3.2	Numerical simulation and experimental setup.	90
4.3.3	Numerical and experimental results	92
5	Clinical applications	99
5.1	Cardio-vascular imaging.	99
5.2	Thyroid imaging	102
5.3	Tissue viability assessment	103
6	In vivo imaging results.	105
6.1	Non-invasive imaging	105
6.2	Towards intraoperative imaging	114
7	Discussion and Conclusion	121
8	Appendix	130
8.1	List of figures.	130
8.2	List of tables	137
8.3	List of publications.	137
8.4	References	138

Introduction

Modern clinical diagnostic procedures have come to rely to a great extent on medical imaging modalities developed or refined in the course of the last century. The most prominent and common in use can be categorized by the physical quantity employed for sampling: X-rays, γ -rays, ultrasound waves and magnetic fields. The fifth category uses the electromagnetic field at visible wavelengths: optical imaging. To date quantitative optical imaging (as opposed to visual perception) has been used only sparingly in a clinical context and even then it has been mostly limited to microscopy in the process of histological analysis, due to its limited penetration depth and resolution beyond 1-2 mm of tissue depth. Therefore, in this work we strive to bring to the clinics the full force of optical imaging at resolutions and tissue depths relevant for diagnosis in humans. However, before delving deeper into the subject, we start by reviewing the four clinically established modalities [1] and then discuss how novel imaging requirements can be addressed by optical imaging. Next we reproduce a brief history of optoacoustic (also photoacoustic) imaging and summarize previous efforts at non-invasive clinical application. We also review the state of the art in optoacoustic handheld imaging and characterize important parameters of clinical optoacoustic systems. We end the introduction by detailing the organization of chapters.

1.1 Modern clinical imaging

X-ray/XCT

The earliest medical imaging technology was planar X-ray radiography, which is able to visualize differences in absorption of X-rays by diverse tissues. As the name suggests the method constitutes a projection of a three-dimensional volume to the two-dimensional plane by illuminating the volume with directed radiation originating in a source that is positioned opposite of the detection plane. Because X-rays undergo mostly absorption and are not scattered, each image pixel is the projection or sum of all absorbers along a straight line from the source to the detector element.

Synchronized rotation of source and detection plane around the patient allows the acquisition of different projection views. If enough views have been acquired and digitized, the collected data can be used to compute a 3D volumetric image. In this case the procedure is known as X-ray computed tomography (XCT). Both acquisition methods provide mostly anatomical information, whereby planar X-ray imaging is routinely employed for screening of acute injuries such as bone fractures or suspected diseases affecting for example the kidneys or the respiratory system. Due to the ionizing nature of the modality however, great care is taken to minimize its use for a given time interval. In cases where the benefit outweighs the incurred tissue damage or risk, exposure to higher doses of radiation is accepted. As it consists of many X-ray projections, XCT imaging is performed to obtain a more detailed diagnosis in severe cases such as suspected cancer or in preparation of difficult surgery. Due to the large size of XCT equipment, interventional use is severely limited, mostly to minimally invasive procedures. Both methods feature as standard clinical equipment, because they are easy to use while offering full body penetration depths and resolutions on the μm scale. Drawbacks, in particular of XCT, include cost of manufacture, equipment size, sensitivity, specific contrast and safety concerns.

PET/SPECT

A second modality using ionizing radiation is known as nuclear medicine tomographic imaging and is based on injection of targeted radioactive agents. Radiotracers, as these agents are known, are injected intravenously in very small quantities (nanogrammes) and subsequently distributed throughout the body. Rate, amount and location of accumulation are important parameters for diagnosis. In general there are two imaging systems that can be distinguished by the energy of γ -rays detected: single photon emission computed tomography (SPECT) using radioisotopes emitting γ -rays at 140 keV and positron emission tomography (PET), where employed radionuclides emit positrons that recombine with tissue electrons after traveling for about 1 mm and re-emit two γ -rays at 511 keV in opposing directions. Planar imaging of SPECT radiotracers can be achieved using gamma cameras and is known as scintigraphy, a method comparable to planar X-ray imaging. To obtain a full SPECT dataset the detection plane (gamma camera) is rotated around the patient, producing a 2D projection image at each position. A 3D volumetric image can then be reconstructed, which is usually displayed as a cross-sectional 2D image through the organ of interest. Similarly, PET also requires tomographic scanning to reconstruct a 3D volume, albeit using two gamma cameras positioned opposite of each other – modern implementations often use a full ring of detectors encircling the patient. Based on higher γ -ray energy and “timed” photon pairs, arriving at opposite detectors at the same time, PET generally has a higher spatial resolution and sensitivity compared to SPECT. This is paid for by higher cost in producing the short lived PET radionuclides in a small cyclotron that also increases equipment cost. Nonetheless, both methods offer full body penetration and high sensitivity but comparably low resolution (PET: 1-2 mm, SPECT: 5-10mm) and high cost and size of equipment. As with all modalities involving radioactive materials, safety concerns additionally increase cost of handling and may

cause tissue damage. Even so, availability is high because of the ability to observe functional and molecular parameters with high sensitivity. For this reason PET is often employed in combination with CT to provide complementary molecular information for oncological diagnoses or in the search for metastases. Intraoperative use is known, but typically not employed, due to the size of equipment and the required scanning time.

MRI

Magnetic resonance imaging (MRI) is another modality that can achieve full body penetration depths and 3D volumetric imaging at sub-millimeter resolutions. In contrast to nuclear medicine or X-ray imaging MRI does not employ ionizing radiation but rather strong magnetic fields, which have been shown to have no negative effects on patients. The basic principle of MRI is to expose tissue to a strong and constant magnetic field, usually around 3 Tesla, in order to align the magnetic polarization of atomic nuclei. Then, an electromagnetic pulse at the resonance frequency of protons causes the same to precess until fully re-aligned. Proton precession generates electromagnetic fields at radiofrequencies (RF) that can be detected by RF-coils placed close to the body. By simultaneously enabling a magnetic gradient only protons generate signals that are contained in a slice, whose orientation is perpendicular to the magnetic gradient and whose thickness is determined by the bandwidth of the electromagnetic pulse. Usually gradients along the three Cartesian axes are employed, resulting in coronal, axial and sagittal slices. By appropriate scanning 3D volumes can be reconstructed. As proton densities vary by organ, MRI enables strong soft tissue contrast and can hence be used to diagnose a broad range of pathological disorders. Typical clinical applications comprise neurology, hepatology or cardiology. Besides providing anatomical information specialized MRI methods, such as functional MRI (fMRI), diffusion MRI or MR angiography, extend its use to the detection of functional and molecular parameters. Under severe circumstances intraoperative scans can also be performed, yet usually require a temporary interruption of the surgical procedure. The biggest drawbacks of the modality include applicability, procedural cost and availability. Generally, patients that carry ferromagnetic implants are not eligible for MRI scanning. However, even eligible patients are not always prescribed a scan, because of the high costs associated with a procedure that can take several hours and involve several medical personnel. Moreover, very high costs of procurement and maintenance greatly reduce MRI penetration, such that few machines are usually available within a state or country. As a consequence patients are often scheduled according to severity of their case even though early diagnosis may prevent disease progression.

Ultrasound imaging

As the most cost effective and scalable clinical imaging modality ultrasound is widely available in clinics and private practices. Unlike the other established modalities no ionizing radiation or strong magnetic fields are employed but rather mechanical waves at frequencies typically ranging from 1-15 MHz. The technology is similar to synthetic aperture radar as waves are emitted from a device and their echo received by the same. For ultrasound imaging this device is usually an array of up to thousands of individual piezoelectric elements, each capable of both, emitting a pressure wave upon electrical stimulation and generating a voltage proportional to the received pressure. By exciting elements in a defined order a focused wave can be emitted and its echo appropriately time-delayed by element to form an image. As the modality has been developed since the 1950s, it has reached a highly sophisticated and optimized state that allows real-time imaging at resolutions of tens to hundreds of micrometers, depending on the penetration depth chosen. Thereby, the contrast achieved is proportional to the amount of reflected energy and thus mostly depends on the difference in acoustical impedance of various tissues. This enables imaging of structure and physiology but also of flow velocity and directivity if advanced techniques, such as Doppler Ultrasonography, are employed. Modern systems range from laptop-integrated mobile devices to cart-based high-performance platforms configurable to include probes for specialized tasks. Such probes are usually single-axis linear or convex curved arrays, whose cylindrical focusing enables cross-sectional 2D imaging, also known as B-mode. In addition, newly developed probes with elements spread across a surface can achieve imaging of a 3D volume. Due to its low cost and risk free mode of operation, ultrasound imaging has become a standard procedure in many clinical applications such as cardiovascular disorders, in gynecology or for guidance in needle biopsies to name but a few.

Table 1 – Major clinical imaging modalities and Multi-Spectral Optoacoustic Tomography (MSOT)

	Sensitivity	Throughput	Contrast	Size	Safety	Cost	Depth
MSOT	pmol (10^{-12})	High	High	Small	Good	Low	cm
MRI	nmol (10^{-9})	Low	High	V large	Good	V High	Full
XCT	μ mol (10^{-6})	Low	Average	V large	V bad	High	Full
PET/ SPECT	fmol (10^{-15})	Low	High	V large	Bad	V High	Full
US	nmol (10^{-9})	High	Low	Small	V good	Low	cm

1.2 Novel imaging requirements

Starting in the mid-1990s advances in molecular and cell biology brought about a desire to visualize in the living organism biological processes at the cellular and molecular level to better study and understand disease progression and evaluate treatment [2]. Previously such parameters could be studied only indirectly through observing physiological abnormalities or by histology after excision. By bringing

together multiple disciplines such as biology, chemistry, pharmacology, physics, mathematics and engineering the field of “molecular imaging” introduced a new paradigm to biological and medical imaging. It became now possible to observe pathological pathways and drug response, to monitor the distribution and uptake of targeted drugs, and to quantify relevant parameters [3, 4]. A natural extension to nuclear medicine, molecular imaging research initially focused on PET and SPECT imaging. However, disadvantages relating to the use of ionizing tracers and cost in case of PET or low spatial and temporal resolution in case of SPECT drove the development of optical methods based on bioluminescence, fluorescence and photonic absorption [5]. Their low cost, ease of use and the increasing availability of fluorescent contrast agents facilitated the development of tomographic methods such as diffuse optical tomography [6] and fluorescent molecular tomography [7], which both achieve penetration depths in tissue of few cm and resolutions on the mm scale. Above all however, optical contrast is a powerful source of cellular and molecular information, especially when combined with multi-spectral techniques [8-10]. Intrinsic tissue chromophores, such as hemoglobin, melanin or lipids, can be used to determine for example the oxygenation state of tissues or their composition. To achieve higher specificity and sensitivity numerous targeted and untargeted contrast agents can be used. Extrinsically administered optical compounds, such as organic dyes, plasmonic particles or fluorochromes, have already shown their clinical potential for example in oncology research [11] or drug discovery [12]. However, to effectively leverage this potential in a clinical setup, higher resolution at tissue depths up to a few cm is required. This can be achieved using the photoacoustic effect, first described by Alexander Graham Bell in 1880 [13] and only much later applied in a biological context by Rosencwaig [14].

Since then optoacoustic (photoacoustic) imaging has emerged as a non-ionizing imaging technique that provides information on optical absorption in tissue up to a few centimeters tissue depth. It achieves ultrasonic resolution from few hundreds to tens of micrometers with strong optical contrast. Thereby tissue is illuminated with an ultra-short laser pulse (10-100 ns). Part of that energy is absorbed and converted into heat, which in turn causes a thermo-elastic expansion followed by the generation and propagation of ultrasound waves. By means of ultrasound detectors one-dimensional time signals can then be acquired. To form an image of the optical absorption the region of interest has to be interrogated at multiple tomographic detection positions. Depending on this detection geometry various inversion algorithms are available. On the excitation side, the typical wavelength range (650 – 950 nm) used in optoacoustics is known as the “diagnostic window”, because the molar extinction coefficients (MEC) of oxy- and deoxy-hemoglobin show a significant drop, thus allowing for deeper light penetration in tissues.

The foundations for optoacoustic imaging were laid in the late 1980s and 1990s when the first theoretical and experimental work treated optoacoustic signal generation, acquisition and reconstruction [15-18]. On the other hand non-invasive imaging of small animals *in vivo* was first introduced by Wang et al. in 2003 as a single element scanning setup [19]. Since then numerous systems have been developed that

use single detectors, scanned in one or more dimensions [20-22], detector arrays shaped in one dimension along linear, curved or circular trajectories [23-26] and two-dimensional detector compositions, whose elements are distributed on planar or curved surfaces [27-29].

1.3 Non-invasive clinical optoacoustic imaging

Early in the development of optoacoustic imaging technology applicability to the detection of breast cancer was considered [30, 31], due to the high prevalence and the advantageous optical and geometrical properties of the breast. The reduced light absorption allows deeper light penetration while the breast's shape allows for spherical array detection. Hence, 3D imaging up to a depth of 40 mm below the skin surface has been reported [32]. Although the application certainly is worthy of investigation and achieved results are impressive, limitations may not be easily addressed. A general problem in 3D imaging is the number of projections necessary to achieve high-resolution within a large volume of interest. Thus 3D systems typically require scanning, which may be incompatible with real-time imaging, especially when the tissue is interrogated using multiple wavelengths to incorporate spectral information into the dataset; the alternative being lower resolution and reduced volume of interest or higher repetition rate lasers at reduced pulse energy, which again lowers the achievable penetration depth and reduces the signal to noise ratio (SNR). However a more practical impediment to clinical propagation is the limited use of the proposed systems in terms of application to other body parts, due to the stationary design.

An alternative handheld design for clinical use was first proposed by Niederhauser et al. in 2005 [33] and subsequently also implemented by others [24, 34-39]. Common to all systems is the use of a standard linear ultrasound array, cylindrically focused in elevation and employed with an ultrasound pulser for pulse-echo ultrasound imaging as well as for receive-only optoacoustic imaging. In optoacoustic mode, illumination is provided by a combination of output-shaped fiber bundles and various other optical components. Thereby light is delivered either on one or both sides of the main (linear) array axis; except in [39] where the illumination is well aligned with the acoustic field of the array. While such integrated or clip-on arrangements have some desirable properties such as the ability to generate inherently co-registered ultrasound and optoacoustic images, a small footprint and a high degree of flexibility, they significantly limit achievable optoacoustic image quality and penetration depth. The use of linear arrays for optoacoustic imaging is further discussed in detail in chapter 4.

Finally, it is worth mentioning that some progress has been made recently towards non-invasive handheld imaging in 3D [40]. The system described in [40] arranged individual detectors on a two-dimensional partially spherical surface. Illumination in this design is provided by a round-output fiber bundle, which is located at the center of the surface and pointed at the volume of interest. In this configuration volumetric imaging at 10 Hz repetition rate and up to several mm below the skin has been demonstrated. However, this design involves trade-offs that restrict its application to cases where the

volume of interest is small (<10 mm diameter) and close to the skin surface, i.e. up to a few mm tissue depth. A fundamental limitation common to most 3D systems is the number of individual detectors that can be employed per area, i.e. single element size and field of view. While a higher detector density is desirable for both a larger region of interest and higher resolution, available technology imposes lower limits on element size due to achievable SNR and also on the total number of elements that can be sampled in parallel. Additionally, the two-dimensional probe surface increases its footprint and weight, thus limiting access or usability; a limitation that becomes worse when increasing the radius of the detection surface to accommodate more elements and increase the field of view. Thus the characteristics of a versatile optoacoustic probe for handheld clinical imaging of human patients can be stated as follows.

1. High image quality

Anatomical features should be preserved; in particular vessels should be depicted as round in a cross-sectional view perpendicular to the vessel length. This is of major importance to understand probe movement and allow better co-registration with other modalities, for example ultrasound. In addition a good signal-to-noise ratio (SNR) is required on a per frame basis, as averaging is not available due to movement of probe and patient. Additionally, artifacts should be avoided or sufficiently suppressed during inversion or post-processing to enable better contrast.

2. Large field of view

Field of view refers to the total area or volume where detectable signals have been induced. On the other hand the effective field of view can be defined as a subset thereof, limited by a measure of achievable resolution. For diagnostic imaging in humans both need to be large. The overall visibility field should be large enough to reflect underlying anatomy, which is necessary for navigation or probe positioning in a handheld mode of operation. However the effective field should be equally large to capture with good accuracy and resolution the organ or site of investigation.

3. Deep tissue penetration

In humans imaging of even superficial organs or tissues requires at least a penetration depth below the skin surface of 20-30 mm. For example the tissue depth of the human carotid can easily reach 30 mm or more, depending on a patient's physical constitution; a diseased thyroid may reach even deeper.

4. Resolution

Given the previous requirements, resolution may be adjusted by the individual use case, however should generally be on a sub-millimeter scale. Moreover, to cover many use cases the detection array should be able to capture with good sensitivity signal frequencies corresponding to 100-200 μm .

5. Small footprint

To be versatile, i.e. applicable to multiple body parts, and also support precise positioning the probe should require a minimal contact surface on the patient. Ideally it should enable visual inspection by the operator of the illuminated surface area.

6. Light weight

Consequently, versatility and ease of use require a handheld design that is sufficiently light-weight to avoid operator fatigue and allow precise positioning.

1.4 Objectives and outline

The overall goal of the present work was to identify and develop handheld optoacoustic imaging solutions for point of care and intraoperative clinical applications. Priority was given to system parameters relating to penetration depth and versatility. To this end we followed an application driven approach, identifying fields of clinical practice where diagnostic value could already be generated with available contrast mechanisms and technology. Due to the high prevalence of diseases of the cardio-vascular and endocrine systems, we chose imaging of the anterior neck region as a first objective. This approach appeared particularly promising, due to the proximity and comparable tissue depth of the common carotids (atherosclerosis) and thyroid gland (various diseases). The second objective concerned intra-operative assessment of tissue viability, which is mandatory during any surgical procedure. Quantitative assessment is especially desirable when tissue perfusion is weak even in healthy tissue. Hence, we chose a specific application, cancer resection and anastomosis in the lower colon, to develop tools and methods for obtaining quantitative measures on blood perfusion and tissue oxygenation. Finally, a third objective were improvements of key hardware and algorithmic components, and the advancement of understanding of detector design.

In **Chapter 2** we reproduce fundamental theoretical, technological and algorithmic concepts necessary to understand experimental results and decisions regarding systems design. **Chapter 3** details the derivation of and reasoning for the proposed imaging systems. **Chapter 4** expands upon the configurations presented in the previous chapter and introduces mandatory improvements to ensure clinical deployability, e.g. real-time image reconstruction algorithms or array density. **Chapter 5** summarizes the two applications in terms of clinical relevance, available alternative imaging methods and the benefit expected from the adoption of optoacoustic imaging. Subsequently, in **Chapter 6** results obtained in-vivo from human volunteers are presented for the non-invasive imaging probe, and from mice and porcine tissue samples in case of the intra-operative setup. Finally, in **Chapter 7** we conclude with a discussion of achieved results, highlight necessary developments to realize high impact clinical studies and illuminate possible avenues to a future where optoacoustic imaging routinely improves clinical outcome.

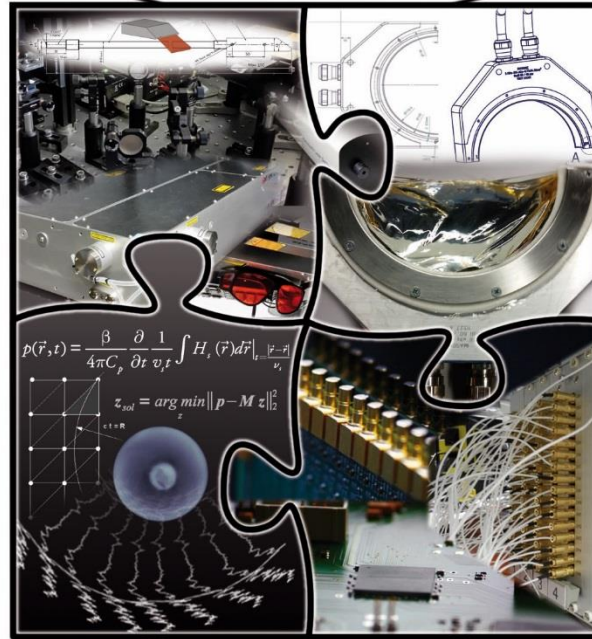
Optoacoustic imaging: instrumentation and theory

In 1880 Alexander Graham Bell discovered the photoacoustic (also optoacoustic) effect, which describes the generation of acoustic waves arising from the absorption of focused light with transient amplitude [13]. Not only did he discover the physical principle, he also determined that different materials produced different acoustic spectra (i.e. sounded differently), which also depended on the spectrum of the employed light source. Bell applied his knowledge to build a device, the Spectrophone [41], to measure the optical absorption characteristics of materials. While theoretically sound, the Spectrophone was neither sufficiently sensitive nor quantitative, because the technology needed for implementation was unavailable. It took almost 100 years of technological advancement to re-start scientific interest in applying the photoacoustic effect to measuring optical properties of materials and tissue [14]. Today significant progress in optics, electronics, material and computer sciences allows us to consider implementing optoacoustic imaging for the benefit of the patient.

In the following we will re-examine all aspects of optoacoustic imaging that are critical to designing clinical optoacoustic imaging systems. First, we consider the basic concepts regarding the fate of photons in tissue, the propagation of sound and also the optoacoustic chain of events giving rise to the optoacoustic signal. We then focus on the four cornerstones of optoacoustic technology, depicted in Figure 2.1, which drive the development of optoacoustics and are themselves driven by it.

Illumination

Detection



Reconstruction

Data acquisition

Figure 2-1 – Essential aspects of optoacoustic imaging

In the beginning there was light – laser light to be more precise. We will review all components necessary to generate and deploy ultra-short pulsed monochromatic light on tissue, from the fundamental principles of Light Amplification by Stimulated Emission of Radiation (LASER) to optical parametric oscillators (OPO) to light-guiding and -shaping optics. Next we discuss methods for the detection of acoustic waves in tissue with special attention given to piezoelectric materials, which at the time of writing represent the method of choice in the construction of shaped detector arrays discussed separately. The third component, data acquisition, bridges the gap between an analog world and the digital domain wherewith which we are so accustomed to work in. As reviewing all components involved in this endeavor (such as FIFOs, bus systems or various microcontrollers) is beyond the scope of this work, we will highlight only the most important concepts necessary to leverage optoacoustic imaging from a sequential bench-top scanning modality to a fully parallel array-based implementation. Once in the digital domain, we review two of the most widely used algorithms employed in the reconstruction of optoacoustic images from a set of one-dimensional acoustic signals. Finally, we also introduce the core principle of MSOT as well as available methods for spectral unmixing.

2.1 Propagation of light and sound in tissue

2.1.1 Light and tissue

The interactions of light with matter, and biological tissue in particular, are so manifold that they give rise to numerous optical imaging techniques ranging from simple photography to more advanced methods utilizing for example coherence, polarization or fluorescence. Thereby interactions can be studied by employing either the particle nature of light (photons) or its wave nature (electro-magnetic waves), depending on the effect one intends to elucidate. For example, the term “light” is commonly understood to mean electro-magnetic waves within the visible wavelength range, i.e. ultra-violet (300nm) to near-infrared (750nm). In the context of optoacoustic imaging we are mostly interested in the particle nature of light and two phenomena of light-tissue interaction that determine optoacoustic contrast: the first, **absorption**, is the source of the optoacoustic signal, which linearly depends on the amount of light absorbed; the second, **scattering or diffusion**, determines how much light fluence is locally available to be absorbed and thus also influences the achievable signal strength. In the following we summarize aspects of photon propagation in biological tissue that are described with much more detail in chapter 5 of reference [42].

Viewed at the molecular level light is a stream of photons, quantities of electromagnetic energy without mass or electric charge propagating at the speed of light and a given direction. When a photon interacts with an atom or molecule without transferring energy, the process is known as elastic or Rayleigh scattering, which may change the photon’s direction of propagation but does not change its wavelength – assuming particle speed remains unchanged (constant frequency). The relativistic relation between photon energy E , speed c and wavelength λ is given by

$$E = h\nu = h \frac{c}{\lambda}, \quad (1)$$

where h is Planck’s constant and ν the frequency of oscillation. Figure 2.2 depicts elastic scattering events for (a) one photon and one molecule, (b) one photon and multiple molecules and (c) multiple photons and multiple molecules.

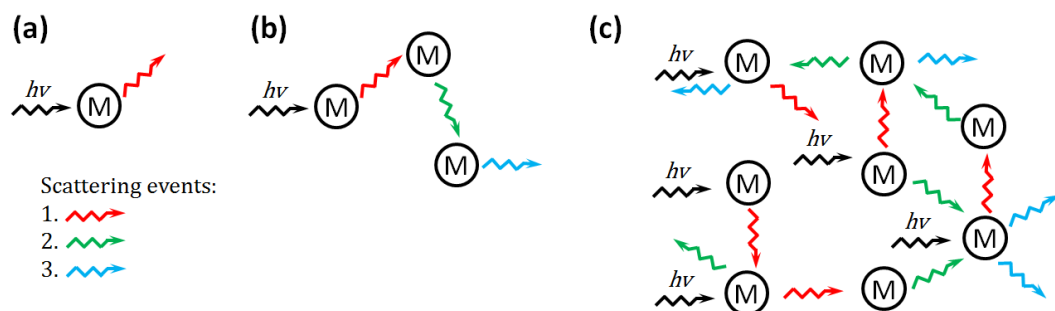


Figure 2-2 – Scattering at the molecular level. Photons ($h\nu$) undergoing elastic scattering with molecules (M), up to three scattering events are shown.

On the other hand a photon is absorbed, i.e. transfers its energy to the molecule and ceases to exist, if the energy it carries equals the difference of two molecular energy levels. To return to a stable energy level the absorbed energy must be released by either radiative or non-radiative decay. Radiative decay describes the re-emission of a photon carrying the same energy (elastic scattering) or less energy (longer wavelength) compared to the absorbed photon. Re-emission of longer wavelength photons is usually termed fluorescence and requires a further (non-radiative) decay of overhead energy, which is most commonly achieved through vibrational relaxation, i.e. collisions with surrounding molecules. At the macroscopic level the absorptivity of a molecule is described by the molar extinction coefficient (MEC) that measures absorption as a function of concentration and path length and is also dependent on the incident wavelength. The MEC can be obtained by producing a non-scattering solution of known concentration (of the molecule of interest) and employing a spectrophotometer to irradiate (irradiance I) a known volume (path length L) and measure the transmitted irradiance (I_0).

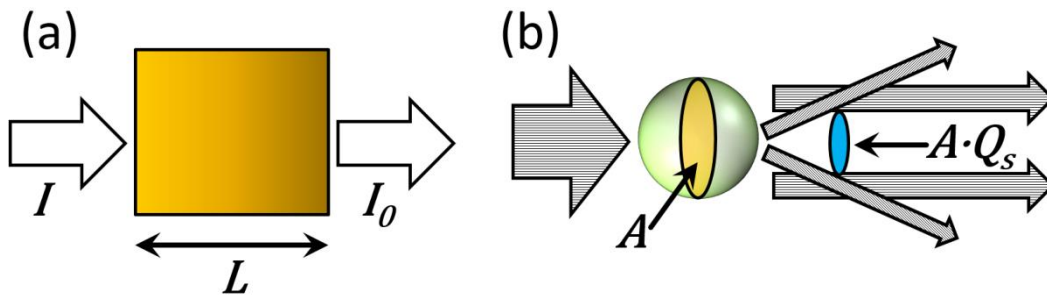


Figure 2-3 – (a) Setup employed to measure the absorption coefficient of chromophores. (b) Simplified analogy employed in the definition of the scattering coefficient.

Figure 2.3(a) illustrates the setup that allows the definition of an absorption coefficient μ_a per propagation length, historically defined in $[\text{cm}^{-1}]$ and using the natural logarithm (\ln).

$$\mu_a = -\frac{1}{L} \ln \frac{I}{I_0} \quad (2)$$

Alternatively, absorbance or optical density (OD) is often used to define absorptivity of fixed-width samples, by quantifying transmittance using a logarithm of base 10:

$$OD = -\log_{10} \frac{I}{I_0} = \mu_a \frac{L}{\ln(10)}. \quad (3)$$

Both quantities linearly depend on concentration C as stated by the Beer-Lambert law, which can be used to define the MEC ε as

$$\varepsilon = \frac{OD}{CL} = \frac{\mu_a}{C \ln(10)}. \quad (4)$$

A similar macroscopic perspective is also instructive when considering the effect of scattering on the available light fluence over tissue depth. While individual scattering

events, as described in Fig. 2.2(a), have a high probability of re-emission in the forward direction, the cumulative effect of multiple events reduces this probability with increasing number to the point where photon propagation is fully diffusive and thus completely loses directionality. In biological tissues this state is reached already after about 1 mm [43]. Figure 2.4 illustrates the increasingly diffusive pattern produced when increasing the number of scattering events per propagation length of an initially directional incident beam.

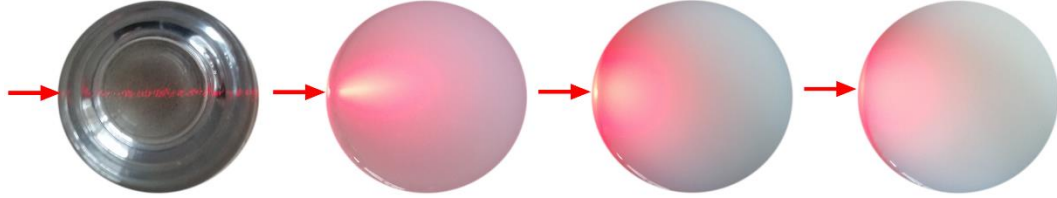


Figure 2-4 – Effect of increasing density of scattering events (left to right, red arrow indicates source of illumination): directional beam propagating in water with increasing amounts of lipid added.

In analogy to the absorption coefficient the scattering coefficient μ_s can be defined in [cm^{-1}] by introducing a surrogate for the probability of photon redirection. Such a simplified schematic is illustrated in Figure 2.3(b): a spherical entity of cross-section A may scatter a stream of incident photons by redirecting those photons whose trajectory is closest to the center of the sphere, thus leaving a gap between photons whose direction it did not alter. Assuming a concentration C_s of scattering particles defined per volume in [cm^{-3}] and a dimensionless parameter Q_s describing the scattering efficiency of the scattering particle species, we can define μ_s as

$$\mu_s = C_s A Q_s \quad (5)$$

and are able to determine the probability of photon transmission T over the path length L without redirection as

$$T = e^{-\mu_s L} . \quad (6)$$

In the human body most tissues are of highly scattering and absorbing nature. Furthermore, most body parts feature an elaborate composition of different tissues such that any sample under investigation is characterized by significant heterogeneity of optical properties. Therefore, an analytical expression of the available light fluence at a given tissue depth is generally not available, but rather subject of optical tomography methods [44]. To nonetheless approximate the dependency of fluence over tissue depth we can assume a homogeneous tissue mass with average properties for scattering and absorption. In this case we can apply the solution presented in table 5.2.2 of reference [42]. If we further assume constant illumination (i.e. $\varpi = 0$) over a broad surface for the duration of the light pulse, we obtain the following expression for fluence $\Phi(\vec{r})$ as a function of distance $r = \|\vec{r}\|$:

$$\Phi(\vec{r}) = \Phi_0 e^{-r \sqrt{\frac{\mu_a}{D}}} . \quad (7)$$

In eq. (7) we used the diffusion coefficient $D = 1 / (3 \mu_s' + 0.6 \mu_a)$, which includes the reduced scattering coefficient μ_s' and a weighting of 0.6 for μ_a , which has been found empirically when illuminating biological tissue in the near-infrared window. The reduced scattering coefficient $\mu_s' = \mu_s (1 - g)$ links the molecularly observed anisotropy of tissue particles (i.e. preference for photon re-emission in the forward direction) to the scattering behavior measurable at the macroscopic level. In most biological tissues μ_s' has been found to be two orders of magnitude higher than μ_a , which underlines the difficulty of purely optical methods when imaging biological tissue. In turn equation (7) also highlights the severe decay of available light fluence exponentially amplified by strong optical absorption and scattering.

In addition to the properties discussed so far, both scattering and absorption exhibit a dependence on the wavelength of the incident photons. Since this dependence is stronger in case of absorption, which is the primary contrast mechanism for optoacoustic imaging, and also because in optoacoustics we usually cannot measure scattering, it is worth recalling the spectral dependence of major tissue chromophores, i.e. intrinsic light absorbing molecules. Figure 2.5 depicts the molar extinction coefficient spectra for deoxygenized hemoglobin (Hb), oxygenized hemoglobin (HbO₂), water (assuming a molar concentration of 55.3 M for water at 25 °C), lipid (assuming a molar concentration of 1.1 M) and melanin, plotted on a logarithmic scale. Using figure 2.5 we can compute the expected μ_a for specific tissues. For example arterial blood has an approximate water content of 75%, assuming 55% of blood volume is plasma (of which 92% is water) and 40% cells (of which 60% is water). At 800 nm this yields an absorption coefficient of 0.035 cm⁻¹ for the water content of blood. On the other hand 99% of hemoglobin in arterial blood is oxygenated and at 800nm yields μ_a of 4.37 cm⁻¹, if we assume an average hemoglobin mass of 150 g per liter blood (molecular weight of Hb 64,500 g/mole). Hence the absorption contribution of water at 800nm can be neglected in blood. The equivalent values at 700nm and 950nm would be 0.011 / 0.512 cm⁻¹ for water and 1.55 / 6.45 cm⁻¹ for HbO₂. These values illustrate why the spectral window between 700–950nm is well suited to medical optical imaging: no significant contribution of water (which dominates absorption beyond 1000nm) and reduced absorption by hemoglobin compared to the visible wavelength range. At the same time the contribution of water absorption has to be considered when illuminating through a body of water; after just 3 cm of water almost 80% of energy at 850nm has been lost before reaching its destination.

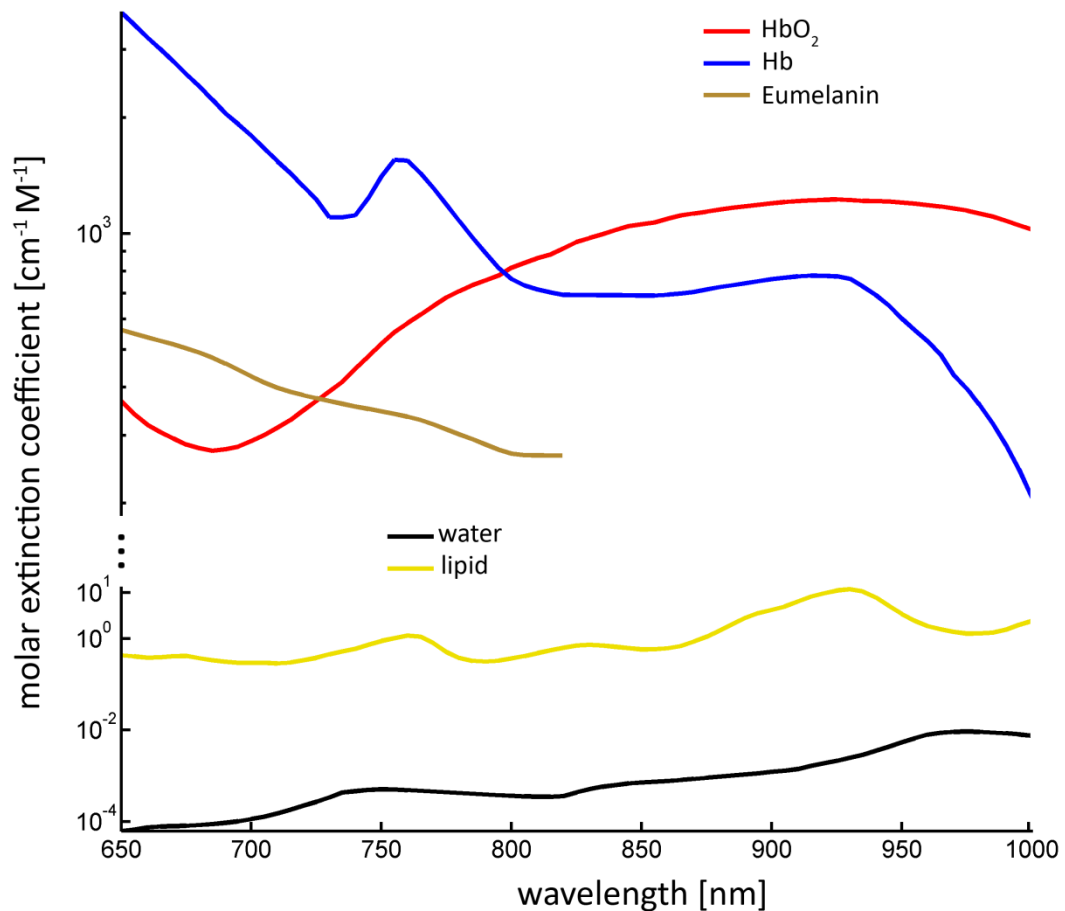


Figure 2-5 – Molar extinction coefficient of major intrinsic tissue chromophores: de-oxygenated (Hb) and oxygenated hemoglobin (HbO₂) data compiled by Scott Prahl (Oregon Medical Laser Center / OMLC), water (inferred from [45]), lipid (from [46] by approximating molecular composition, weight and density of purified pig oil) and eumelanin (from OMLC who deduced data from [47]).

2.1.2 Sound and tissue

Sound, unlike light, is the result of mechanical oscillations of particles. In tissues, where due to the high content of water a fluid model is usually adopted [48], sound takes the form of longitudinal compression waves with particles moving back and forth along the direction of propagation. When the frequency of oscillation reaches into the MHz regime, we talk of ultrasound.

Although particles are disturbed from their resting position by a physical force, in the case of sound this force is not sufficient to permanently displace them. Instead the force is transmitted to neighboring particles that may not re-transmit the force fast enough, in which case involved particles are compressed. When the local pressure reaches its maximum an opposing force is induced that pushes particles towards their equilibrium and beyond. This process can be visualized as a network of springs being disturbed by the application of force. The physical properties of the medium (e.g. type of tissue) that determine the amplitude of local pressure and time to re-transmission are density (number of particle interactions per unit of volume) and adiabatic

compressibility (maximum particle density reachable without transfer of heat or matter). Using these quantities we can define the speed of longitudinal wave propagation as

$$c_L = \sqrt{K \frac{1}{\rho}}, \quad (8)$$

where ρ is the density of the medium and K the bulk modulus of elasticity corresponding to the force resisting compression. Another concept employed in the study of ultrasound wave propagation is the acoustic impedance Z (measured in Rayl or $\text{kgm}^{-2}\text{s}^{-1}$) and derives from the same physical properties of the medium:

$$Z = \sqrt{K\rho} = \rho c_L. \quad (9)$$

Using acoustic impedance, the localized instantaneous pressure induced by particles displaced by a length ∂u within a time ∂t , i.e. with particle velocity of $v_d = \partial u / \partial t$, is given as

$$p = \rho c_L v_d = Z v_d. \quad (10)$$

We note that the quantity accessible by measurement is an intensity I that relates to pressure by $I = p^2 Z$. We further introduce the wavenumber k , a notion often employed when describing waves in the spatial domain. Analogous to the time domain ($\text{Hz} = \text{s}^{-1}$), spatial frequencies are the reciprocal of the wavelength λ and hence the wavenumber is defined as

$$k = \frac{2\pi f}{c_L} = \frac{2\pi}{\lambda}. \quad (11)$$

The three-dimensional wave equation describing the propagation of pressure in time and space can be formulated as

$$\nabla^2 p - \frac{1}{c_L} \frac{\partial^2 p}{\partial t^2} = 0. \quad (12)$$

For propagation in a homogenous medium we could substitute pressure for particle velocity (v_d), as stated in eq. 10. Often an artificial velocity potential Φ is substituted instead, by defining

$$v_d = \nabla \Phi \quad \text{and} \quad p = -\rho \frac{\partial}{\partial t} \Phi. \quad (13)$$

A solution to eq. 12 in spherical coordinates can be found for an outwards traveling spherical wave as

$$p(r, t) = \frac{p_0}{r} RE[e^{i(\omega t - kr)}] = \frac{1}{r} p_0 \cos(\omega t - kr). \quad (14)$$

Eq. 14 tells us that the intensity of an acoustic wave will degrade with the square of distance traveled. In addition acoustic attenuation, due to acoustic absorption and scattering, further reduce the measurable intensity. The situation is comparable to, yet

significantly better than, the propagation of light (when considering its wave nature). While light scattering was by far the dominant contributor to light attenuation (100x stronger than absorption), the ratio is much more favorable for ultrasound attenuation. According to [49] scattering contributes about 10-15 % in soft tissues, while the rest is due to acoustic absorption, which is not yet fully understood. However, in general ultrasound attenuation in tissue can be formulated as an exponential decrease following

$$p = p_0 e^{-\alpha r}, \quad (15)$$

where r denotes the distance traveled and α is an empirically determined and frequency dependent attenuation coefficient defined in [$\text{cm}^{-1}\text{MHz}^{-1}$]. In soft tissues α is in the range of $0.0576\text{--}0.1151 \text{ cm}^{-1}\text{MHz}^{-1}$ for frequencies up to 50 MHz; in distilled water the attenuation can be extrapolated from measurements made by Pinkerton [50]. Figure 2.6 illustrates transmission of ultrasound up to 7.5 MHz through several path lengths of water and tissue.

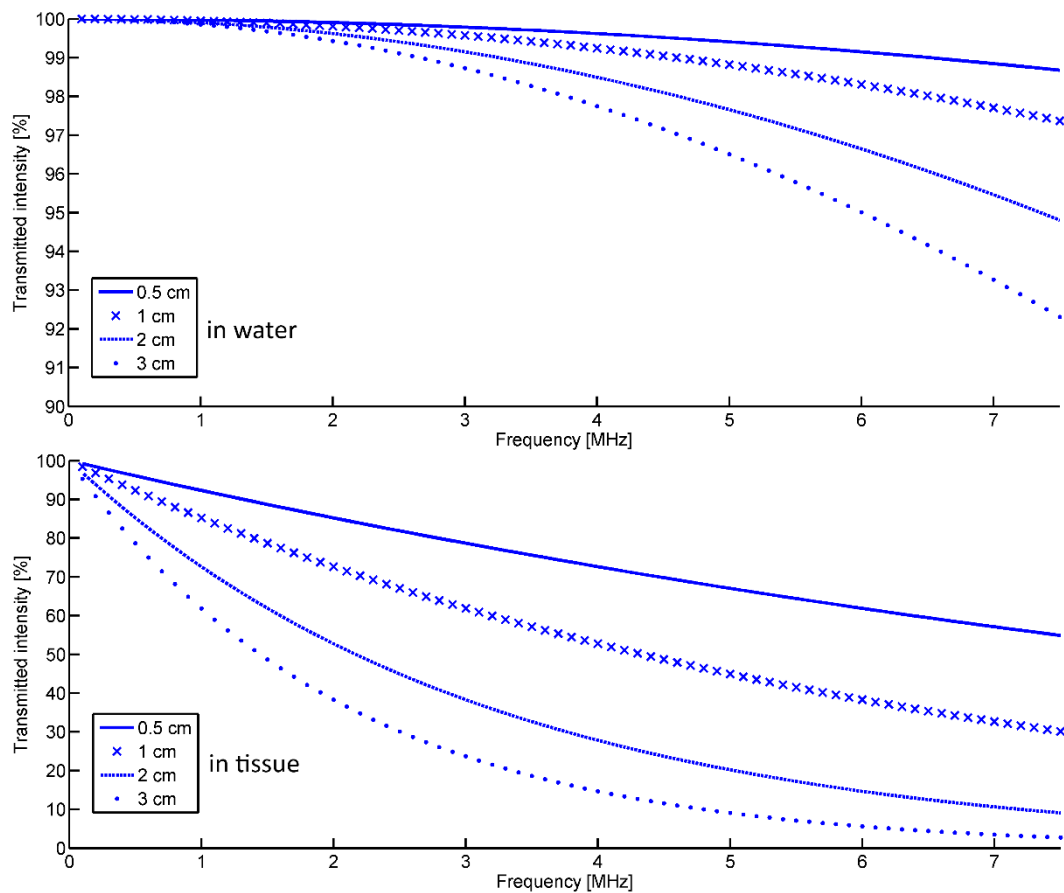


Figure 2-6 – Measured signal amplitude versus frequency of a longitudinal acoustic wave after travel through 5mm, 10mm, 20mm and 30mm of (top) distilled water and (bottom) average tissue.

Specular reflection and refraction, describes the situation when an interface between two tissues of different acoustic impedance is smooth and large compared to

the wavelength of the acoustic wave incident on it. The angle of reflectance and transmittance can be determined according to Snell's law

$$\frac{\sin \varphi_2}{c_2} = \frac{\sin \varphi_1}{c_1}, \quad (16)$$

which links the speed of sound in tissue 1 (c_1) and tissue 2 (c_2) to the incident angle (φ_1 , angle between the normal to the interface and the propagation direction of the wave) and the transmittance angle (φ_2 , angle between refracted propagation direction and normal). Note that the angle of propagation of the reflected wave equals the negative incident angle relative to the normal of the interface. For normal incidence (perpendicular to interface) intensity coefficients of transmission (T) and reflection (R) can be derived that require only knowledge of the acoustic impedances of the two tissues (Z_1, Z_2):

$$T = \frac{4Z_1Z_2}{(Z_1 + Z_2)^2} \quad \text{and} \quad R = \left(\frac{Z_1 - Z_2}{Z_1 + Z_2} \right)^2. \quad (17)$$

Due to only small variations of acoustic impedance in soft tissues, i.e. $Z_1 \approx Z_2$, most energy of an acoustic wave is transmitted without major re-direction. These properties enable deeper interrogation of tissue using ultrasound compared to optical methods. Consequently, ultrasonography must apply high intensities when sending, since reflections are weak and the tissue in between sender and the reflecting interface has to be traversed twice before receiving the echo. On the other hand an interface where the two tissues or regions have significantly different acoustic properties (like bone or air), will reflect most of the wave energy and become virtually impassable to ultrasonic waves.

2.2 The Photoacoustic effect

The Photoacoustic (also Optoacoustic) effect describes the generation of pressure waves by light absorbing particles upon illumination with light of time-variant amplitude. While the effect itself had already been observed by Alexander G. Bell in 1880, the field only took off in the 1980s, empowered by the rise of novel light sources such as lasers and the availability of advanced electronics for detection and computational evaluation. Over the last 30-40 years a large number of original contributions and reviews have been published that study the generation and nature of sound produced in various materials and states of matter (gaseous, liquid or solid). And not always had the transient temperature increase been induced by electro-magnetic waves from the visible or near-infrared wavelength range, hence the phenomenon is sometimes also referred to as the Thermoacoustic effect. One of the latest reviews available [51] also includes references to these more general applications. In this work however we concentrate on nanosecond pulsed laser illumination in the near-infrared wavelength range (680-950nm). Further we consider only generation and propagation of

ultrasound in biological tissue (human in particular). Therefore we describe the optoacoustic effect and relevant guiding equations from a practical point of view – leaving out theoretical aspects such as equations for 2D or infinite detection surfaces be they layers or cylinders.

In general when considering the effect of quasi-instantaneous (thermal) energy deposition within a limited volume, we have to observe the laws of thermodynamics. Applied to our scenario we can assert: if, within the duration of the pulse, the deposited energy cannot leave the heated volume (thermal diffusion) and cannot be transferred by means of mechanical work (volume expansion or stress relaxation), then it must give rise to a pressure increase. As soon as the light is switched off, a quasi-instantaneous increase in volume causes the generation of ultrasonic waves – we refer to this period as the thermoelastic expansion. Tissue parameters that determine the required laser pulse length are the speed of sound (v_s), the thermal diffusivity (α_{th} in m^2/s) and the size of the spherical volume considered (represented by the diameter d_c that equals the resolution to be achieved). A thermal relaxation time τ_{th} and a stress relaxation time τ_s can be defined as:

$$\tau_{th} = \frac{d_c^2}{\alpha_{th}} \quad \text{and} \quad \tau_s = \frac{d_c}{v_s} \quad (18)$$

When the optical pulse length is significantly shorter than both times in eq. 18, we refer to thermal and stress confinement and are able to derive the optoacoustic wave equation linking the heating function $H(\vec{r}, t) = \eta_{th}\mu_a(\vec{r})\Phi(\vec{r})\delta(t)$ and the pressure $p(\vec{r}, t)$:

$$\left(v_s^2 \nabla^2 - \frac{\partial^2}{\partial t^2} \right) p(\vec{r}, t) = -\Gamma \frac{\partial H(\vec{r}, t)}{\partial t} \quad (19)$$

We note that $H = 0$ for $t > 0$, i.e. heating is instantaneous, H further linearly depends on the available light fluence Φ and optical absorption μ_a (η_{th} is approximately constant and describes the conversion efficiency from electro-magnetic to thermal energy). The dimensionless Grüneisen parameter Γ can be assumed constant in tissue of approximately constant temperature – the global temperature increase due to optical heating is negligible (the temporal gradient gives rise to the optoacoustic signal!). As the heating function depends only on space but not time, i.e.

$$H(\vec{r}, t = 0) = \eta_{th}\mu_a(\vec{r})\Phi(\vec{r}) = H_s(\vec{r}) \quad \text{and} \quad H(\vec{r}, t > 0) = 0,$$

we can describe the pressure $p(\vec{r}, t)$ at a point in time $t > 0$ and spatial position \vec{r} as

$$p(\vec{r}, t) = C \frac{\partial}{\partial t} \left(\frac{1}{v_s t} \int_{v_s t = |\vec{r} - \vec{r}'|} H_s(\vec{r}') d\vec{r}' \right). \quad (20)$$

Equation (20) gives the forward solution of the optoacoustic wave equation, where C is a constant related to heat capacity and volume expansion (including the Grüneisen parameter), v_s the speed of sound and H_s describes the spatial heating function that is directly proportional to the pressure field at $t=0$. A geometrical interpretation of the forward solution is this: an ideal point detector sampling in time the propagating wave field will sense at any time point t the sum of waves generated by sources with equal distance $r = v_s t$ from the detector as a derivative over time. Two important conclusions can be inferred from this: **(1) optoacoustic sources are highly directive**, if they appropriately align on a macroscopic scale; **(2) real detectors can introduce a geometrical impulse response**, if their finite aperture surface is not significantly smaller compared with the distance to the initial optoacoustic pressure field. We will inspect both conclusions further, but first consider what an ideal optoacoustic source looks like and what signal we can expect from it.

An analytical description of ideal optoacoustic sources can be found for example in [51]. Of those we prefer to consider only the spherical source in 3D as it lends itself well to analyses on the microscopic as well as the macroscopic scale. The ideal optoacoustic signal from a spherical source, homogenously illuminated throughout its cross-section, is depicted in figure 2.7, where some common parameters for imaging up to 7.5 MHz were assumed ($v_s=1500$ m/s, sphere diameters $d_{sph} = 150/450\mu\text{m}$).

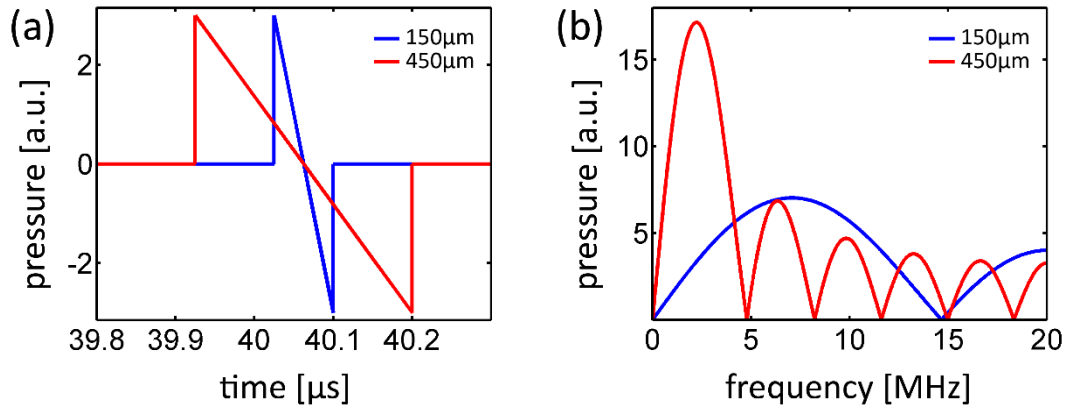


Figure 2-7 – Ideal optoacoustic signals from microspheres of different diameters: 150 μm diameter in blue; 450 μm diameter in red. The time signals are depicted in (a) and the corresponding absolute frequency domain values in (b). The larger sphere attains a frequency maximum at a lower frequency compared to the smaller sphere. Both spheres have repetitions of decreasing amplitude at higher frequencies. (a.u. = arbitrary units)

To characterize a feature size, such as the diameter of a sphere, we refer to its *central frequency* f_c defined as the frequency of the maximum amplitude in frequency domain. A rough approximation of f_c for any given feature size d_{sph} can be found as

$$f_c \sim \{0.7 \dots 0.8\} \frac{v_s}{d_{sph}}.$$

In practice however it is near impossible to measure the signals plotted in figure 2.7. First the electrical impulse response of the measurement system (detector and data acquisition) is convolved with the signal – more on the topic in chapter 2.4. Furthermore, the volume of the sphere cannot be heated uniformly as the fluence

rapidly decays towards the center of the sphere (approximations are possible for spheres small enough compared to other system parameters). Finally, the positioning of the sphere relative to the detector may influence the signal shape (geometrical impulse response discussed below). Figure 2.8 depicts an exaggerated illustration of the measurement setup and the resulting optoacoustic signal of a microsphere placed such as to avoid distortion by a geometrical impulse response and small enough to assume homogenous illumination of the sphere's volume. The electrical impulse response has also been approximately removed, nonetheless the tail following the main signal in figure 2.8(b) highlights the limited sampling bandwidth available in reality.

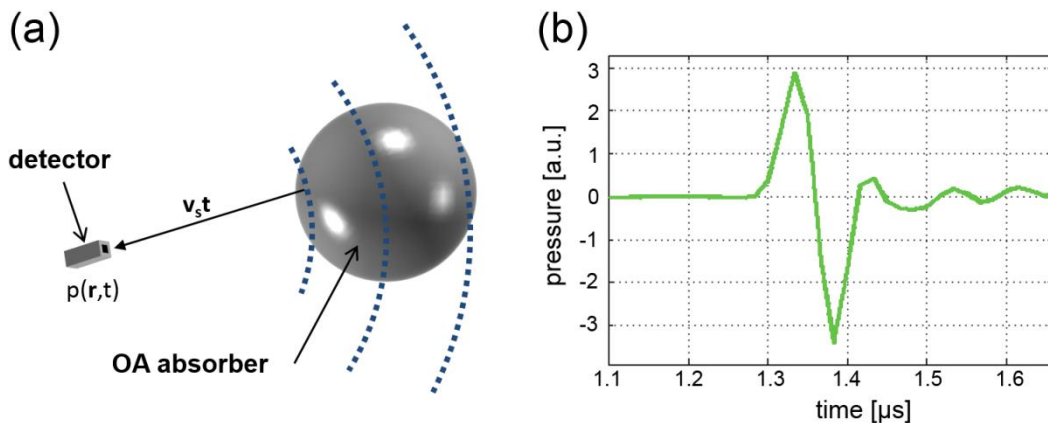


Figure 2-8 – (a) Illustration of the measurement setup used to acquire the optoacoustic signal from a microsphere, which was small enough to assume homogenous illumination of the full volume of the sphere. (b) The corresponding signal (in arbitrary units, a.u.) measured after de-convolution with the electrical impulse response and placed such as to avoid distortions by a geometrical impulse response of the detector; diameter of sphere approx. 150 μm .

Using equation (20) and the corresponding geometrical interpretation, we can theoretically study directivity of optoacoustic sources. Figure 2.9 depicts an ideal setup where a spherical source emits an ideal optoacoustic signal. In fig. 2.9(a) this signal is detected by two ideal detectors both at distance r but different angles to the source. Fig. 2.9(b) shows the same setup but for a “shaped” source, here a line, represented as a series of point sources placed close to each other relative to r . We observe that detector 2 measures largely the same signal (signals start with the first sphere). However detector 1 acquires the sum of signals from all spheres contributing to the line approximation (each signal slightly time-delayed) and thus shows a much stronger amplitude and different shape (i.e. frequency response). A similar observation but in reverse order can be made for fig. 2.9(c) where the ideal signal as depicted in 2.9(a) is also convolved with the geometrical impulse response of a line detector of identical length as the line of sources in 2.9(b). To numerically produce 2.9(c) we assumed 40 times higher density of detector segments compared to the sources in 2.9(b) and similarly delay-summed the ideal signal, albeit in a 40 times over-sampled space. The noise present in 2.9(c) was introduced by down-sampling back to the signal space and serves to remind us of band limitations of real detection elements. Further we can interpret the geometrical impulse as a kind of low-pass filter, who's strength and

frequency response varies with the angle to the source. As the wave travels along the surface of the detector different segments are compressed over time, thus lowering the maximum amplitude detected and also “smearing” the wave over time. The exact same interpretation can be applied for the directivity of optoacoustic sources – but, again, in reverse order.

In a real measurement both effects interact with each other, i.e. directivity of source meets directivity of detection. Therefore, in practice it is highly desirable to obtain measurements from as complete a tomographic projection set as possible, countering source directivity, and also to correct for the geometrical impulse response of detectors or otherwise choose a detection setup such that these effects are negligible.

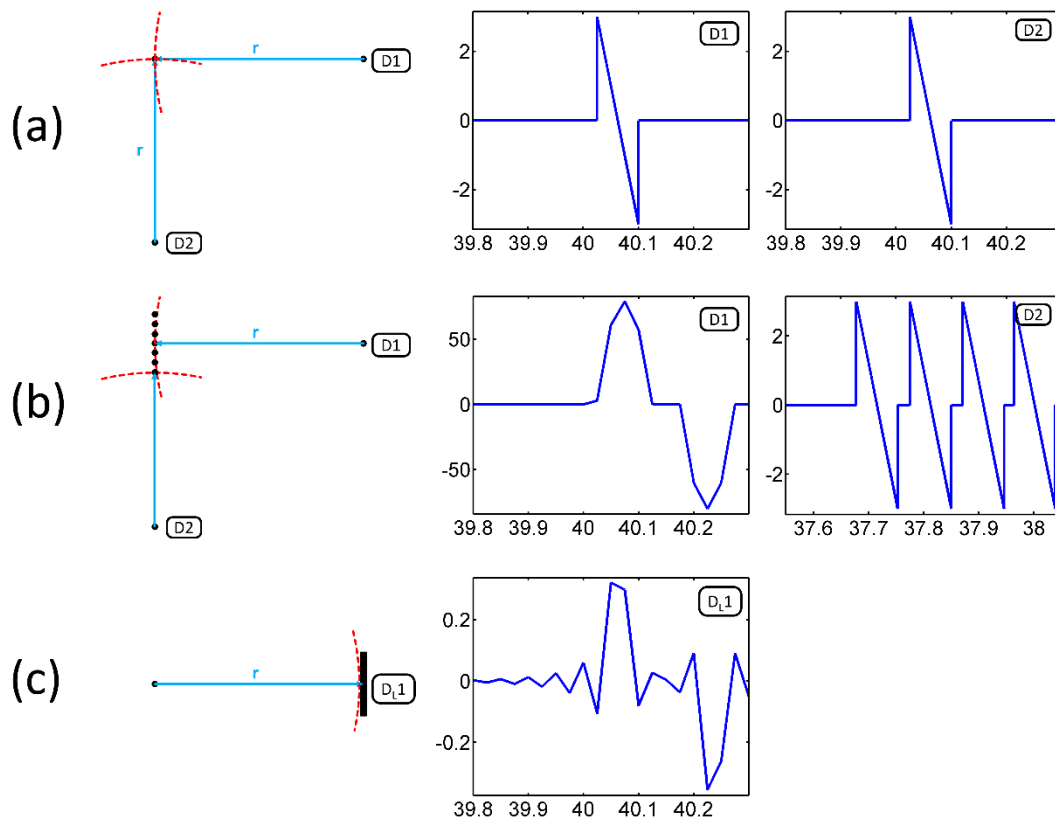


Figure 2-9 – Directivity of optoacoustic (OA) sources and detectors. Row (a) depicts two ideal detectors (D1, D2) measuring optoacoustic signals (plotted on the right) from an ideal spherical OA source at distance r . Row (b) shows the same detectors measuring signals (plotted right) from multiple ideal sources arranged in a line with distance r to detector 1 (D1). For D2 signals start with the first source viewed from D2. The red dashed lines in (a) and (b) highlight traces of integration as defined in eq. (20), i.e. v_{st} . In row (c) a line detector (D_{L1}) has the same length as the maximum distance between sources in (b) and measures signal from a single source, as in (a). The red dashed line represents the wave front. Plots show time on the x-axis and pressure on the y-axis, both in arbitrary units.

2.3 Laser excitation and illumination

To generate an optoacoustic response excitation with broad-band light (i.e. white light) of transient amplitude would suffice. However, to also apply optoacoustic spectroscopy, we require excitation by monochromatic light – or as narrow-band as possible. The principle of light amplification by stimulated emission of radiation, commonly known as laser, has been described over 50 years ago and has come to be deployed in a wide variety of applications nowadays. Similarly, related technologies such as optical amplifiers or light-guides (also waveguides) have seen rapid development in terms of application and sophistication. For the purpose of developing multi-spectral optoacoustic imaging systems an understanding of three major components involved in the generation and delivery of monochromatic light is necessary: the pulsed pump laser, the optical parametric oscillator (OPO) and the fiber bundle. Figure 2.10 shows the components in order of photon propagation (from left to right).

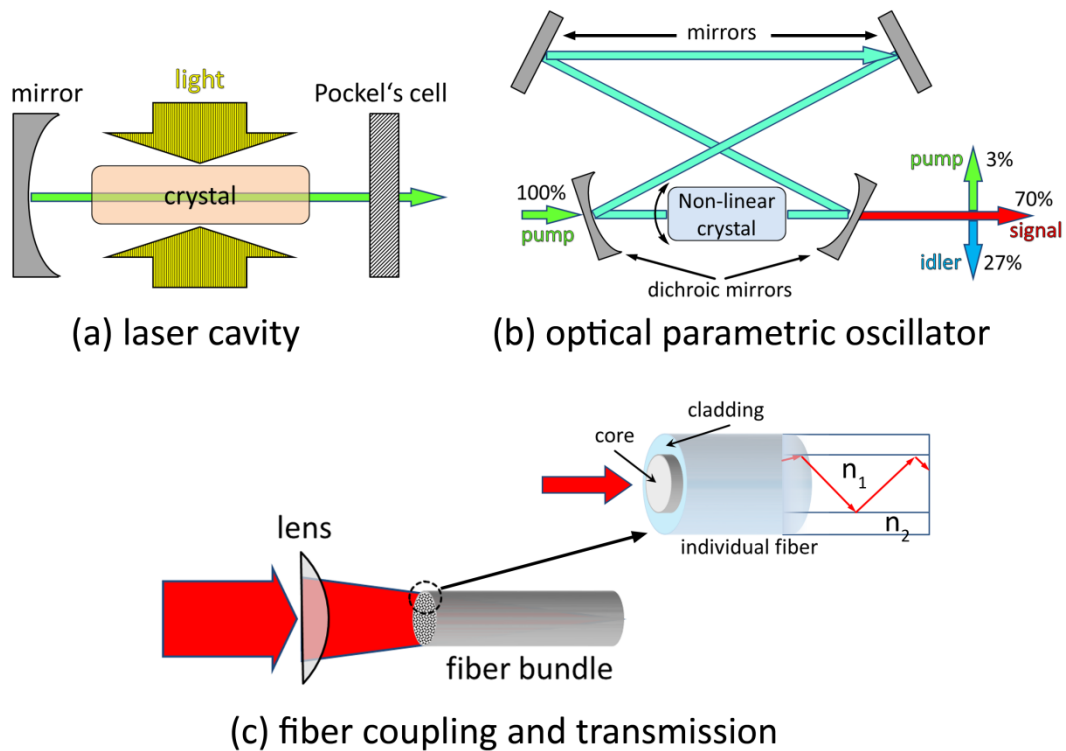


Figure 2-10 – Main stages of laser light generation and transmission. (a) The pump laser beam (green) is generated by optical excitation of a gain medium (crystal) and subsequent resonant amplification. (b) The monochromatic pump beam is tuned to the desired wavelength by uni-directional oscillation through a non-linear crystal. The pump energy is divided into the desired signal beam, the idler and the remainder of the pump. (c) The signal beam is coupled into a fiber bundle for safe and flexible transmission. Each fiber consists of two materials with different refractive indices ($n_1 > n_2$) resulting in total internal reflection. Typical transmission efficiencies of fiber bundles are between 60-70%.

The pump laser is the only active device and responsible for providing the initial energy, only a fraction of which will actually reach the tissue for imaging. At its core is a laser crystal (gain medium) where the lasing or amplification takes place. An optical pump, which can be either a flashlamp (broad-band light, low repetition rate) or an array of laser diodes (narrow-band light, high repetition rate), is used to inject an initial amount of light energy into the resonant cavity. The cavity consists of two strongly reflecting mirrors with the crystal in between. As light resonates back and forth between the mirrors it passes through the crystal where the wavelength corresponding to the physical properties of the crystal is amplified. When the peak (monochromatic) energy is reached, one of the mirrors can be turned transparent for the desired pulse-length (e.g. nanoseconds). In fact this mirror or output coupler is an electro-optical crystal whose refractive index can be almost instantly changed by application of an external voltage. In Q-switched lasers this device is usually a Pockel's cell. Other steps such as further amplification or frequency doubling may follow, but are omitted here as these stages depend on the specific implementation of a tunable pulsed laser system.

In order to address a broad range of wavelengths, in our case within the NIR, the second stage, the optical parametric oscillator (OPO), employs a non-linear material in an oscillation cavity. The setup involved is comparable to the laser setup except for the crystal and the pump, whose beam is collimated (unidirectional within a certain cross-section) and of high spatial coherence (i.e. strong correlation between E-field at different positions within the beam cross-section). The specific properties of the non-linear crystal are 1) unidirectional parametric amplification and 2) parametric sensitivity of 3) signal and idler beam generation. Figure 2.10(b) illustrates the unidirectional oscillation through the crystal between 2 dichroic and 2 highly reflective mirrors. The pump beam is thereby split into two beams of separate but complementary wavelengths, satisfying conservation of energy, i.e. $\frac{1}{\lambda_0} = \frac{1}{\lambda_1} + \frac{1}{\lambda_2}$. The parameter commonly used to achieve phase matching and thereby determine the relation between signal and idler is inclination of the crystal relative to the trajectory of oscillation, as indicated in 2.10(b). Modern tunable OPO systems employ piezo-electric rotation stages to precisely rotate the crystal into position within few milliseconds, allowing operation at 100Hz or more with a different wavelength for each pulse. As the process is non-linear, careful calibration of the rotation stage is necessary. A common problem in pumping OPOs with short pulses is that the resonance process has very little time to reach the steady state. Consequently pulse to pulse variations can be significant (10-20%) and pulse-energy measurements become mandatory on a per pulse basis. Another consequence is enlarged linewidth, i.e. range of wavelengths contained per pulse, which gradually broadens towards larger inclination angles.

Exiting from the OPO a beam usually contains three spatially mixed wavelengths (signal, idler and residual pump). For most applications, including optoacoustic spectroscopy, the idler beam is separated and dumped into a ceramic beam dump (water cooled). In newer systems the idler beam may also be redirected towards a second output. To remove the residual pump beam an optical filter can be deployed within the beam path, but this is often avoided as the signal beam is also affected

(every bit counts in optoacoustic imaging). Finally, the tuned beam needs to be deployed where it is needed, e.g. on the tissue under investigation. In a laboratory setup the still collimated beam, having very low divergence, can be guided by mirrors, lenses and other beam guiding and shaping optics. This free-beam approach however is highly susceptible to misalignment and not very flexible in terms of positioning, not to mention laser safety. Therefore, in a clinically useful probe the beam needs to be safely and flexibly guided to where it is needed. Enclosed bundles of optical fibers, similar to those deployed for broad-band telecommunications, are then used. Figure 2.10(c) depicts the coupling of a collimated beam of given diameter into a typically round fiber bundle of another diameter using a lens. Thereby, the focal point of the lens should be sufficiently far away from the bundle surface (before or after) such that the diverging beam diameter perfectly matches the diameter of the fiber bundle. The lens as well as the distance to the bundle should be chosen such that the maximum incidence angle on any single fiber is well within the acceptance angle of the chosen fiber material. Fig. 2.10(c) also illustrates the construction of individual fibers within the bundle.

A cylindrical and highly transparent (within the wavelength range chosen) inner core of refractive index n_1 is enclosed by a mantle of material with refractive index $n_2 < n_1$. The refractive index contrast is chosen such as to achieve a minimal numerical aperture at the fiber end (divergence angle of distal beam), but sufficient to guide the beam along the core, i.e. no transmission into the cladding. The effect exploited for transmission is called total internal reflection (TIR) and occurs when the incident angle onto the cladding (relative to the normal on the cladding) is large enough. A derivation of this angle is possible by remembering Snell's law, as stated in equation (16) but using n (refractive index) instead of c (speed of sound). Imposing zero transmission into the cladding requires setting $\varphi_2 = 90^\circ$, which yields $\varphi_{tr,min} = \arcsin\left(\frac{n_2}{n_1}\right)$. If angles incident on the cladding are larger than $\varphi_{tr,min}$ all energy will be reflected inside the core. Figure 2.11 depicts the cross-section of an individual multi-mode fiber including relevant angles for coupling, transmission and emission at the distal end. The TIR requirement directly relates to the maximum acceptance angle $\varphi_{A,max}$, the sine of which equals the numerical aperture (NA) of the fiber.

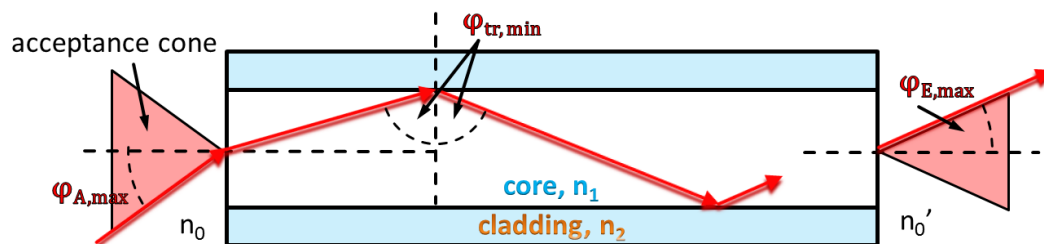


Figure 2-11 – Cross-section of individual fiber illustrates coupling in air (n_0), guided transmission within the core of the fiber and emission at the distal end in water (n_0').

NA can be defined in terms of n_1 , n_2 and n_0 , the refractive index of the medium in which the beam propagates before/after the fiber:

$$NA = \frac{1}{n_0} \sqrt{n_1^2 - n_2^2} = \sin \varphi_{A,max} . \quad (21)$$

Note that $\varphi_{A,max}$ is also the maximum angle of acceptance defined as the half-angle of the acceptance cone used for coupling. Depending on the medium, e.g. air ($n=1$) or water ($n=1.33$), this angle may be different – as depicted in fig. 2.11.

Of the total energy incident upon the fiber bundle about 30-40% is lost due to various losses. The most energy (15-17%) is lost due to incidence upon the cladding, which has a very high attenuation rate. Almost as much energy (9-11%) is lost due to incidence upon interstitial space between individual fibers – packaging efficiency of cylinders is determined by their diameter. This loss, however, can be almost completely eliminated by fusing together the bundle end at the point of coupling. Finally, there are Fresnel losses (total of ~8%, see Snell's law) to be considered, which occur at the ends of the bundle where the bundle interfaces a different medium (e.g. air, water or oil). To limit the energy being reflected upon entering/exiting the bundle, specialized coatings for different wavelength ranges are available. A further consideration for operation of fiber bundles in environments other than clean-air rooms is that over time particles may be ablated at the bundle ends, due to the high fluence rate required in clinical applications. Ablated particles build up an absorbing layer over time and thereby increasingly reduce transmission efficiency.

2.4 Ultrasound detection

Two methods of ultrasound detection are commonly used: optical interferometry and piezoelectric detection. The latter is the far more developed technology and will be discussed in detail in the following. Interferometry however is a rapidly developing field that has the potential to disrupt sensing of ultrasound in the future.

The core concept of interferometry is that a reflected beam will exhibit a phase shift relative to the originally beam sent. This shift is relative to twice the path travelled and can thus be used to assess the distance to the reflective surface. Of course we know from previous considerations involving Snell's law that incidence and reflection angle are the same and that reflectivity (i.e. amount of energy reflected) depends on the difference of refractive indices of transport medium and interface medium. These properties often require perpendicular incidence on the surface to be sampled for displacement. Furthermore, they leave little space for alignment errors and may require methods of phase-shift amplification (e.g. Fabry-Perot film) to achieve good enough resolution. On the other hand interferometers promise contactless measurements, thus reducing weight and size of detection hardware as well as opening up applications where contact must be avoided such as wound healing or difficult to access intra-operative sites. Careful choice of materials may allow co-axial excitation and optoacoustic signal detection, by illumination through the same surface, yielding a more compact system or allowing optimal excitation-detection patterns as demonstrated by [21, 52] in a laboratory setup. Unfortunately, the potential of this

technology has not yet been well developed to achieve sensitivity and operational robustness comparable to piezoelectric detection.

Technology based on the piezo-electric effect is far more advanced, mostly due to its utility in pulse-echo ultrasound, which has been under constant development since the first applications of underwater SONAR (sound navigation and ranging) in the early 20th century. As a reminder to the unacquainted reader, the piezo-electric effect describes an alteration of volume of a material upon application of voltage, usually a shortening or lengthening of the distance between two electrodes responsible for the difference in potential. The effect being reversible, i.e. compression of volume generates a potential difference on the electrodes, it is ideally suited to sending an excitation wave and receiving the echo by first applying a voltage and subsequently reading the answer. Many materials exhibit piezo-electric properties, but of particular interest for ultrasound detection are ceramics and polymers, the former due to their superior sensitivity and dynamic range, the latter due to their broad frequency band. A mixed material, termed piezo-composite, has also been developed to combine the best of both and is the preferred material when constructing shaped array-based geometries, as described in the next chapter. For planar geometries and single-element transducers the material of choice is PZT (lead zirconate titanate), a ceramic.

Figure 2.12 depicts the simplified construction layout of a PZT ultrasound transducer as employed in an ultrasound detection system, characterized by the combined electrical impulse response of transducer, cabling and A/D-electronics (DAQ). The active element of an ultrasound transducer is the piezoelectric material (e.g. PZT as depicted) shaped and positioned such that pressure waves are perpendicularly incident on a surface whose area size must remain constant and is typically much larger than the thickness of the material. This way a longitudinal compression wave will change only the thickness of the active element and thereby induce a voltage between the two electrodes connected to the surface on each side of the element. Since the active element is usually of different acoustic impedance than the coupling medium (water or oil) matching layers are applied on the surface facing the couplant to effect a gradual matching of acoustic impedance. The thickness of matching layers and of the active material itself are determined by the desired frequency range. Both are chosen such as to facilitate resonance at a particular frequency (equivalent wavelength λ) with active element thickness $\lambda/2$ and matching layers $\lambda/4$. To avoid influence of waves other than those perpendicularly incident on the active surface (e.g. from the side) acoustic insulators are deployed along the sides of the casing. A backing material, highly attenuating in nature, is also placed behind the active element to control sensitivity and detection bandwidth, and avoid acoustic reflections from the casing. Choosing a backing of matched acoustic impedance to the active element will result in increased detection bandwidth but at lower amplitude i.e. sensitivity. On the other hand increasing mismatch will result in higher sensitivity but a reduced detection bandwidth.

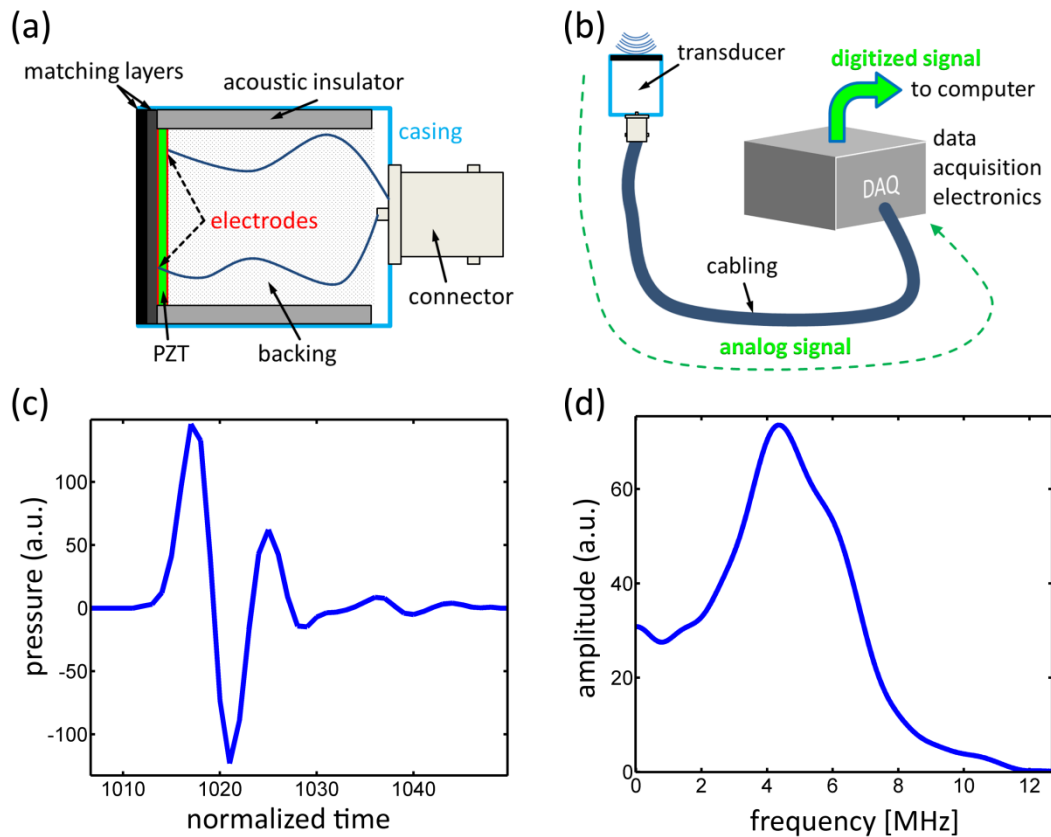


Figure 2-12 – Ultrasound detection depicting (a) a single element ultrasound transducer layout, (b) the detection system including cabling and data acquisition electronics and (c) the electrical response of the system upon excitation by an impulse. (d) Frequency domain plot of (c).

To practically improve the quality of detected signals we have to account for this limited bandwidth by measuring the electrical impulse response. As figure 2.12(b) illustrates, the digitized measurement signal includes not only the transducer impulse response but also the response of cabling and data acquisition hardware (DAQ). Therefore an electrical impulse response is only valid for a given combination of transducer, cabling and DAQ – with some leeway in terms of actual instance, i.e. identical designs but different physical instances may be considered as having the same electrical impulse response. Figure 2.12(c) depicts such an impulse response in the time domain and 2.12(d) shows the equivalent absolute amplitude in frequency domain. We can see that the detection system depicted here has a central frequency of about 4.5 MHz and a fairly large bandwidth. Nonetheless we can only correct for the electrical impulse response within a reasonable band, i.e. frequencies at too low SNR cannot be recovered. In the example shown the effective band where signals could be reasonably improved stretches to 7-7.5 MHz, although in practice we do not consider signals below 50 kHz, because SNR of optoacoustic signals in this range are too low.

An important effect that can be exploited in the design of ultrasound transducers relates to the geometrical impulse response as previously described in terms of optoacoustic signals. While this effect is undesirable in an ideal optoacoustic detection

system (infinite bandwidth in time and space, infinite sensitivity), practical implementations require trade-offs to achieve sufficient sensitivity in a region of interest (ROI) versus avoiding detection of signals from outside the ROI. Therefore detection elements are typically shaped according to specific objectives. Two of the most common shapes are spherical and cylindrical – others exist (e.g. flat, circular etc.) but are not considered here. Their design parameters are thereby determined by the desired sensitivity field within the ROI. The sensitivity field can be understood as a volumetric map representing the maximum amplitude detectable from signals generated within the volume, e.g. the maximum amplitude of detected signal $s(t)$ generated by a wave originating at point (x,y,z) is $A(x,y,z)$. Of course we are aware that the actual effect of detector geometry is to “smear” signals along the time axis thereby contributing to the general noise floor, if the origin of the signal is sufficiently far outside the focus. In case of signals generated within the ROI and assuming appropriate detector design, these geometrical distortions can be taken into account during image reconstruction. Signals originating outside the ROI can be assumed too low in amplitude to be recovered during reconstruction (i.e. they have blended into the noise floor). Figure 2.13 shows a spherically focused transducer and a cylindrically focused transducer with sections in three planes (x - y , x - z , y - z) through the region of interest. The near field is not shown here as it is of no consequence to optoacoustic imaging, if proper precautions are taken in terms of illumination, e.g. not inducing optoacoustic signal in the near field. The spherical design, shown in 2.13(a), is useful when tomographic placement of detectors is not possible. The sensitivity fields show why: fields in x - y and y - z are elongated along the y -axis and rather tight on the other axes, as can be seen in x - z . This cigar shape can be modified by choosing other parameters of detector curvature and size. An ideal field would be a single line along y (point in x - z), because in this case y represents the time axis resolved by the bandwidth of the detector. In practice the trade-off is between cigar length and thickness: the longer the cigar (smaller curvature and/or size) the thicker it becomes and vice versa. While spherical detection is useful when scanning along a planar raster, it cannot recover directivity as previously explained. Hence, signals of strong amplitude but propagating perpendicular to the y -axis are lost.

When tomographic arrangement of detectors is possible within a single plane (but not other planes, e.g. forming a sphere), the cylindrically focused design shown in figure 2.13(b) is desirable. Again the sensitivity fields provide the rationale. Sensitivity in x - y is sufficiently good within a broad region, while the field in x - z is very tight and in y - z approximately tight (tighter at the center, broader with increasing distance to the detector). Tomographic scanning with this detector would occur within the x - y plane with a center of rotation at or close by the maximum sensitivity. In this case waves primarily emitted in direction of the z -axis would be lost as well, whereas waves emitted in x and y direction could be detected. Practically this means that we could not differentiate between a small sphere placed within the x - y plane and a rod or tube elongated along z and perpendicularly crossing through x - y . That is, unless we collect multiple x - y -scans along the z -axis, in which case the sphere would at some point lose signal strength and shape and eventually completely disappear. Twice the

displacement necessary to reach half the signal strength (in positive and negative z -direction, relative to the scanned x - y plane) would then characterize our achievable resolution in z , also known as full-width half-maximum (FWHM) resolution.

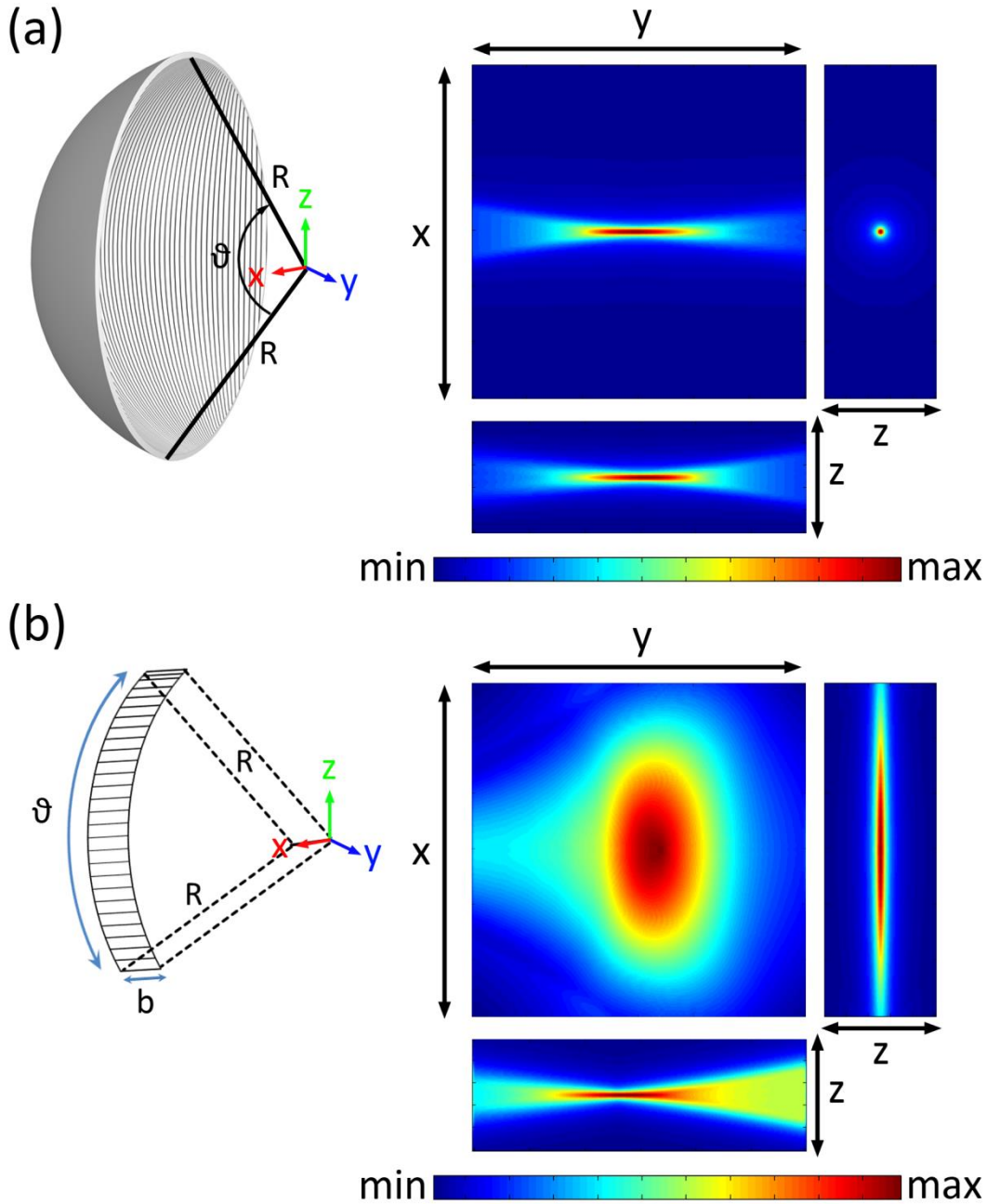


Figure 2-13 – Focused acoustic transducers with sections of respective sensitivity field around the origin: (a) spherically focused, (b) cylindrically focused. Both elements are comparable in their characteristic size, i.e. radius $R=60\text{mm}$, $\vartheta=22^\circ$ ($b=0.7\text{mm}$). Sections in color indicate maximum and minimum receivable amplitude of signals up to 7.5MHz from points within each depicted plane.

2.5 Array-based optoacoustic detection geometries

The dataset collected from scanning a single transducer as described above can also be achieved in parallel when employing an array of detectors equivalent in number to the scan positions covered using a single element. Traditional ultrasonography arrays are mostly flat as far as the active element layer is concerned. Focusing can then be achieved by adding a shaped silicon acoustic focusing lens or shaping the active element itself. As already mentioned PZT would be the piezoelectric material of choice, however ceramics do not easily lend themselves to shaping.

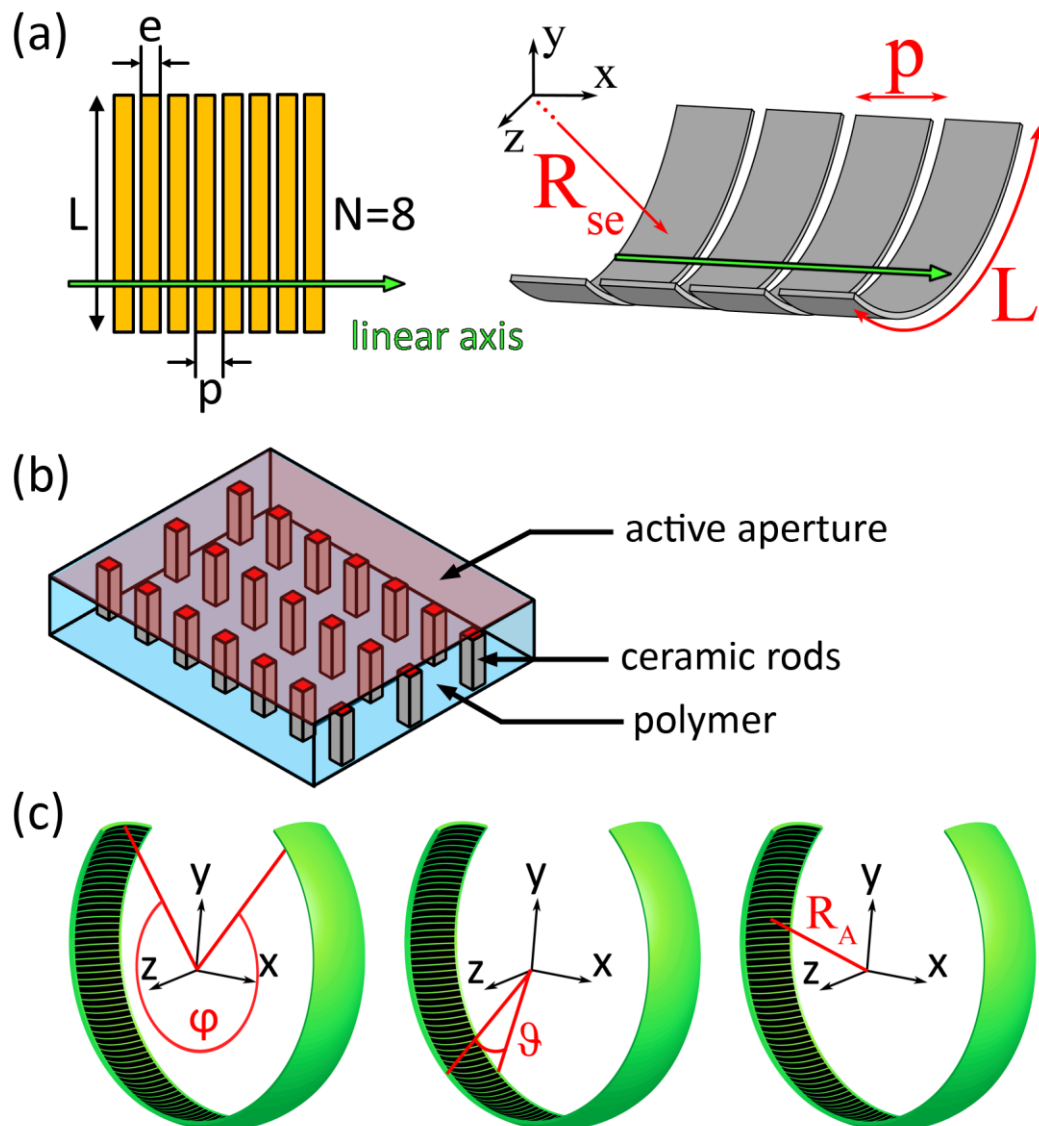


Figure 2-14 – Definitions of parameters used to characterize focused ultrasound arrays. (a) Definitions describing individual elements. (b) Structure of piezo-composite material. (c) Definitions describing array geometry.

Similarly, extensive backing to broaden the detection bandwidth cannot be provided in an array configuration due to the limited space. Therefore, piezo-composite materials have been developed that combine higher sensitivity offered by ceramics and broader bandwidth and flexibility characteristic of polymers. Figure 2.14(b) depicts the schematic of such piezo-composite materials: thin ceramic rods are embedded in flexible polymer, one side of which is considered the active aperture. The construction of linear arrays is illustrated in figure 2.14(a), whereby the aperture length along the linear axis can be computed from the number of detection elements (here $N=8$) and the pitch p . The pitch is defined as the sum of element width (e) and inter-element spacing. Element height (L) determines the focal parameters of the array along the lines discussed for single elements. To additionally increase focusing individual elements may also be cylindrically bent (or an equivalent lens may be added); in this case the additional parameter R_{se} describes the radius of single element curvature. The other array geometry considered herein is circularly curved, allowing tomographic imaging in 2D as previously described by scanning a single element. In the remainder of this text we will refer to this geometry as a curved array. Figure 2.14(c) illustrates parameters relevant for this design. The same single element specifications as shown in 2.14(a) may be used, but elements are now distributed along a circular curve spanning an angle of φ in the x-y plane. Angle φ is the main determinant of 2D image reconstruction quality as it defines the (tomographic) view, also referred to as limited view for $\varphi < 360^\circ$. The other parameters, angle ϑ and array radius R_A , determine the focus in elevation (z-axis) and the distribution of sensitivity. Note that array radius R_A and single element radius R_{se} must not necessarily be the same – although they should not differ too much either.

Figure 2.15 depicts three cylindrically focused arrays with an identical number of single elements, each element characterized by figure 2.13(b). The full tomographic view (360°) is given in 2.15(a), showing also perfect symmetry of the sensitivity field on all axes. The region of interest (ROI) is fully enclosed within the detection region, which is highlighted in yellow and marks the region in which perfect reconstruction is theoretically possible, i.e. inversion is mathematically well-posed (and no other limitations are considered). A reduced, half-tomographic (180°), view is illustrated in 2.15(b), with the full view represented by the green dashed circle. The detection region has been reduced to half, because reconstruction of objects located in the upper half has become ill-posed [53]. A round object graphically illustrates the problem: waves propagating along directions indicated by the gray arrows cannot be detected and are lost. As a consequence the dashed object boundaries cannot be stably recovered. The sensitivity field is comparable to the full-view, however slightly asymmetric on the y-axis reflecting an array radius slightly larger than the single element radius. Finally, 2.15(c) shows a linear array geometry with a severely limited-view of 53° . No detection region is available as waves propagating along a direction perpendicular to the linear detection axis will be lost independent of their origin.

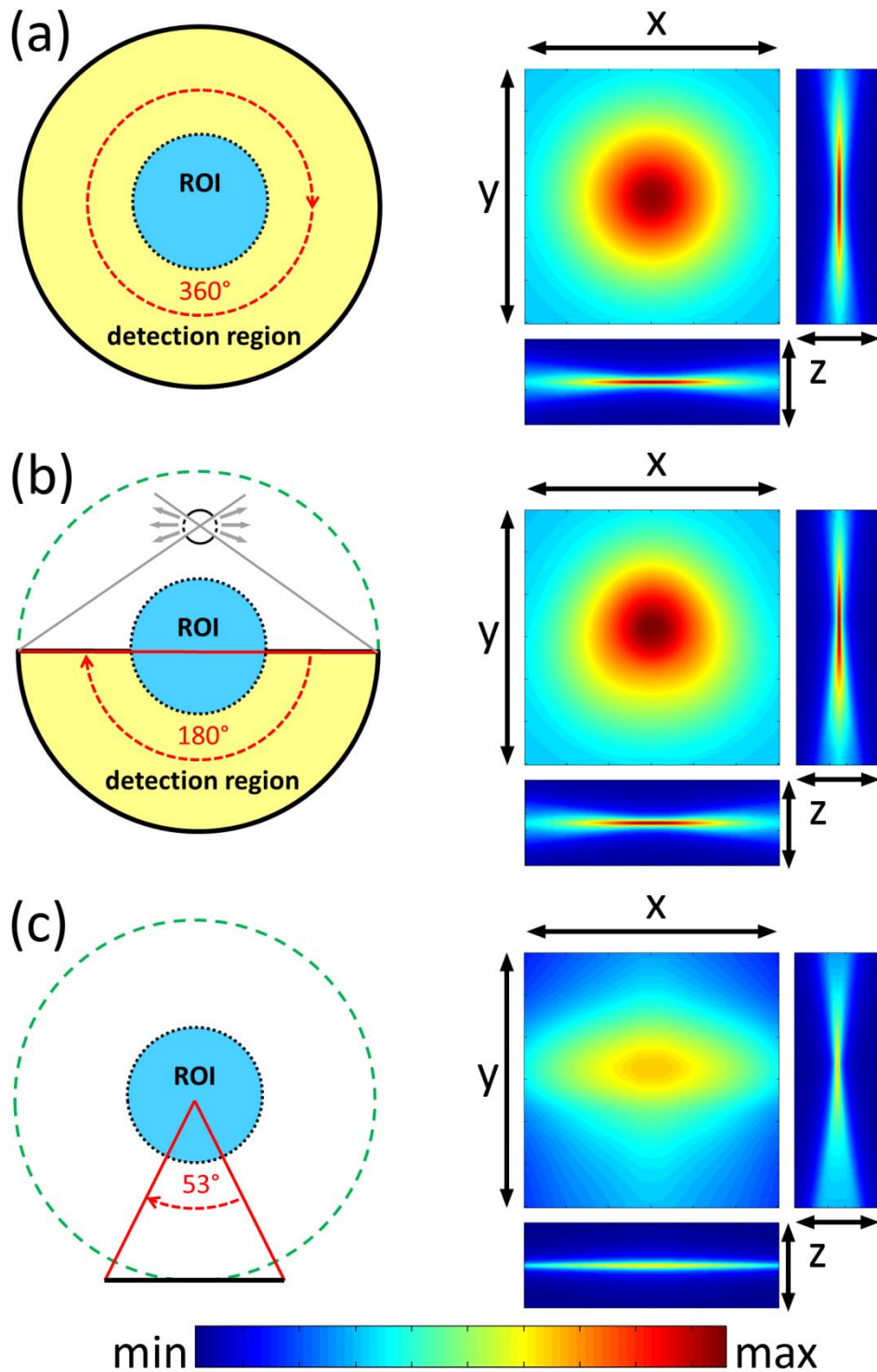


Figure 2-15 – Focused detection arrays and their sensitivity fields depicted as sections along x-y, x-z and y-z (centered on the origin). Row (a) depicts a full-tomographic view, i.e. the array fully encloses the ROI. Row (b) depicts only half-tomographic detection. Row (c) depicts the view obtainable from a standard linear ultrasound array. All images are on the same colorbar.

We can however see that more of an object's boundary can be detected the closer the object is to the array. We also notice that the linear array is much less sensitive compared to the curved geometries, because individual elements' sensitivity fields do not overlap as much as in case of curved array detection.

Before discussing image reconstruction algorithms, whose performance obviously depends on the detection geometry employed, we need to mention three-dimensional detection arrays. This class of arrays includes the ideal spherical detection surface. Such arrays employ detection elements with equal width and length (i.e. $e = L$) in order to achieve the same sensitivity in x-z and y-z as in x-y, see figure 2.13(b). The 3D pressure distribution can then be recovered from full-tomographic detection along φ and ϑ . However, this detection geometry comes with significant drawbacks such as weight, size and number of required channels to be sampled in parallel. To reduce the complexity (and cost) of the problem, to allow better access on the patient and to reduce the burden placed on the user holding the probe, we chose to reduce one degree of freedom by focusing in elevation (z-axis).

2.6 Image reconstruction

The goal of image reconstruction is to find the initial pressure distribution $p_0(\vec{r})$, which is a linear combination of the spatially variant optical fluence (Φ_s) and the optical absorption coefficients (μ_a) of spatially heterogeneous tissues within the heated region. Ultimately, the holy grail of optoacoustic imaging would be to obtain an image (or volume) of the absorption coefficients only. However, due to strong optical scattering in tissue, fluence heavily depends on scattering and absorption. From illumination with a single wavelength, the best we can obtain is the initial pressure distribution and its subsequent (relative) changes following excitation with light of other wavelengths.

The starting point for image reconstruction is the set of one-dimensional acoustic data acquired from ultrasound detectors distributed on a surface that tomographically surrounds the heated volume (or slice in case of focused detection elements). Thereby, each detector contributes a projection of the volume under investigation (3D pressure distribution to 1D acoustic signal). Optimal results can be achieved, if the data has been acquired in parallel (see chapter 2.5) so as to avoid motion artifacts – a typical optoacoustic measurement can be completed in few to tens of μs , depending on the size of the volume interrogated. We refer to such data as *data frame*, because it represents the unprocessed image frame and can be expressed as a matrix with m rows (number of time samples) and p columns (number of projections). For simplicity we define the image to be reconstructed in terms of a single quantity n such that the pressure distribution is fully enclosed within n^3 voxels or n^2 pixels when using focused detection. These definitions allow us to interpret the process so far as a discrete projection from $n^3 \rightarrow m \times p$ or $n^2 \rightarrow m \times p$ with equation (20) defining the projection operator. To recover the original information all we need to do is apply the inverse operator. Of course in a real measurement system the information is not discrete but continuous

and the transmission channel reduces the available bandwidth while adding also non-Gaussian noise. To cope we need to limit ourselves with respect to n as well as optimize the system to achieve the best results for a given transmission channel. More on the topic can be found in chapter 3 and 4. In the following we will rather focus on inverting the projection operator without considering specific constraints other than those imposed on any practical measurement setup.

Unlike in other imaging modalities, such as XCT or ultrasonography, no clearly superior inversion algorithm exists in optoacoustic imaging, i.e. an algorithm that produces the best achievable image in the shortest time possible while using a minimum of resources. This state may not last, but is reinforced by the physical properties of tissue with respect to propagation of light and sound. Hence, a large body of different inversion algorithms has been developed in both time and frequency domain. Most methods thereby fall into one of three categories: time-reversal [54, 55], backprojection [56, 57] or model-based [58, 59]. Others for example adopted signal processing techniques from ultrasonography [60]. In this work we focused on two time-domain reconstruction algorithms with properties such as to allow either very fast or very precise reconstruction. In chapter 4 we describe original work contributed towards enabling high-resolution reconstruction at frame rates up to 50 Hz (backprojection) and high-resolution reconstruction with high accuracy of a large region of interest (model-based). In the following we review both algorithms to better understand advantages and drawbacks.

One approach to inversion of equation (20) is to find an analytical solution for H_s , which involves making certain assumptions such as infinite bandwidth in time and space. The analytical solution is known as **filtered backprojection** and given by

$$\Gamma H_s(\vec{r}) = p_0(\vec{r}) = 2 \int_{\Omega} p(\vec{r}_k, t) - t \frac{\partial}{\partial t} p(\vec{r}_k, t) \frac{1}{\Omega} d\Omega \Big|_{v_s t = |\vec{r} - \vec{r}_k|}. \quad (21)$$

In eq. (21) Ω denotes the solid angle spanned by the detection surface enclosing the pressure field, whereas $d\Omega$ is the solid angle spanned by a single detection element and the point at \vec{r} ; each detector located at point \vec{r}_k measures pressure as a function of time, $p(\vec{r}_k, t)$. Ideally there are $k \rightarrow \infty$ number of detectors on a surface that entirely encloses the pressure field ($\Omega=4\pi$). In practice however k is a finite number of detectors having a limited frequency response (bandwidth in time) and a limited field of view (bandwidth in space). Hence, eq. (21) is usually implemented as two delay and sum operations on a discrete set of data points in time and space, the data frame. The first part sums k pressure values, each value measured at a different time $t = \frac{1}{v_s} |\vec{r} - \vec{r}_k|$, while the second part sums the time derivative thereof. Because $t \frac{\partial}{\partial t} p(\vec{r}_k, t) \gg p(\vec{r}_k, t)$, the second part dominates contrast in the reconstructed image and the direct contribution can be omitted. Figure 2.16(a) depicts the optoacoustic signal from an ideal spherical pressure source and 2.16(b) the corresponding derivative multiplied by time. Additionally, figure 2.16(c) depicts the same signal as in 2.16(a), but convolved by the electrical impulse response of a real

ultrasound detection chain (transducer and DAQ). As can be seen from figure 2.16(d), the derivative of a real optoacoustic signal does not resemble the one expected from 2.16(b). If backprojected (i.e. signals delayed and summed for all pixels of an image and for all detector positions) the resulting pressure distribution will include sharp boundaries with strong negative values. Furthermore, low frequencies will be severely attenuated, because the time derivative in eq. (21) corresponds to an increasing ramp filter in frequency domain. A reconstruction from the signal shown in figure 2.16(c) is depicted in figure 2.17(b) for the setup given in 2.17(a). The setup chosen is not ideal, but resembles the compromise necessary for practical implementation with respect to weight and size, detector density and number of detection elements that can be sampled in parallel. We expect a disk of constant values above 0 – there is no negative absorption! Although 2.17(b) shows a disk of approximately constant value, we also note strong positive and negative values at the boundary.

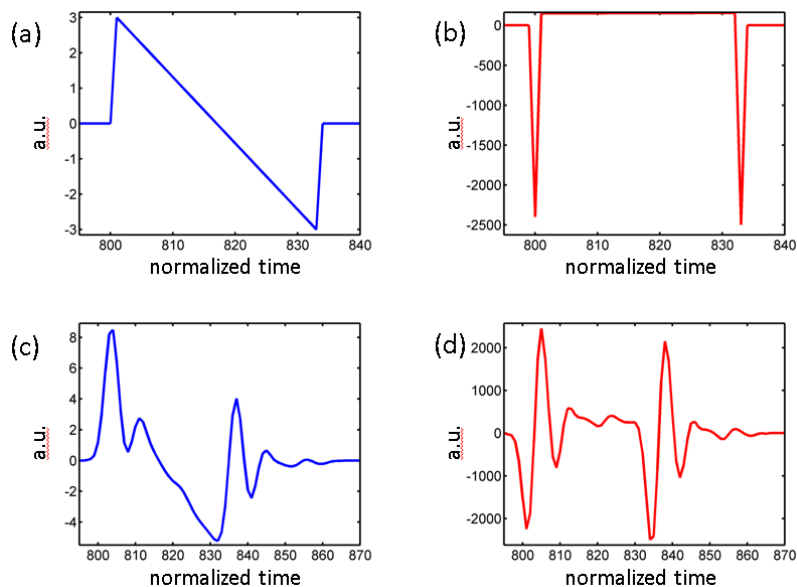


Figure 2-16 – Numerical analysis of the optoacoustic signal from an ideal spherical pressure source: (a) ideal conditions, (b) numerical derivative of (a), (c) same as (a) but filtered by the impulse response of a real detector, (d) numerical derivative of (c).

The other inversion approach to inversion does not attempt to analytically invert equation (20), but instead aims to establish a model of the projection operator such that any given (discrete 2D or 3D) pressure distribution can be numerically converted to a set of 1D projections. The **model-based algorithm** employed in this work numerically evaluates eq. (20) on a discrete two-dimensional grid to produce a model-matrix of size $[m \cdot p \times n^2]$. This 2D algorithm is a sufficient first approximation for the system designs chosen in this work; chapter 3 details design choices made. The model-matrix essentially connects $[m \cdot p]$ measured pressure values with the appropriate pixels – henceforth called unknowns – within the region of interest, thereby producing a system of linear equations of equal size, i.e. $[m \cdot p]$. An important assumption is that the image (also referred to as the region of interest or ROI) includes the whole pressure field induced. It is important to understand that the algorithm only

establishes an $m \times n^2$ matrix per projection with the full matrix being a stack of p submatrices. The geometrical information of detector placement is thus contained per projection matrix. As only a small subset of n^2 total unknowns are non-zero per equation (see v_{st} in eq. 20) the full model-matrix is extremely sparse and sparsity increases with n . The main advantage in establishing a matrix-notation for the description of the projection operator is that additional effects can be easily taken into account, even without modifying the model-matrix algorithm. Furthermore, image reconstruction is generalized to a problem of matrix inversion, for which numerous algorithms are available. This flexibility can be exploited to model effects such as the geometrical impulse response [61] or acoustic heterogeneities [62, 63]. If, unlike shown in fig. 2.17(a), the enclosure is not fully tomographic, meaning that the detection surface does not fully enclose the pressure field (limited-view), artifacts would be introduced during model-based or backproject inversion. In case of model-matrix inversion however regularization techniques could be applied to reduce artifacts. Similarly, matrix-factorization algorithms may be used to study the effects of certain geometrical arrangements of detection elements, for example singular value decomposition (SVD). To speed up reconstruction the inverse matrix could be approximated by either SVD or using the Moore-Penrose pseudo-inverse, however, as the inverse matrix loses sparsity, memory consumption increases dramatically. In this case an iterative least-squares optimization method such as LSQR [64] may be adopted. The method computes an estimate of the pressure field for each iteration and applies the model-matrix to compute estimated signal data, which is then compared against the measured data to yield a new estimate of the pressure field and so on until stopping criteria have been fulfilled. Figure 2.17(c) shows a model-based reconstruction of the same data as in 2.17(b). Although the pressure distribution within the source is not perfectly homogenous, boundary artifacts and negative values are much weaker compared to backprojection.

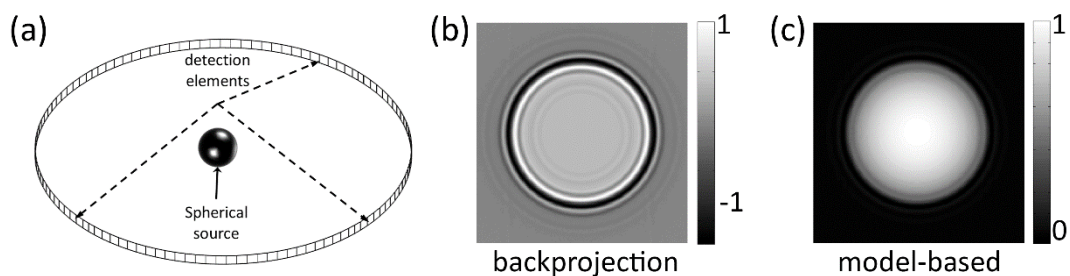


Figure 2-17 – Numerical study comparing backprojection and model-based reconstruction algorithms. (a) Simulated setup where each of 256 detectors measures the signal shown in 2.16(c), i.e. the source is centered within the ring of detectors. (b) Backprojection reconstruction showing strong positive and negative values at the boundary. (c) Model-based reconstruction achieving a smooth boundary.

2.7 Multi-spectral unmixing

Array-based detection of optoacoustic data and subsequent image reconstruction can reveal the initial pressure distribution upon excitation with monochromatic laser light. The data frame and thus the image are thereby acquired within tens of microseconds rendering the acquisition almost instantaneous, comparable to a snapshot of the tissue state. It is only logical to repeat the procedure at as high a repetition rate as possible, in the process producing a video of tissue dynamics. In many instances this is a useful property and indeed almost unmatched by any other modality. However, the true strength of optoacoustic imaging is to be found in the optical spectrum. As we have seen in chapter 2.1.1, and in figure 2.5 in particular, optical absorption properties of tissue chromophores can vary significantly over wavelength. Therefore, if dynamics do not change too fast and/or the imaging repetition rate is sufficiently high, we could equally acquire a “multi-spectral video”, meaning a set of image frames each taken at another excitation wavelength. If the observed scene can be assumed static or constant, then we have obtained a multi-spectral dataset that can be used to identify the concentration and precise location of known chromophores in tissues examined. Multi-spectral optoacoustic tomography (MSOT) can thus produce inherently co-registered images of absorption morphology, physiology and biochemistry in general.

The basic concept of multi-spectral, also called hyper-spectral, imaging is well known and applied in many fields, for example remote sensing, food processing or mineralogy among others. A basic review on the topic can be found in [65]. In medicine the method is also well established [66] and applied to study intrinsic tissue chromophores and extrinsically administered contrast agents (often fluorescent). The fundamental concept of multi-spectral imaging is illustrated in figure 2.18. An arrangement of three optical absorbers or absorbing regions is to be analyzed, defined by a triangle, a circle and a rectangle. It can be assumed that three chromophores are present, but their concentration and localization is unknown. The multi-spectral dataset is shown in the box at the top and consists of three images taken at 600nm, 700nm and 800nm. The ground truth is shown in the 3 rows below, for each (color coded) chromophore. Chromophore 3 is present in all regions at concentration c_4 , while chromophore 1 is only present within the circle and the rectangle at concentration c_1 . Similarly, chromophore 2 can be found within the rectangle and the triangle, but with different concentrations c_2 and c_3 . Each row shows the images attainable at the three wavelengths, if only the respective chromophore was present. At the bottom the absorption spectra for all chromophores are given. We can see that the intensity of images in the chromophore rows reflect the spectral absorption behavior and were indeed generated using this information. We also note that chromophore 2 shows higher intensity in the rectangular region than the triangular region, because concentration c_2 is higher than c_3 . The observable data can be generated by summing intensity images for each chromophore at the same wavelength. This linearly weighted mixing is described in equation (22).

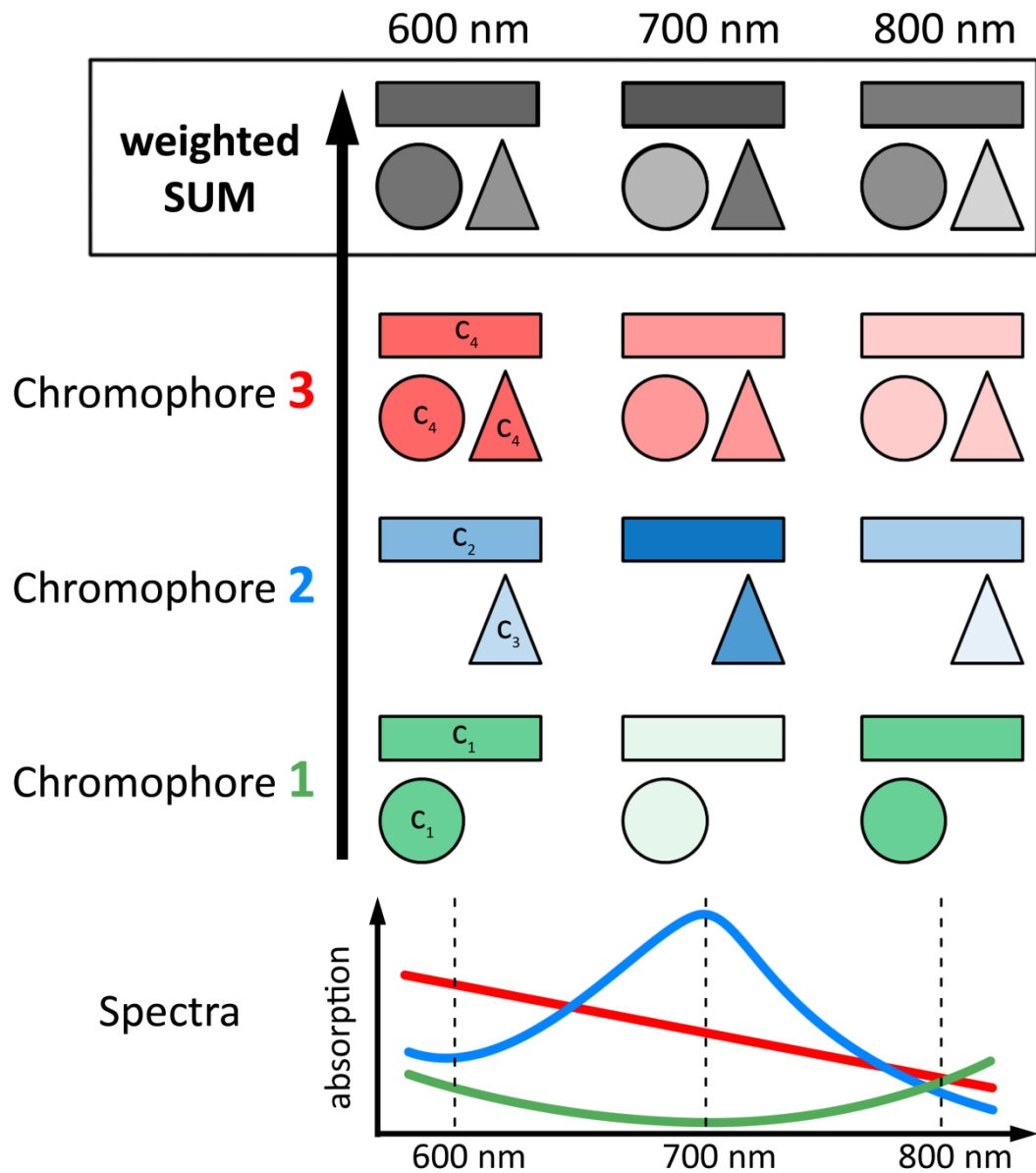


Figure 2-18 – Multi-spectral unmixing problem illustrated: top box represents the accessible data consisting of 3 images acquired at 600, 700 and 800 nm wavelength. The observed “scene” is composed of a rectangular, a circular and a triangular region. Three chromophores are present and distributed within the regions as shown with concentrations c_1 - c_4 . The absorption spectra of each chromophore are given at the bottom.

$$Im(i, j, \lambda) = c_1(i, j)S_1(\lambda)\Phi_0 + c_2(i, j)S_2(\lambda)\Phi_0 + \dots + c_k(i, j)S_k(\lambda)\Phi_0. \quad (22)$$

An image $Im(i, j, \lambda)$ can be obtained by summing for each pixel (i, j) all concentrations $c_{x=1\dots k}(i, j)$ multiplied by the appropriate spectrum $S_x(\lambda)$ and available fluence Φ_0 . Equation (22) contains k unknown concentrations and can be solved for each pixel individually by sampling at k different wavelengths.

Although multi-spectral imaging has been widely applied, even in medicine, all applications have in common their superficial nature. In most applications this may not matter. In medicine however it limits the scope of applications. Due to the low time resolution of optical systems (compared to the speed of light) and the wavelength dependent absorption characteristics of tissue, superficial imaging is prone to signal averaging over tissue depth. This can be a particular problem for near-infrared spectroscopy methods [67, 68]. MSOT can improve upon this situation by spatially resolving absorption values even at depth. Nonetheless, there are significant obstacles towards truly quantitative MSOT. The most significant problem is often referred to as “spectral coloring” and concerns the optical properties of tissue (scattering, absorption): as monochromatic light incident on the tissue surface travels deeper in tissue it undergoes wavelength-dependent absorption and scattering, which reduce the available fluence with depth. In a volume of tissue with heterogeneous optical properties (as is typically the case) the resulting fluence distribution is itself heterogeneous and changes strongly with wavelength. Even in a homogeneous but absorbing volume the fluence at any point located at some depth will be modulated over wavelength by the optical properties of the volume between that point and the surface (upon which a known illumination is incident). Therefore the fluence Φ_0 , in eq. (22) assumed constant, becomes a function of point $\mathbf{x}=(i, j)$ and wavelength λ , $\Phi(\mathbf{x}, \lambda)$, and cannot be solved by a simple system of linear equations. An excellent review on the topic can be found in [69], where this effect is described as coloring the measurable spectrum at any point and also geometrically distorting each single-wavelength optoacoustic image. A suitable comparison is also provided: it’s as if “seeing the world through colored glass”. Despite this fundamental problem methods exist to detect special chromophores (like contrast agents) using for example statistical properties [70, 71]. Other methods include linear unmixing as in [72], which is not applicable beyond a few mm, or model-based inversion approaches [73, 74] that suffer from heterogeneity and insufficient data.

Besides spectral coloring, which is an inherent problem, there are also obstacles relating to the image quality of multi-spectral data, i.e. the sequence of single-wavelength images. The quality of an image is largely defined by three aspects: 1) signal-to-noise ratio (SNR), which typically depends on tissue depth as well as amount of pulse energy available and the characteristics of detection array and DAQ; 2) artifacts, generated either by acoustic reflections at impedance boundaries in the tissue or introduced by the detector design and reconstruction algorithm; 3) spatial resolution, largely defined by detector and array design. One of the specific goals of the research presented herein was to achieve the best possible image quality given parameters for clinical application.

Imaging systems

In this chapter we describe the technical developments and experimental studies that led to the final design of a unique non-invasive handheld MSOT probe as well as the intraoperative setup and methodology. Off the rack components employed in both systems included tunable wavelength pulsed lasers and fiber bundles with multiple output arms. Both, lasers and light guides, had previously been employed within a pre-clinical small animal imaging system [75].

Two types of lasers enabled illumination with optical pulse widths of 6-8 ns within a tunable wavelength range of 680 – 950 nm. Initially a Phocus™ (Opotek Inc., CA/USA) was used, which was later replaced by a SpitLight 600 OPO (InnoLas Laser GmbH, Germany). Both models were comparable and included an OPO (optic parametric oscillator) for wavelength tuning, flashlamp pumped by a Nd:YAG source (neodymium-doped yttrium aluminum garnet). The maximum attainable repetition rate was 10 Hz with maximum pulse energy of approximately 90 mJ at 740 nm, but never less than 50 mJ throughout the tunable range. These lasers were also capable of providing per shot measurements of pulse energy and peak emission wavelength – highly relevant information due to the inherent pulse-to-pulse instability of OPOs. Additionally, the SpitLight was capable of inter-pulse wavelength tuning using a fast and precise piezo-electric rotation stage to attain the calibrated OPO phase matching condition. At later stages we upgraded to a SpitLight DPSS OPO (diode-pumped solid-state based), which featured similar operational characteristics to the SpitLight 600 OPO but could attain repetition rates up to 100 Hz at pulse energies above 20 mJ throughout the tunable wavelength range. The newer model also included advanced features such as programmable wavelength sweeps, per-pulse attenuation and a remote control API (application program interface). The necessary software control was also implemented within the course of this work using C# (assembly) and wrapped in a Matlab class structure to provide easier access from Matlab. The laser output was coupled into custom made fiber-bundles (Ceramoptec GmbH, Germany) with initially 8, later 4, branching arms, each with a 2.5 mm active inner diameter at the distal end.

For the non-invasive probe a new fiber bundle geometry was developed adapted to the overall probe design and sledge-based illumination concept.

3.1 Data acquisition electronics

To achieve better detection sensitivity and cost efficiency compared to commercially available multi-channel solutions, e.g. National Instruments PXI-5105 as employed in [76], we co-developed custom data acquisition (DAQ) electronics. A third party, Falkenstein Mikrosysteme GmbH (Germany), was tasked with design and production. We accompanied the development with specification, testing and software support. The goal was to realize a system capable of highly sensitive detection (noise floor of few μV per least significant bit RMS) within a frequency range up to 15 MHz and a dynamic range of few tens of mV. Additional parameters included: parallel sampling of at least 128 channels each capable of storing >2000 samples, SMB connector interface towards the detection array, (parallelizable) broad-band Ethernet connection to the PC for transfer of digitized data, TTL level acquisition trigger with low jitter for synchronization with the laser pulse, capable of operation at 10 Hz repetition rate. The initial prototype was realized with 128 channels, each capable of recording 2032 samples with 40 MSamples/s, 1 M Ω input impedance, 12-bit vertical resolution and dynamic range of 16 mV. The repetition rate was 10 Hz and data transfer facilitated by TCP/IP communication (including drivers and API) using the iPORT NTx-Mini Embedded Video Interface (Pleora Technologies Inc., Canada). The latest device available is capable of operating in parallel up to 512 channels at 50 Hz or 256 channels at 100 Hz – now using Harting 68-pin connectors for plugging 32 channels at once (differential signal). Additionally, the IP serial communication interface allows programmatically setting input gain, trigger delay, sample length and anti-aliasing cut-off frequency. In the following we will detail contributions made during development.

To facilitate efficient testing and assist debugging graphical user interface (GUI) software was developed to acquire, display and analyze acquired signals on the fly. Figure 3.1(a) shows the GUI front end accessible by the user. The software allows connecting a DAQ by MAC address and setting parameters such as sample length and number of channels. Given a trigger signal the software acquires data and computes the running average of the detected frame rate as well as plotting a selection of channels (displaying also the min/max values over this data set). Signal plots are attempted live within the time between incoming data frames and depend on the hardware specifications of the test PC. A measurement session can be parametrized in terms of acquired data frames and averages per frame, upon completion of which the data is stored to the location specified. An alternative mode of operation (free run) allows indefinite acquisitions without storing the data. This mode may be interrupted by unselecting the “free run” checkbox and allows command line based analysis of the last data frame received. Figure 3.1(b) qualitatively illustrates a selection of signals measured and analyzed during testing and debugging of the first prototype. Similarly, fig. 3.1(c) and 3.1(d) depict identical simulated optoacoustic signals (using a function

generator) sent to the DAQ for assessing the ideal input impedance. In ultrasonography it is common to choose impedance matching (i.e. $50\text{-}80\Omega$) between transceiver electronics and ultrasound transducer. However, our experience showed that for optoacoustic imaging in the lower frequency range (up to 7.5 MHz) unmatched (high) impedance ($1\text{ M}\Omega$) yielded better results. The experiment depicted in figure 3.1(c) and 3.1(d) highlights superior SNR and frequency response for the high impedance acquisition.

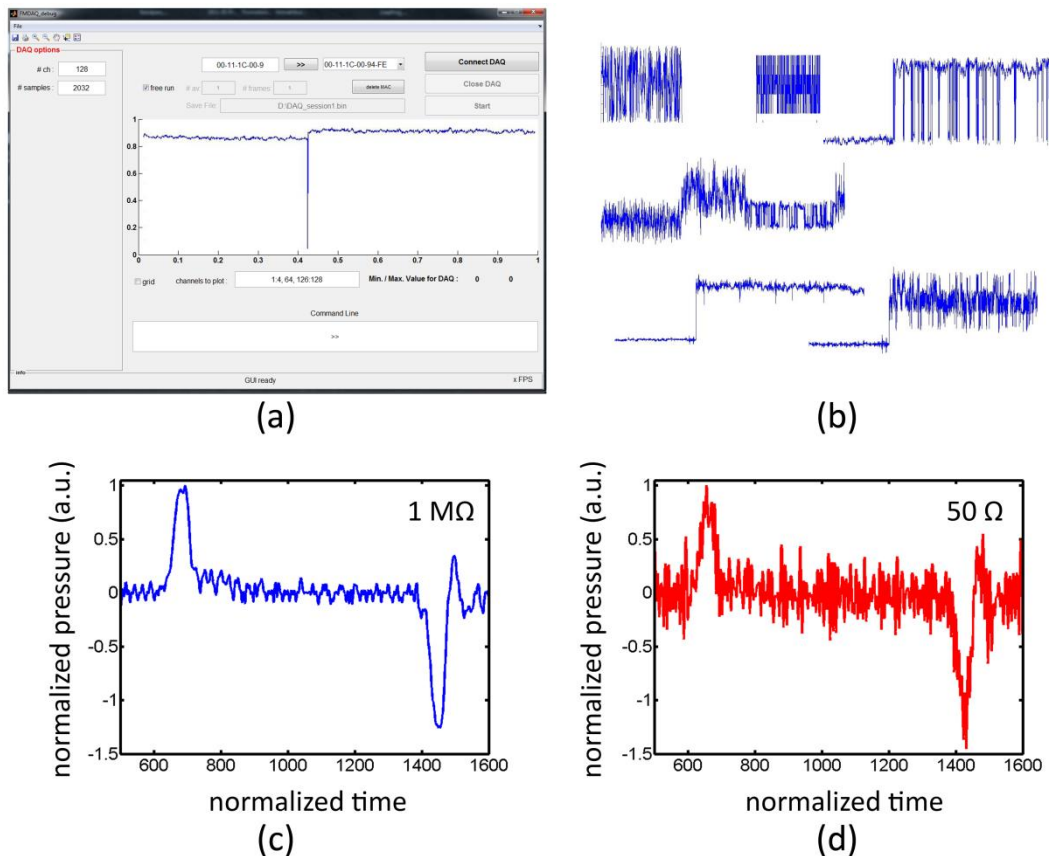


Figure 3-1 – (a) Graphical user interface software implemented for testing and debugging of the custom multi-channel DAQ. (b) Selection of first signals measured by the DAQ prototype in the course of testing and debugging. Simulated optoacoustic signal measured by a DAQ using (c) high impedance ($1\text{ M}\Omega$, not matched to cabling) and (d) low impedance ($50\ \Omega$, matched to cabling).

The core of data acquisition software developed for testing and debugging was also deployed in productive systems of all configurations (2D/3D data, scan-frame based, instantaneous capture, endoscopic, high-resolution, linear, curved, etc.). The acquisition and interfacing concept is depicted in figure 3.2 and the initialization routine is shown in figure 3.3, top half. A Matlab class library has been implemented that allows unified (API like) control of hardware (DAQ, laser, translation/rotation stages) and interfacing to algorithms implemented in C/C++ or C# (OpenCL) for improving execution time – see chapter 4.1 for an example. In the case of data acquisition a Matlab class method (“initDAQ” available through class “HOTEngine”) is invoked with DAQ specific parameters (channels, samples, MAC).

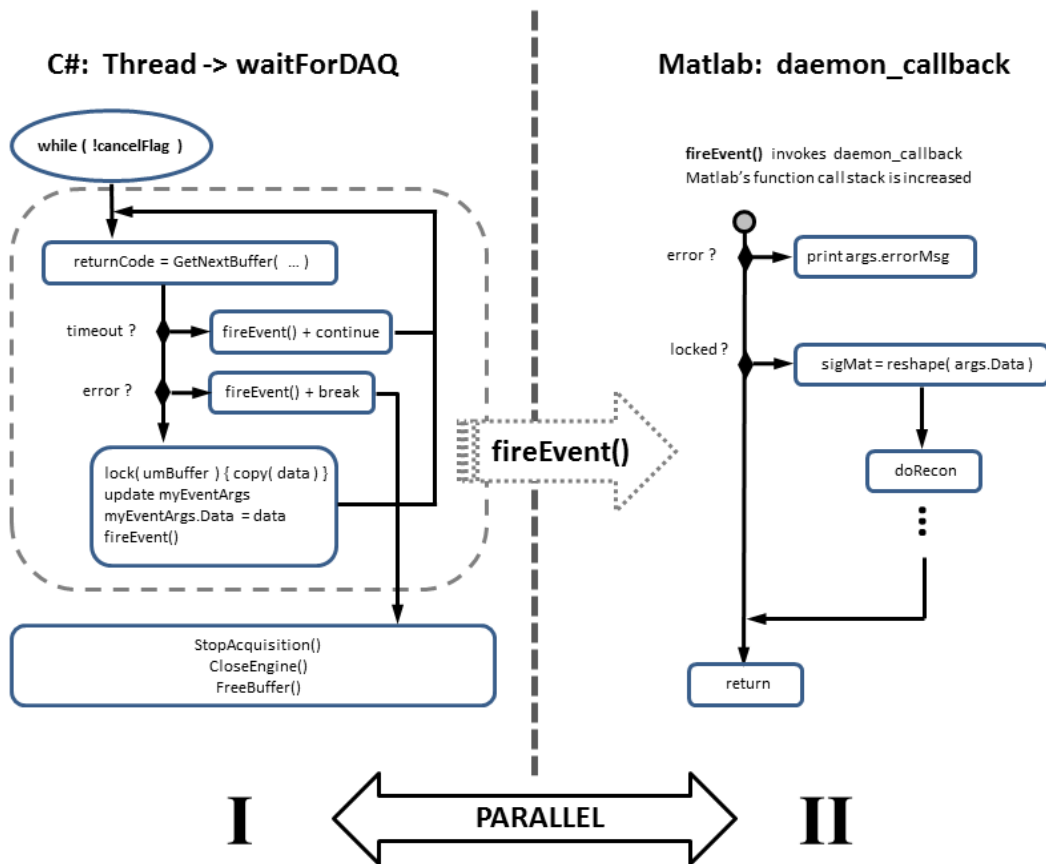


Figure 3-2 – Flow charts showing multi-threaded execution of data acquisition (retrieval and error handling) implemented as a C# assembly (part I) and Matlab based data processing (part II).

The method initializes instance variables and parameters (buffers, control parameters, etc.) and then instantiates the C# class “ThreadWrapper” and invokes its main method. This method opens a connection to the DAQ and starts a thread that permanently polls the DAQ-API (actually Pleora API) for newly available data. This thread is essentially a daemon as it executes code inside a while-loop that can only be broken by an error or the external (Matlab) setting of the “cancelFlag” (recommended method of stopping threads). The code executed by the thread performs one of three actions: 1) if an error is detected breaks the loop and sends an error message to Matlab; 2) if a timeout is detected relays the timeout message to Matlab and continues listening for new data; 3) if data is available safely copies the data from the Pleora API buffer and sends the data with received messages to Matlab. Upon thread termination the acquisition is stopped, the connection closed and the buffers freed (clean-up). The interface to Matlab is realized by means of a delegate function defined in C# and set (initialized) from within Matlab.

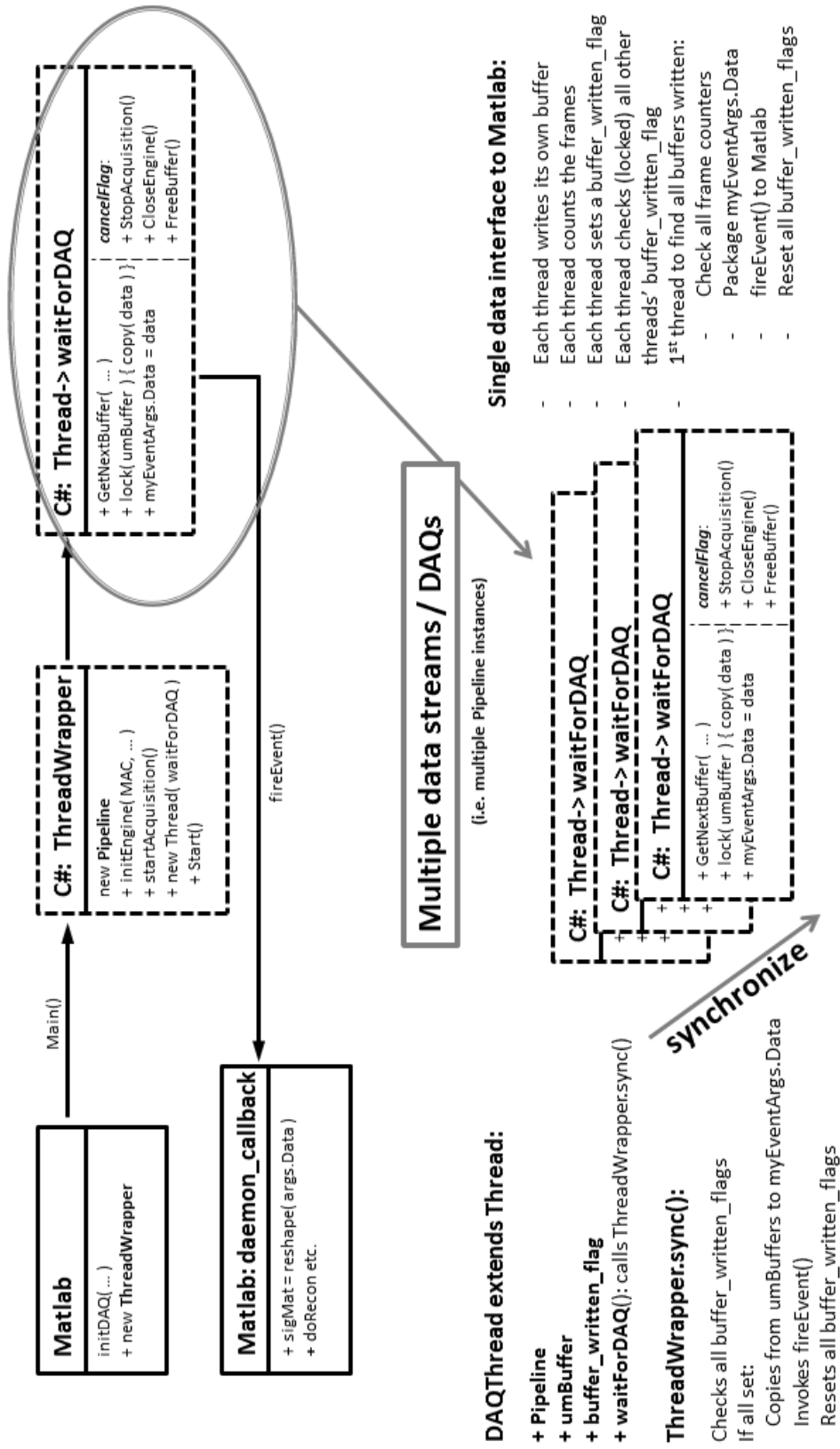


Figure 3-3 – Initialization routine and inter-process data flow is shown in the top half. The bottom half provides a template for acquisition using multiple DAQs in parallel by means of C# multi-threading. Care has to be taken in this scenario to properly synchronize threads and present a single data interface to Matlab.

The delegate end point within Matlab is called “daemon_callback” (but could be set to any function known to Matlab). The method is only invoked by the thread and is executed within Matlab’s own process environment, while the C# thread runs within a parallel .NET virtual machine (VM) environment. As a side note, the difference to Java (as of Matlab R2010b), which is also available in Matlab, is that a JVM is already instantiated by Matlab and heavily used, for example to display the graphic interface. The result is that execution within the .NET VM is much more reliable compared to the JVM. In any case, the invoked Matlab code can now execute data processing algorithms or data storage within (slightly less than, data transmission overhead!) the time frame determined by the repetition rate of the laser. In principle this setup could be extended by more C# threads, each obtaining data from another DAQ. The limiting factor of course would be processing power and bandwidth available on the mainboard (number of Ethernet ports and bandwidth reserved for them). However, operating 2-4 DAQs in parallel should be possible by multi-threading, if care is taken to properly synchronize the threads and present a unified data interface to Matlab. Figure 3.3 bottom half depicts a possible concept for implementation.

Deployment testing and characterization steps are depicted in figure 3.4. First, we compared a stable DAQ (FM-DAQ) to a readily available National Instruments 64-channel DAQ (NI-DAQ) based on PXI-5105 cards. To facilitate comparability we utilized a half-arc curved detector array setup similar to the one reported for example in [75] and placed a cylindrical scattering and absorbing Agar phantom ($\mu_s = 10 \text{ cm}^{-1}$, $\mu_a = 0.25 \text{ cm}^{-1}$) at its center. Figure 3.4(a) depicts signals (left) from one channel acquired by the NI-DAQ and FM-DAQ and the respective reconstructions using a model-based algorithm (right). Data were acquired from a single laser pulse at 750 nm excitation wavelength. Signals and reconstructed images were found to be largely comparable. Subsequently, we measured the electrical impulse response of the curved array setup including the newly developed DAQ. We thereby employed three different methods as described in [77]: method I (planar illumination of a semi-transparent slab) yielded the best and most reproducible result. This measurement was later established as the default impulse response applicable for deployment. Figure 3.4(c) demonstrates benefits attainable by correction of measurement data. To establish a link between impulse response measurement accuracy and attainable image quality we studied the influence of variations in accuracy of the measurement. Figure 3.4(b) summarizes the study: we simulated OA data for the 64-element curved array (routinely employed at the time) for the initial pressure distribution marked as (1). We then convolved each signal with a different impulse response shown in fig. 3.4(b) top left. Each impulse response was based on the best measurement available (method I) and subsequently distorted by multiplication with a random Gaussian distribution in the frequency domain. In addition we phase shifted each response by a random value and added noise taken from real measurements.

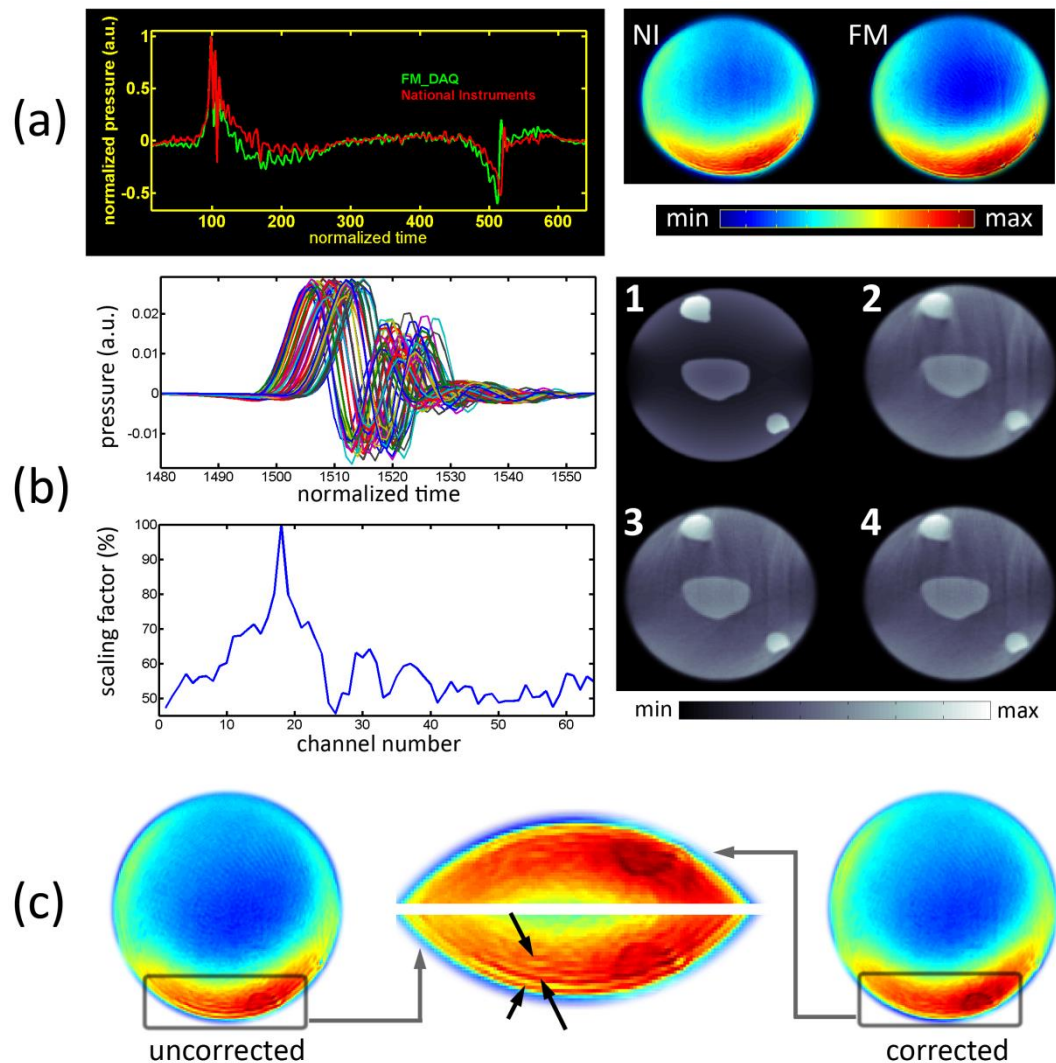


Figure 3-4 – Studies relating to DAQ development. (a) Comparative measurements between the National Instruments (NI) DAQ and the custom developed Falkenstein Mikrosysteme (FM) DAQ. (b) Study of electrical impulse response: 64 simulated OA signals were convolved by 64 impulse responses each slightly phase shifted and frequency distorted (top left), scaled (bottom left) and added on noise measurements taken from the FM-DAQ. Reconstructions on the right (1 shows reconstruction target) were performed from uncorrected signals (2) and signals de-convolved by two impulse response measurements (3 and 4) as described in [77]. (c) Reconstructions from identical data showing improved image quality after impulse response correction (de-convolution).

Each of the 64 OA signals was further scaled by factors depicted in fig. 3.4(b) bottom left to reflect gain variations of real data. Reconstruction results are shown on the right of 3.4(b): the ground truth is marked 1; a reconstruction without taking account of any impulse response is marked 2; reconstructions marked 3 and 4 were obtained by correcting with impulse responses measured by point illumination of a highly absorbing slab of Agar (3) or by planar illumination of a microsphere (4). We can see that correcting for an impulse response improves boundaries of absorbers and reduces reconstruction artifacts even if the measured response is not ideal. Figure 3.4(c)

highlights improvements attainable when correcting with the best available impulse response. Ripples manifested as concentric rings at sharp boundaries (arrows) were removed while preserving other frequency characteristics. The optical imperfection accidentally created when constructing the phantom gained signal strength compared to the surrounding background and also displays improved shape allowing for better recognition in the corrected image.

3.2 Performance of linear versus curved array

Having established a setup capable of providing integrated illumination and cost-efficient data acquisition, we investigated the performance of curved versus linear arrays. The 64-element half-arc curved array previously employed in the development of the FM-DAQ was compared against a standard linear array commonly used in ultrasonography (Acuson L7). We have previously published part of the text and data presented herein in [78].

In order to characterize and compare the optoacoustic imaging performance, we have chosen two imaging target configurations simulating clinical scenarios. Both configurations are based on a cylindrical “background” medium (Agar based or porcine tissue) of 60 mm diameter and 60 mm height. In the first configuration (type A), depicted in figure 3.5(a), we inserted a transparent cylindrical Tygon tube of 7 mm outer and 5 mm inner diameter concentrically into the background medium. The type A configuration was employed to examine the sensitivity and the overall image quality of the two detection arrays employed. In the second configuration we extended type A by inserting a second clear cylindrical Tygon tube of 3 mm outer and 1 mm inner diameter into the 5 mm diameter tube, as shown in fig. 3.5(b). We termed this second configuration as “type B”. The type B configuration allows us to examine the ability of resolving an agent in the environment of strong absorbers. A simulation of real tissue properties was attempted by preparing the porcine muscle phantom depicted in fig. 3.5(c). Furthermore, figure 3.5(d) shows the absolute absorption spectra of contrast agents employed.

To evaluate the sensitivity achieved as a function of depth, under well controlled conditions, we employed 4 agar phantoms to simulate the acoustic and optical properties of tissue. All 4 phantoms were made of agar material, which contained a fatty emulsion to impart a background reduced scattering coefficient of $\mu_s = 10 \text{ cm}^{-1}$. Two of the four phantoms additionally contained black ink (to impart photon absorption) as described in the following.

Phantom A1 (type A geometry) had no background absorption. The inner 5 mm tube contained India ink in water solution imparting an absorption coefficient of $\mu_a = 5.75 \text{ cm}^{-1}$ at 750 nm wavelength, which simulated the absorption of oxygenated hemoglobin in an artery. In the following this ink concentration will be referred to as the “ink solution”.

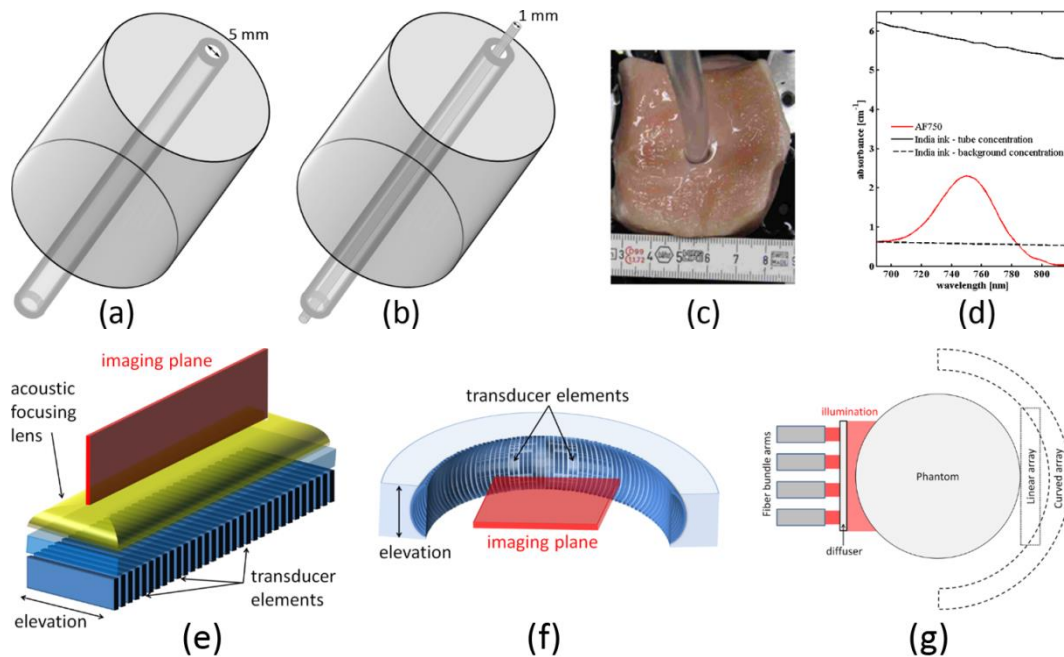


Figure 3-5 – (a)-(c) Phantom types: (a) Type A configuration. (b) Type B configuration. (c) Porcine muscle phantom. (d) Spectra of employed absorbers. Schematic showing construction of (e) linear array and (f) curved arrays. (g) Measurement setup chosen to attain the ideal illumination/detection pattern.

Phantom A2 (type A geometry) was identical to A1, whereby the 60 mm diameter agar material further attained an average background absorption coefficient of $\mu_a = 0.25 \text{ cm}^{-1}$.

Phantom B1 (type B geometry) had no background absorption. The 5 mm tube contained the ink solution. The innermost tube of 1 mm diameter contained a water based solution containing ink and an optical contrast agent, AlexaFluor750 (AF750). The solution was created by adding AF750 to the ink solution until an absorption coefficient of $\mu_a = 8.05 \text{ cm}^{-1}$ at 750 nm was achieved.

Phantom B2 (type B) was identical to B1, but the 60 mm agar medium also attained an average absorption coefficient of $\mu_a = 0.25 \text{ cm}^{-1}$.

In addition, we employed two more phantoms made of fresh porcine muscle tissue of similar thickness as the agar phantoms, i.e. approximately 60 mm in diameter and 60 mm in height. **Phantom A3** was of type A with the 5 mm dia. tube containing the ink solution. For multi-spectral imaging a type B arrangement was also established using porcine muscle (**phantom B3**), whereby the 5 mm inner diameter and the 1 mm inner diameter tubes attained the same optical properties as in phantoms B1 and B2 (see table 1).

All phantoms were submerged in water inside a tank large enough to hold the entire measurement setup. An Oportek Phocus laser provided laser pulses, which were coupled into a fiber-bundle (Ceramoptec GmbH, Germany) with 4 branching arms, each with a 2.5 mm active inner diameter at the distal end. A rectangular region of about 40 mm length and 10 mm width was then illuminated on the phantoms by arranging the fiber bundles in a line, 8 mm apart in front of an optical diffuser. Figure

3.5(g) shows the trans-illumination arrangement. For multi-spectral acquisition eleven wavelengths, equally spaced from 700 nm to 800 nm, were selected. Data acquisition was facilitated by the FM-DAQ in parallel. Before image reconstruction using a model-based algorithm [59], the data was filtered using a bandpass with upper edge frequency of 5 MHz and a variable lower edge frequency in the range of 300 kHz. The reconstructed images were post-processed by window and leveling to improve contrast. A multi-spectral dataset was then unmixed using Independent Component Analysis (ICA) as described in [71].

Table 2 – Optical properties of employed phantoms at 750 nm

Phantom	60 mm cylinder		5 mm tube		1 mm tube	
	μ_s' in cm^{-1}	μ_a in cm^{-1}	μ_s' in cm^{-1}	μ_a in cm^{-1}	μ_s' in cm^{-1}	μ_a in cm^{-1}
A1	10	0	10	5.75	N/A	N/A
A2	10	0.25	10	5.75	N/A	N/A
A3	porcine tissue	porcine tissue	10	5.75	N/A	N/A
B1	10	0	10	5.75	10	8.05
B2	10	0.25	10	5.75	10	8.05
B3	porcine tissue	porcine tissue	10	5.75	10	8.05

Evaluation of individual element signals

To study the sensitivity and the signal to noise ratio (SNR) achieved in the measurements, we performed first an analysis of raw data collected from the different phantoms. Figure 3.6(a) shows the signal obtained from phantom A1 captured by one of the curved array elements.

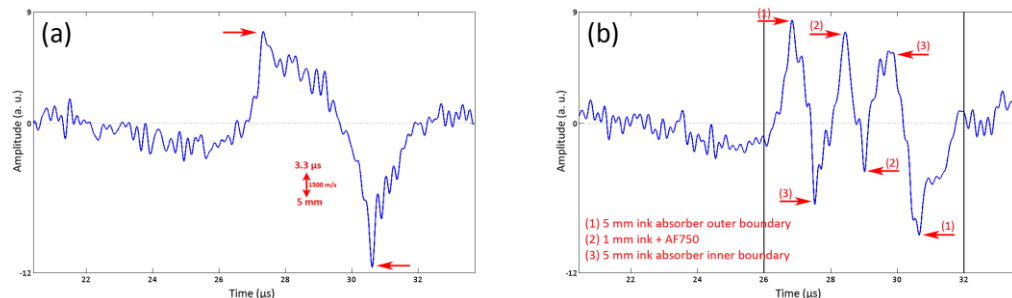


Figure 3-6 – Optoacoustic signal of absorber(s) within inner tube(s) from (a) phantom A1, (b) phantom B1. Arrows indicate object boundaries.

The position of the absorber is clearly identified on the measurement, as indicated by the arrows. Correspondingly, figure 3.6(b) shows a measurement obtained from phantom B1, detected by the same element of the curved array. Indicated by (2) is the thinner innermost absorber (1 mm), which gives a bipolar signal as in 3.6(a) albeit for a smaller diameter. Due to the tube-in-tube configuration a ring shaped absorber has been created by the transparent wall of the inner tube; its boundaries are indicated by (1) and (3). To compare the signal to noise ratio (SNR) of raw data collected by the curved and linear array, we analyzed data obtained from phantoms B1 and B2 for channel 32 (curved array) and channel 64 (linear array). Those channels represent a

centrally located detection element placed in approximately the same position relative to the phantom imaged. Then we selected data that represented the insertion signal (absorber within the 1 mm and 5 mm tubes). In figure 3.6(b) we marked the start and end of the extracted signal data by vertical solid lines at 24 μ s and 32 μ s. We also selected data of equal length from the beginning of the data vectors (2-10 μ s), where we expected only noise due to an absence of absorbers (except water) and the extremely reduced light fluence. To obtain the SNR we calculated the root-mean-square (RMS, standard deviation) of signal and noise, and inserted them into Eq. (23):

$$SNR = 20 \log_{10} \left(\frac{RMS_{signal}}{RMS_{noise}} \right). \quad (23)$$

All data employed in the SNR calculation were band-pass filtered (0.1 – 5 MHz). The data acquired from the linear array was averaged ten times more than the curved array data. Hence, to approximate comparability, the ratio calculated for the linear array was divided by the square root of 10 before taking the logarithm to obtain the 10 average equivalent SNR. Table 2 shows channel 32/64 SNRs achieved by the detection geometries for phantoms of type B. Similar values can be computed for the remainder of phantoms. The results in table 2 demonstrate the superior sensitivity of the curved geometry given the same number of averages. When taking the average over all channels (e.g. the image contrast to noise ratio), we expect significantly larger differences due to the different overlap in sensitivity fields at the ROI, see figure 2.15. As expected there is also an observed drop in SNR of the center absorber as background absorption increases in the phantom. Conversely, small SNR differences were observed between phantom B2 and the porcine muscle phantom B3, indicating that the agar phantom resembles the tissue phantom with respect to its optoacoustic properties.

Table 3 – Achieved SNR in this study

SNR	Phantom B1	Phantom B2	Phantom B3
Curved array	14.6 dB	11.1 dB	11.8 dB
Linear array	8.8 ^a dB	4.1 ^a dB	4.3 ^a dB

^a10 average equivalent

Results obtained from the linear array

Figure 3.7 summarizes experimental results obtained from the linear array probe. All image axes are given in millimeters. Each image shows the same object and region as the corresponding image of fig. 3.8. **The first column** depicts results from phantoms A1 and B1: fig. 3.7(a) shows the reconstruction of phantom A1 at 750 nm. The ink absorber within the 5 mm diameter tube could be resolved, albeit with limited quality compared to the corresponding reconstruction using the curved array, shown in fig. 3.8(a). Although changes are expected between linear and curved arrays, the image comparison between corresponding panels in fig. 3.8 and fig. 3.7 allows for a more detailed comparison of the relative performance achieved when using the same target but different imaging systems. Missing horizontal boundaries are a prominent feature

of optoacoustic imaging with incomplete projection data (see [79]) and can be attributed to the highly limited angle of reception (about 68°) afforded by the linear array. Fig. 3.7(d) shows the distribution of ink in Phantom B1, presented in color and superimposed on a single wavelength image in grayscale. For brevity, we will henceforth refer to this manner of presentation as “color overlay”, i.e. a thresholded color overlay of the respective distribution (ink or AF750) on top of the same single wavelength image of the corresponding type B phantom. Due to the severely limited quality of reconstructions in this case, we marked the boundaries of both tubes with white arrows. In Fig. 3.7(g) the distribution of AF750 in phantom B1 is visualized as color overlay on the same grayscale image used in 3.7(d). Correspondingly ink was correctly identified in both tubes (5 mm and 1 mm), whereas AF750 was detected only within the innermost 1 mm tube.

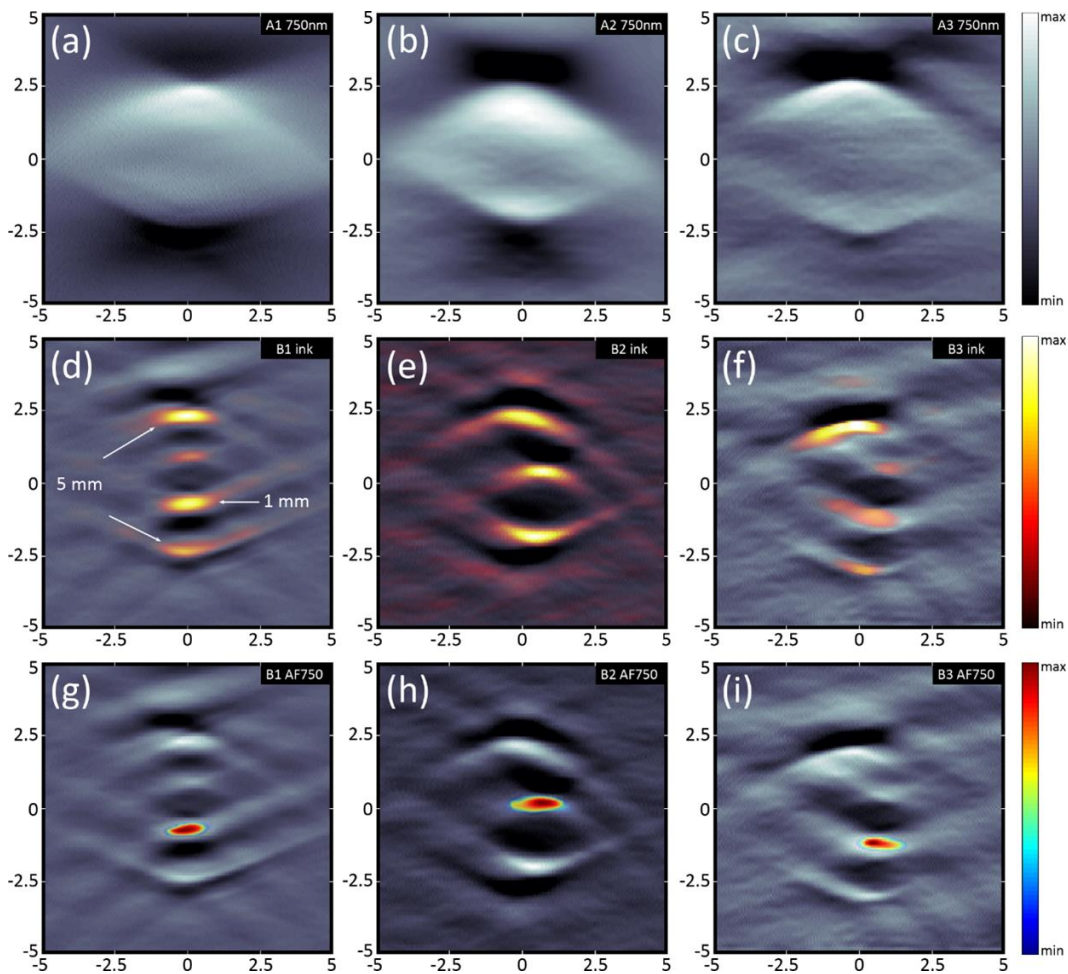


Figure 3-7 – Linear array reconstructions. The first row shows single wavelength images of (a) phantom A1, (b) phantom A2, (c) phantom A3. The second row shows the distribution of ink from (d) phantom B1, (e) phantom B2, (f) phantom B3. Grayscale represents a single wavelength image, whereby the color overlay shows the resolved ink concentration. The third row shows the distribution of AF750 from (g) phantom B1, (h) phantom B2, (i) phantom B3. Grayscale images are the same as in the second row; however the color overlay shows the AF750 concentration.

The second column shows results for phantoms A2 and B2. As expected from the SNR analysis the single wavelength reconstruction of phantom A2, depicted in fig. 3.7(b), displays more background noise, yet is qualitatively comparable to 3.7(a). The distribution of ink in phantom B2 is presented in fig. 3.7(e) as color overlay on top a single wavelength image of phantom B2. The ink solution was correctly identified within both tubes. In addition we resolved the presence of ink within the background medium. Similarly, Fig. 3.7(h) shows the distribution of AF750 in phantom B2. Again the AF750 content of the 1 mm tube can be localized beyond doubt. **The third column** shows results for the porcine muscle phantoms A3 and B3. Fig. 3.7(c) represents the reconstruction of phantom A3 at 750 nm. Background noise and contrast are worse compared to Fig. 3.7(b), but nonetheless allow the identification of the ink solution contained in the 5 mm tube within the bounds of what is achievable with the linear array. Fig. 3.7(f) depicts the distribution of ink in color and superimposed on a single wavelength image of phantom B2. The color overlay correctly resolves the ink solution within both tubes; however imaging and multi-spectral performance was visibly worse compared to fig. 3.7(e). Results for phantom B3 obtained from the curved array, fig. 3.8(f),(i), showed similar background artifacts. Therefore we believe that the weaker acoustic focus and limited angle of reception of the linear array affected image reconstruction for phantom B3 more than was the case for phantom B2. Nevertheless, the AF750 concentration, depicted in Fig. 3.7(i) in color on top of the identical grayscale image used in fig. 3.7(f), could be identified unambiguously.

Results obtained from the curved array

Figure 3.8 summarizes results obtained using the curved array detector. All image axes are given in millimeters. The images show the same region of 8x8 mm centered on the phantom as depicted in figure 3.7. **The first column** shows results from phantoms A1 and B1. The images represent the best SNR achieved in the study, because these phantoms had no background absorption; all light attenuation was only due to scattering. Fig. 3.8(a) depicts an image of the 5 mm inner diameter tube in phantom A1 reconstructed at the 750 nm wavelength. The tube is clearly visible even at single wavelength measurements and its shape is accurately reconstructed. Stronger signal intensity appears on one side of the image due to the orientation of the illumination employed that deposited higher energy at the top part of the tube. Fig. 3.8(d) shows in grayscale the single wavelength image (750 nm) from phantom B1 (configuration Type B, fig. 3.5), whereby a 1 mm inner diameter tube was present inside the 5 mm tube. The distribution of ink in the phantom was found by spectral unmixing using ICA. The corresponding image of ink distribution is also shown on fig. 3.8(d) in color. The image was thresholded to 50% of the maximum to remove background and superimposed on the single-wavelength grayscale image. In fig. 3.8 (d) the ink solution, present in both, 5 mm and 1 mm inner diameter, tubes, is clearly congruent with the inner volume of both tubes. The black ring shaped area, denoted as "tube wall" in fig. 3.8(d), thereby represents the transparent and therefore non-absorbing wall of the 1 mm diameter tube. Fig. 3.8(g) correspondingly shows the same single wavelength image as in fig. 3.8(d), but this time the distribution of AF750,

thresholded to 50% of maximum, is superimposed in color. Thus fig. 3.8(g) confirms that the 1 mm tube, besides ink, also contained AF750, whereas the 5 mm tube only contained ink.

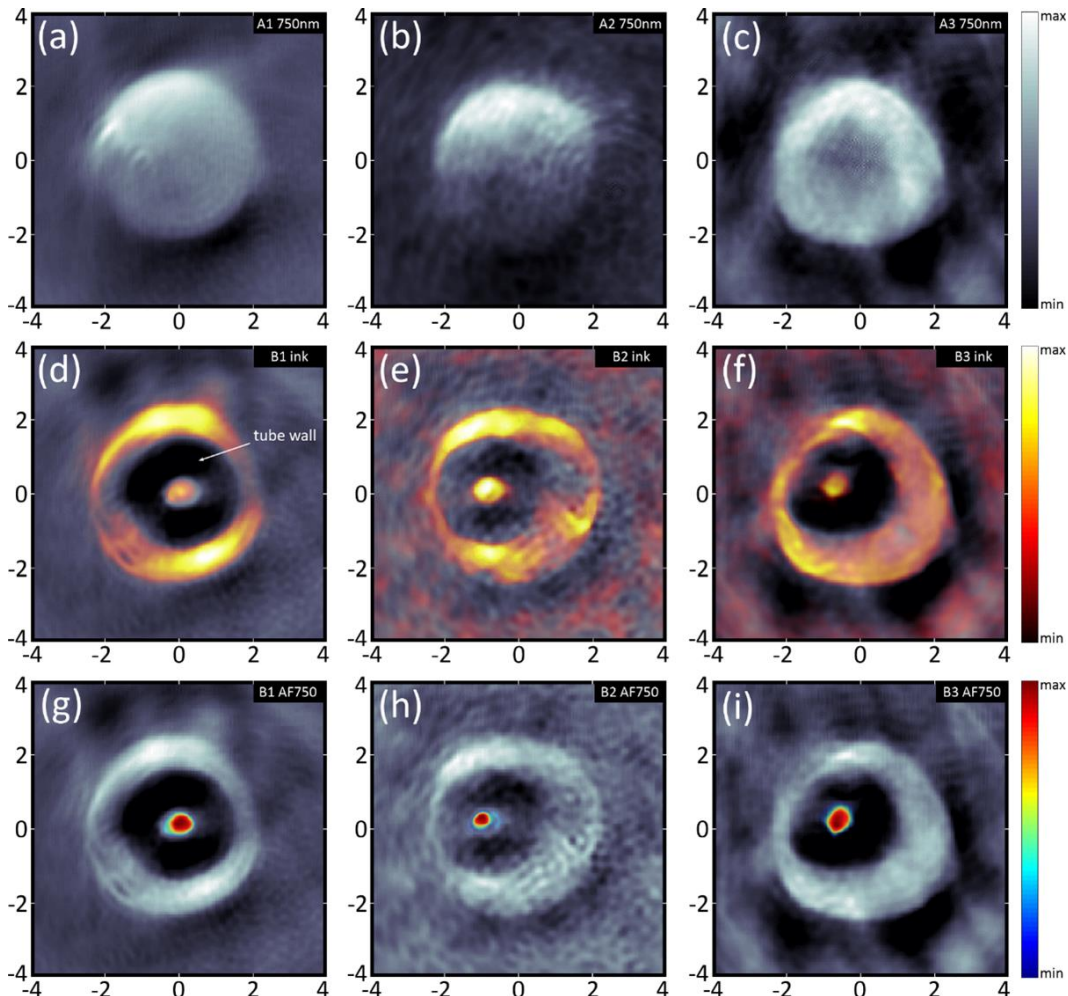


Figure 3-8 – Curved array reconstructions. The first row shows single wavelength images of (a) phantom A1, (b) phantom A2, (c) phantom A3. The second row shows the distribution of ink from (d) phantom B1, (e) phantom B2, (f) phantom B3. Grayscale represents a single wavelength image, whereby the color overlay shows the resolved ink concentration. The third row shows the distribution of AF750 from (g) phantom B1, (h) phantom B2, (i) phantom B3. Grayscale images are the same as in the second row; however the color overlay shows the AF750 concentration.

The second column shows results obtained from phantoms A2 and B2. Fig. 3.8(b) shows the reconstruction of phantom A2, whereby the 5 mm inner diameter tube is clearly visible, but with reduced contrast compared to fig. 3.8(a). This is due to a weaker light intensity that reaches the 5 mm tube, due to the presence of absorption in the background medium. Fig. 3.8(e) shows the distribution of ink as color overlay on top of a single wavelength reconstruction (in grayscale) of the 5 mm tube within phantom B2. Again, the reconstructed image confirms the presence of ink solution in both tubes (5 mm and 1 mm). Strong color variation is also observed in the background of the image in this case, because of the utilization of ink for background absorption.

Fig. 3.8(h) depicts the same single wavelength image as Fig. 3.8(e), with the AF750 distribution depicted as color overlay and thus confirms that spectral un-mixing accurately localized the AF750 in the 1 mm tube. **The third column** shows reconstruction and multi-spectral processing performance achieved from the fresh porcine muscle phantoms (A3 and B3). Fig. 3.8(c) shows the 5 mm tube reconstructed at 750 nm from phantom A3, whereby the ink solution contained in the 5 mm tube yielded higher contrast compared to fig. 3.8(b). This can be attributed to a lower than assumed absorption in the porcine tissue sample employed, due to blood drain from the muscle. In addition a stronger absorption variation is observed at the background, compared to the agar phantoms, possibly due to the higher optical heterogeneity of the tissue sample. Fig. 3.8(f) depicts the distribution of ink in color overlaid on a single wavelength image in grayscale for phantom B3. The color overlay correctly resolves an increased absorption in both tubes (5 mm and 1 mm). Fig. 3.8(i) depicts the distribution of AF750 superimposed in color on the grayscale image as in Fig. 3.8(f).

Conclusion

The results from the linear array showed that it is possible to detect absorbers of 1-5 mm sizes seated deep inside tissue. Single wavelength reconstructions provided sufficient contrast and image quality to capture insertion anatomy. In addition multi-spectral processing was deployed to locate the AF750 dye, which in a single wavelength image could not be distinguished from other absorbers. The weaknesses of the employed array, i.e. a significant number of averages and weak elevational focus, could be addressed by designing a linear probe, which is optimized with respect to sensitivity in the frequency range up to 4-5 MHz and elevational slice thickness at the depth of 15-30 mm. However a major drawback remains image quality. Missing horizontal boundaries and reduced horizontal resolution is an inherent feature of any linear array geometry in optoacoustic imaging. A probe width of about 40 mm and depth requirement of 30 mm allows us to observe our region of interest from within an angle of about 68° . In echo ultrasound this poses no problem as imaging is based on detection of reflected echoes following a directed sending pulse. In this way all interfaces, even round ones, can be imaged. Yet in optoacoustic imaging sources are generated inside the region of interest and radiate spherical waves in all directions. By limiting our view angle we therefore limit our image quality with respect to horizontal resolution.

The images derived from the curved array show markedly better imaging performance compared to the images obtained by the linear array. Shape, position and absorption values of the insertions could be resolved with much higher quality. The curved array delivers viewing angles of 172° , which offers more complete tomographic data sets that can reconstruct vessels with better fidelity. Due to the heightened sensitivity of the array around the center, compared to the linear probe, it was also possible to reduce the number of averages to manageable levels and showed potential for further reduction. Besides having its sensitivity peak at 5 MHz and thus closer to the frequency range of interest, this is due to two conceptual differences: the curved array elements are larger in size and are all looking at the same point, the center of

the array. As a consequence the area around the center can be imaged with much higher sensitivity than is possible with a linear array assuming the same number of averages. Unfortunately we have to pay with a limitation in terms of usability. If less depth is required, the probe would have to be physically retracted and the resulting cavity filled in order to provide acoustic coupling.

In both cases MSOT identified the absorption spectrum of a fluorochrome. The resulting images of fluorochrome distribution confirmed the performance betterment when employing the curved array, over the linear array. The ability of MSOT to image fluorescent probes is clinically appealing although the detection sensitivity needs to be investigated on a per disease and agent case. The light attenuation conditions examined herein within phantoms were an approximation of in-vivo optical properties, which were selected to be $\mu_a = 0.25 \text{ cm}^{-1}$ and $\mu_s = 10 \text{ cm}^{-1}$, modeled after average human tissue as given in table 5.1.3 in [42].

3.3 Non-invasive handheld probe

As we have shown, for optoacoustic imaging curved arrays are clearly superior to linear arrays in both SNR and image quality, yet so far studies attempting non-invasive handheld optoacoustic imaging have focused exclusively on linear arrays [33, 34, 36, 38]. The reasons may include a desire to provide co-registered ultrasonography together with optoacoustic images, the lack of customized DAQs (compared to readily available ultrasonography electronics) or the additional difficulties involved in efficiently coupling the cavity opened by curved arrays. Whatever the reasons, these publications and our own efforts enabled us to draw valuable conclusions about the sources of low SNR, poor image quality and image artifacts.

Hence, our concept for designing a non-invasive handheld optoacoustic probe can be summarized by the schematic drawing and caveats depicted in figure 3.9(a). A curved array is generally larger and heavier compared to a linear array and will additionally require a coupling medium to enable ultrasound wave propagation. Therefore large coupling mechanics or casings are to be avoided and instead light-weight acoustically transparent foil should be used, which should be also optically transparent due to the need for epi-illumination. To further save weight and increase robustness, illumination should be delivered by a shaped output fiber bundle, ideally delivered at the focal plane of the array, i.e. at an angle to the array sides. Similarly, the foil should not be too flexible such as to allow the object imaged (e.g. limb of patient) to penetrate too deeply into the cavity. Thereby, “too deeply” is defined by the available imaging ROI: all signals must be contained within the ROI, otherwise accurate reconstruction is not possible (comparable to out-of-plane illumination).

We realized these design parameters in iterative steps, a select few of which are shown in figure 3.9(b). Initial measurements (left image) were accomplished by mounting the appropriate excitation/detection geometry in a fully water-coupled environment without implementing the coupling mechanics for handheld operation.

The array employed was previously reported in [75, 76] and studied in depth in chapter 4.3, also published in [80].

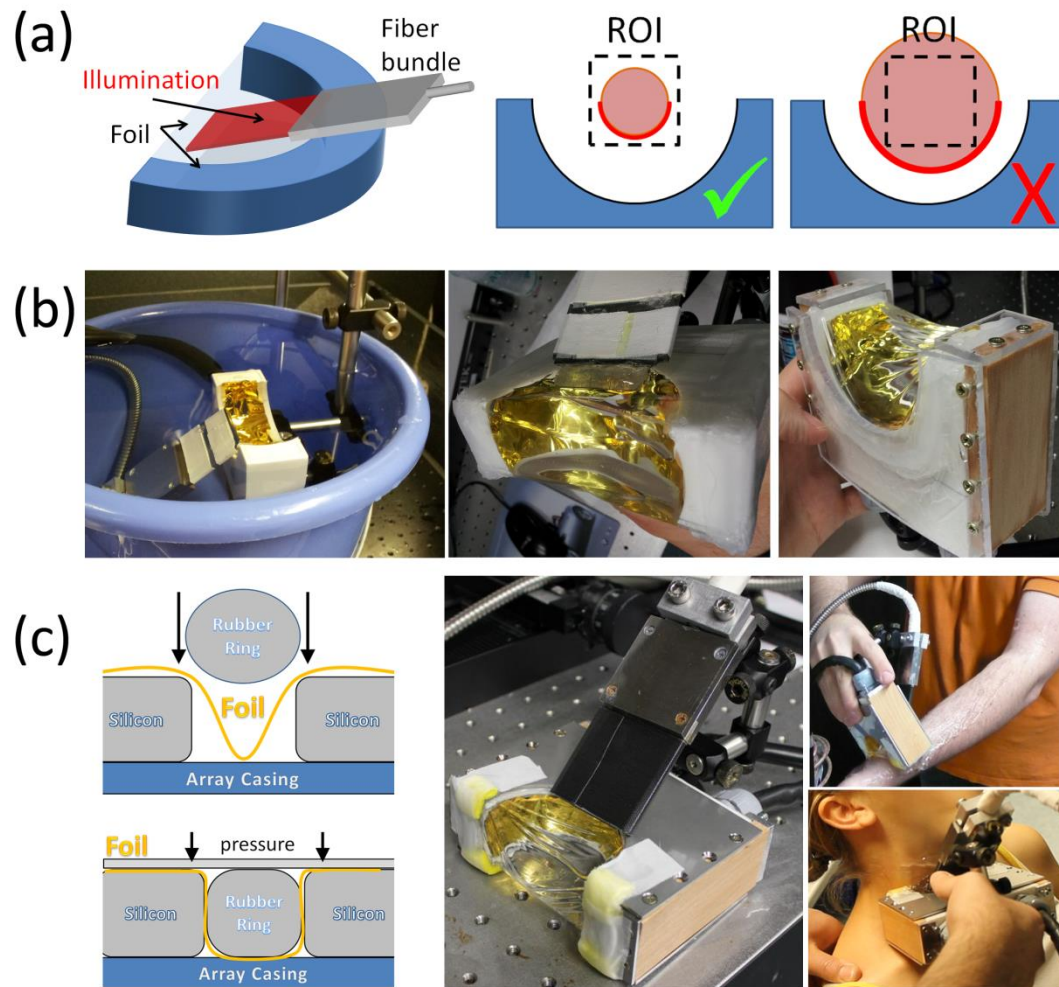


Figure 3-9 – Phases of development: (a) Top row depicts the developed concept (left) and conclusions for illumination gained from phantom studies. (b) The middle row shows a “free” concept implementation (left) without sealing the array cavity, the intermediate stage attempting handheld operation with sealed cavity (middle) and an advanced sealing design (right). (c) The bottom row illustrates the devised “double O-ring” sealing mechanism (left), the final operational prototype (middle) and two experimental applications (right).

The next step required filling the array cavity with water and efficiently sealing it. A first attempt involved transparent foil glued to the array by silicon (3.9(b) middle image). While this configuration allowed several minutes of measurement, it rapidly leaked water, because the silicon did not adhere to the foil. Further study concerned with mechanically solving the problem, we devised a pressure based system, depicted in figure 3.9(b) right image. A silicon ring was deposited on the sides along the cavity outline and allowed to cure. This “silicon ring” was enclosed under water with foil and the depicted casing assembled in order to compress the foil against the silicon ring. This setup allowed several imaging sessions before eventually leaking small amounts

of water, which were acceptable until air penetrated the cavity. Our analysis showed that leakages were a consequence of increasing pressure in what essentially is a hydraulic system during measurement contact. The chosen materials and sealing mechanism were not sufficient to effectively contain the pressure required. Thus, we upgraded the employed materials, now using stainless steel plates, and, more importantly, devised what we refer to a “double O-ring” configuration, depicted on the left of figure 3.9(c). Viewed along the cross-section of one side two silicon pads are deployed on the array casing with a gap left in between. The foil is placed on top and compressed into the gap by a second rubber O-ring, which itself is pressed into the gap by the metal casing. The metal plates, one on each side, were tightened into an additional element placed along the length of the array. This way the plates generated the necessary counter-pressure for each other. To also exert pressure onto the front (more than is available from friction) we included a counter-screw on the back of the array, pulling the casing towards the array cables. The image in the middle of figure 3.9(c) shows the fully assembled prototype (version 1) including shaped and directed fiber bundle illumination, water coupled and ready for measurement. Images on the right depict two applications of handheld imaging on human volunteers.

Based on this prototype we decided to expand operational characteristics and at the same time reduce the weight and number of components involved in this design. We expanded the radius of the curved array from 40 to 60 mm, while keeping the elevational (z-axis, perpendicular to focal plane) aperture constant, i.e. $L = 24.35$ mm, see fig. 2.4(a) for definitions. To improve ROI and resolution we also opted for 256 elements at a pitch of 0.71 mm, each element focused at 65 mm. The ultrasound detection bandwidth remained identical $f_c = 5$ MHz, i.e. same frequency response. The breakthrough in terms of design refinement is depicted in figure 3.10 and concerns the mechanical water coupling design and illumination concept. This prototype version 2 (termed HOT-256) is currently in operation and involved in several clinical studies, of which some initial results will be presented in chapter 6. The HOT-256 probe is capable of operating several weeks without maintenance, mostly necessary to remove air bubbles. The double O-ring concept has been extended towards integrating the retention mechanism into the array casing. Figure 3.10(a) depicts the parts involved: the array (left image) provides screw threads and the trench into which the first O-ring is placed; stainless steel counter-plates provide the pressure. The first O-ring (depicted in the middle) is characterized by a mushroom shaped cross-section and the clip like overall shape, which perfectly fits into the trench on the array casing. After applying transparent foil a second O-ring (right image) is placed onto the foil, perfectly aligned with the first O-ring and providing additional contact to the array. Four plates are placed on each side of the cavity and tightly screwed to the array, providing the necessary pressure in the process.

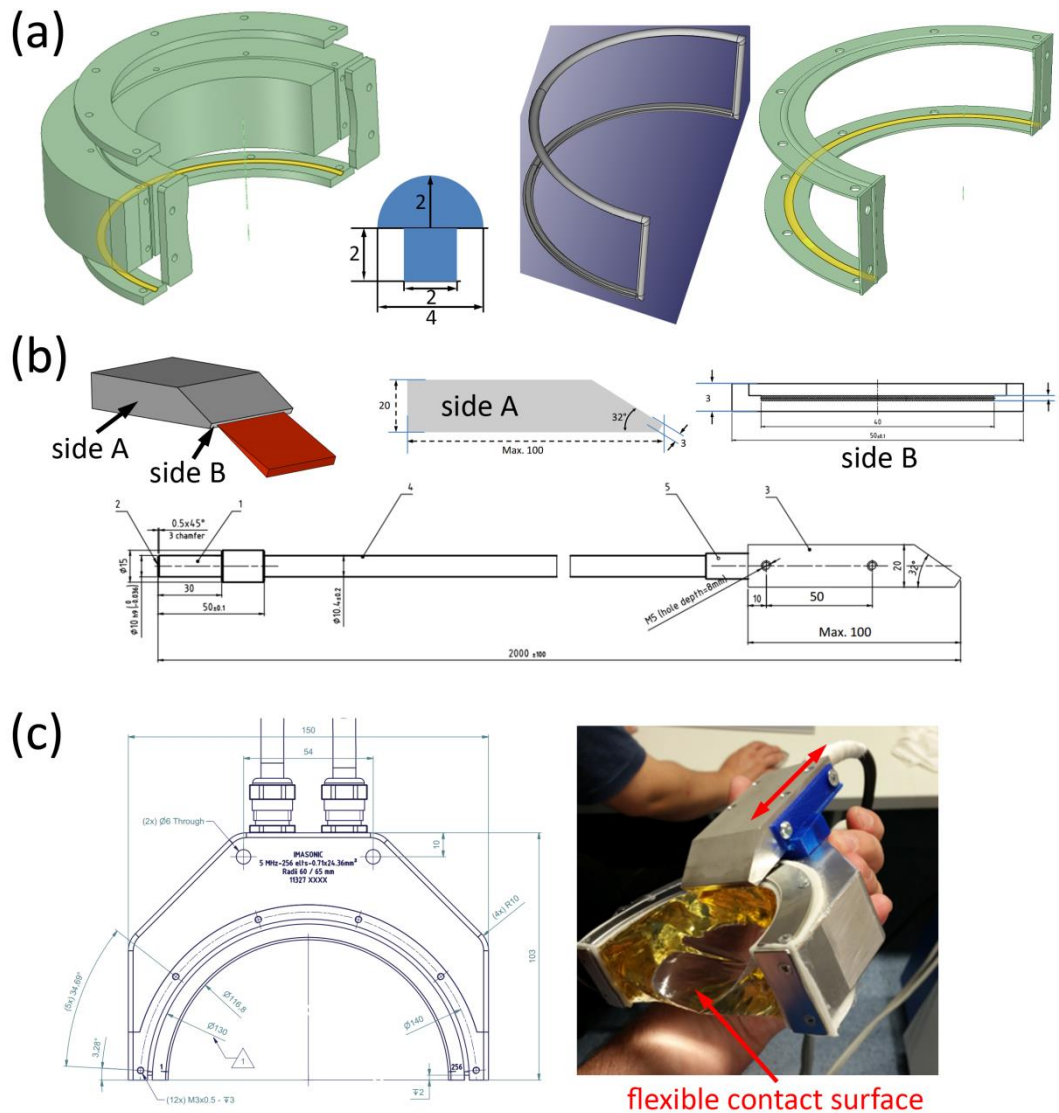


Figure 3-10 – Design and implementation of the deployment prototype. (a) 3D-CAD model of the new water coupling concept: array and counter-plates are depicted on the left; the first O-ring is depicted with a cross-section in the middle; a second O-ring is depicted on the right. (b) Novel illumination concept showing light exiting the rectangular fiber output at a 32° angle. (c) Technical drawing of the new detection array with integrated coupling mechanics (left) and the fully assembled implementation (right) coupled with water and featuring a movable carriage (back and forth) to optimize illumination according to the shape of the flexible contact surface (foil).

Figure 3.10(b) depicts the specially designed fiber bundle, featuring a rectangular output of 1 x 40 mm². Fibers inside the head (depicted in the top row) are bent at a 32° angle. The head also includes screw threads to allow assembly within a specially designed carriage, which is mounted onto the detector array. Figure 3.10(c) shows the technical drawing (left) of the HOT-256 array and a photograph (right) of the actual implementation. The movable carriage is highlighted by a double-sided red arrow indicating possible displacement. By adjusting the distance to the flexible contact surface it is possible to target the optimal illumination spot (i.e. co-planar with the

acoustic focal plane, referred to as “in-plane” illumination). Together the enlarged array radius, the flexible foil and the adjustable illumination allow measurements with adjustable pressure onto the patient, which in turn enables imaging of structures seated deeper below the skin surface with improved imaging quality.

3.4 Intraoperative setup and methodology

The imaging performance of linear ultrasound arrays may not render them very appealing for non-invasive epi-illumination assemblies, yet they offer other strengths that are only hard to match by curved arrays. As the primary probe design for ultrasonography there are a multitude of readily available models, most typically weighing less than 100g and of small dimensions. What is more, commercially available probes are highly cost effective, offering maintenance free operation and high reliability. In addition most medical staff are trained in their use. Therefore, we studied how and in what circumstances linear arrays may be usefully deployed for optoacoustic imaging.

A particular strength of our optoacoustic setup (laser and DAQ) is the ability to acquire acoustic data from up to 256 channels in parallel and with repetition rates up to 100Hz. This good time resolution may be deployed with linear arrays in a scanning setup as described in [81] or to capture dynamics [82]. Scanning is typically unavailable in a clinical setup, yet there are multiple applications where imaging of dynamics can reveal useful information. Moreover, high flexibility of probe positioning combined with high repetition rate video may enable the medical expert to assess tissue geometry beyond what a single shot image can provide in terms of resolution and image quality. One such application identified is intra-operative assessment of tissue viability, discussed in chapter 5.3. In the following we will provide the technical and methodological foundations identified for successful translation towards clinical application. Part of this text and data were previously published in [83].

Application parameters were chosen by targeting tissue viability assessment in the lower colon. Imaging of the lower colon requires a field of view on the order of the diameter of the colon (3-4 cm) and a resolution of up to 200 μm in order to observe the vasculature with sufficient accuracy. Therefore we chose the standard medical linear ultrasound array (Acuson L7, Siemens Healthcare) previously studied, which is capable of providing the required resolution and field of view. As a vascular probe, its handling and imaging principle (selective plane, B-mode) are well known to medical doctors. For initial evaluation we chose a bundle with four arms at the distal end each with a round 2.5 mm diameter output; other bundles could be easily substituted. The bundles were mounted on mechanical assemblies above the sample such that directivity and distance to the sample could be adjusted to efficiently illuminate the region of interest. Figure 3.11(a) shows a schematic of the devised geometry and photographs of experimental implementations, fig. 3.11(b), (c).

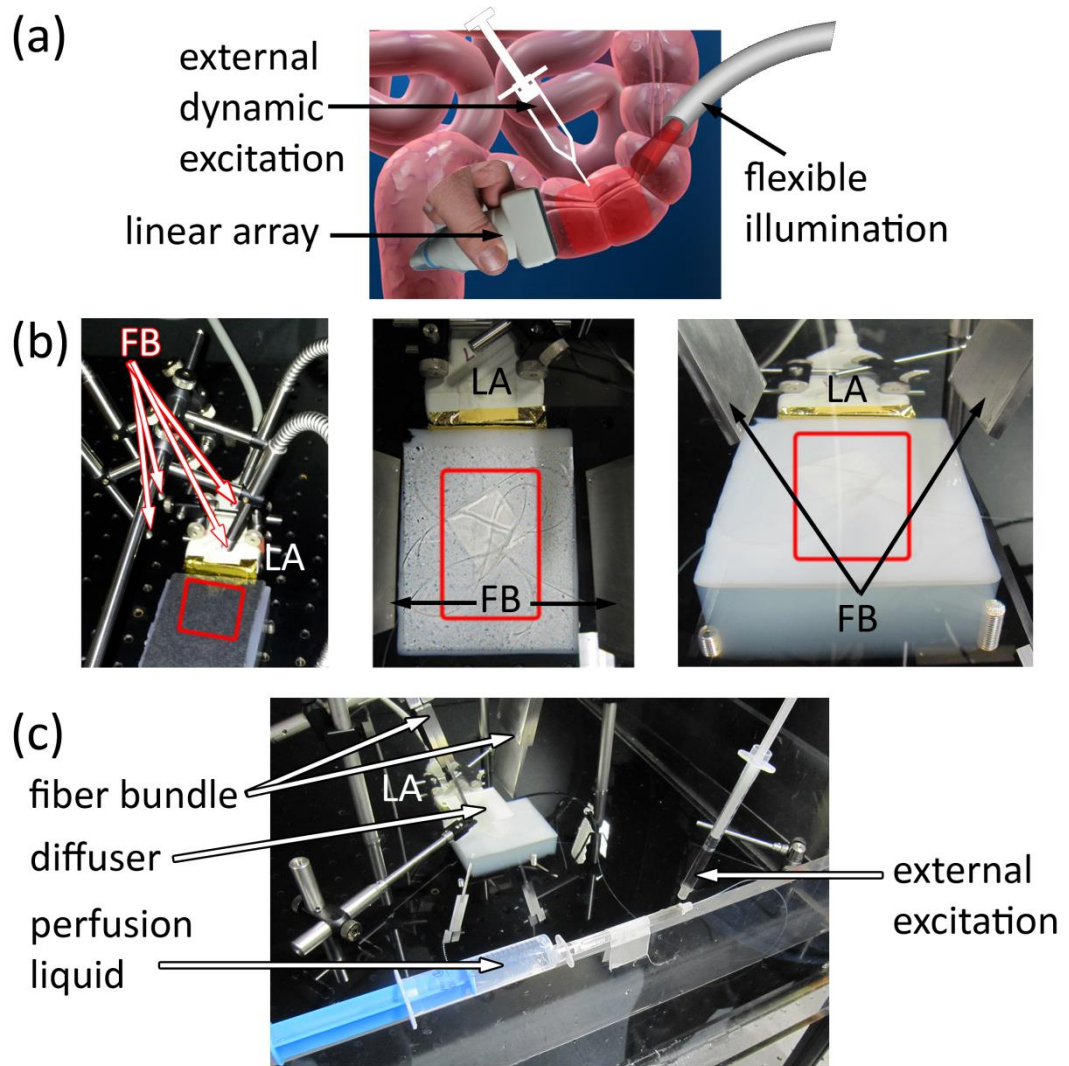


Figure 3-11 – (a) Schematic illustration of tissue viability assessment in the lower colon. (b) Laboratory setups employed for studying perfusion dynamics. FB: fiber bundle; LA: linear array; ROI: red frame. (c) Experiment simulating the target application: a bolus of highly absorbing ink (external excitation) is injected into a stream of background perfusion liquid (blood or water). The configuration is similar to the one depicted in the rightmost image of (b) but extended by an optical diffuser.

The imaging goal defined in cooperation with medical practitioners was to assess the perfusion of blood within the vascular network of the lower colon during the surgical procedure. After studying constraints imposed by the application we decided to split acoustic detection and laser illumination to obtain a maximum degree of freedom. As figure 3.11(a) shows, we envisaged a mechanically suspended and flexibly adjustable illumination. This would allow the surgeon to dynamically re-position the incident light beam as required. The linear detection array would be operated by the surgeon or an assistant by hand, interrogating the tissue as needed by manual scanning. To compensate for the poor image quality of the linear array and obtain a quantifiable measure of perfusion, we chose to externally disrupt the equilibrium of tissue contrast (mostly vasculature vs. background) by injecting a contrast agent. We studied the

achievable imaging performance using Agar based Phantoms in fully submerged experimental setups also using different illumination approaches, as depicted in figure 3.11(b). Further experiments involved setups as depicted in 3.11(c) simulating the operational environment: a constant stream of background liquid (water or blood) was deployed to perfuse a catheterized phantom placed inside the illuminated region of interest. On top of the background stream we injected a bolus of “external excitation” liquid (saline, ink or ICG) into the stream, thereby creating a transient change of average optical absorption. In the process we found that a transient decrease of absorption (injecting saline) was just as useful for quantifying perfusion as an increase (injecting ink or ICG). This transient change within the vessel lumen allows quantification of perfusion and can be achieved by flushing the vascular network with saline as described in the following.

Proposed methodology

Optoacoustic imaging relies on optical absorption for contrast. Therefore visualizing the propagation of blood along a vessel can be achieved directly by a transient change of the average absorption of the vessel content. The more intuitive change, i.e. absorption increase by means of a positive contrast agent, has already been shown in mice [75]. Here we suggest the opposite, i.e. a sudden reduction of average absorption by local injection of medical saline, followed by an increase caused by the reperfusion of fresh blood. The resulting initial dilution of hemoglobin concentration, up to the point of clearing, provides “negative contrast” during injection, meaning that the vasculature cannot be distinguished from the background. Afterwards, the subsequent reperfusion of blood enables intrinsic “positive contrast”, i.e. the vessels reappear above the background. The resulting cycle of negative/positive contrast allows accurate localization and even tracking of blood perfusion pathways. Before the injection, appropriate positioning of the probe is recommended. Vessels generally have a cylindrically elongated shape and thus generate optoacoustic waves whose amplitude is strongest perpendicular to the elongation axis. Therefore, the linear detector array should be positioned as parallel as possible to the branching vasculature. High frame-rate imaging facilitates choosing the best measurement position. Image reconstruction and post-processing were also adapted to account for the unique measurement setup and imaging goal.

Incident illumination could be assumed approximately perpendicular to the acoustic imaging plane, which ensured stronger and lower frequency signals compared to the non-invasive epi-illumination case. Hence, to focus on vascular features, we first removed the background by filtering the acquired optoacoustic data using a bandpass from 1-9 MHz. Next, we employed delay and sum beamforming to reconstruct an image of 600x600 pixels over the full field of view, e.g. 40x40mm² centered at 30 mm immediately in front of the array. Filtering and image reconstruction were parallelized, as described in chapter 4.1 but implemented on a graphics card, and thus fast enough (<30ms) to enable live visualization during the measurement. Data acquisition and reconstruction were set to 10 image frames per second such that for each measurement we obtained an image sequence proportional in length to the

measurement time. Analysis was performed in two ways. First, an image representing the strongest observed signal in the sequence was selected. Then, minimum and maximum pixel values were extracted from this image, and were used to threshold each image in the series before visualization in grayscale using a constant colorbar ranging from minimum to maximum. In a second step, to provide more quantified information than is possible by mere visual inspection of the image sequence, we designed a fast automated feature extraction and processing algorithm. For each image we computed the absolute sum of all pixel values above a fixed threshold, which we set to 15-20% of the global maximum value previously determined. This resulted in a dynamic "mask", adaptive for every frame and therefore robust to motion of the sample within the illuminated region of interest. The method, termed masked absolute sum (MAS), allowed us to compute a measure of the optical absorption of vascular features over time.

Optimizations for clinical deployability

Translation of optoacoustic technology from small-animal imaging based on controlled environment scanning towards handheld large ROI clinical applications requires careful study of critical performance parameters. The most important such parameter, without which no viable translation can succeed, is image reconstruction speed. Lag-free image reconstruction and display at ideally the pulse repetition rate of the laser system (i.e. latency $< 1/f_L$) is mandatory. In combination with image quality and achievable well-resolved region of interest, reconstruction speed forms a strong indicator of user acceptance. For this reason we paid equal attention to improving reconstruction speed, image quality and observable region of interest both for live imaging and for post-measurement evaluation. In the following we will detail contributions made towards 1) enhancing reconstruction speed for live imaging, 2) enhancing/enabling accurate model-based reconstructions of large ROIs from equally large datasets and 3) improving the understanding of curved arrays in preparation of more advanced array designs.

4.1 Improving image reconstruction speed

Just-in-time image reconstruction depends on the time frame provided for the task. In satellite imaging frame rates of one image every 15 min may be considered live. In optoacoustic imaging of small animals few images per second are sufficient to enable adequate positioning within a controlled environment. Subsequent imaging sessions are typically determined by translation/rotation stages, number of averages and repetitions; data analysis is performed offline after the measurement. Clinical handheld operation cannot afford this approach as the environment is usually highly dynamic. Both, patient and optoacoustic probe are moving, often involuntary and in an

asynchronous fashion. Therefore, averaging is undesirable and when applied, even under the best of circumstances, associated with reduced resolution. When acquiring multi-spectral data, wavelength tuning, even if fast enough (i.e. per pulse), may incur motion in between image frames. To limit this influence developments of DAQ and laser have been driven towards ever fast repetition rates. Initially only 10-20 Hz was available at the required pulse-energies; current state of the art allows up to 100 Hz. To provide smooth live video during a handheld measurement it is thus necessary to complete image reconstruction within 100 – 10 ms (10-100 Hz), depending on the setting chosen. Other characteristics of the sought after image additionally impose demands on the image reconstruction implementation. For example, newer handheld designs (HOT-256) enable a larger ROI, which in turn requires an increase in the number of image pixels to reproduce the available spatial resolution. Similarly, the demand for high image quality may necessitate post-acquisition but pre-reconstruction or even post-reconstruction processing steps.

To improve reconstruction speeds from the original Matlab based implementation, we implemented a simple delay and sum reconstruction algorithm in C, which was later adapted for OpenCL execution on GPU hardware. Figure 4.1 depicts the core of the algorithm. All detection elements and pixels of an image are associated with a unique position in the common coordinate system, in case of 2D imaging x and y (Cartesian coordinates). Each possible combination of pixel and detector is characterized by a physical distance in meters, which can be converted by the speed of sound into a time delay, equal to the propagation time of the acoustic wave that was emitted at the pixel location. An example is given in figure 4.1(a): detection element k and pixel px_i are positioned at a distance $d_{k,i}$ from each other. This distance can be converted into a delay time by dividing with the speed of sound, and by multiplication with the sampling rate of the DAQ into an index $k_{k,i}$ into the signal s_k . If there are K projections and n^2 image pixels, we must extract $K \cdot n^2$ values from the acoustic data. Next, figure 4.1(b) shows how these values are combined to form the image. Each data value taken from data space ($m \cdot K$) is added into the appropriate position in the image buffer (image space). Multiple pixels can be assigned the same value as well as other values, i.e. each pixel accumulates multiple data values.

The simplest implementation is a cascade of two for-loops iterating through n^2 pixels and K projections, at each tuple computing the lookup index into the acoustic data and adding this value to the current pixel. Implemented using Matlab, this is also the slowest possible design. An alternative suggested for Matlab is to use vectorization to generate a lookup matrix of size m -by- n^2 , and use that for indexing into the data matrix (m -by- K). In this case a significant speed-up can be obtained as such cumulative matrix-vector operations are implemented by Matlab in machine code. However, directly implementing the two for-loops using C and then interfacing through a special DLL (called Matlab executable or mex) allows a speed-up compared to Matlab's vectorization approach of about one order of magnitude. At this stage parallelization by means of OpenMP offered another speed-up proportional to the number of CPU threads available.

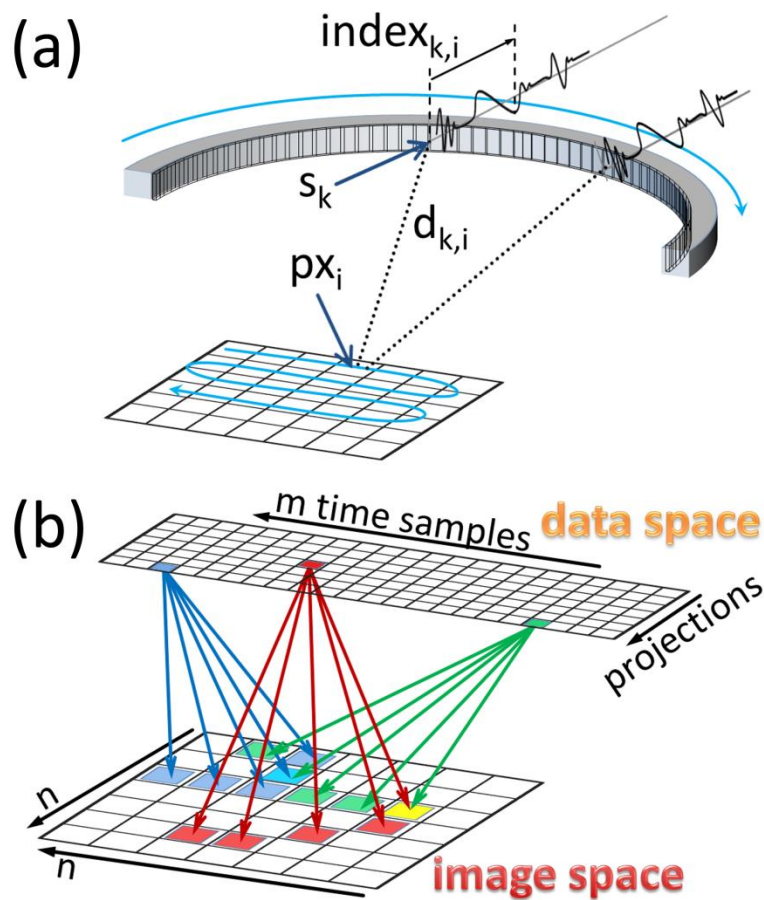


Figure 4-1 – Delay and Sum image reconstruction algorithm: for each image pixel (px_i) and each detection element k (a) the time of propagation (also referred to as delay) is computed and converted by the average speed of sound to an $index_{k,i}$ into signal s_k . (b) The identified value is then added to the appropriate position in the image buffer. All pixels are the sum of multiple input data values.

Parallelization of an operation as depicted in figure 4.1(b) should be carefully considered. There are two approaches that can be undertaken each with its own caveat. One way is to parallelize the for-loop iterating through n^2 pixels, i.e. $i = 1 : n^2$. This way each buffer location accumulates values independently of the others, except that different pixels may require read access to the same data value. This mapping has been color coded in fig. 4.1(b). Another parallelization approach is to parallelize pixel-detector tuples, since each tuple is unique. Now each read access into the data is unique, yet multiple tuples may require write access into the same pixel. The first method imposes a race condition when multiple threads attempt reading the same data location, while the second method imposes a race condition upon writing the image data. We chose to implement the first method, because it involves only simple read access, while the second requires a longer sequence of instructions (read-modify-write). On multi-core CPUs, even workstations with 24 CPU threads or more, both methods may execute at comparable speed.

However we also targeted deployment of the parallel code on graphics processing units (GPUs). The necessary modifications and framework were implemented by an

external company specialized in such developments. We specified OpenCL as the parallelization framework, because it offers hardware independent execution allowing speed-ups on high-end GPUs from any manufacturer as well as multi-core CPUs or distributed virtual devices. The final CL kernel achieved reconstruction times for images of 600x600 pixels using data of size 256-by-2030 in less than 30ms per image, thereby allowing video display at up to ~33 frames per second. Data acquisition at rates above that were also possible, but not all frames could be reconstructed – although all were stored for later analysis. Further improvements of reconstruction speeds could be achieved on newer GPUs with large and fast GDDR5 memory (3GB+). By broadcasting the data to as many GPU processing cores as possible we could avoid the read race condition. Assuming single precision, 2000 cores and relevant data of 256-by-1015 samples we would require about 2.1 Gbyte of memory, if parallelizing along pixels. The alternative, parallelization of tuples, could be implemented using only 370 Mbyte, 4 byte for each of 600*600*256 tuples. However a subsequent accumulator step, would again involve some race conditions for writing the image. Both approaches should be investigated. The first will likely improve execution the most. Yet the second could also improve execution as the index finding computation could be performed fully in parallel with the write race condition only present during the accumulator step (shorter execution per tuple!).

4.2 Transformation-based Optoacoustic Modeling (TOM)

Currently image reconstruction from optoacoustic data involves a trade-off between computation time and reconstruction accuracy. Analytical inversion algorithms suitable to real-time imaging such as simple filtered delay-and-sum or backprojection [56] implemented on consumer graphics processing units (GPU) have shown sufficient performance to achieve frame rates of up to 50Hz in 2D imaging [82]. However, these algorithms make idealized assumptions about system parameters and as a consequence introduce imaging artifacts or reconstruction imprecisions. An alternative class of algorithms that offer higher precision and less artifacts does not use explicit inversion, but rather employs numerical modeling of the forward problem, which typically results in a linear system of equations separable into a large model matrix, a set of measured data along different projections and the unknown image to be reconstructed in vector form [59, 84]. A numerical forward model can account for arbitrary detection geometries, the influence of finite detector apertures or heterogeneous speed of sound distribution. It also enables the application of image regularization for optimally accounting for data noise and other imperfections. Generally two approaches to forward modeling and inversion exist. In one approach, the model-matrix is pre-calculated and stored in memory. Inversion is then executed by multiplying the data with a pseudo-inverse of the forward matrix [59, 85] or by iterative multiplication of the forward matrix during an optimization procedure [84]. In the other approach, the matrix is calculated on the fly as required. The advantage of pre-calculation is that it enables the use of slower but more accurate computation of

the time-domain model [62, 86, 87] and also speeds up the inversion procedure, because matrix-vector multiplication is a highly efficient operation. However, memory consumption becomes an issue with increasing resolution and region of interest in 2D and becomes truly challenging when generalizing to 3D. Specifically, when an efficient (GPU) implementation is sought, the memory occupied by the pre-calculated model matrix may prevent storing it in GPU-memory. An alternative approach employs on the fly techniques to avoid large memory requirements by re-calculating matrix elements at each iteration step without storing them. As iterations are repeated multiple times, the model has to be based on highly efficient calculations. In time-domain such processes involve discontinuous interpolation functions [88, 89], which could result in sub-optimal reconstruction results. In frequency-domain analytical solutions are available, however have been shown to lead to instabilities in the reconstruction [59].

Here we developed a methodology for discrete time-domain modeling in optoacoustic tomography that is both accurate and computationally efficient. The new methodology is based on transformation-based optoacoustic modeling (TOM), in which separate treatment is given to the discretization of the underlying physical equations and to the geometry of the tomographic detector arrangement. Using TOM, the optoacoustic model calculated for a single tomographic projection may be generalized to arbitrary projections by applying appropriate Euclidian image transformations. Since discretization is performed for only a single projection, the most sophisticated and precise modeling of physical reality available may be applied with significantly relaxed restrictions on either computation time or memory requirements, compared to method previously developed. In the inversion procedure, the transformations may be performed on the fly with high numerical efficiency to calculate all the projections in the optoacoustic system from the optoacoustic model pre-calculated for a single projection. Moreover, as our attempts at CPU parallelization show, GPU implementation can be expected to dramatically reduce execution time, as the operation of GPUs is highly optimized both algorithmically and in hardware to enable the rapid calculation of image transformations [90, 91]. We note that TOM shares common features with the work published in [92], where a similar distinction was made between the physical and tomographic underpinning of the optoacoustic model. However, in [92] the extension of the optoacoustic model was not based on applying geometric transformations, but rather on rearranging the order of rows of the pre-calculated model matrix. As a result, that algorithm is compatible only with detector arrangements that coincide with the grid on which the optoacoustic image is defined. Since optoacoustic modeling is generally performed on a Cartesian grid, the algorithm was appropriate only for detection geometries based on linear (raster) scans. In contrast, TOM is compatible with any geometry. We demonstrate TOM in a 2D circular tomographic geometry for both numerical and experimental data, where comparable performance is obtained in comparison to the iterative inversion of the full forward matrix. In such a geometry, the use of TOM leads to over 2 orders of magnitude reduction in memory requirement. Thus, at least in case of 2D cross-sectional imaging, TOM is suitable for an all-GPU real-time image reconstruction in which a small pre-

calculated matrix is saved and all other operations, i.e. image transformations and vector-matrix multiplications, are parallelized.

4.2.1 Proposed algorithm

As previously discussed in chapter 2.6 the model-based algorithm chosen for our investigation establishes a matrix vector notation for the forward solution of the optoacoustic wave equation [59]:

$$p(\mathbf{x}', t) = \frac{\Gamma}{4\pi c_0} \frac{\partial}{\partial t} \int_{A(t)} \frac{H_x(\mathbf{x})}{R} dA \quad (24)$$

where \mathbf{x}' represents the position of measurement and $R = |\mathbf{x}' - \mathbf{x}| = c_0 t$ is the radius of a sphere with center \mathbf{x}' that spans the surface $A(t)$ to be integrated. For each projection data set (\mathbf{p}_i) a matrix \mathbf{M}_i is computed such that $\mathbf{M}_i \mathbf{u} = \mathbf{p}_i$, which implements a set of linear equations connecting for each measurement position i a total of R unknown image pixels/voxels, rearranged in vector form $\mathbf{u} = [u_1, u_2 \dots u_R]^T$, with the set of measured pressure samples \mathbf{p}_i by means of the model matrix \mathbf{M}_i . For inversion m measurement positions enclosing the area/volume of interest are required, each being described by a different forward matrix \mathbf{M}_i and sample vector \mathbf{p}_i . Stacking m individual matrices and sample vectors establishes the full forward model $\mathbf{M}\mathbf{u} = \mathbf{p}$, as depicted in figure 4.2.

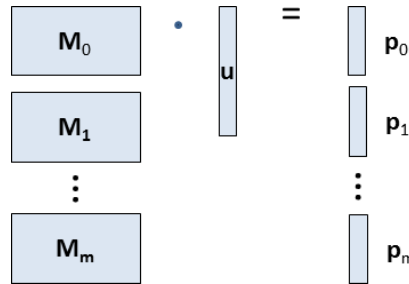


Figure 4-2 – The full forward model established by stacking matrices and data vectors of all measurement positions.

We can now apply square error minimization using the LSQR algorithm [64] to obtain the reconstructed image, i.e.

$$\mathbf{u}_{image} = \arg \min_{\mathbf{u}} \|\mathbf{p} - \mathbf{M}\mathbf{u}\|_2^2, \quad (25)$$

where $\|\cdot\|_2$ denotes the l_2 norm. As a detailed review of LSQR is beyond the scope of this paper, we reproduce only a qualitative description of the algorithm, which we deem sufficient to understand the modification proposed later in the text. For initialization LSQR computes an initial guess of the image by multiplying the data vector with the transpose of \mathbf{M} , then a number of iterations follow until either a certain condition is fulfilled or the maximum number of iterations has been reached. All iterations thereby include up to 4 stages: multiply \mathbf{M} with a vector equal in size to the image vector; compute a set of parameters; check conditions and either break or

update the current guess; multiply the transpose of M with a vector equal in size to the data vector. Table 3 summarizes the LSQR algorithm.

Table 4 – Summary of LSQR algorithm.

Initialization: $\mathbf{u}_{iter} = \mathbf{M}^T \mathbf{p}$ and initialize \mathbf{v}'_{iter}	
for $iter = 1 : max_iter$	1. $\mathbf{d}_{iter} = \mathbf{M} \mathbf{v}'_{iter}$
	2. Compute parameter set and update \mathbf{d}'_{iter}
	3. Check conditions
	<input checked="" type="checkbox"/> <input type="checkbox"/> Break for Update \mathbf{u}_{iter}
4. $\mathbf{v}_{iter} = \mathbf{M}^T \mathbf{d}'_{iter}$ and update \mathbf{v}'_{iter}	
$\mathbf{u}_{image} = \mathbf{u}_{iter}$	

For simplicity we will consider the 2D tomographic imaging case, where the ideal detection geometry is defined to be a circle surrounding a rectangular region of interest, which itself is discretized into n -by- n pixel. Notwithstanding, an extension to 3D imaging can be derived following the same methodology. Figure 4.3 graphically summarizes the problem and illustrates the proposed alternative solution.

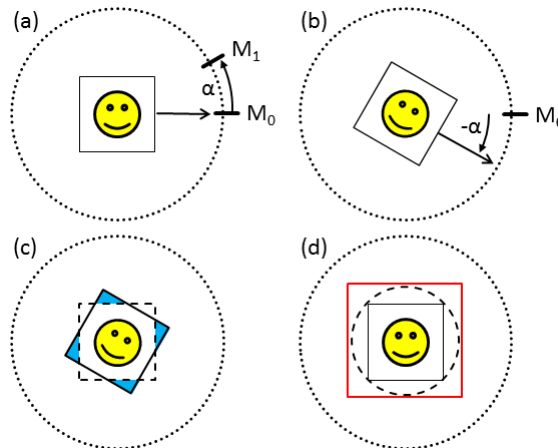


Figure 4-3 – The tomographic imaging problem in 2D requires detection along the dotted circle, which encloses the solid square that represents the image to be reconstructed. (a) The forward problem modeled by computing a second matrix M_1 for a new detector position rotated by α . (b) Alternative solution based on M_0 and rotating the image grid by $-\alpha$. (c) Light blue areas indicate pixels missing in M_0 . (d) M_0 is extended to include all pixels enclosed by the dashed circle.

The previously described standard model requires the computation of a second partial forward matrix \mathbf{M}_1 , if the detector is rotated by an angle α along the ideal detection geometry, depicted in fig. 4.3(a). An alternative solution however would be to transform, in this case rotate, the grid that defines the sought after image as shown in fig. 4.3(b). The 'view' from the detector position captured by \mathbf{M}_0 now corresponds to the one at \mathbf{M}_1 in fig. 4.3(a). This simple relation can be expressed by re-defining the

matrix vector notation as if each projection pertained to another sought after image: $\mathbf{M}_0 \mathbf{u}_i = \mathbf{p}_i$, while the optoacoustic wave propagation (\mathbf{M}_0) remains the same. Of course the underlying image remains unchanged, what has changed is the relative perception of the detector. At this point we have to note that the pixels included in \mathbf{M}_0 are insufficient to fully describe the transformed image. Figure 4.3(c) indicates the pixels included, framed by the dashed square, while missing pixels are highlighted blue. A solution to this problem is shown in fig. 4.3(d). The minimum required pixels that should be captured by \mathbf{M}_0 are surrounded by the dashed circle. This can be achieved by computing \mathbf{M}_0 for the red square and then remove from it columns representing pixels outside the dashed circle. It follows that \mathbf{M}_0 in our algorithm is $\left(\frac{\pi}{2} - 1\right) \cong 57.1\%$ larger than the forward matrix for a single detector position. Nonetheless, for simplicity we will assume in the following that \mathbf{M}_0 contains all pixels within the red square ($2n^2$). Thus, we can transform each image \mathbf{u}_i by a transformation matrix \mathbf{T}_i that connects the base image \mathbf{u}_0 (previously \mathbf{u} without index) with what is observed at position i , such that $\mathbf{M}_0 \mathbf{T}_i \mathbf{u}_0 = \mathbf{p}_i$.

\mathbf{M}_0 now connects k measured samples with $2n^2$ pixels, such that \mathbf{M}_0 attains a size of $k \times 2n^2$ and \mathbf{u}_0 and \mathbf{p}_i a size of $2n^2 \times 1$ and $k \times 1$ respectively. This implies that the size of \mathbf{T}_i is $2n^2 \times 2n^2$, which represents the matrix connotation of an image transformation. As the geometric problem in optoacoustic tomography is sufficiently defined by rotation and translation, \mathbf{T}_i is restricted to Euclidian transformations and can be obtained by employing inverse mapping and an interpolation method of choice. First, a point-to-point transformation matrix is defined in homogenous coordinates (3×3 in 2D, 4×4 in 3D) to allow matrix based description of translation and also to ensure compatibility with methods used in computer graphics. In 2D tomography with rotational detection, as described in fig. 4.3, the matrix

$$\mathbf{A}_T = \mathbf{R}_z(\alpha) = \begin{pmatrix} \cos \alpha & \sin \alpha & 0 \\ -\sin \alpha & \cos \alpha & 0 \\ 0 & 0 & 1 \end{pmatrix}$$

is sufficient. For other geometries in 2D and 3D, \mathbf{A}_T can be obtained by sequentially multiplying any number of rotations/translations in the order that correctly describes the used detector positions. To find \mathbf{T}_i the inverse of \mathbf{A}_T is multiplied onto the matrix of 3-tuples $(x,y,1)$ containing all output pixel locations, i.e.

$$\mathbf{L}_{intp} = \mathbf{L}_{out} \mathbf{A}_{T,inv}$$

with \mathbf{L}_{intp} and \mathbf{L}_{out} of size $2n^2 \times 3$. For rotations that are not grid synchronous (e.g. multiples of 90°) \mathbf{L}_{intp} will contain positions in between pixels of the input image (\mathbf{u}_0). Therefore interpolation is necessary. For our purposes a simple bilinear interpolation is sufficient and can be implemented by finding the four closest pixels for each row of \mathbf{L}_{intp} and computing bilinear weights. By this we have linked each output pixel to a weighted sum of input pixels and can assemble \mathbf{T}_i by appropriately distributing weights along the columns of \mathbf{T}_i , whereby the rows represent the pixels of the output image and the columns the pixels of the input image. A similar approach can be applied in case

of 3D imaging using trilinear interpolation. Note that \mathbf{T}_i is highly sparse and contains only $8n^2$ non-zero values. Using interpolation of a higher order, e.g. cubic, will of course reduce sparsity.

4.2.2 Fast inversion

Thus far we have introduced TOM as an alternative method to obtain a forward matrix for each detector position. For inversion however we still need to stack individual matrices as LSQR requires the full forward matrix (see table 3). Fortunately we may apply \mathbf{T}_i to the image. As the iterative steps 1 and 4 of LSQR are separable matrix vector multiplications, we can execute them one detector position at a time. Table 4 summarizes the modified LSQR routine. Vectors $\mathbf{d}_{iter}/\mathbf{d}'_{iter}$ attain a size of $(m * k) \times 1$ and $\mathbf{d}_{iter,i}/\mathbf{d}'_{iter,i}$ a size of $k \times 1$ and therefore can be interpreted as a substitute for \mathbf{p} and \mathbf{p}_i respectively. Consequently, \mathbf{v}_{iter} , \mathbf{v}'_{iter} and $\mathbf{v}_{iter,i}$ are equivalent in size to \mathbf{u} or \mathbf{u}_{image} , i.e. $2n^2 \times 1$. To summarize, we can describe step 1 as 'get data' implemented by transforming the input image (\mathbf{v}'_{iter}) followed by multiplication with \mathbf{M}_0 and subsequent stacking to obtain the data (\mathbf{d}_{iter}). On the other hand we can describe step 4 (also the initialization) as 'get image' implemented by multiplying partial data ($\mathbf{d}'_{iter,i}$) with \mathbf{M}_0^T , transforming the resulting image and summing all such partial images to obtain the full image.

Table 5 – Summary of modified LSQR algorithm.

Initialization: $\mathbf{u}_{iter} = 0$		
<i>for</i> $i = 1 : m$	$\mathbf{u}_{iter,i} = \mathbf{T}_i^T \mathbf{M}_0^T \mathbf{p}_i$	
	$\mathbf{u}_{iter} = \mathbf{u}_{iter} + \mathbf{u}_{iter,i}$	
Initialize \mathbf{v}'_{iter}		
<i>for</i> $iter = 1 : max_iter$	1. $\mathbf{d}_{iter} = 0$	
	<i>for</i> $i = 1 : m$	$\mathbf{d}_{iter,i} = \mathbf{M}_0 \mathbf{T}_i \mathbf{v}'_{iter}$
		$\mathbf{d}_{iter} = [\mathbf{d}_{iter} ; \mathbf{d}_{iter,i}]$
	2. Compute parameter set and update \mathbf{d}'_{iter}	
	3. Check conditions	
		<input checked="" type="checkbox"/> <input type="checkbox"/> Break <i>for</i> Update \mathbf{u}_{iter}
	4. $\mathbf{v}_{iter} = 0$	
	<i>for</i> $i = 1 : m$	$\mathbf{v}_{iter,i} = \mathbf{T}_i^T \mathbf{M}_0^T \mathbf{d}'_{iter,i}$
		$\mathbf{v}_{iter} = \mathbf{v}_{iter} + \mathbf{v}_{iter,i}$

	update \mathbf{v}'_{iter}
$\mathbf{u}_{image} = \mathbf{u}_{iter}$	

Finally, the numerical inversion using actual input images ($\mathbf{v}'_{iter}, \mathbf{M}_0^T \mathbf{d}'_{iter,i}$) enables us to replace the intermediate step of constructing \mathbf{T}_i with actually computing the transformed image by interpolating from the input image. This significantly speeds up the algorithm in table 4 by eliminating the instantiation of and multiplication with a sparse matrix. Additionally, the execution time is further reduced by employing highly optimized and parallelized interpolation algorithms.

4.2.3 Evaluation using simulated data

To evaluate the performance of our algorithm numerically we chose a numerical 2D phantom containing absorbers of varying size, shape and absorptivity. Figure 4.4(a) shows the initial pressure map for uniform illumination throughout the imaging plane, i.e. no fluence decrease. Thereby, the image width was chosen to be 20 mm containing 600x600 pixels. This constitutes the ideal reconstruction target that we would like to reconstruct from the acoustic data. Forward 3D simulation of 360 tomographic projections at full view (i.e. 360°) and 40 mm radius was performed using the k-wave toolbox described in [93]. This produced a dataset containing 360 independent measurement positions each 4500 time samples in length and sampled at 100 MSamples/s. Similarly, we produced data for two additional scan geometries, spiral tomography and translate-rotate tomography, as depicted in fig. 4.6(a) and 4.6(d) respectively. Additionally we evaluated reconstruction accuracy in noisy environments by adding normal distributed random noise at ten different levels. For this we normalized the simulated tomographic data to a range of [-1 1] and at each level added noise ranging from [-0.05 0.05] * NL, with scaling factor NL = 1:10. Fig. 4.4(c) shows the noisy signal at NL=1, NL=5 and NL=10. For reconstruction we used the standard interpolated-matrix-model inversion (IMMI) algorithm described in [59] and the proposed algorithm (TOM), for which IMMI also provided the single projection forward matrix \mathbf{M}_0 . Parameters for IMMI and TOM were identical and chosen such as to enable a theoretical resolution of 100 μm , i.e. the number of pixels to be computed was 400x400. Larger values were possible for TOM, but not for IMMI due to memory limits imposed by the PC hardware.

Experimental validation was performed on a dataset obtained in-vivo on the lower arm of a human volunteer using the handheld implementation detailed in chapter 3.3 (version 1). Data were acquired by a stable version of the FM-DAQ, while illumination was provided by the Phocus™ laser. Measurements were performed without averaging and at 800 nm wavelength. At this wavelength the peak light fluence on the tissue was below 20 mJ/cm² and thus safely below ANSI maximum permissible exposure standards. Fig. 4.4(b) shows the experimental assembly (left) and a photograph of the actual measurement (right). During handheld operation a maximum field of view is required for optimal navigation. Therefore we reconstructed a frame of size 40x40 mm² and chose 400x400 pixels to allow a theoretical resolution of up to 200 μm . Due to the

limited amount of data (64 detectors) and the limited view angle of 172° , we chose to interpolate the dataset to 256 virtual detectors and stopped the LSQR procedure after only 25 iterations to limit partial-view reconstruction artifacts. Both measures, i.e. interpolation of original data and stopping LSQR, are forms of regularization designed to provide stable and fast inversion.

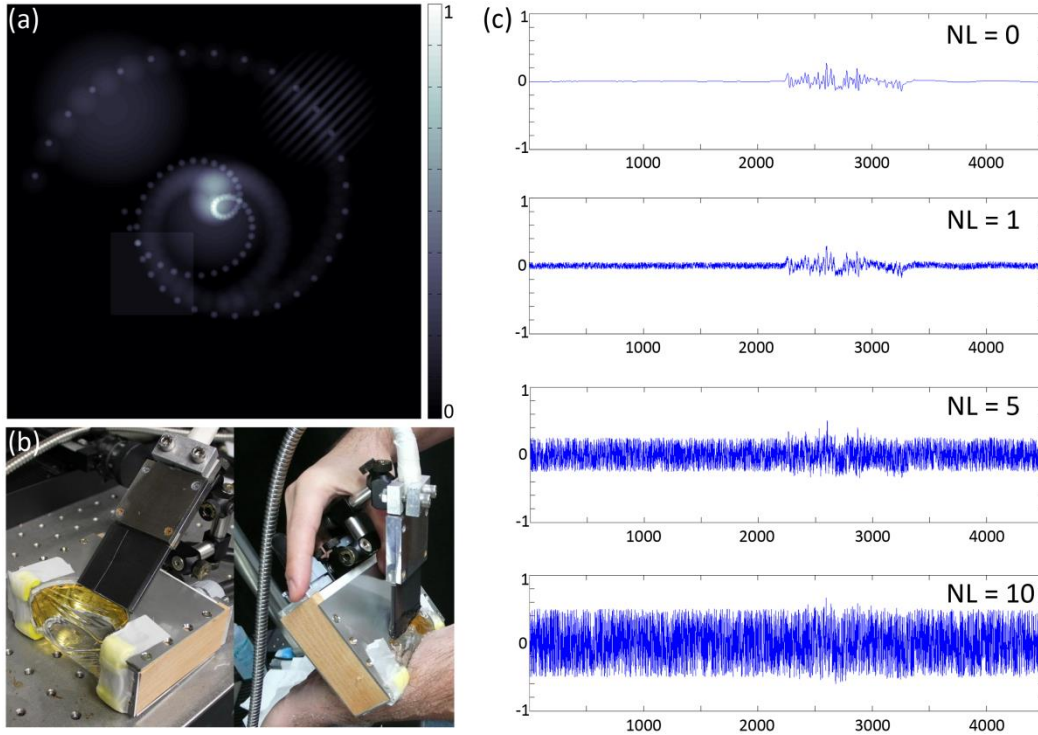


Figure 4-4 – (a) Initial pressure distribution used for forward simulation of acoustic data and represents the reconstruction target. (b) Handheld optoacoustic imaging probe employed to obtain data in-vivo. (c) Simulated acoustic data for channel 200 (of 360) at four noise levels: no noise, minimum noise (NL=1), intermediate noise (NL=5) and maximum noise (NL=10).

Noiseless simulation results are shown in figure 4.5. The IMMI algorithm converged (i.e. norm of residual $< 10^{-6}$) after 82 iterations, whereas TOM did not converge after 100 iterations, at which point we stopped the LSQR routine. To preserve comparability fig. 4.5(a) and 4.5(b) show the reconstructions after 80 iterations for IMMI and TOM respectively. No difference is visually discernible. Thus, we subtracted the IMMI and TOM images. From the resulting difference image we further subtracted the (negative) minimum and show the result in fig. 4.5(c) on the same colorbar that was also used for figs. 4.5(a) and 4.5(b). To enhance contrast we additionally rendered the original zero values (i.e. identical in TOM and IMMI) before subtraction of the minimum in bright green; we indicate their position on the colorbar after addition of the absolute minimum (0.048) with a green stripe. A more quantified analysis of algorithmic behavior is given in fig. 4.5(d), where we show the sum of squared differences (SSD) over the number of iterations. At each step we computed the SSD by subtracting from the target image, given in fig. 4.4(a) and down-sampled to 400×400 pixels, the resulting IMMI or TOM image and then summing the square of each pixel. For reference we also

included the SSD for two commonly used reconstruction algorithms, backprojection (BP) and delay and sum (DS). As BP and DS do not depend on iterative LSQR inversion, both are shown constant in fig. 4.5(d). We notice that the full model-matrix method (IMMI) converges faster than the reduced single-matrix method (TOM). However the TOM curve closely follows the IMMI curve and after 60 iterations is indistinguishable from it. The SSD behavior therefore numerically confirms the visual impression.

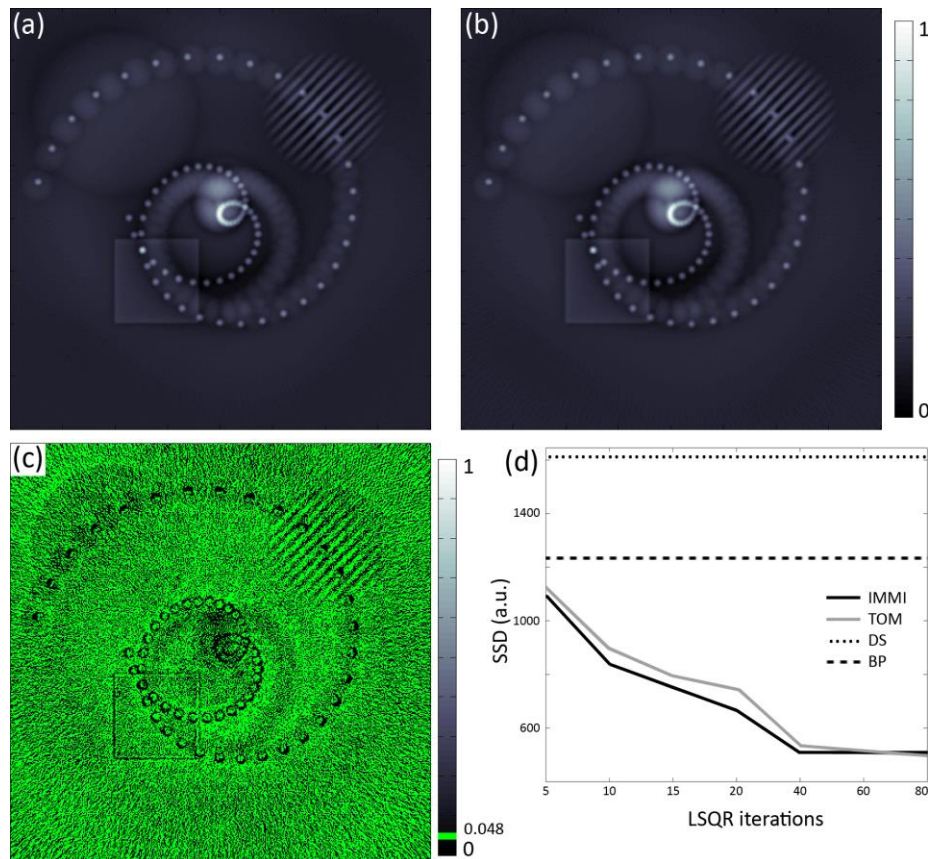


Figure 4-5 – Reconstruction of the noise free simulated dataset obtained after 80 LSQR iterations by (a) the standard IMMI algorithm and (b) TOM. Both images were normalized to values between 0 and 1 and are shown on the same colorbar. (c) Difference image between (a-b) after minimum subtraction to fit the same colorbar as in (a,b); to improve contrast original 0 values have been rendered bright green. (d) Plot showing the sum of squared differences (SSD) over number of LSQR iterations for IMMI and TOM. For reference values for backprojection (BP) and delay and sum (DS) algorithms are also given.

Similar qualitative and quantitative convergence could be observed for the two additional scan geometries. Figure 4.6 depicts the scan geometries as well as reconstructions achieved by IMMI and TOM after 80 iterations. The first row shows the scan pattern of spiral tomography in fig. 4.6(a), followed by reconstructions obtained from IMMI, depicted in fig. 4.6(b), and TOM, depicted in fig. 4.6(c). The second row shows in the same order the scan pattern and reconstruction results for a translate-rotate tomography that could be implemented by rotating a linear array. Each reconstructed image includes in the bottom right corner a value indicating the SSD

relative to the target image. Achieved reconstruction quality and SSD values are virtually indistinguishable from the rotate-only pattern presented in figure 4.5.

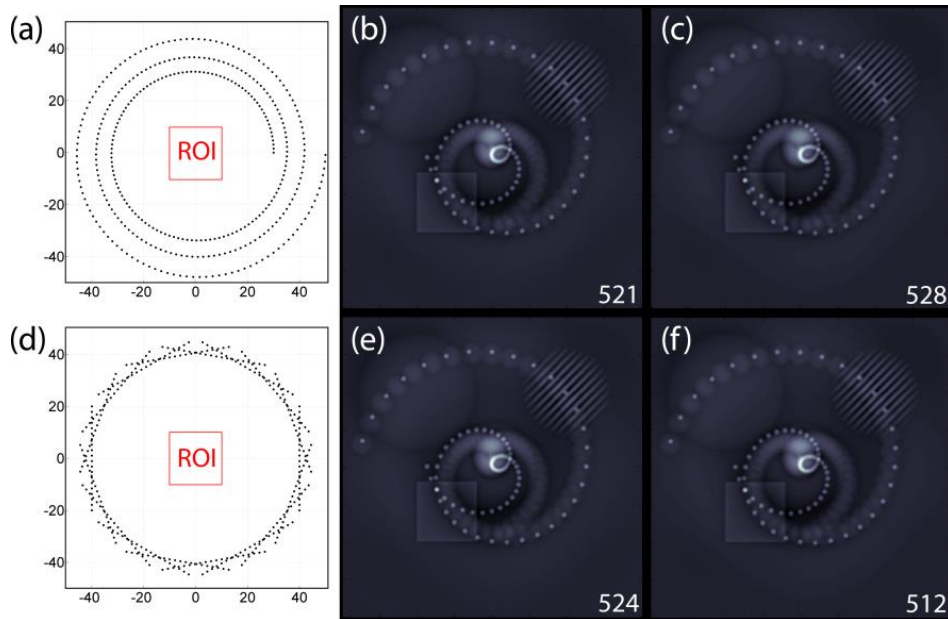


Figure 4-6 – Additional detection geometries considered in simulation. (a) Spiral tomography covering 360 unique angles over a span of 1080° with radii ranging from 0.03 m to 0.05 m. (b) IMMI and (c) TOM reconstruction of spiral geometry. (d) Rotate-translate tomography covering 18 angles over 360° , each featuring 20 linearly translated detector positions. (e) IMMI and (f) TOM reconstruction of rotate-translate geometry. Each reconstruction includes the SSD relative to the reconstruction target in the bottom right corner.

Simulation results obtained from the tomographic dataset after addition of normal distributed random noise are shown in figure 4.7. All images were obtained by stopping LSQR after 80 iterations. Fig. 4.7(a) depicts reconstructions attained by IMMI (top row) and TOM (bottom row) from three noise levels: minimum (NL=1), intermediate (NL=5) and maximum (NL=10). No significant difference can be perceived visually as both algorithms produce reconstructions whose noise is proportional to the signal noise level. To quantify results for each algorithm, fig. 4.7(b) shows the sum of squared differences (SSD), relative to the target image in fig. 4.4(a), and at each noise level. We notice that TOM performs progressively worse the noisier the input data. On the other hand even the minimum noise level (NL=1) employed in this evaluation would be considered extreme in any experimental measurement system.

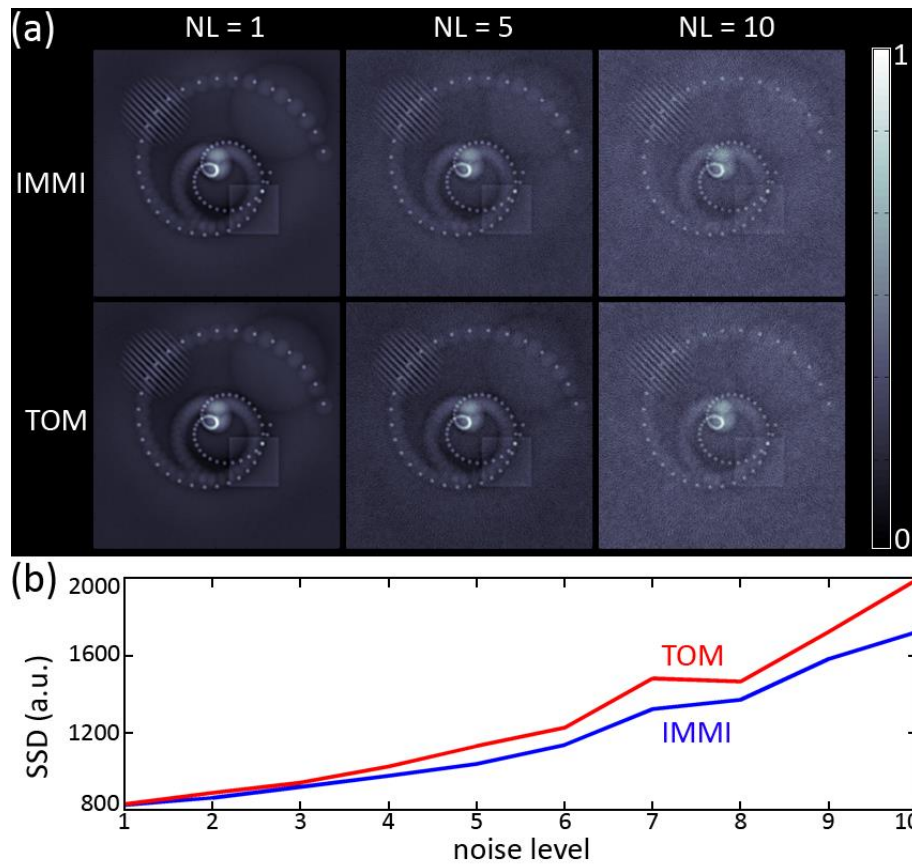


Figure 4-7 – (a) Reconstructions for IMMI (top row) and TOM (bottom row) at three noise levels (NL=1,5,10). (b) Sum of squared differences (SSD) for TOM (red) and IMMI (blue) at increasing noise level.

4.2.4 Evaluation using handheld measurement data

From the large dataset obtained from the lower arm of a human volunteer we selected two frames close to the wrist, where the radial artery was approximately 5 mm below the skin surface. Each row in figure 4.8 shows results for one frame. The position of the detector array was such that it surrounded the top image half. To facilitate comparability, results from IMMI were thresholded to extreme values found in the TOM image and subsequently all images were normalized to values from 0 to 1. The colorbar on the right is thus valid for all six images shown in fig. 4.8. Fig. 4.8(a) and (b) depict frame 1 reconstructed by IMMI and TOM respectively. Both images clearly resolve relevant features such as the radial artery and various veins, marked 'ra' and 'v'. Equally, frame 2 is shown in fig. 4.8(d), reconstructed by IMMI, and 4.8(e), reconstructed by TOM. Again the vascular structure is well captured by both methods. However, in both frames we note an increased level of limited-view artifacts in the IMMI images. When subtracting the TOM image from the IMMI image on a pixel basis for the two frames, we obtain figures 4.8(c) and (f). These difference images reveal for both frames that reconstructions from IMMI contained only additive artifacts and no additional features. It can be assumed that the slower convergence of TOM acted as

a form of regularization that additionally suppressed limited-view artifacts. Figure 4.9 illustrates this behavior for increasing LSQR iterations.

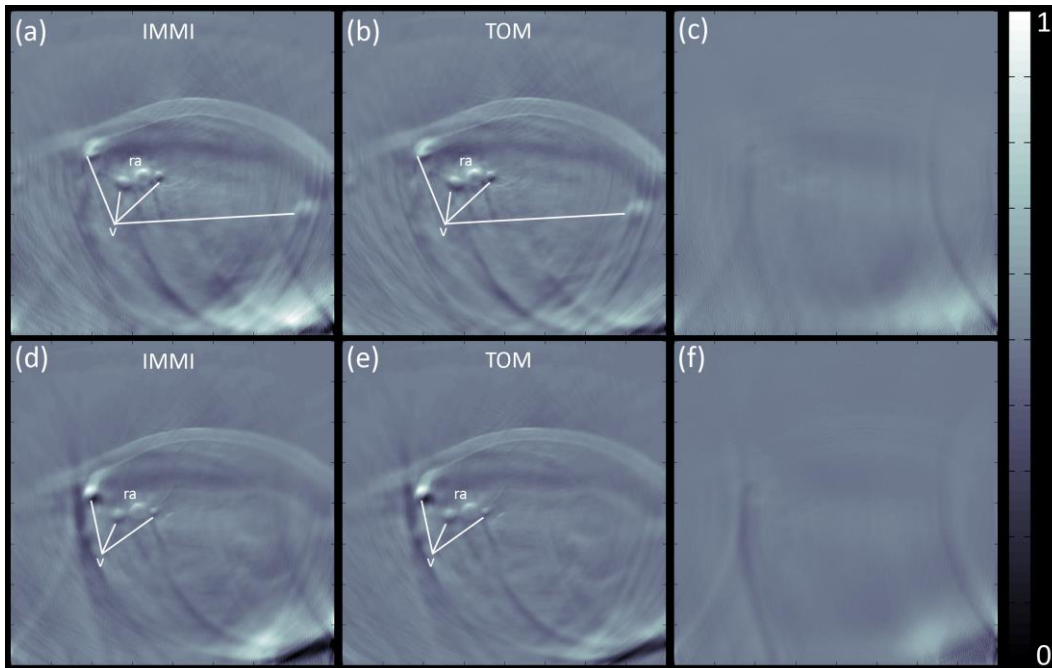


Figure 4-8 – Reconstructions of a dataset obtained in-vivo from the lower arm of a human volunteer. The first row shows a frame ($40 \times 40 \text{mm}^2$) close to the wrist after 25 LSQR iterations for (a) IMMI, (b) TOM and (c) the difference image (a)-(b). The second row shows another frame of the same size a few mm towards the elbow reconstructed by (d) IMMI, (e) TOM and (f) the difference image (d)-(e). Image values in (a) and (d) were restricted to extreme values found in (b) and (e) respectively. Subsequently, images (a,b) and (d,e) were normalized to values between 0 and 1. Furthermore, all images are shown on the same colorbar. ra: radial artery; v: vein.

A more thorough analysis of the regularizing effect of TOM for limited-view tomography is provided in figure 4.9. We selected two regions contained in frame 1, the area at the radial artery (feature region) and an artifact area at the bottom right, and show their evolution over iterations (1, 3, 7, 11, 15 and 25) in the manner established in fig. 4.8, i.e. IMMI on the left, TOM in the middle and the difference image on the right. For each iteration included, fig. 4.9 shows six images: first row shows the artifact region; second row the feature region. After only one iteration both IMMI and TOM are virtually identical. For the remainder of iterative steps both IMMI and TOM show increasing values for the artifact region. However, as can easily be observed from the difference image, IMMI exhibits progressively stronger artifacts than TOM. The feature region in the second row behaves differently. First an increase in the difference image is visible (iterations 3, 7), then values in the difference image decrease (iterations 11, 15) up to the point where there is no other difference visible except fine streak artifacts.

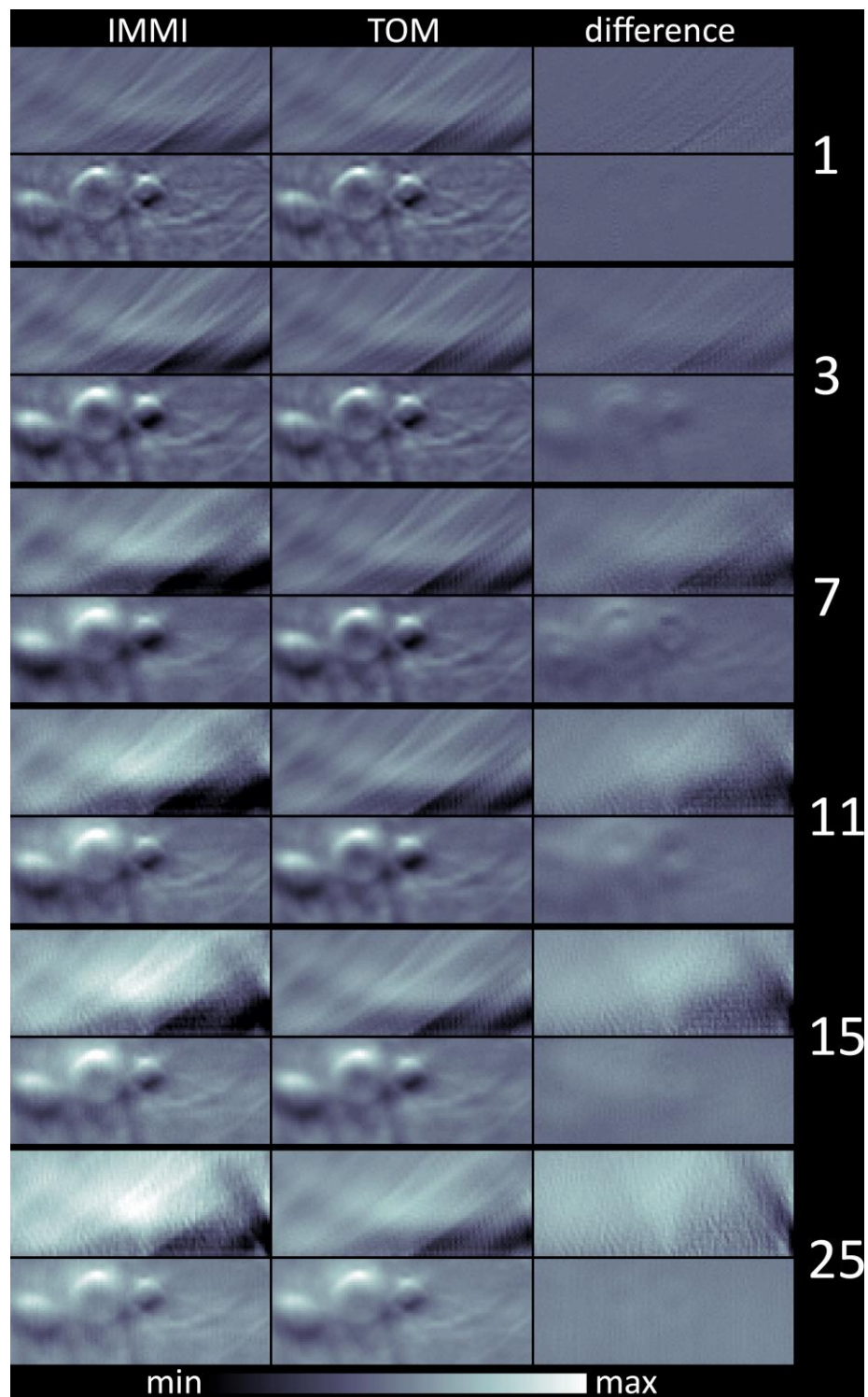


Figure 4-9 – Results from IMMI and TOM after 1, 3, 7, 11, 15 and 25 iterations for frame 1, depicted in Fig. 6(a) and (b). For each iterative step six images are shown: a region dominated by artifacts in the top row and a region containing relevant features in the bottom row. The column order is IMMI, TOM and the difference image. At each iteration full images obtained by IMMI and TOM were

processed in the same manner as described in Fig. 6. The colorbar is valid for all images at one iterative step.

To quantify computational overhead induced by the use of TOM, we measured computation times for all reconstructions. As reconstruction time depends linearly on the size of the forward matrix, we report results only for experimental data. In this case the full forward matrix size was 6.4 GB and inversion required 25 iterations. Reconstruction of one image frame took 37s for IMMI and 286s for TOM, both using one CPU thread of an Intel Core i5-2400 PC. The single projection forward matrix required by TOM occupied 0.038 GB of memory. To showcase the achievable speed up on multi-core CPUs, we parallelized the TOM algorithm (Visual C++ 2010, OpenMP) and measured reconstruction times using an increasing number of CPU threads. Figure 4.10(a) shows results obtained on an Intel Core i5-2400 PC, while fig. 4.10(b) shows results obtained on an Intel Xeon X5650 workstation. The longer single thread execution time of TOM running on the workstation is due to the lower operating frequency. Similarly, IMMI required more time on the workstation compared to the consumer PC. Results from both machines show that a significant speedup can be achieved by parallelization, even though it does not scale linearly with the number of threads. Indeed performance improvements level off close to the maximum number of available threads. Nonetheless, on the Xeon workstation TOM required only 46% more time for execution than IMMI. On the Core i5 PC TOM required a more significant 200% time overhead, due to the reduced number of available threads. Moreover it is worth noting that, when including time required for computing the full forward matrix, IMMI took 1216s on the workstation and 641s on the PC for image reconstruction.

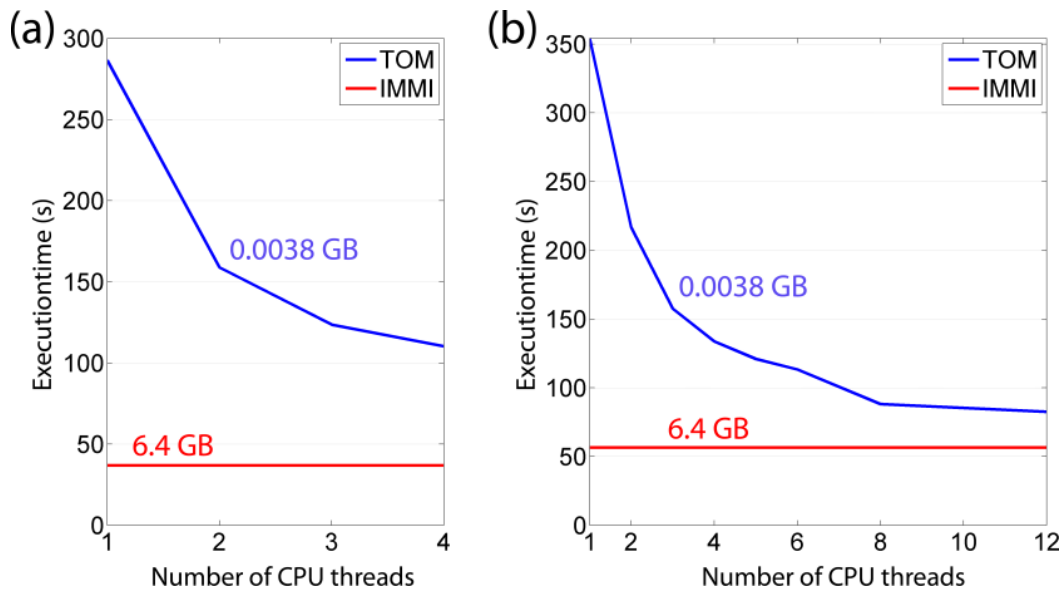


Figure 4-10 – Execution times over number of CPU threads for parallelized TOM and IMMI with pre-computed matrix. (a) Intel Core i5-2400 (max. 4 threads). (b) Intel Xeon X5650 (max. 12 threads).

4.3 Array density – practical considerations

To improve upon the initial handheld curved array probe design we also investigated how changes in array geometry could affect imaging performance in terms of quality and resolution. Advanced mechanical solutions improving weight, volume size and flexibility of illumination were already discussed in chapter 3.3. In the following we seek to justify choices made for the final prototype (termed HOT-256) by presenting an experimental investigation of three comparable curved detection arrays that were available for study at the time, i.e. during the design phase of HOT-256. We have previously published the data and text presented in the following in [80].

4.3.1 Characterization of arrays

All three arrays employed in this study were custom-made cylindrically focused curved-arrays (Imasonic S.A., France) with varying geometrical properties, yet manufactured from the same piezocomposite material to cover the frequency band up to 7.5 MHz with peak sensitivity at 5 MHz. To facilitate a concise description for the rest of this chapter, we define abbreviations based on the number of elements per array: MSOT64 (64 elements), MSOT128 (128 elements) and MSOT256 (256 elements). Figure 4.11 illustrates apertures and overall arrangements of the three systems (left column MSOT64, right column MSOT128/256) and defines the coordinate system, which we will refer to in the following.

The MSOT64 geometry is depicted in fig. 4.11(a). This spherically concave array spans 172° in azimuth (xy -plane) and 10.8° in elevation (zy -plane) with a radius of 40mm. We define the origin of the coordinate system to coincide with the center of the hypothetical sphere described by the array such that the xy -plane at $z=0$ represents the imaging plane offering a cross-sectional view of the object. Translation along the z -axis thereby enables controlled scanning of the object. Of the 64 elements making up the array each has a radius of 40mm, an azimuthal pitch of 1.88mm and a chord in elevation of 15mm (parallel to z -axis). At $z=0$ the extended length of the curvature in elevation constitutes cylindrical focusing along the z -axis, while a comparably small pitch in azimuth allows a sufficient field of view (FOV) for tomographic imaging in the xy -plane. As the elements of all three arrays in this study are composed of the same piezocomposite material, but with varying geometrical sizes, we chose as the norm a single element of the MSOT64 and give it the area size and sensitivity of 100%. Both measures were determined by the manufacturer using standardized protocols and are thus comparable between arrays.

MSOT128, depicted in fig. 4.11(b), covers a larger arc compared to MSOT64, spanning 270° in azimuth and 10.1° in elevation. This increase in azimuth coverage enables a more complete tomographic view, which is expected to significantly improve image quality. Together with the reduction of single element pitch to 1.47mm in azimuth, which increases the FOV of a single element, we also expect an improved transversal resolution, i.e. perpendicular to the radius. The resulting single element area size is only 72% of the MSOT64 norm and the sensitivity 55%. Nonetheless, due

to twice the number of elements compared to MSOT64, the resulting full array sensitivity within areas of overlapping FOV should be 110% on average.

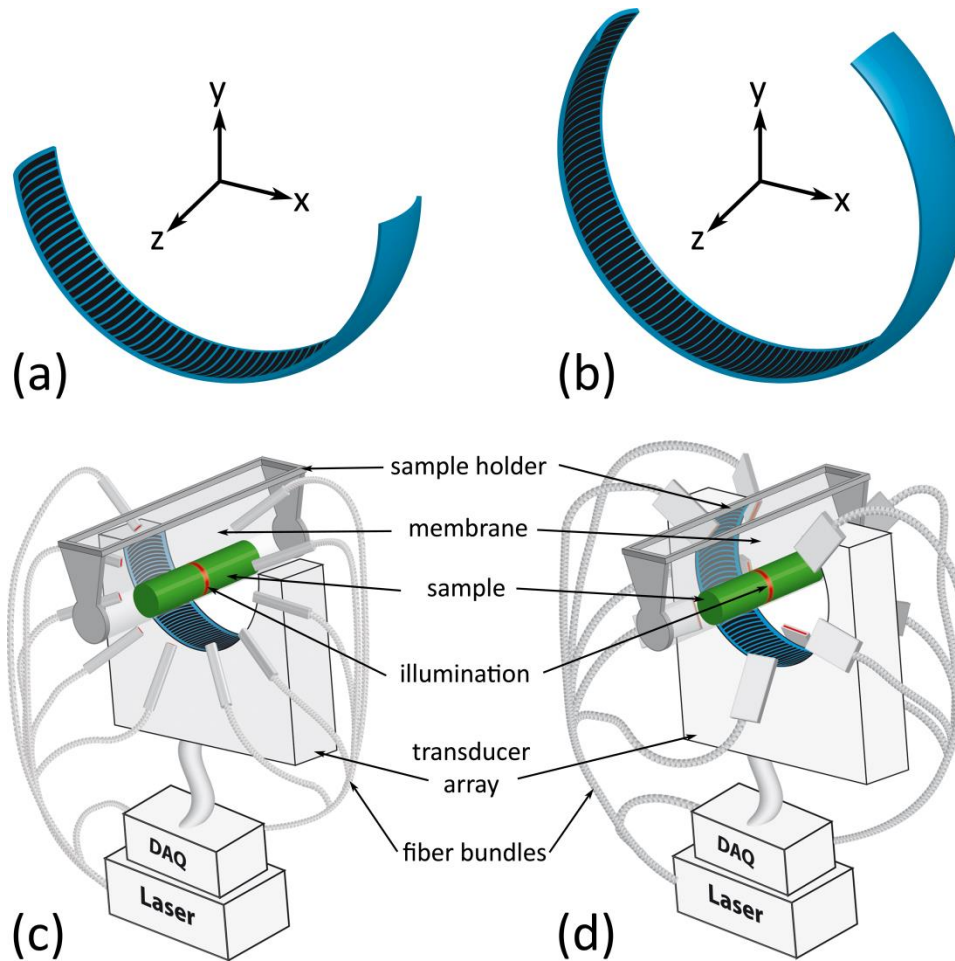
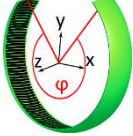
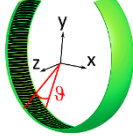
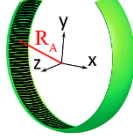
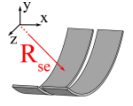
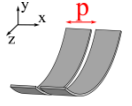
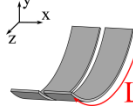


Figure 4-11 – The first row shows the transducer geometries for (a) MSOT64 and (b) MSOT128/MSOT256. The second row illustrates the two system setups including laser, data acquisition (DAQ) and sample holder with transparent membrane. (c) MSOT64 achieves even in-plane ($z=0$) illumination by using a ten arm fiber bundle arranged from one side at an angle of 33° relative to the circumference of the sample. (d) MSOT128/256 enables similar illumination by arranging a second ten arm fiber bundle symmetrically from both sides at an angle of 24° . Both fiber bundles cover an angle of 270° in the xy -plane.

MSOT256 shares most of the geometrical characteristics with MSOT128, i.e. radius of 40mm, span in azimuth of 270° and 10.8° in elevation, and is also characterized by fig. 4.11(b). The difference lies in its number of elements (doubled again) and their geometry. A single element of MSOT256 is positioned on the array segment describing a sphere with radius 40mm, but is itself focused at 37mm radius, thus achieving toroidal array focusing – as opposed to confocal focusing. Considering also the 270° azimuthal coverage including a reduced pitch of 0.735mm and the higher angular sampling by 256 elements, we expect yet more improvement in transversal resolution throughout a larger FOV. Even though the area size of a single element is merely 36% of the MSOT64 norm and corresponding sensitivity 29%, total sensitivity

of the MSOT256 is expected to be 114% on average within overlapping FOV. Table 5 summarizes the array and individual element characteristics for each array.

Table 2 - Geometric specifications (SE = single element)

						
	Azimuth span φ	Elevation span ϑ	Array radius R_A	SE radius R_{se}	SE pitch p	SE length L
MSOT64	172°	21.6°	40	40	1.880 mm	15.08 mm
MSOT128	270°	20.2°	40	40	1.470 mm	14.10 mm
MSOT256	270°	21.6°	40	37	0.735 mm	13.95 mm

Using an ultrasound field simulation program (Field II [94, 95]) and the geometrical characteristics of a single element we have numerically simulated the expected sensitivity field up to 7.5MHz in the imaging plane ($z=0$) for the single elements of each array – sensitivity being defined here as the maximum expected amplitude from a given position ($x,y,0$). By appropriately rotating and summing single element sensitivity fields we can obtain compound sensitivity fields for the three arrays employed (fig. 4.12). The short solid lines marked by arrows and an element number on the images indicate the first and last element of the transducer. Black ellipses designate the region of full-width half-maximum (FWHM), i.e. where the amplitude drops to at most 50% of the peak value. For MSOT64, depicted in fig. 4.12(a), the expected field is characterized by a diameter at FWHM of 15.5mm and a small displacement from the center of the array, due to the limited coverage of 172°. For MSOT128, shown in fig. 4.12(b), calculations show a horizontal extent of 21mm and vertical extent of 17.1mm, due to the asymmetric distribution of detectors. The reduced pitch and toroidal focusing of MSOT256 elements result in a FWHM diameter of 32.6mm, shown in fig. 4.12(c).

A second parameter relating to image quality is the angular coverage of the imaging plane. It has been shown [53] that boundaries, whose normals do not pass through at least one detection element, are invisible and after reconstruction lead to blurring or reconstruction artifacts [79]. For better understanding, fig. 4.12(d) and (e) characterize visibility for MOST64 and MSOT128/256 respectively. The detection or visibility region is thereby highlighted in gray and marks the region in which reconstruction of all features and boundaries is stable. The complementary white region with the dashed circle on the other hand allows only some boundaries to be reconstructed stably. In MSOT64 less than half of a 30 mm diameter region of interest (ROI) lies within the visibility region, while for MSOT128/256 the ROI is fully covered.

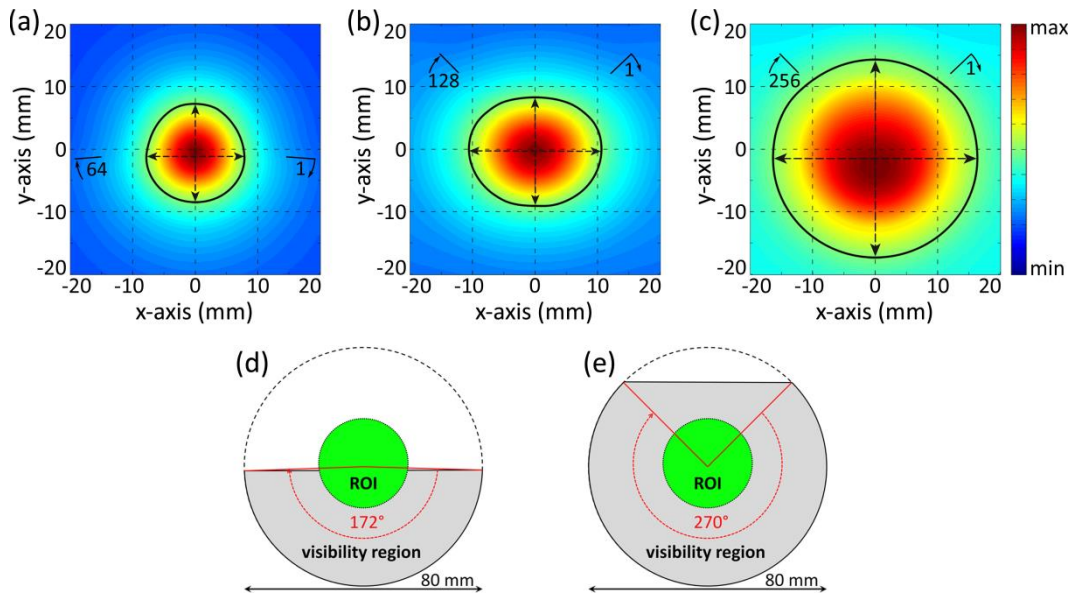


Figure 4-12 – Numerical estimation of the 2D sensitivity field of detection (0.5-7.5 MHz) within the imaging plane of the array. Black ellipses mark the full-width half-maximum (FWHM) range. The first and last element of each array is noted on the images by a short solid line marked with an arrow and element number. (a) 64 element array covering 172°; diameter at FWHM: 15.5 mm. (b) 128 element array covering 270°; vertical diameter at FWHM: 17.1 mm; horizontal diameter at FWHM: 21.0 mm. (c) 256 element array covering 270°; diameter at FWHM: 32.6 mm. (d) “Visibility region” (gray) for MSOT64 and (e) MSOT128/256 that allows stable reconstruction of feature boundaries (ROI = region of interest).

4.3.2 Numerical simulation and experimental setup

Pulsed laser light was provided by the Phocus™ laser, whose beam was coupled into a ten arm fiber bundle. The MSOT64 system employed a bundle with rectangular outputs of size 3.2x0.72mm² at the distal end. The arms were arranged over an arc of 270° next to the detection array, as shown in fig. 4.11(c), and established ring illumination at the imaging plane. The systems housing the MSOT128 and MSOT256 employed a slightly different illumination arrangement, depicted in fig. 4.11(d). Ring illumination was implemented by five rectangular outputs of 12.4x0.2mm² size covering 270° in azimuth on both sides of the arrays. In all setups the maximum light fluence at the surface of a cylinder of 20 mm diameter, as depicted in fig. 4.11, did not exceed 17 mJ/cm² at 750nm. Data acquisition was performed with the same operationally stable and tested FM-DAQ discussed in chapter 3.1. Based on the results from our study of impulse response variations and due to the fact that all three arrays were built from the same piezo-composite material, we de-convolved signals from all three arrays using a single high-quality impulse response measurement. Image reconstruction was performed using the TOM algorithm introduced in chapter 4.2 with parameters set to reconstruction a square ROI of 30x30mm² using 450x450 pixels.

To facilitate objective observations between the three detectors we employed numerical simulations. The simulations assumed a rectangular region of 30x30mm² centered at the origin in the xy-plane (z=0) and placed 900 microspheres equally

spaced by 1 mm in x- and y-direction. Figure 4.13(a) shows the numerical setup, which also represents the reconstruction target. To obtain acoustic data for the three arrays we first employed an ultrasound field simulation program (Field II) to compute the acoustic field received by each detection element following a Dirac-like excitation at the 900 microsphere positions. Then we convolved these geometric impulse responses, sampled at 40 MSamples/s, with the analytical optoacoustic signal emitted by a spherical absorber [15] and obtained acoustic data frames of size 2030x64, 2030x128 and 2030x256. Microsphere size was chosen to span six acoustic samples at 40 MSamples/s, i.e. 125ns or 187.5 μ m at 1500 m/s speed of sound.

Tissue mimicking control phantoms were also employed to provide measurements that could compare the performance of the three detectors employed. Validation of numerical results was achieved using black polyethylene (PE) microspheres of diameters ranging from 180-212 μ m (Cospheric LLC, USA). Due to practical difficulties replicating the regular sampling grid used in the numerical simulation we decided to implement an irregularly sampled disk of 30 mm diameter. For this we prepared a cylindrical tissue mimicking agar (2%w/v) phantom of 50 mm height and 30 mm diameter including a fatty emulsion imparting a reduced scattering coefficient of $\mu_s'=10\text{cm}^{-1}$. The phantom also included a cylindrical cavity at the bottom of 25 mm length and 8 mm diameter. We then dispersed microspheres on top of the phantom aiming to achieve distribution of microspheres as even as possible. This way the microspheres described an absorbing disk, which was illuminated from one side through \sim 25mm of scattering agar using a cylindrical fiber bundle inserted through the bottom cavity of the phantom. Fluence variations within the disk were captured by a CCD camera at 680nm and these measurements were later employed for correction of the reconstructed image. Fig. 4.13(b) shows the acquired photograph from the back-illuminated microsphere layer.

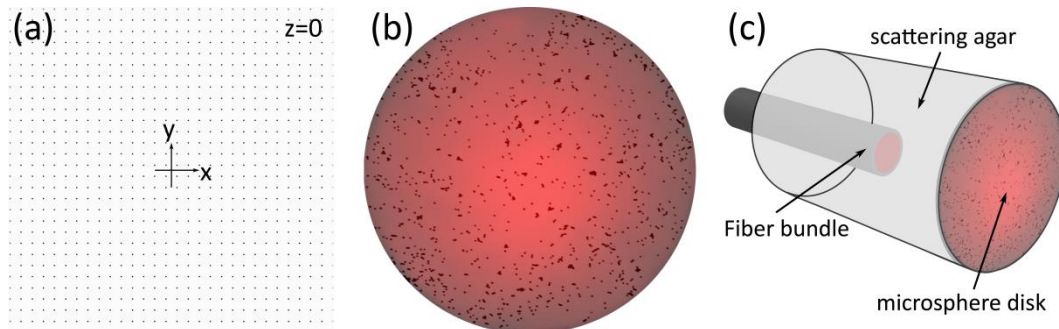


Figure 4-13 – (a) Numerical setup covering a rectangular region of 30x30mm² – 900 microspheres of 187.5 μ m diameter equally spaced in 1mm steps. (b) Top view photograph of the microsphere-containing phantom showing the sphere distribution and the fluence distribution. The disk diameter was 30 mm; the PE spheres attained diameters of 180-212 μ m. (c) Schematic of the experimental phantom assembly.

To extend numerical and experimental phantom findings to tissue observations, we imaged an eight-week-old female CD-1[®] Nude mouse *in-vivo* (Charles River Laboratories, Germany). Animal handling was conducted in compliance with protocols approved by the Bavarian Animal Research Authority. The animal was anesthetized

using 1.8% Isoflurane (Forene[®], Abbott AG, Switzerland) vaporized in 100% oxygen at 0.8L/min and subsequently placed within an animal holder, as described in [26], in a supine position relative to the arrays. The holder, designed to fit into all three systems, ensured identical positioning of the animal in relation to the detector for the three experimental arrangements. The imaging protocol involved a single-wavelength full-body scan at 850nm and with a step size of 0.5 mm. At each step we recorded 50 frames to capture periodically occurring motion induced by heart beat or breathing. This imaging sequence was repeated for all three systems.

4.3.3 Numerical and experimental results

Results obtained from numerical simulation are shown in figure 4.14. Fig. 4.14(a) corresponds to the reconstruction obtained from MSOT64, fig. 4.14(b) from MSOT128 and fig. 4.14(c) from MSOT256. All images were normalized to 1 and negative values were set to zero as they have no physical meaning. Two rectangular regions ($4 \times 4 \text{mm}^2$) from the center and the periphery of each array are shown magnified at the bottom of each of the images they were taken from. The images demonstrate two major differences. First, a broader region of the object is visualized for an increasing number of elements employed, as predicted by the sensitivity fields of Fig. 2. The second difference regards transversal resolution, i.e. the resolution perpendicular to radial lines originating in the middle of the image. Close to the array center all systems reconstruct the simulated microspheres with a similar performance and accuracy in obtaining their actual dimensions as shown at the bottom right magnification insets in fig. 4.14(a-c). However, the further from the image center a microsphere is positioned the more its reconstruction is transversally elongated. The strength of this effect is directly related to the pitch of the detector elements in each array, i.e. MSOT64 elements have the largest pitch and cause the strongest distortions; MSOT256 elements the smallest pitch and the least distortions. The bottom left magnification insets in fig. 4.14(a-c) illustrate this effect.

A quantitative assessment of both improvements seen as a function of detector elements employed is given in fig. 4.14(d) and 4.14(e), which show a profile (cross-section) of the six magnified images from top-left to bottom-right. Close to the image center, fig. 4.14(e), all geometries correctly resolve a microsphere diameter of $190 \mu\text{m}$ at FWHM with comparable sensitivity (amplitude). The noise appearing between the four distinct peaks is a consequence of the high resolution and large imaging region chosen ($30 \times 30 \text{mm}^2$), which required a degree of regularization inversely proportional to the number of detectors, i.e. stronger for MSOT64 than for MSOT256. On the other hand, transversal resolution at 10mm distance from the array center, shown in fig. 4.14(d), drops for all systems. MSOT64 resolves elongated microspheres of approximately $730 \mu\text{m}$ length; MSOT128 achieves $450 \mu\text{m}$ and MSOT256 $270 \mu\text{m}$ for an actual microsphere size of $187.5 \mu\text{m}$. On the radial axis all systems resolve microsphere width as approx. $250 \mu\text{m}$. fig. 4.14(d) and (e) also illustrate the drop in amplitude when moving further from the array center. While all systems exhibit reduced sensitivity with increasing distance from the center, the drop is sharpest for MSOT64

and marginally better for MSOT128. By contrast, MSOT256 achieves twice the sensitivity of MSOT64.

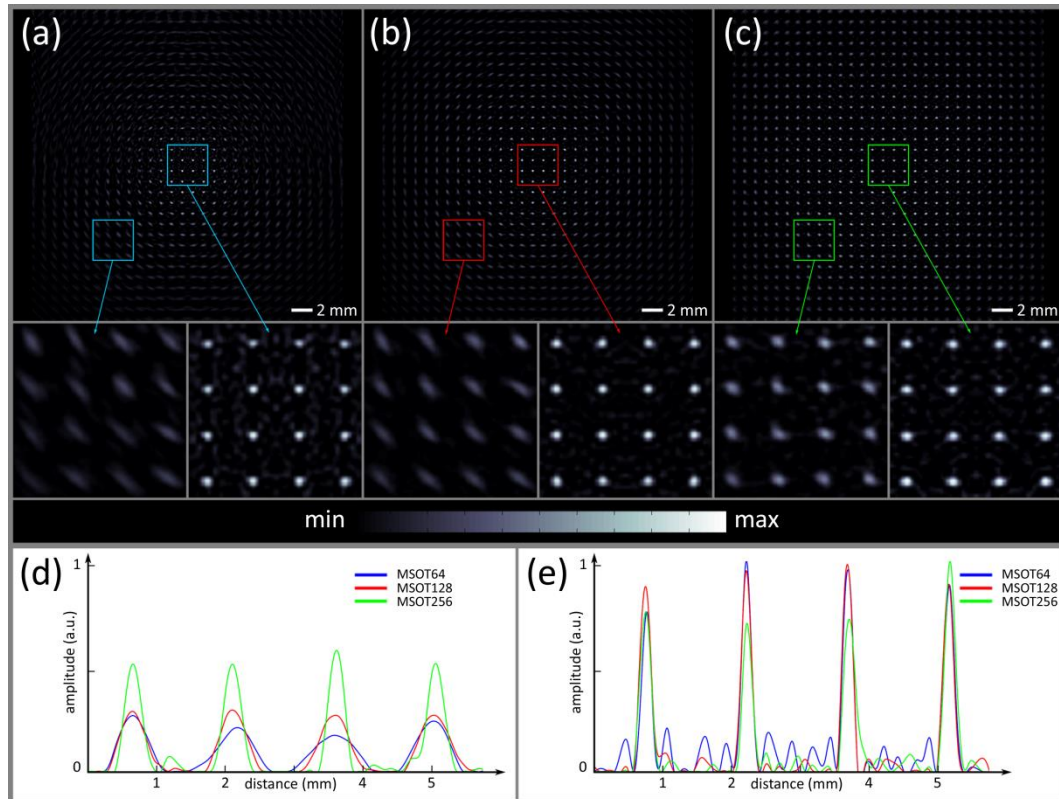


Figure 4-14 – Top row shows simulated reconstruction results from (a) MSOT64, (b) MSOT128 and (c) MSOT256. For each image negative values were removed and the remainder normalized to 1. Details at the periphery and the center, framed ($4 \times 4 \text{ mm}^2$) and color-coded by array, were magnified for display at the bottom left and right respectively. Graphs below depict diagonal cross-sections (top-left to bottom-right) of the magnified detail images for (d) the periphery and (e) the center.

Experimental results from the PE microsphere phantom are shown in figure 4.15, which similarly arranged to fig. 4.14. Due to irregular sampling, we selected three central (4-6) and three peripheral (1-3) microspheres, which were captured sufficiently well by all geometries, and plotted their transversal profiles in fig. 4.15(d, e). We note that variations in amplitude and shape within close spatial proximity, e.g. within the magnification insets, are due to experimental imperfections such as microsphere clustering, see fig. 4.13(b), alignment between phantom and array center or elevational displacement of individual microspheres (on the order of hundreds of μm along z -axis). Nonetheless, selected microspheres confirmed the observations derived from numerical simulation. In particular, microspheres 4-6 from the array center show similar shapes, amplitudes and resolutions for all systems. Fig. 4.15(e) shows profiles obtained along the diameter of the microspheres revealing a FWHM of $\sim 200 \mu\text{m}$ for all detectors employed. Conversely, selected microspheres (1-3) from the periphery were resolved with different diameters as a function of the number of detector elements employed, as shown in fig. 4.15(d). We also observed higher sensitivity for MSOT128 compared to MSOT64 and the highest sensitivity for MSOT256. Similar observations

can be made for transversal resolution in 10mm distance from the array center (microsphere 3): MSOT256 resolves a width of $200\mu\text{m}$, MSOT128 $300\mu\text{m}$ and MSOT64 $450\mu\text{m}$. In relative terms, i.e. from MSOT64 over MSOT128 to MSOT256, improvements in transversal resolution were expected; compared to simulation however, absolute resolutions seem too high. The explanation for this apparent outperformance of simulation results lies in the necessary light fluence correction and segmentation, which both are non-linear operations but consistent for all arrays. Considering the pixel size of $67\mu\text{m}/\text{pixel}$, the transversal resolution discrepancy for MSOT256 is approximately 1 pixel, for MSOT128 close to 2 pixels and for MSOT64 close to 4 pixels. Thus, experimental results from the phantom confirm the superior image quality of MSOT256.

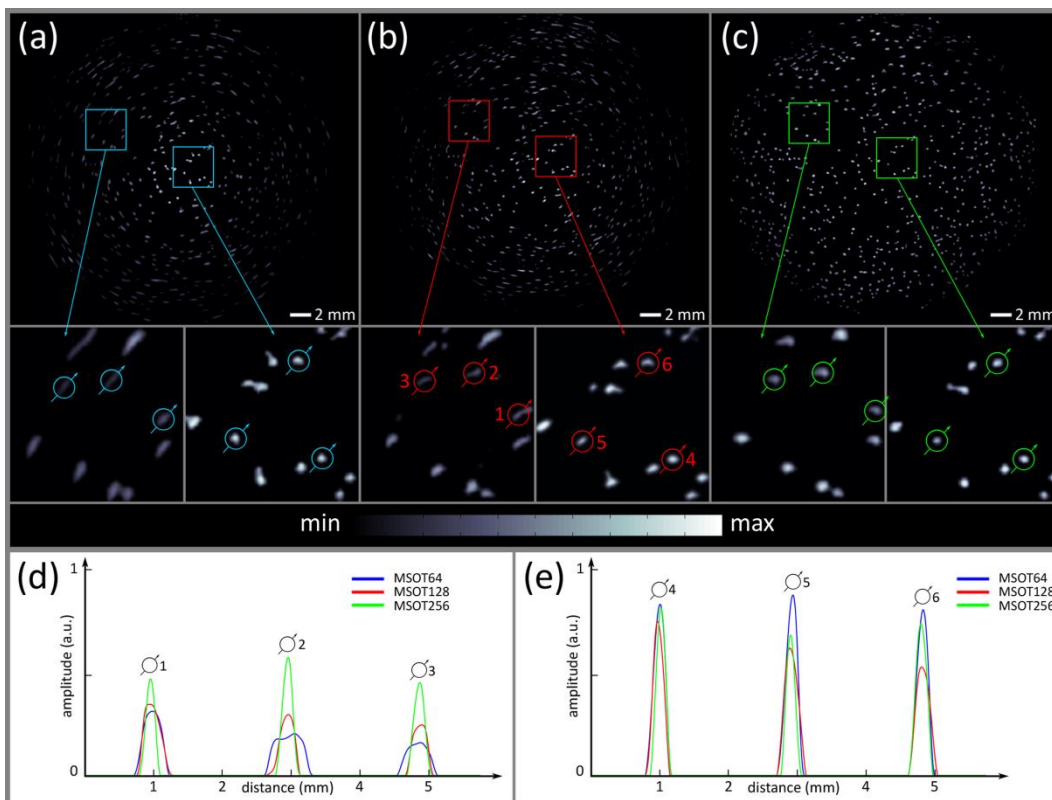


Figure 4-15 – Top row shows experimental phantom reconstruction results from (a) MSOT64, (b) MSOT128 and (c) MSOT256. For each image negative values were set to zero and the remainder normalized to 1. Furthermore, images were segmented based on their local maxima. Details at the periphery and the center, framed ($4 \times 4 \text{mm}^2$) and color-coded by array, were magnified for display at the bottom left and right respectively. Graphs below depict diagonal cross-sections of individual microspheres (circled blue, red and green) for (d) the periphery (numbered 1-3) and (e) the center (numbered 4-6). Individual cross-sections were artificially spaced to allow sufficient distance for comparison.

Figure 4.16 shows results obtained from the same nude mouse imaged sequentially and without averaging in all three systems. To qualitatively compare achievable imaging performance we have selected three content rich anatomical regions of increasing diameter. As the mouse was identically positioned during all three scans

and we took 50 frames per position, we were able to precisely choose the same cross-sectional image at the same respiratory time point for all three systems. Columns of Figure 6 show results by system, with the last column depicting cryoslices at equivalent positions from a comparable mouse. Analysis of the mouse head revealed that all arrays captured large vascular structures on the periphery as well as deep inside the brain. Compared to other body segments, the mouse head was covered reasonably well by all geometries. The temporal artery (marked 2), the sagittal sinus (marked 1) and deep seated extra-cranial (marked 3) and cerebral blood vessels (marked 4) were visible in all cases. However, closer inspection of fig. 4.16(a-d) reveals improving resolution for increasing number of detector elements. For example the sagittal sinus is only vaguely captured by MSOT64 with a transversal diameter of 600 μm at its widest point, whereas it is more accurately reconstructed with MSOT128 (550 μm diameter) and MSOT256 (450 μm diameter). Similar inspection of the temporal artery revealed a reconstructed size of 670 μm , 470 μm and 380 μm from MSOT64, MSOT128 and MSOT256 respectively. Comparison of the MSOT256 image and the cryoslice photograph on fig. 4.16(d) shows that MSOT256 achieves the most accurate reconstruction of vessels over MSOT64 and MSOT128, offering an overall appearance that is very close to the one seen on the photograph.

MSOT results from the liver level are depicted in fig. 4.16(e-h). MSOT64, shown in fig. 4.16(e), allows localization of larger features, such as the spinal cord (marked 5), the aorta (marked 6) or the vena cava (marked 7). However several anatomical details in the periphery of the animal are lost, consistent with the findings in figures 4.14 and 4.15. Conversely, MSOT128, fig. 4.16(f), and MSOT256, fig. 4.16(g), reveal finer structures and more elaborate views of vasculature showing improved peripheral resolution and fewer artifacts. Similar observations were obtained from images at the kidney region, where the diameter of the mouse body was about 23 mm. Fig. 4.16(i), obtained from MSOT64, exhibits resolution drop and visualization of coarse features, especially in the animal periphery as in fig. 4.16(e) and affords only limited transversal resolution. Nonetheless, characteristic landmarks (spinal cord, aorta, vena cava) and large organs (both kidneys marked 11, spleen marked 12) can be identified. Fig. 4.16(j) depicts the MSOT128 result and shows better clarity in resolving anatomical features compared to MSOT64. As expected from the liver cross-section, the best image quality is achieved by MSOT256, depicted in fig. 4.16(k). The significantly improved transversal resolution and sensitivity field is best demonstrated in the right kidney (marked 11).

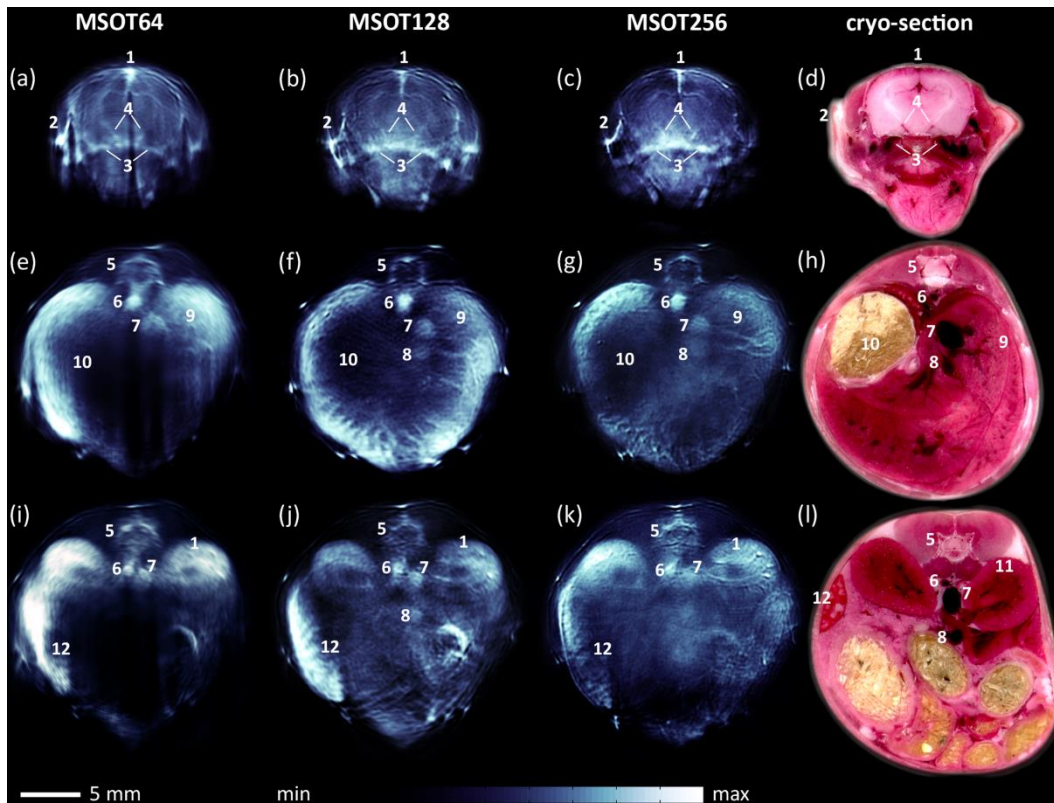


Figure 4-16 – Single-shot in-vivo mouse images at 850 nm wavelength: the first column shows results obtained from MSOT64; second column MSOT128; third column MSOT256. The last column shows mouse cryoslices at equivalent positions. The mouse head is shown in (a-d): 1. sagittal sinus; 2. temporal artery; 3. extra-cranial blood vessel; 4. deep cerebral vessel. The liver region is shown in (e-h): 5. spinal cord; 6. aorta; 7. vena cava; 8. vena porta; 9. liver; 10. stomach. The kidney region is shown in (i-l): 11. kidney; 12. spleen.

Due to its feature rich content, the liver region enables a detailed comparison of cryosection and MSOT images. Fig. 4.17 compares the performance of MSOT256 against a corresponding cryoslice photograph serving as the gold standard, to offer a more elaborate explanation of the signals observed on the optoacoustic images. Five significant landmarks have been encircled and numbered (1-5), whereby higher brightness in the MSOT image, fig. 4.17(a), corresponds to darker colors in the cryo-section, fig. 4.17(b). The first landmark encloses the vasculature surrounding the spinal disk; its structure comprises a bright dot at the center top, which is characteristic of a blood vessel perpendicular to the imaging plane, and a surrounding bracket indicating blood vessels in-plane. Landmarks 2-4 highlight different regions within the liver. Area 2 is dominated by elongated in-plane vasculature bifurcating from the vena cava and vena porta towards the periphery. On the other hand areas 3 and 4 contain vessels perpendicular to the imaging plane – bright dots that correspond to dark dots in the cryo-section. Additionally, MSOT highlights short branches originating from these dots. Such features can be attributed to vascular branching close and perpendicular to the imaging plane. Finally, we also marked the stomach (area 5), because of its prominent position and sharp boundary.

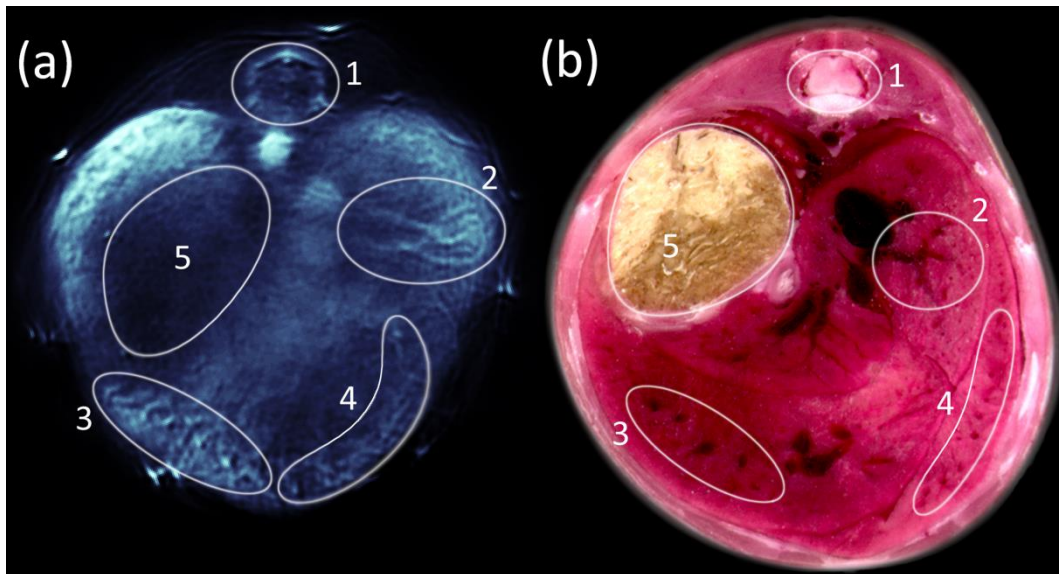


Figure 4-17 – Mouse cross-section at the liver level. (a) MSOT256 result in-vivo at 900 nm wavelength. (b) Equivalent cryoslice obtained from a similar mouse. Corresponding features have been encircled and numbered: 1. Spinal cord; 2-4. Vascular structures within the liver; 5. Stomach.

A better understanding of the relative in-vivo performance of the three systems employed is provided in fig. 4.18, which offers a quantitative comparison between the reconstructions obtained by the 64, 128 and 256 element systems on the spinal disk. Image profiles taken from the radial and transversal directions (marked r and t) are highlighted on fig. 4.18(a) as dashed (MSOT64), dotted (MSOT128) and solid (MSOT256); corresponding traces are shown in figures 4.18(b) and (c). A blood vessel perpendicular to the imaging plane was selected to mark the intersection point for orientation purposes. This vessel could be resolved with 128 and 256 elements, but not with 64 due to its close proximity to the top and sides of the surrounding structure. The radial profile illustrates how the transversal resolution of the three systems can affect the result. In MSOT64, the vessel and the adjacent top edge are fused with emphasis given to the edge. In MSOT128 the vessel gives the stronger signal, however cannot be resolved from the edge. Finally only MSOT256 is able to clearly determine the distance between the two as $280\mu\text{m}$ (peak to peak). On the other hand, from the transversal profile the vessel diameter can be resolved as $560\mu\text{m}$ using MSOT128 and as $350\mu\text{m}$ with MSOT256. MSOT64 again cannot resolve the vessel due to a lack of sensitivity and transversal resolution.

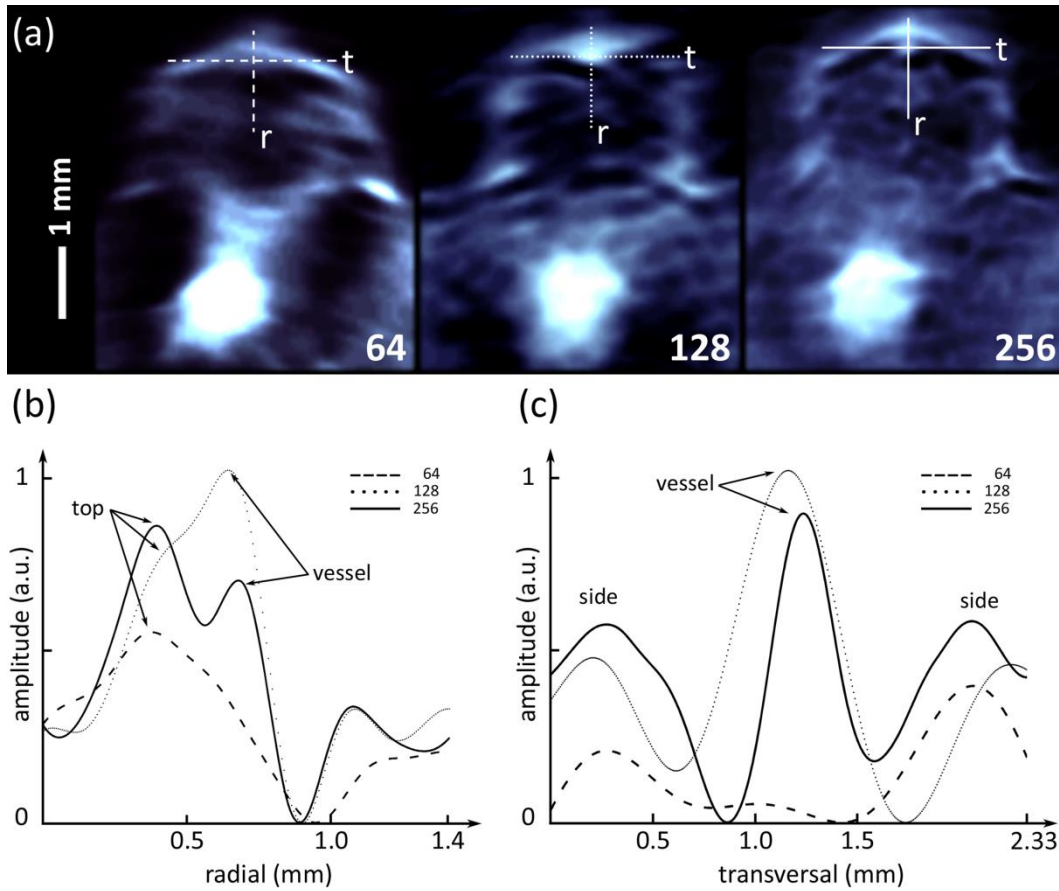


Figure 4-18 – Profiles of spinal cord at liver level. (a) Magnifications for MSOT64, MSOT128 and MSOT256. Cuts in radial (marked r) and transversal (marked t) direction are line-coded by array. (b) Profile of radial trace from top to bottom. (c) Profile of transversal trace from left to right. Prominent features: top and sides of in-plane vascular structure, blood vessel perpendicular to the imaging plane.

Clinical applications

Due to the high concentration of hemoglobin in blood, optoacoustic imaging is highly sensitive to vascular features stretching from large supplying vessels down to capillaries a few μm in size. By sampling the optical absorption spectrum of tissue multi-spectral optoacoustic tomography can complement vascular morphology with molecular information such as oxygen saturation. Many diseases that require clinical assessment and treatment relate directly or indirectly to vascularization and/or oxygenation level, e.g. over- or under-expression, necrosis or oxygen insufficiency. A majority of those is addressable by optoacoustic imaging at all levels of treatment using various modes of operation, i.e. non-invasive, intra-operative, intravascular or endoscopic. In this work we focused on two common types of disease, carotid artery disease and thyroid disease. We also addressed the often encountered problem of tissue viability assessment – in particular during surgery. In the following we will briefly review each application and discuss currently employed diagnostic imaging.

5.1 Cardio-vascular imaging

According to the United States National Institutes of Health the incidence of cardiovascular atherosclerosis is linked to a number of major risk factors that are usually associated with a countries' income level (e.g. high blood pressure and cholesterol levels, obesity, old age, diabetes, unhealthy diet or lack of physical activity). Hence, rising living standards in low and middle income countries contribute to the already high prevalence of the disease known from high income countries [47]. To enhance early diagnosis and perpetual assessment of disease progress novel imaging tools are sought that can also improve cost efficiency and reduce radiation exposure.

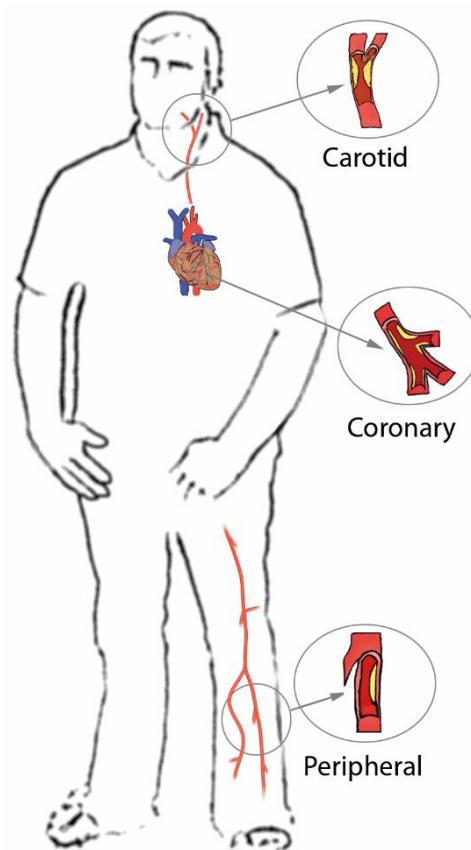


Figure 5-1 – Cardiovascular atherosclerosis

Cardiovascular atherosclerosis can be subdivided into three diseases depending on what part of the vascular system is affected (see Fig. 1). The most common of these is coronary artery disease, which can lead to myocardial infarction (heart attack). Second by incidence is carotid artery disease, which is the major cause of stroke following the rupture of an atheromatous plaque that is often located at or close to the bifurcation of the common carotid artery into internal and external carotid. Atherosclerosis of other arteries is subsumed as peripheral arterial disease, although most such sclerotic pathologies are found in the legs. Common to all categories is a hardening of the arterial wall due to atheromatous plaque that is formed by the infiltration and accumulation of white blood cells (WBCs). The formation of plaque is initiated by an inflammation of the endothelium that is directed at removing remnant low-density lipoprotein (LDL). If this process is repeated too often a layer forms that contains dead cell material and living WBCs, causing continued inflammation. Over time multiple stages of the lesion develop that can also contain cholesterol, calcium and other crystallization products. Figure 5.1 depicts the progression of atherosclerosis, which at later stages is composed of three parts: a base of cholesterol crystals, the central lump and calcifications on the outer base. In the presence of sufficient extracellular matrix (separating the plaque from the arterial lumen) and smooth muscle cells the lesion is considered stable – otherwise the plaque is unstable

or vulnerable. A sudden rupture of the plaque can lead to occlusion of the artery within seconds to minutes and subsequently to heart attack, stroke or even death.

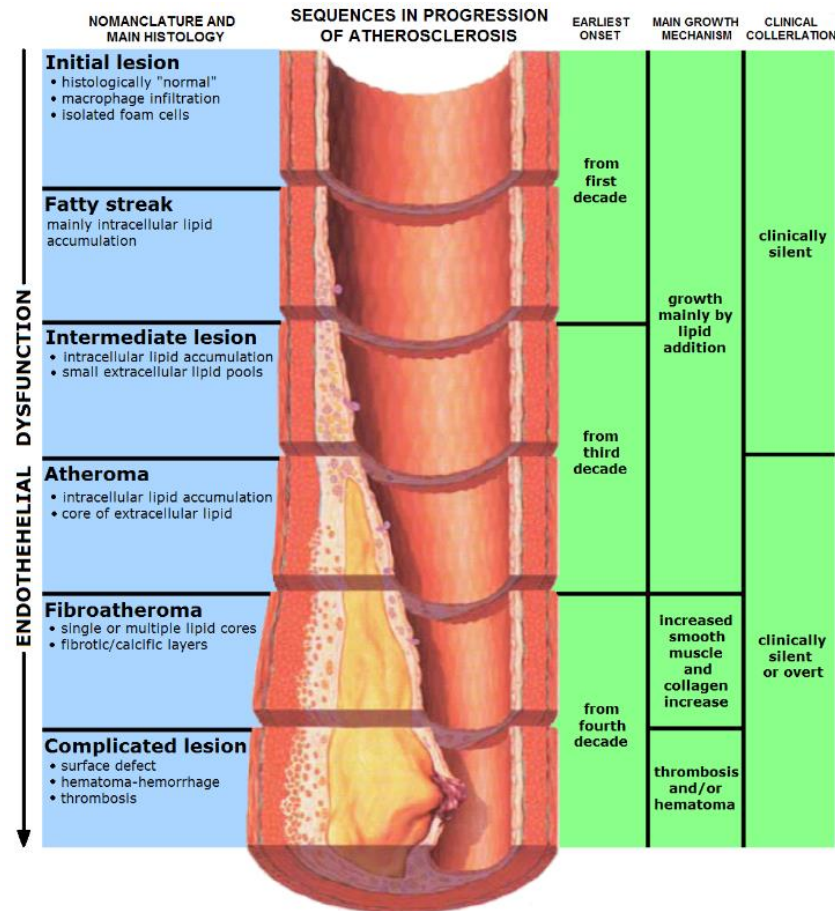


Figure 5-2 – Stages of atherosclerosis.

The difficulty in identifying vulnerability is that both stable and unstable lesions may or may not develop a stenosis (reduced diameter of the arterial lumen). In practice arterial imaging focuses on detecting stenosis rather than the cause thereof, i.e. the plaque. Indications for carotid imaging (also coronary or peripheral) are age and gender or a family history, but also transient event such as neurologic dysfunction or chest pain caused by ischemia or other high-risk factors as mentioned above. As a widely available and easily administered imaging modality Duplex ultrasonography (DUS), i.e. anatomical grayscale ultrasound with color-Doppler ultrasound superimposed, is often the first to be applied. Because of its moderate specificity and sensitivity, DUS is often followed up by angiography, mostly contrast-enhanced projection radiography, computed tomography angiography (CTA) or magnetic resonance angiography (MRA). While each modality has its advantages and disadvantages, e.g. low resolution and movement artifacts (MRA) or radiation exposure (CTA and to a lesser extent radiography), only few try to directly measure the atheroma (plaque). An indirect attempt by measurement of the arterial wall

thickness, known as intima-media thickness (IMT), by non-invasive ultrasonography or intravascular ultrasound (IVUS), has also been studied, yet its usefulness to predicting vulnerability is still disputed. Recently molecular imaging techniques such as PET/SPECT have been employed to image inflammation as a secondary indicator of plaque. Similarly, MSOT promises to enhance arterial imaging by adding molecular information of plaque composition and localization without radiation exposure.

5.2 Thyroid imaging

Thyroid nodules have a high and rising incidence in the general population [96, 97]. While the routine application of neck ultrasonography enables detection of most nodules, even at an early stage, a large majority is not malignant, only in 5-15% of cases thyroid cancer can be confirmed. To identify malignancy a suspicious ultrasound result is also examined by other modalities such as radioiodine scanning or radioactive 2-deoxy-2-[¹⁸F]fluoro-D-glucose positron emission tomography (FDG-PET). In FDG-PET a labeled glucose analog is injected systemically into the blood stream and accumulates in regions of high cell metabolism. Imaging of positron emissions then reveals sites of increased activity which point to malignant tumors. Similarly radioiodine scanning involves systemic administration of iodine-123 (a radioactive isotope) and subsequent imaging of emissions (captured by an x-ray camera). Diagnosis is then performed by evaluating the local distribution of uptake and activity within the gland. In addition invasive fine needle aspiration (FNA) is applied to extract tumor cells for subsequent cytopathology. Despite all efforts, too often unnecessary surgical removal is performed [98], due to indeterminate cytology, unsuspecting appearance or morphological similarities between malignant and non-malignant lesions [99].

MSOT as an additional imaging modality can add vascular information with high sensitivity and also include co-registered conventional ultrasonography, i.e. could be deployed cost-efficiently as a screening modality. The most exciting contribution of MSOT though is the ability to add functional and molecular information similar to FDG-PET or radioiodine scanning, but without the need for radioactivity and the therewith accompanying cost in terms of handling and infrastructure.

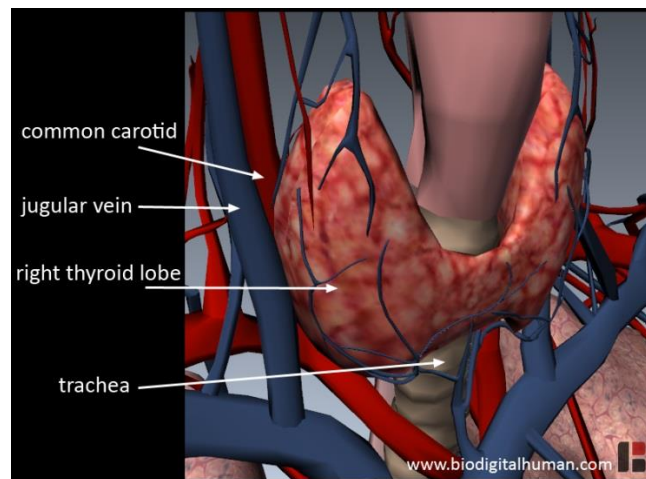


Figure 5-3 – Thyroid anatomy and location relative to the respiratory and cardio-vascular system.

5.3 Tissue viability assessment

Assessing tissue viability is a routine task during surgery and tissue viability is a major indicator of surgery related complications. Postoperative ischemic events may risk patient health and increase hospital stay or require further surgical intervention. The two most important parameters for deciding tissue viability are tissue perfusion and oxygenation. Both are typically assessed by the surgeon using tactile or visual cues to inspect pulse (perfusion) and color (oxygenation). Such unassisted evaluation is thus highly dependent on the experience of the surgeon and the vascularization and pulse-strength of the tissue treated. When perfusion is weak even in healthy tissue, a reliable method to identify and localize ischemic tissue is highly desirable as it allows the surgeon immediately address the problem.

To date many techniques have been proposed for measuring tissue viability, however none has found its way into clinical practice due to various deficiencies [100]. Methods assessing physical parameters of tissue viability such as pH value, temperature or elasticity are insufficiently reliable as they provide only secondary or indirect cues. On the other hand directly assessing tissue oxygen saturation is possible using optical imaging modalities such as near-infrared (NIRS) or visible light (VLS) spectrophotometry. However, the images provided represent an average of optical properties over depth and thus suffer from low reproducibility, further impaired by endogenous tissue fluorescence and movement (angle of detection). Optical imaging can also be employed to measure perfusion. Laser fluorescence angiography (LFA) captures real-time perfusion videos of systemically injected fluorescent contrast agents that show good superficial contrast during the first pass. Assessing perfusion in deeper layers of tissue is obstructed by the strong photon scattering in tissue. Furthermore, the contrast agent typically leaks through the vessel walls into the surrounding tissues and is rapidly cleared from the blood stream, which together lower available contrast and resolution during the subsequent circulation of the agent. Imaging perfusion

without a contrast agent is also possible by measuring blood flow velocity using the Doppler frequency shift. Laser Doppler flowmetry (LDF) is based on a flow induced shift in optical wavelength (inverse to frequency), while Duplex ultrasonography (DUS) uses the equivalent Doppler shift in mechanical waves. Both methods have drawbacks that limit their usefulness. As an optical method LDF is limited in terms of tissue penetration and also suffers from long acquisition time (motion artifacts). In contrast DUS could achieve high resolution even at depth, but requires tissue contact and pulsatile/arterial blood flow and is highly sensitive to motion, which naturally occurs in handheld mode.

As an imaging modality combining ultrasound resolution and optical contrast MSOT is ideally placed to provide both cues of tissue viability, oxygen saturation and perfusion. Relying on ultrasound detection for resolution optoacoustic imaging can see deeper into tissue than purely optical methods and at the same time exploit optical absorption contrast to visualize oxygen saturation. Similarly, high frame rates capturing transient changes in contrast can be exploited to visualize perfusion.

In vivo imaging results

From the first non-invasive measurements acquired using the first handheld prototype to the currently ongoing clinical studies a plethora of data has been collected. At 50 Hz repetition rate a typical 5 minute scan using the latest prototype (HOT-256) accumulates 15,000 acoustic data frames, each 2030*256*2 byte long (total of 14.5 GByte). An interactive format capable of displaying video would therefore be ideal to cast the achieved results in the correct light. The format of this work however does not allow this, and so, much detail is lost that can only be properly grasped through video, e.g. dynamics of perfusion, venous compression/expansion or the virtual 3D imaging based on free detector scanning (facilitated by a viewer's own interpolating brain power). Anyhow, in this chapter we will attempt to present some of the most exciting data retrieved while investigating the applicability of our designs to the clinical challenges presented in the previous chapter. We begin with cardiovascular imaging of extremities and move on to the head and neck region where we study achievable imaging performance targeting the common carotids and the thyroid gland. Results for the intraoperative setup are more limited as the optoacoustic system (cart including DAQ, laser and PC) was preferentially deployed for non-invasive imaging. For this reason we also include results from porcine tissue even though the experiments were performed ex-vivo. Similarly, proof-of-concept experiments, while being in-vivo, were performed on mice.

6.1 Non-invasive imaging

All images presented herein were obtained from healthy human volunteers after ensuring proper laser safety (eye protection, secured measurement space). We studied several measurement positions on the human body that can be separated into two groups: 1) head and neck: carotid arteries, thyroid gland; 2) extremities: lower and upper hands, legs. Unless otherwise specified images presented here were acquired using the first curved array prototype with radius 40 mm and 64 detection elements;

images obtained using the latest prototype HOT-256 (60mm radius and 256 detection elements) are designated as such. In the following we first present results previously published in [78] focusing on the carotid arteries. As the thyroid gland is located nearby, we then show achievable imaging performance of the thyroid. Next we expand upon imaging the extremities, mostly the arms. We complete the section by showing alternative imaging sites such as shoulder and the female breast.

Figure 6.1(a) shows an optoacoustic image of lower arm vasculature obtained at 800 nm excitation wavelength. The skin surface (marked as 1) starts at about 2 mm on the depth axis of the image (top-down with array on top) and is dominated by superficial hair and small sub-cutaneous blood vessels. During imaging we applied pressure to achieve good acoustic coupling and reach deeper into the tissue. This caused a flattening of the observed veins including the intermediate antebrachial vein (marked as 2), which is seated 6-7 mm under the skin surface. Deeper into the tissue we are also able to identify the radial artery (marked as 3), which, due to the muscle of the arterial wall, shows no sign of deformation and thus allows localization at 12-14 mm from the skin surface.

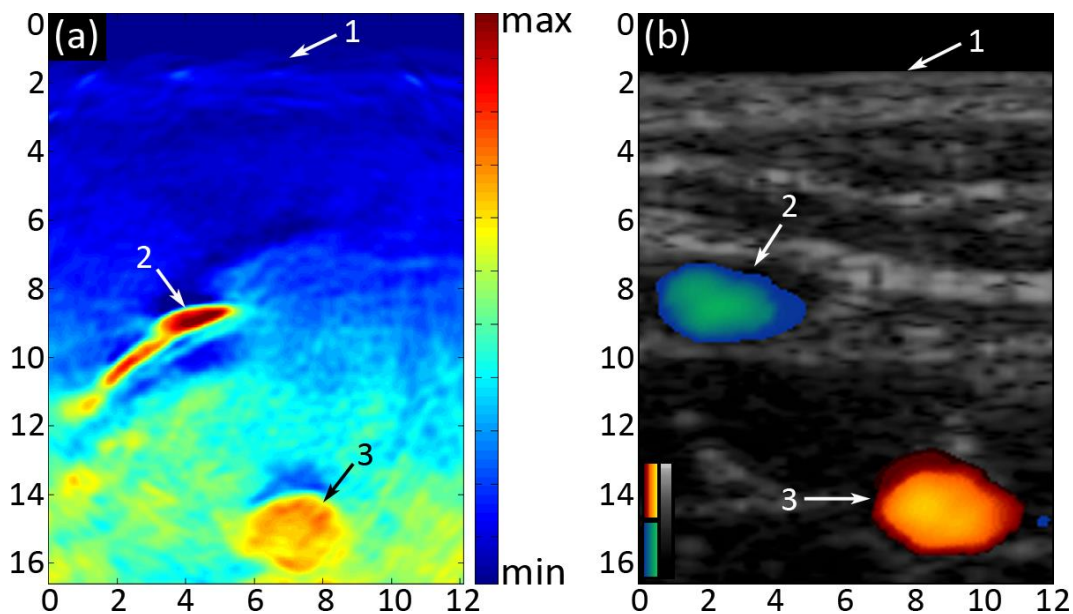


Figure 6-1 – Cross-sections showing lower arm vasculature of a male volunteer 7 cm from the elbow – axes are given in mm. (a) Optoacoustic image using the initial curved array prototype. (b) Directional ultrasonography image, overlaid on standard ultrasonography image in gray, indicating positive flow in yellow/red; negative flow in green/blue. Annotations: 1.Skin surface; 2.Intermediate antebrachial vein; 3.Radial artery.

To validate the optoacoustic findings we show in fig. 6.1(b) a directional Doppler ultrasonography (DUS) image of approximately the same measurement position. Flow directionality is represented in yellow/red for positive and green/blue for negative flow. Below the skin surface (marked as 1) we can clearly identify the intermediate antebrachial vein (marked as 2) and the radial artery (marked as 3). Both vessels appear closer to the skin surface and further apart horizontally from each other than in fig. 6.1(a). This can be explained by the linear surface of the ultrasound probe, which

pushed tissue and vessels horizontally apart, while the half-cylindrical surface of the optoacoustic assembly better preserved the tissue shape. The visibly lower resolution and increased shape of both vessels, but especially of the vein, are due to the choice of DUS parameters necessary to visualize the relatively weak blood flow. On the other hand the absolute position in the tissue as well as the relative position to each other corresponds very well with the optoacoustic image.

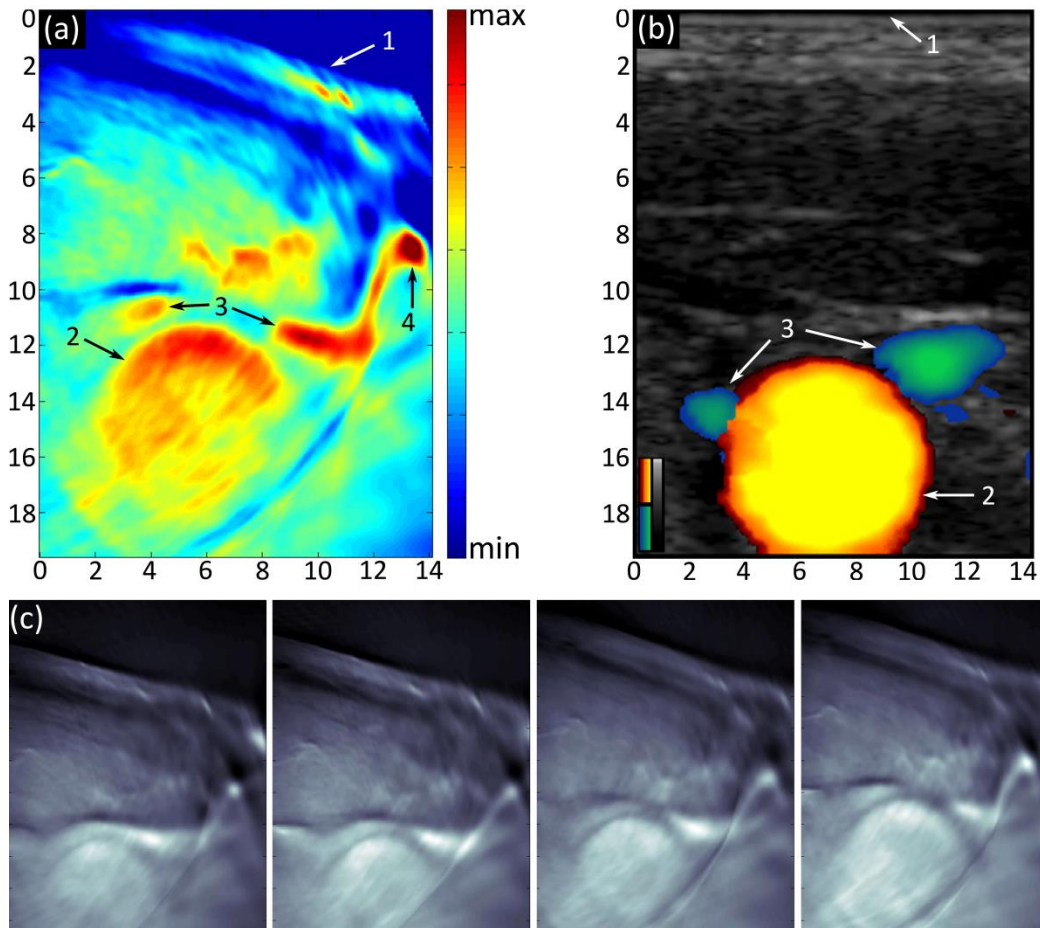


Figure 6-2 – Cross-sections showing cardio-vascular features of a female volunteer at the lower neck level – axes are given in mm. (a) Optoacoustic image from the initial curved array prototype. (b) Directional ultrasonography image, overlaid on standard ultrasonography image in gray, indicating positive flow in yellow/red; negative flow in green/blue. Annotations: 1.Skin surface; 2.Common carotid; 3.Internal jugular vein; 4.External jugular vein. (c) Screen capture of video sequence showing carotid enlargement due to heartbeat.

In the same measurement session we also successfully imaged the right side of the lower neck of a female volunteer several times and obtained similar results. Fig. 6.2 shows a representative experimental result at the peak of the volumetric expansion caused by heartbeat. Fig. 6.2(a) depicts the optoacoustic image at 800 nm wavelength. We can clearly identify the right common carotid (marked as 2) as it extends from 12-18 mm beneath the skin surface (marked as 1) and is almost perfectly round. Close by we can identify the right internal jugular vein (marked as 3), which, viewed from the

skin surface, lies on top and can be divided in two separate volumes at peak expansion of the common carotid – compare fig. 6.2(c). Because of the semi-cylindrical shape of the detector as well as the applied pressure, we can also spot the external jugular vein (marked as 4). In an anatomically relaxed state of the neck we would have expected it several millimeters further to the image right. Again validation of optoacoustic findings is depicted in fig. 6.2(b) using directional DUS at approximately the same position on the lower neck. The same color maps as in fig. 6.1(b) were used (positive flow: yellow/red; negative flow: green/blue) and simplify identification of the carotid and vein. The linear array flattened the skin surface in this case (marked as 1) and also pushed the external jugular vein out of the imaging window. Because we applied less pressure than for optoacoustic imaging, the carotid (marked as 2) is shown to be seated at 13-19 mm beneath the skin surface. As expected, we also captured the internal jugular vein (marked as 3). The vascular structures observed herein correspond very well with the structures identified in the optoacoustic image.

Two more female volunteers were chosen for imaging of the anterior neck region specifically targeting the thyroid gland. Measurements were similarly validated by directional DUS and echo-ultrasound, recording short image sequences at corresponding positions. For each ultrasound position a matching set of optoacoustic images could be identified by manual inspection.

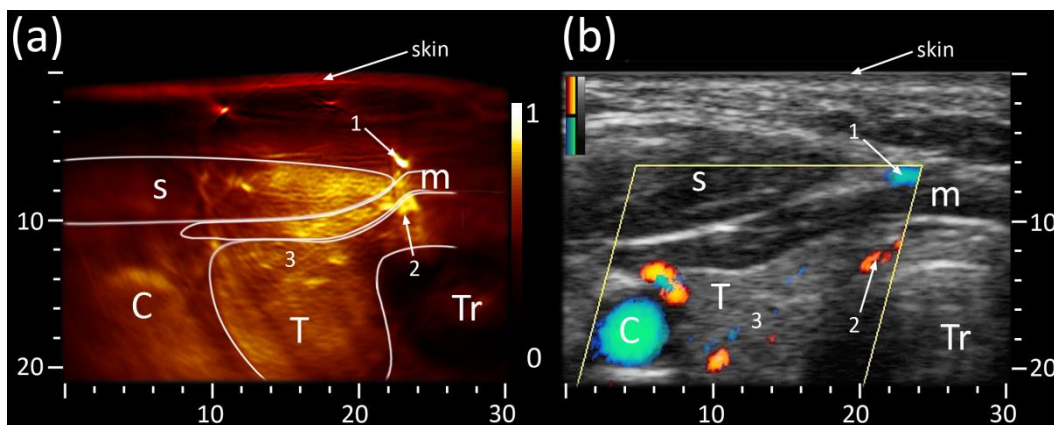


Figure 6-3 – (a) Optoacoustic and (b) ultrasound cross-sections of the left thyroid lobe of the first volunteer. The optoacoustic image, leveled and normalized from 0 to 1, shows with high sensitivity vascular features of skin, muscles (1,2) and within the thyroid lobe (3). The corresponding ultrasound image in grayscale also depicts Directional Power Doppler signals superimposed in color (red/blue colormaps indicating opposite flow directions). C: Carotid, T: Thyroid, Tr: Trachea, s: sternocleidomastoid muscle, m: infrahyoid muscle; axes in mm.

Figure 6.3 shows results from the left thyroid lobe of the first volunteer. The optoacoustic image, depicted in fig. 6.3(a), allows immediate identification of large features characteristic of the anterior neck such as the carotid artery and the trachea, which appears round and dark as ultrasound cannot penetrate or escape from air filled cavities. Similarly, high vascularization within muscles allows identification of the sternocleidomastoid and an infrahyoid muscle. Although deeper seated the thyroid lobe can also be distinguished. In particular thyroid vascularization within the anterior part is clearly visible as indicated by the group of vessels surrounding marker 3.

Vessels appearing as round bright dots traverse the imaging plain in a perpendicular angle while others, elongated or dashed in shape, cross through the imaging plane at lower angles. To validate these findings fig. 6.3(b) depicts the corresponding ultrasound image in grayscale with directional DUS signals superimposed in color (red/blue colormaps representing opposite flow directions). Anatomical landmarks, such as trachea, carotid artery and muscles, confirm the optoacoustic assessment. Size and position of the thyroid lobe also coincide with the optoacoustic result. Vascularization however does not provide sufficient echo and thus requires application of Doppler ultrasound to identify vessels by measuring blood flow. In fig. 6.3(b) the Doppler signal is only measured within the yellow rhombus and confirms two major findings from fig. 6.3(a): two strong vessels above (marked 1) and below (marked 2) the infrahyoid muscle as well as various vessels within the anterior part of the thyroid (surrounding marker 3) of different size and flow directions.

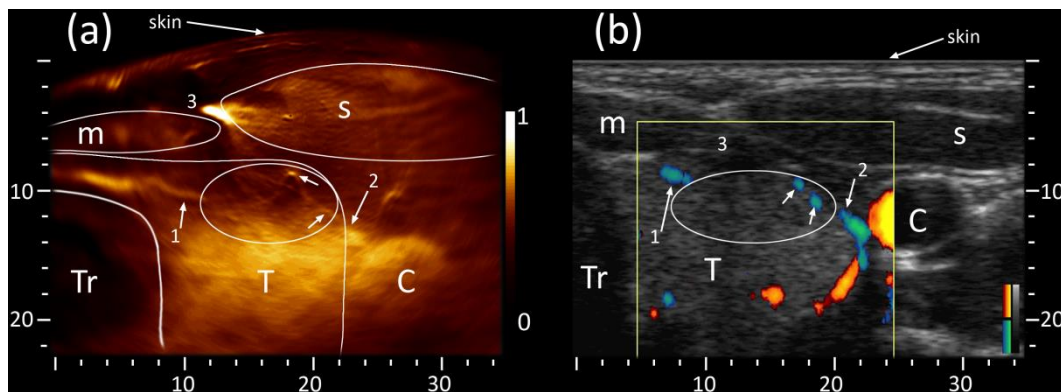


Figure 6-4 – Cross-section of right thyroid lobe of the second volunteer. (a) To limit the influence of strong absorbers (large vein marked 3) on available contrast the optoacoustic image was range limited with respect to high intensity values before leveling and normalization from 0 to 1. Besides larger features (e.g. muscles, thyroid) optoacoustic imaging allows identification of prominent vascularization (1, 2) and a fine vascular network (oval highlight) stretching inside the imaging plane and perpendicular to it (fine dots). (b) The corresponding ultrasound image confirms features detected in (a), whereby grayscale represents the pulse-echo and color the Directional Power Doppler signal (red/blue colormaps indicating opposite flow directions). C: Carotid, T: Thyroid, Tr: Trachea, s: sternocleidomastoid muscle, m: infrahyoid muscle; axes in mm.

Results from the right thyroid lobe of the second volunteer are shown in Figure 6.4. During the optoacoustic scan, depicted in fig. 6.4(a), the sternocleidomastoid muscle was tense and therefore pushed the carotid artery and the thyroid lobe further from the curved skin surface. An infrahyoid muscle is also discernible, however due to its peripheral position at reduced resolution and intensity. The thyroid lobe, taking up the space between trachea and carotid artery, is clearly visible. Three prominent vascular features have been highlighted as they extend mostly inside the imaging plane. An elongated vessel (marked 1) stretches from the isthmus towards the anterior part of the thyroid lobe. A second vessel (marked 2) similarly reaches from the vicinity of the carotid artery towards the same area. To highlight patterns within this anterior part we have encircled the area with an ellipse and pointed out two features. The vessel marked as “2” appears to continue within the ellipse (lower arrow) extending towards the bright spot (upper arrow) while also branching. Similar patterns can be found when

following the left vessel (marked 1), however at lower signal strength and contrast. In turn ultrasound validation using fig. 6.4(b) is straight forward for large features such as the muscles, trachea or carotid artery. Large vasculature previously identified in the optoacoustic image (marked 1 and 2) can also be found using directional DUS, however at lower resolution and sensitivity due to the indirect measurement based on blood flow. Detecting weak flow in the presence of movement (of probe and patient) is generally difficult and highly operator dependent, which explains the better resolution and more coherent vascular appearance of the optoacoustic image. The same argument can be made for the large vein (marked 3) that generated the strongest optoacoustic signal, but is missing from fig. 6.4(b). We suspect that a combination of applied pressure and chosen Doppler parameters resulted in blood flow too weak to detect. Nonetheless, sufficient echogenicity of the thyroid allows approximate placement of the missing vein in between the two muscles and just above the thyroid lobe. The fine vascular network that we observed in the optoacoustic image (oval highlight) can only be inferred from the echo-ultrasound image as dark spots and patches, again providing too weak flow to yield a Doppler signal.

Other measurements acquired without averaging and using the 64-channel probe are depicted in figure 6.5. The measurement depicted in fig. 6.5(a) and (b) shows results obtained from a male volunteer on the lower arm, where two arteries, ulnar and radial, can be easily located using ultrasound as well as optoacoustic imaging. Data was acquired at 850nm to achieve maximum signal from arterial vessels. We chose to show two time series per measurement. Fig. 6.5(a) illustrates observable changes when moving the probe towards the elbow starting close to the wrist where the radial artery is a tissue depth of about 8 mm below the skin surface (top). The characteristic veins, left and right of the radial artery, become thinner and eventually disappear. Two smaller veins close to the skin surface approach each other until they merge (not shown). Vascular features of the muscle directly adjacent below the radial artery can also be identified. A second time series, shown in fig. 6.5(b), starts at a location closer to the elbow where the radial artery is located at a tissue depth of about 13 mm below the skin surface. The sequence illustrates how the radial artery, starting embedded in a muscle, submerges through the muscle and is lost below the muscle at a depth of about 22 mm. We can also identify subcutaneous fat and vascular features of the muscle as they change over scan distance (time).

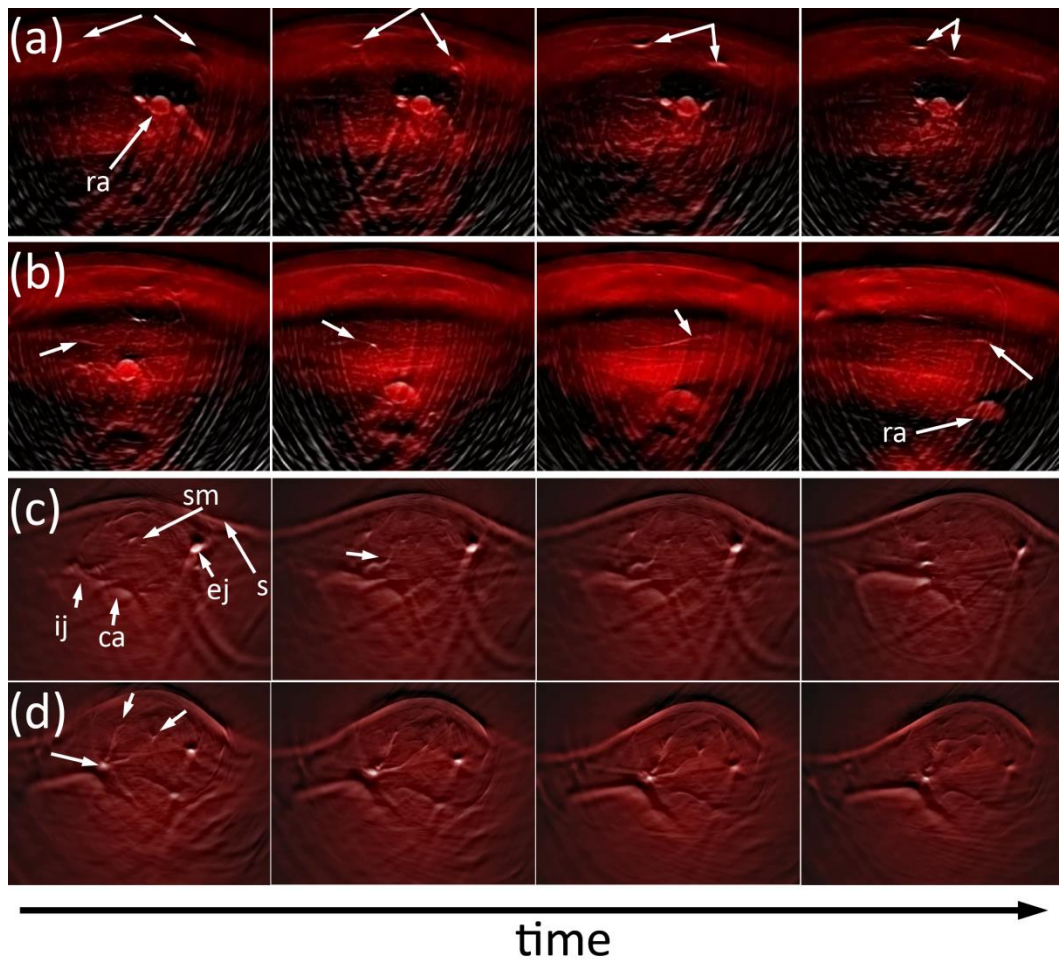


Figure 6-5 – Time series of handheld scans at 850nm wavelength from (a), (b) the arm of a male volunteer (30x30mm²) and (c), (d) the anterior neck region of a female volunteer (30x25mm²). Images show a single wavelength, whereby we chose a red colormap for lower spatial frequencies and superimposed higher spatial frequencies in semi-transparent bright white. The sequence shown in (a) was taken close the wrist where the radial artery (ra) is flanked by two veins. Another sequence, (b), was taken closer to the elbow where the radial artery was located deeper inside the tissue (inside and below a muscle). The sequence in (c) displays the slightly tense sternocleidomastoid muscle whereas (d) shows a sequence under full tension. ca: carotid artery; sm: sternocleidomastoid; ij: internal jugular vein; ej: external jugular vein; s: skin.

The second dataset is shown in fig. 6.5(c) and (d). It was obtained from a female volunteer on the anterior neck region at the same wavelength. Once again we selected two sequences showing changes in vascular features as captured by scanning. We can clearly identify common features such as the internal and external jugular veins, the carotid artery and the sternocleidomastoid muscle. Fig. 6.5(c) highlights a vessel located in the center of the muscle (pointed at by the sm arrow) and how its 3D shape can be gauged by moving the probe along the neck up and down as required. The second sequence depicted in fig. 6.5(d) starts at a time point when the sm-muscle was very tense as can be seen by the bell shaped skin surface. Again we are able to understand the 3D shape of the vessel highlighted by the white arrows. It represents

the branching of a vessel perpendicular to the imaging plane, whose branches elongate approximately within the imaging plane towards the center of the muscle. We arrive at this conclusion, because a bright round spot remains visible throughout the sequence – characteristic for a vessel perpendicularly crossing through the imaging plane. The elongated branch however rapidly fades away as the probe is moved.

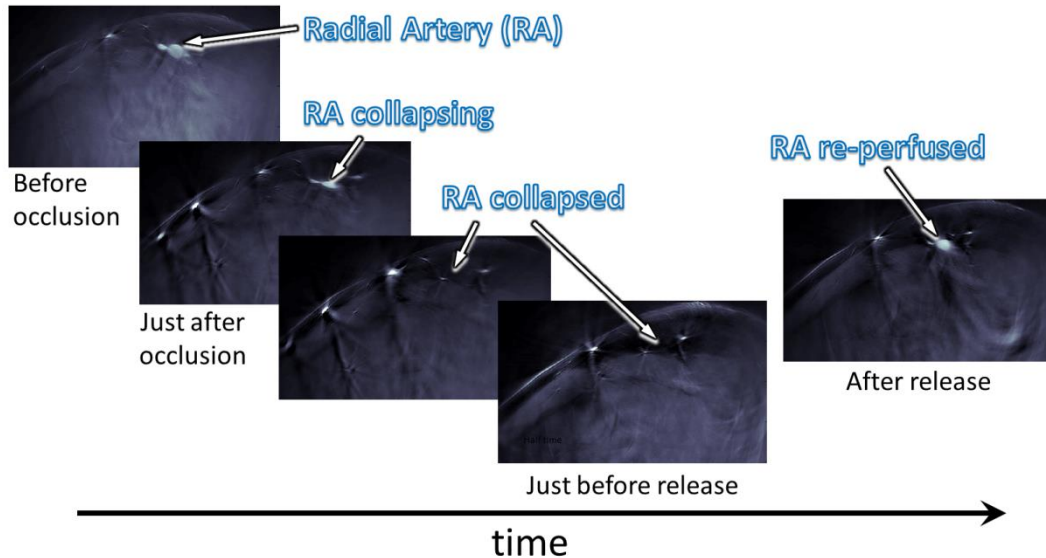


Figure 6-6 – Time series showing a controlled occlusion experiment at critical time points. Upon occlusion of the vascular system using a sphygmomanometer the radial artery starts collapsing. Just before the release it has fully disappeared. Re-perfusion increases its size and visibility. All images show the same frame of 40 mm width and 20 mm height, held constant during the experiment. Data were acquired using HOT-256 and 800nm wavelength.

For comparison we also show data obtained using the newer prototype, HOT-256. Figure 6.6 summarizes a simple experiment of vascular occlusion by means of a blood pressure meter (or sphygmomanometer). The data were acquired at a similar position on the lower arm as the sequence shown in fig. 6.5(a), although on a different volunteer. The wavelength chosen (800nm) is close to the isosbestic point of optical absorption of oxy- and deoxy-hemoglobin and thus a good indicator of total blood volume. The experimental protocol involved acquisition of about 6 minutes of data at 50Hz. The upper arm was occluded after 30s, during which time the radial artery can easily be identified by its characteristic location and anatomy. Shortly after occlusion can already see a reduction in blood supply; the artery is collapsing until we completely lose signal. After 5min and 30s into the measurement the occlusion is released and the blood supply is restored, which can be quantified by the size and intensity of the artery signal. We hypothesize that this and similar measurements could be usefully employed in the study of vascular diseases, but this is a topic for further research.

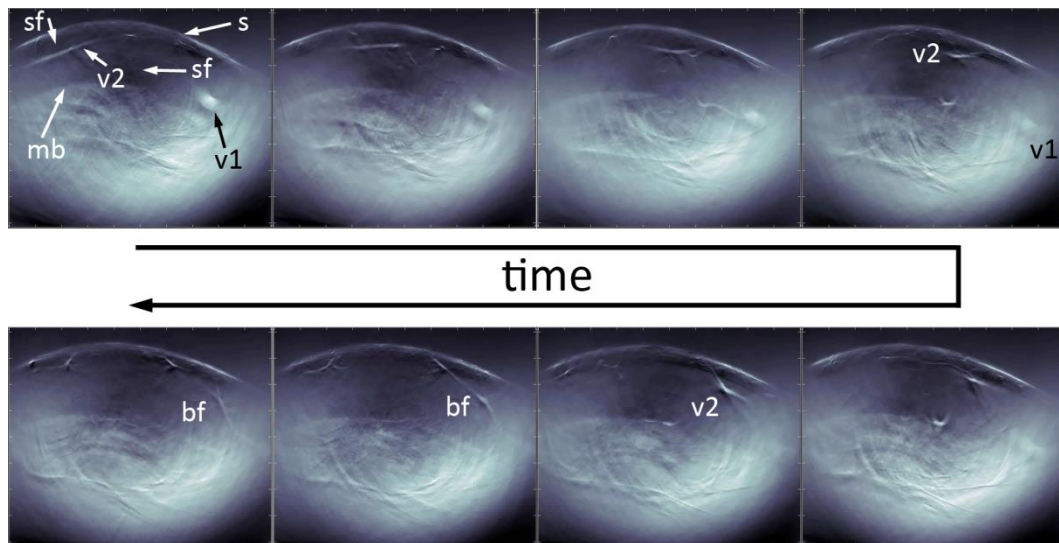


Figure 6-7 – Time series showing a manual scan (top-down) of the calf of a female volunteer acquired using HOT-256 and 850nm wavelength. Vascular features (mostly veins) can be visually tracked on images of 45mm height and 50mm width. The large vein (v1) moves out of focus, while another vein (v2) moves from left to right and then splits, i.e. in 3D it moves diagonally towards the ankle. sf: subcutaneous fat; s: skin; mb: muscle boundary; v1, v2: veins; bf: bi-furcation.

To establish the superior capabilities of the new probe (HOT-256) we chose to image the calf of another female volunteer. The captured data allow identification of multiple vascular features. The time series shown in fig. 6.7 allows tracking of various features over scan position (top-down), as demonstrated before. We highlighted interesting landmarks. The large muscle is clearly visible and displays a sharp boundary (mb) to the subcutaneous fat (sf) layer that also includes lymphatic tissue, which itself does not provide optical contrast but can be gauged by the density and size of subcutaneous vascularization. Two veins are of particular interest as their shape and position changes with movement of the probe. The large vein close to the muscle (v1) slowly moves out of focus and in the third image from the top left even shows a small branch into the imaging plane. A smaller vein (v1) diagonally descends towards the ankle and even branches into the plane where it also bifurcates into two smaller veins (bf). The higher resolution and larger field of view of the HOT-256 probe enables us to accurately assess size, location and anatomy of vessels pertaining to muscular supply or the lymphatic system. We speculate that this information coupled with multi-spectral un-mixing of intrinsic chromophores (obtaining for example tissue oxygen saturation) or extrinsically administered contrast agents could be usefully employed to assess state and development of cardio-vascular disease. But again this is subject of future research.

6.2 Towards intraoperative imaging

To demonstrate the performance of blood perfusion assessment using the optoacoustic setup and methodology developed in chapter 3.4, we used freshly excised portions of porcine lower colon. Experiments were repeated on three separate days, each time using a fresh sample provided by Dr. Dirk Wilhelm (department of surgery, Klinikum rechts der Isar). Resection was performed in-vivo on the anesthetized animal, just before the animal was sacrificed. The excised segment was chosen to comprise the supplying artery and vein. Directly after excision, blood was cleared from the sample and the feeding artery catheterized on one side and ligatured at the other end with the arterial branching in between to ensure perfusion of the excised tissue. To simulate real conditions, arterial blood was extracted intraoperatively into a syringe containing anticoagulant. This blood was injected later during ex-vivo experiments to reproduce perfusion of the sample. Subsequent experiments were performed outside the surgery room and started approximately one hour after extraction. The sample was placed in front of the ultrasound probe along the axis of the colon. Fig. 6.8(b) shows the colon segment in the experimental setup. Before the actual measurement we also evaluated a measurement position perpendicular to the one chosen, see fig. 6.8(a, c). Although illumination was identical for both positions, we chose the position shown in 6.8(b) as vessels were mostly parallel to the linear array axis in this position. During the experiments the sample was immersed in isotonic saline, to ensure tissue preservation and to provide acoustic coupling between the sample and the detector.

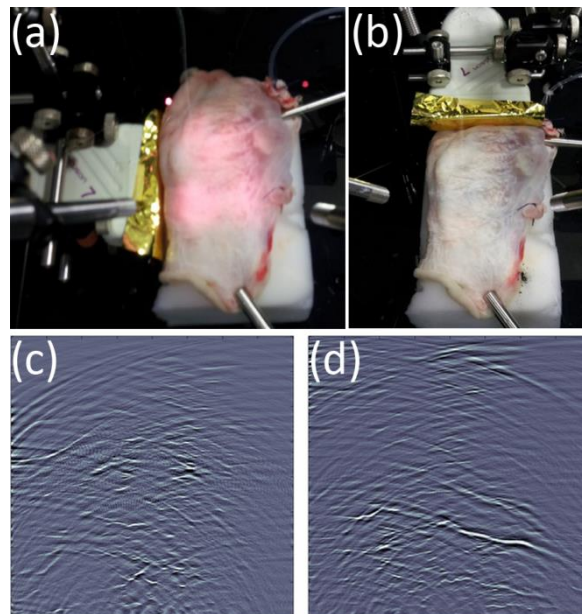


Figure 6-8 – Identifying the best measurement position. (a) This position results in poor image quality, shown in (c), because most vessels elongate perpendicular to the array axis. (b) The position chosen for subsequent experiments as most vessels are approximately parallel to the array axis.

The lack of active perfusion (induced by heart beat) in the ex-vivo colon experiment resulted in a different internal pressure of the vessels and modified the flow conditions. We therefore decided to also demonstrate the feasibility of our proposed method in-vivo. Living adult CD-1 mice (CD-1©, Charles River Laboratories, Sulzfeld, Germany) were used for this purpose and the experiment repeated several times on three different mice. Animal handling was conducted in compliance with the author's institutional guidelines following national and international laws and regulations. Experimental protocols were reviewed and approved by the Bavarian Animal Research Authority. For imaging we chose the mouse tail, because of its easy access for catheterization and simple vascularization. Before the measurement the mouse tail was shaved and the animal anesthetized using Isoflurane-oxygen vapor (Forene©, Abbott AG, Switzerland). Acoustic coupling was achieved using a combination of agar pad (2%w/v) and acoustic gel.

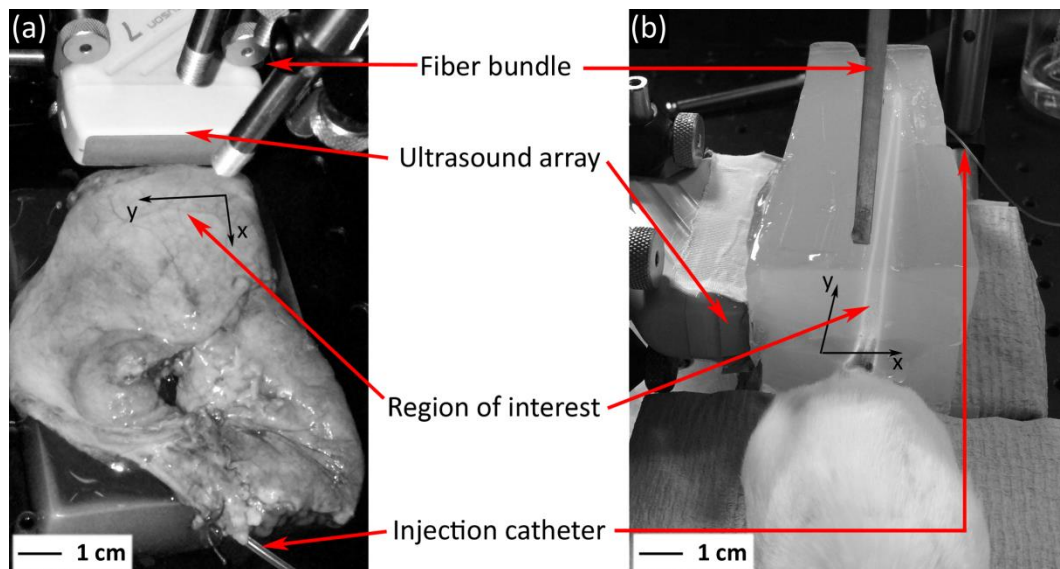


Figure 6-9 – Experimental setup including fiber bundles for illumination, ultrasound array and injection catheter. (a) The excised colon segment with region of interest of 12 mm (x-axis) by 20 mm (y-axis). (b) In-vivo mouse tail (highlighted) with region of interest of 5 mm (x-axis) by 20 mm (y-axis).

All measurements on the excised colon segment yielded similar results. Thus, fig. 6.10 shows results obtained from one sample. The MAS-graph (masked absolute sum introduced in chapter 3.4), depicted in Fig. 6.10(a), is composed of two phases: saline injection (dashed) and blood reperfusion (solid). To characterize this dynamic process we marked four time points during each phase (t1-t8) and show corresponding images in fig. 6.10(b). During the first 1-2 seconds of each injection we observed significant tissue movement, which caused a shift of the sample between injections (compare images at t1 and t8) and an initial signal increase during saline injection. This response was found for all samples and can be explained by the pressure build up needed to induce a flow in the arterial branch, which was in a collapsed state before injection. The steady state of full concentration blood within the vasculature is marked by t1. Subsequent perfusion of saline shows a rapid decrease in concentration (t2), partial

clearing of blood (t3) and finally complete clearing (t4). Due to vanishing contrast we describe this phase as providing negative optoacoustic contrast, whereas the second phase provides positive optoacoustic contrast as reperfusing blood raises vascular absorption above the background. Part of this process is captured by the right image sequence (t5-t8) in fig. 6.10(b), which enables visual tracking of blood propagation throughout the region of interest. The corresponding MAS-value shows a sharp rise followed by a steady increase due to increasing blood concentration as saline is replaced with full concentration blood.

To ensure reproducibility of the method, the experimental protocol was repeated twice for saline and once for ICG on three different mice (total of 9 measurements). Coherent results were obtained for similar injections. Thus, we show here representative results for injections of saline (fig. 6.11) and ICG (fig. 6.12) respectively. Fig. 6.11(a) shows the MAS-graph over time. To establish a reference, we first recorded 20s of steady state (t1) and used the reconstruction at $t=0$ s to extract the parameters for post-processing. Three distinct minima indicate subsequent saline injections, each achieving approximately the same contrast cycle. A representative visualization thereof is given for the first injection (t1–t6) in fig. 6.11(b). The negative phase during injection (t2-t4) allows visual tracking of the disappearing vasculature and is characterized by a rapid decline in MAS-value. Viewed in sequence t1-t4 clearly identify the propagation of saline from the top (distal end of the tail). The subsequent recovery of hemoglobin concentration (t4–t6) offers improving positive contrast that is well quantified by the MAS-graph.

Fig. 6.12 shows results obtained from the same measurement protocol used to produce fig. 6.11, but with ICG instead of saline. This time the MAS-graph is dominated by three local maxima indicating ICG injections. As each injection increased the ICG concentration in the total blood volume and thereby also increased the baseline for the next injection, post-processing parameters had to be chosen after the measurement. Nevertheless, to showcase the achievable contrast cycle, the same time points as in fig. 6.11 were marked in fig. 6.12(a) and visualized in Fig. 6.12(b). A flat MAS-curve, characteristic for the steady state (t1), is followed by a steep jump during injection (t2-t4) and a slow decline during the clearing phase (t4-t6), in which the injected ICG volume is diluted and removed by re-perfusing blood. The corresponding image sequence again allows visual tracking of perfusing ICG, albeit with less intravascular contrast compared to saline injection.

We also studied the effect of increasing the volume of saline injected. As figure 6.13 shows the MAS curve remains flat for longer – approximately correlated to the injection volume and flow speed. The recovery time however remains unchanged. As recovery time is a more useful indicator of the quality of perfusion, we conclude that the same result in terms of perfusion assessment can be obtained by using a minimal amount of saline.

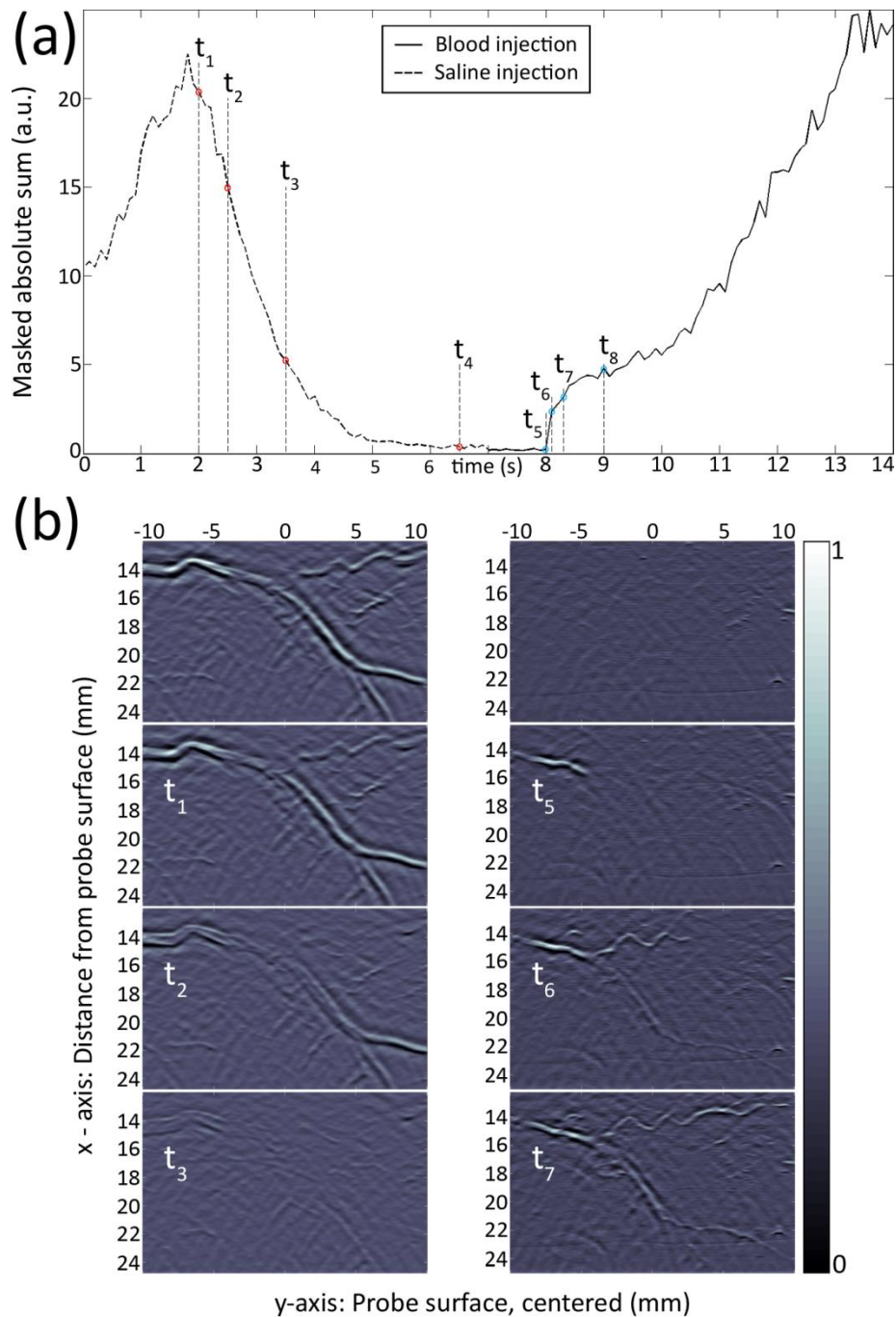


Figure 6-10 – Artificial perfusion of an excised colon segment. (a) Masked absolute sum of reconstructed region of interest over time: saline perfusion in the blood filled vasculature (dotted line) and blood perfusion in the cleared vasculature (solid line). Injections were performed successively. (b) Optoacoustic images of representative time points: t_1 – t_4 for saline perfusion, and t_5 – t_8 for blood perfusion. Images were plotted on a linear scale from 0–1 with 0 and 1 representing the minimum and maximum pixel value over all image frames in the sequence. Axes x and y correspond to the coordinate system displayed in fig. 6.9(a).

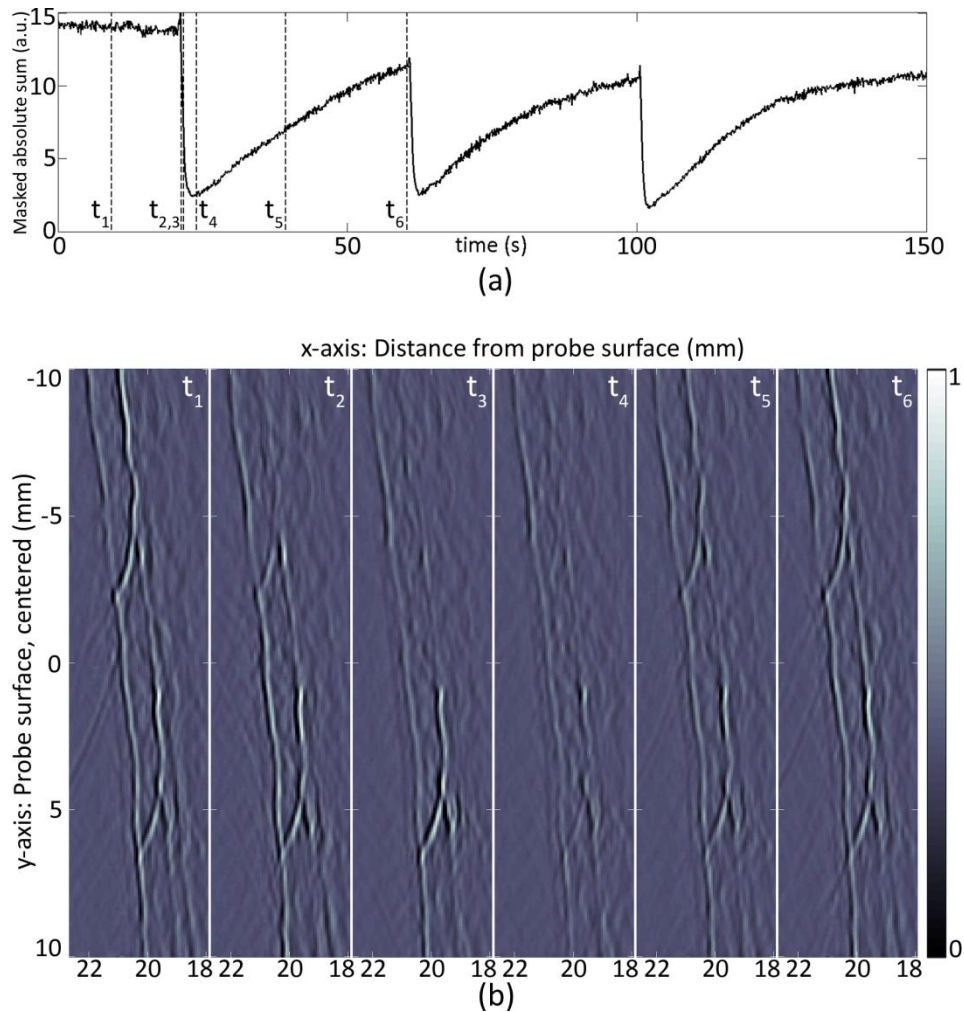


Figure 6-11 – Saline injection in a mouse tail in-vivo: 3 injections in intervals of 40s. (a) Masked absolute sum of reconstructed region of interest over time. The steady state before injections is marked by t_1 ; t_2 and t_4 denote beginning and end of the first injection; t_5 and t_6 mark an intermediate point and the end of the recovery phase. (b) Images obtained at t_1 - t_6 representing the contrast cycle achieved by the first saline injection. Images were plotted on a linear scale from 0–1 with 0 and 1 representing the minimum and maximum pixel value of the first image in the sequence. Axes x and y correspond to the coordinate system displayed in fig. 6.9(b).

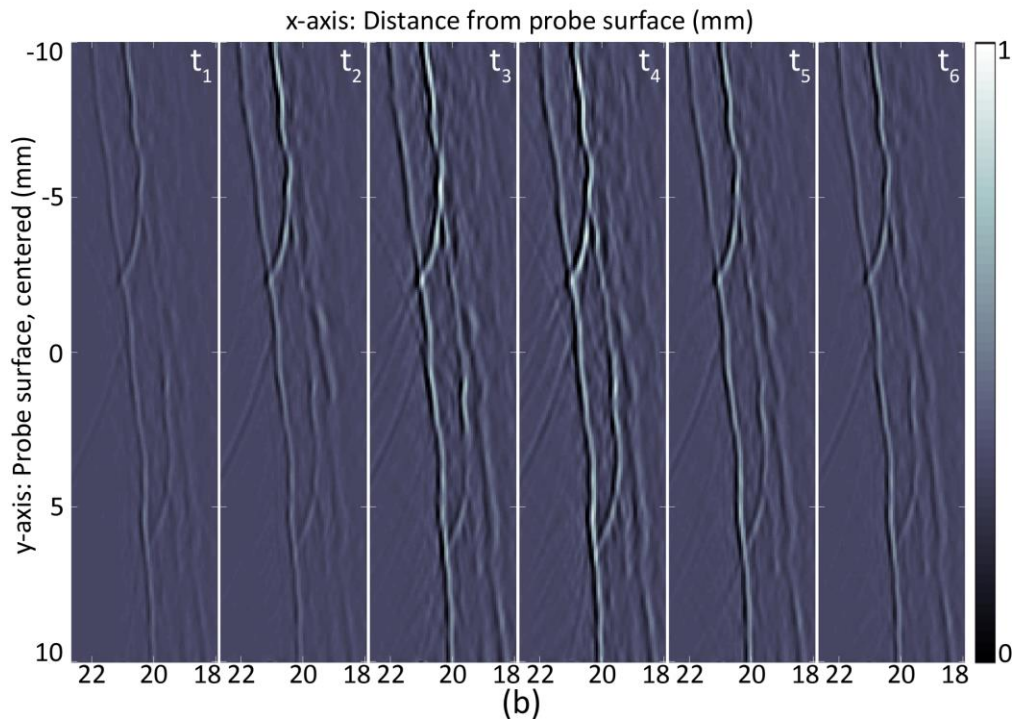
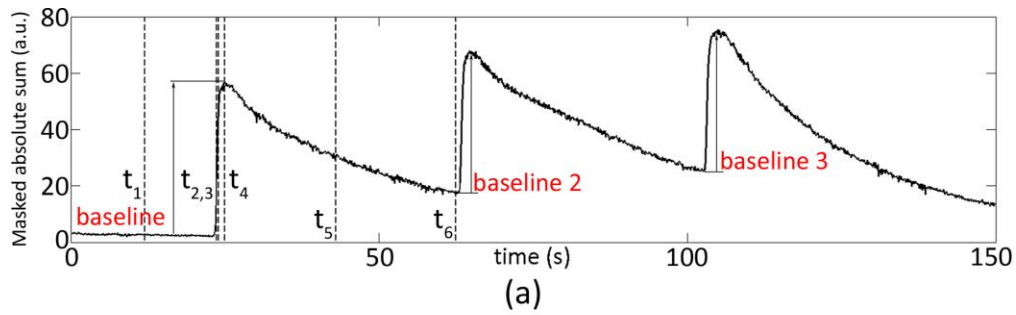


Figure 6-12 – ICG injection in a mouse tail in-vivo: 3 injections of 10 μ l ICG in intervals of 40s. (a) Masked absolute sum of reconstructed region of interest over time. The steady state before injections is marked by t_1 ; t_2 and t_4 denote beginning and end of the first injection; t_5 and t_6 mark an intermediate point and the end of the recovery phase. (b) Images obtained at t_1 - t_6 representing the contrast cycle achieved by the first ICG injection. Images were plotted on a linear scale from 0–1 with 0 and 1 representing the minimum and maximum pixel value over all image frames in the sequence. Axes x and y correspond to the coordinate system displayed in fig. 6.9(b).

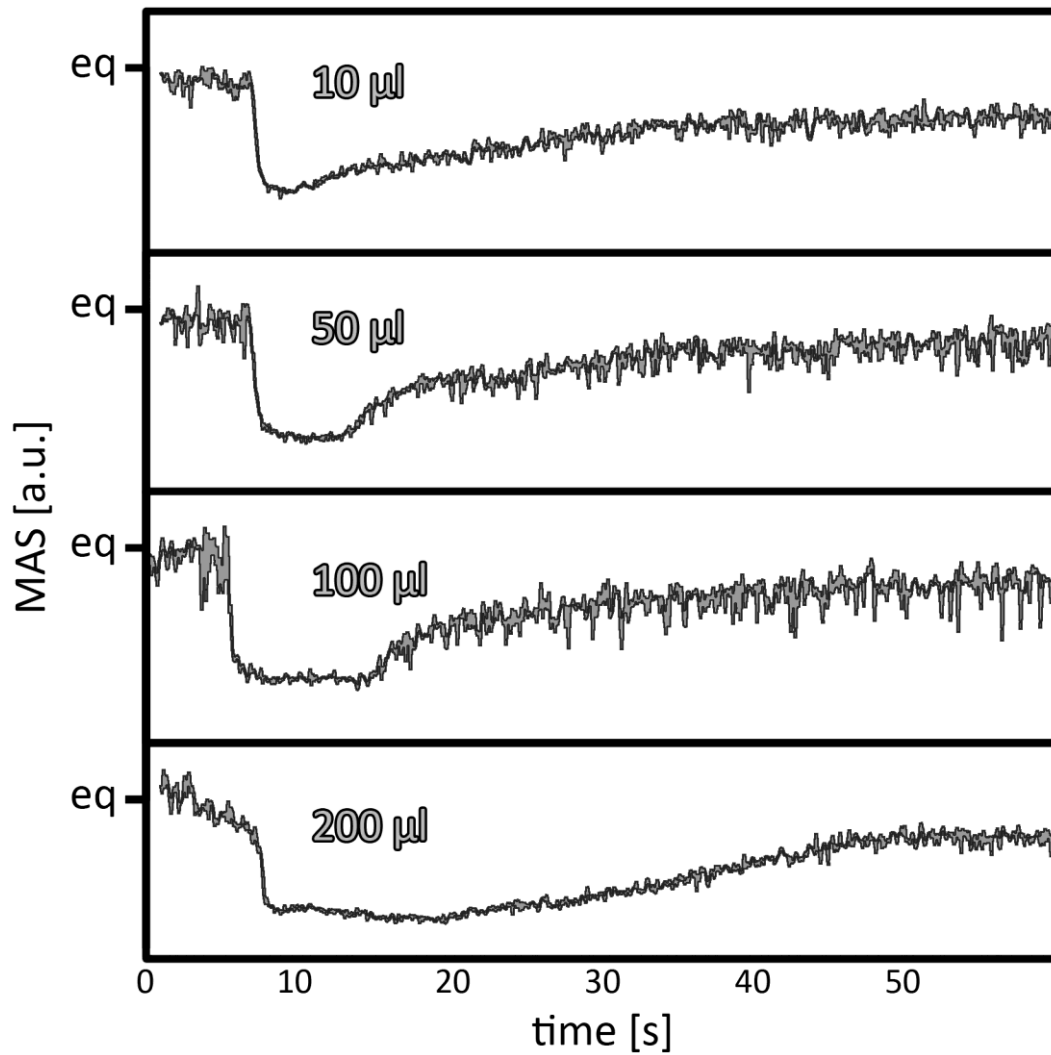


Figure 6-13 – Comparison showing the effect of increasing volume of saline injection on the MAS value. The equilibrium state (eq) is rapidly lowered by the clearing effect of saline on the blood concentration. Higher injection volumes do not seem to influence recovery time but instead just extend the time of minimum blood concentration.

Discussion and Conclusion

MSOT offers complementary features to ultrasonography in standard pulse-echo as well as Doppler mode. The method can be employed to identify functional and molecular aspects of vascular and other diseases. In this work we developed two approaches enabling clinical optoacoustic imaging during non-invasive point-of-care diagnostic assessment as well as during surgical intervention. We chose the linear ultrasound detection array for intra-operative imaging based on its strengths (weight, size) and developed a methodology to improve upon its weaknesses. Similarly, we translated a more specialized curved array from previous exclusive use in small animal research towards clinical handheld operation, finally detecting deep-seated vessels such as the carotids or the thyroid and enabling many more applications that are being currently investigated by other researchers.

Cardio-vascular

The development process started by investigating characteristics of both detection geometries using phantoms that approximated geometrical conditions associated with imaging of vascular features. The linear array employed has been a generic ultrasound sensor appropriate for a broad range of applications with respect to imaging target and depth of view. On the other hand curved arrays are more appropriate for imaging within a smaller volume and at rather fixed tissue depth. The results of that study allowed for a comparison of the relative performance achieved with linear vs. curved arrays and provided insights into the preferred geometry for optoacoustic imaging in different circumstances. The results from the linear array showed that it is possible to detect absorbers of 1-5 mm sizes seated deep inside tissue, when operating in trans- or epi-illumination mode. Single wavelength reconstructions provided sufficient contrast and image quality to capture insertion anatomy. In addition multi-spectral processing was deployed to locate a fluorescent dye, which in a single wavelength image could not be distinguished from other absorbers. The weaknesses of the linear array, i.e. a significant number of averages and weak elevational focus, could be addressed by choosing a linear probe, which is optimized with respect to sensitivity in the frequency range up to 4-5 MHz and elevational slice thickness at the depth of 15-30 mm. However

the major weakness remains image quality. Missing horizontal boundaries and reduced horizontal resolution is an inherent feature of any linear array geometry employed for optoacoustic imaging. A probe width of about 40 mm and depth requirement of 30 mm allows us to observe our region of interest from within an angle of about 68° . In echo ultrasound this poses no problem as imaging is based on detection of reflected echoes following a shaped and directed excitation pulse. In this way all interfaces, even round ones, can be imaged. Yet in optoacoustic imaging sources are generated inside the region of interest and radiate spherical waves in all directions. By limiting our view angle we therefore limit our image quality with respect to horizontal resolution.

The images derived from the curved array show markedly better imaging performance. Shape, position and absorption values of round insertions could be resolved with much higher quality. The curved array used in the comparative evaluation attained viewing angles of 172° , which offers more complete tomographic data sets that can reconstruct vessels with better fidelity. Due to the heightened sensitivity of the array around the center, compared to the linear probe, it was also possible to reduce the number of averages to manageable levels and showed potential for further reduction. Besides having its sensitivity peak at 5 MHz and thus closer to the frequency range of interest, this is due to two conceptual differences: the curved array elements are larger in size and are all looking at the same point, the center of the array. As a consequence the area close to the array center can be imaged with much higher sensitivity than is possible with a linear array assuming the same number of averages. Unfortunately we have to pay with a limitation in terms of usability. Size, weight and increased requirements on coupling and illumination mechanics render the curved array approach much more challenging.

Yet multi-spectral acquisition allowed identification of the absorption spectrum of the chosen fluorochrome. The resulting images of fluorochrome distribution confirmed the performance betterment when employing the curved array, over the linear array. The ability of MSOT to image fluorescent probes is clinically appealing although the detection sensitivity needs to be investigated on a per disease and agent case. The light attenuation conditions examined in phantoms were an approximation of in-vivo optical properties, which were modeled after average human tissue as given in table 5.1.3 in [42]. Conversely, the optical properties of ex-vivo porcine tissue are not an accurate representation of in-vivo conditions, since a significant amount of blood had been drained out from the sample imaged.

The extension of this comparative phantom study using the first curved array prototype available established the feasibility to detect the carotids and other deep-seated vessels in clinically relevant settings. To this end we imaged human vasculature in healthy volunteers. The results showcased imaging at depths of approximately 2 cm. At these depths no signal averaging was required, which implies not only that sufficient signals were collected but also that live imaging can be achieved at frame rates determined by laser repetition and image reconstruction speed. The frame rate of the initial prototype system was determined by the pulsing frequency of the laser at 10 Hz. In this case, live imaging required image reconstruction within 100 ms, which

was achieved through the parallelized delay and sum implementation detailed in chapter 4.1. Imaging deeper in tissues was complicated not by the lack of signals from different structures but mostly by acoustic reflections from either bone or air (trachea and radius bone), which caused image artifacts. Proper optoacoustic modeling of reflective interfaces could thus allow even deeper penetration. Although some reflections such as bone or air cavities in tissue require modelling to correct for, it is possible to reduce reflection artifacts originating from inside the array cavity. HOT-256 demonstrates how the larger array radius pushes such artifacts away from the ROI and thereby enables deeper tissue interrogation. On the other hand, light attenuation reduces SNR at higher depths while acoustic attenuation reduces the achievable spatial resolution. Nonetheless, MSOT can offer significantly higher resolution over optical imaging, even when considering optical imaging methods such as early-photon tomography [101], which reduce the effects of photon scattering. The degree of clinical utility of MSOT will require further investigation measuring disease pathologies in-vivo and identifying relevant biomarkers of cardiovascular disease. Judging from the rapid development of the field in small animal optoacoustic imaging, especially considering developments relating to new diagnostic and theranostic (i.e. those combining therapy and diagnostic assessment) contrast agents, we believe handheld point-of-care MSOT imaging will develop into a reliable high-sensitivity and low-cost routine diagnostic tool.

Thyroid

A similar conclusion can be drawn for thyroid imaging. Thyroid nodules have a high and rising incidence in the general population [96, 97] and imaging is employed as part of the clinical disease management. Neck ultrasonography is routinely applied for nodule detection. A suspicious ultrasound result may be further examined by radioactive 2-deoxy-2-[18F]fluoro-d-glucose positron emission tomography (FDG-PET) or followed up by fine needle aspiration (FNA). Optical imaging techniques, such as optical coherence tomography or elastic light-scattering spectroscopy, have been suggested for differentiating benign from malignant thyroid nodules [102, 103]. However, limitations in terms of depth imposed by the strong optical scattering in tissue prevent their clinical non-invasive application. Herein, we also investigated the possibility of applying optoacoustic imaging for assessing features of the human thyroid. To this end, we examined the anterior-side of the neck of healthy human volunteers in the thyroid area. In volunteers we were able to detect the outline of the thyroid and also identify vascular features at tissue depths up to 20 mm below the skin. For subsequent validation we employed echo-ultrasound and Doppler ultrasound imaging. Large and medium sized vessels, detected using Doppler ultrasound, were captured by the optoacoustic system at better resolution. Additionally, the optoacoustic images revealed finer vascular networks undetected by Doppler ultrasound and provided a more complete picture of thyroid vascularization. Reliable vascular information (over- or under-expression) can yield important clues in the diagnosis of thyroid disease [104], in particular when combined with other diagnostic modalities such as ultrasound. When deciding malignancy of thyroid nodules a high sensitivity to vascularization is especially desirable [105]. Furthermore, subsequent fine needle

aspiration can also be performed using optoacoustic needle guidance [38]. On the other hand, multi-spectral acquisition can further increase accuracy by for example including tissue oxygenation as a diagnostic parameter. A recent study demonstrated the capability of MSOT to differentiate between benign and malignant nodules in diseased thyroid samples after thyroidectomy [106].

To allow efficient navigation during screening and for needle guidance a large field of view is necessary. Here we have chosen a view comparable to that of ultrasound even though the employed detection array enabled high resolution imaging only within a much smaller area. Thus, further investigations will focus on evaluating the extended array radius of HOF-256 when imaging the thyroid. From preliminary scans we already observed improved image quality and reduced imaging artifacts throughout the larger field of view. However, a more focused study is necessary, also including patients showing thyroid pathologies, to objectively assess improvements. In terms of fully exploiting the potential of MSOT, we expect the application of molecularly targeted contrast agents [107] to allow detection of malignant lesions based on molecular features. Ultimately, successfully applying molecular imaging techniques in the diagnosis and treatment of thyroid disease will require further research towards quantitative evaluation.

Tissue viability

Compared to currently available methods of intraoperative perfusion assessment, such as Doppler ultrasonography (DUS) or laser Doppler flowmetry (LDF), the methodology developed herein is not subject to movement artifacts or hindered by tissue depth of up to several millimeters. In the NIR window tissue depths of up to 10 mm are routinely reached and depths up to few cm are within reach. The proposed method's contrast cycle allows direct measurement of accessible perfusion pathways as well as quantitative assessment on blood reperfusion with resolution of up to 150 μm perpendicular to the array surface. Therefore, we investigated the potential deployment of optoacoustic technology for intraoperative tissue viability assessment by imaging blood perfusion. For this we developed a novel technique based on injection of a small volume of saline and demonstrated the applicability of the method ex-vivo on porcine colon segments as well as in-vivo on mouse tails. The method offers direct, high contrast, high resolution imaging of perfusion within the vasculature without suffering from tissue depth or motion artifacts. Compared to positive contrast agents the use of intrinsic contrast mechanisms (saline, blood) renders the method easily repeatable and reproducible in terms of results. Beyond perfusion, the deployment of optoacoustic imaging offers the possibility to add real-time multispectral information (e.g. oxygenation) of the same area being monitored for perfusion, thereby combining two major indicators of tissue viability. Consequently, the method proposed herein has the potential to afford surgeons a more reliable and quantitative measure of tissue viability than is currently available.

The injection of saline offers advantages over positive contrast agents such as ICG – even without considering toxicity. An inverted contrast cycle allows faster and more precise visual tracking of perfusion pathways, because the already cleared path blends into the background while ICG propagation has to be evaluated against the

blood signal. Furthermore live visual inspection is facilitated by the possibility to calibrate post-processing parameters before the first injection as this state yields the strongest signal, whereas ICG increases the signal during injection and thus such parameters would have to be approximated a priori. Similarly, in case of movement of detector or measurement position, the speed of calibrating a negative contrast cycle enables adaptive parameters and thereby allows reproducible comparisons of subsequent injections. This is highly relevant during intervention when the surgeon might need to evaluate multiple tissue parts or detector positions to select the ideal imaging plane. Repeatability within a short amount of time has also been demonstrated with ICG. However, comparing different positions may be more challenging due to leakage into surrounding tissue and limits on how much contrast agent can be administered. Saline, on the other hand, does not influence absorption of surrounding tissue upon leakage and may be administered in much higher quantities, e.g. arterially 300-500 ml per day. Considering that in the human lower colon clearance of an arterial branch can be achieved already with 3-4 ml, application of the method during surgery appears feasible. On the other hand, when local arterial injection is not desirable or possible, arterial clamping could be applied. Replacing injection with clamping, such that the blood content of the vasculature is reduced sufficiently, could be expected to yield a similar contrast cycle.

Technical aspects

The major design decision adopted in this work was to utilize focused detection arrays. Indeed operational characteristics made this unavoidable. The intended use on the human body already limited our freedom of design to the immediate half-volume close to the body, with the skin or other tissue interface representing the demarcation line. On the other hand, parameters relating to clinical utility such as the need to interrogate a large tissue section at the pulse repetition rate of the laser, while attaining a high degree of flexibility, resolution and image quality, rendered the use of focused arrays highly attractive. Although theoretical considerations mandate the detection of optoacoustic waves on a spherical surface enclosing all sources – optoacoustic imaging is inherently a three-dimensional problem – we found 3D arrays lacking in many desirable properties. Chief amongst problematic aspects is the number and size of detectors required to achieve the same spatial resolution within the same region of interest as 2D curved detection affords. Start with the number of detectors needed: a volumetric image of equal voxel size in all three dimensions increases the reconstruction problem from n^2 (2D image) to n^3 (3D image). This would ideally require p^2 detection elements, if we assume p detection elements for a focused 2D array. Such elements would cover very little area per element, thus offering very little sensitivity. On the other hand increasing their size (and sensitivity) would decrease their effective field of view and their total number due to space restrictions on the spherical surface. In turn, the spherical surface itself limits access to many areas of the human body. Moreover, it also limits flexibility during a manual scan, due to its larger contact area and rigid boundary.

Array density

Another design aspect relevant for the refinement of the initial 64-element curved array probe was how many elements are necessary to achieve the imaging goals set. To answer this question we studied MSOT performance achieved in whole-body small animal imaging as a function of increasing number of detectors. By choosing for our investigation arrays of identical radius but with 64, 128 and 256 elements, we could simultaneously obtain a better understanding of element density (single element pitch) and its impact on image quality.

For the three arrays we studied imaging performance numerically and experimentally on phantoms and animals in-vivo. The results highlighted improvements in resolution, region of interest, sensitivity and imaging artifacts with increasing angular coverage and detector density. An important finding was that the use of 256 elements yielded strong improvements over 128 elements, to justify deployment of high density arrays. Qualitatively, the in-vivo mouse images obtained using 256 elements showcased better resolution and image fidelity over those obtained using 64 or 128 elements, allowing the visualization of elaborate vascular patterns in the brain, spine, kidney and liver. In a controlled phantom measurement, we experimentally quantified the improvements. At the critical radius of 10 mm from the image center transversal resolution increased by a factor of 2.25 for 256 elements and 1.5 for 128 elements when compared to results from the 64 element system. Similarly, sensitivity at this radius improved for 128 elements by ~50% and ~150% for 256.

Besides higher transversal resolution, an interesting feature identified is that the field of view can be improved without sacrificing sensitivity when employing more transducers. Given the same azimuthal coverage, the 256 element array achieved a sensitivity field that was broader than the 128. In [108] an array of even higher density was utilized and demonstrated cross-sectional full-body imaging using ring illumination after 10 times averaging, whereby an image represented a time interval of 16s. In contrast, our data frames were obtained from a single laser pulse, i.e. 50 μ s acquisition time per image. This enables an achievable frame rate that depends on the repetition rate of the laser only (10-100 Hz in our setups). Similarly, results from MSOT256 show that to obtain high quality images full view is not mandatory but can be reduced when choosing appropriate system radius and element size. However, in the presence of strong acoustic heterogeneities, such as the lungs or gas filled gastro-intestinal tract, the missing angular coverage results in stronger artifacts than would be the case at full view. In sum, the most important parameter in terms of resolution and field of view is element pitch – the smaller the better. Beyond that array density improves the signal to noise ratio as it acts as a form of averaging. Of course there are technological limits to this line of argumentation: when SNR of individual detection elements becomes too low for averaging to recover, the battle is lost. Similarly, the array should cover sufficient views to include the region of interest in the visibility region; otherwise the battle is equally lost before being fought. Finally, the displacement of elevation focus of individual elements ($R_{se}=37\text{mm}$) versus in-plane focus of the array ($R_A=40\text{mm}$) increases the sensitivity field. Such asynchronous foci should be chosen with care

however. When overlap suffers too much we can expect reduced resolution and an increase in out-of-plane artifacts.

For many biological and medical applications the use of MSOT64 can be regarded sufficient as it provides still a marked improvement over two-dimensional optical imaging systems or tomographic implementations which attain 10 times worse resolution. However with the documented higher transversal resolution and image quality established by the MSOT128 or the MSOT256, these systems offer superior performance and should be preferred for achieving an all-around better imaging quality. Hence, we chose to model the detection array of HOT-256 after the MSOT256 array, due to the largest field of view (FWHM sensitivity field) and resolution of the three systems studied.

Image reconstruction

In the face of increased region of interest and an equally increased number of detection elements, image reconstruction became more challenging as well. A mandatory improvement for live imaging was detailed in chapter 4.1. The simplicity of the algorithm combined with a straight forward C-language implementation, rendered refinement in OpenCL and subsequent execution on GPUs a forgone conclusion. Superior speed and scalability have since established delay and sum live imaging the de-facto standard in online (or on-site) image reconstruction. Yet to fully exploit the observed data, model-based algorithms are still useful. They improve accuracy, limit artifacts and allow corrections of system parameters by taking account of calibration measurements. Such improvements are not to be underestimated as they immediately influence un-mixing performance. Yet reconstruction time and hardware requirements become equally important aspects of reconstruction for model-based algorithms as they have been by default for online imaging. A simple dataset containing 15,000 frames could take weeks to reconstruct when choosing a slow but accurate algorithm. Similarly, when memory requirements become too demanding for ordinary PC hardware, execution may require high-memory workstations or similar high-end machines (or clusters). Such powerful hardware is usually in scant supply and so forms a bottleneck for the many users each with likely multiple datasets to accurately reconstruct.

Therefore, we introduced a memory efficient method for the accurate reconstruction of optoacoustic data using numerical forward models of arbitrary complexity. We termed the new algorithm Transformation based Optoacoustic Modeling or TOM. Our solution is based on the principle of separation of wave propagation physics and detection geometry. By treating the two problems separately we were able to modify an iterative inversion algorithm (LSQR) to allow image reconstruction with only the model-matrix of a single detector position. Thus, we significantly reduced the required memory. We demonstrated comparable 2D imaging performance for full view datasets and achieved higher 2D image quality for limited view data.

Reduction in memory requirements comes at the price of significantly increased computation time. Indeed, tipping the balance between memory consumption and CPU

time in favor of memory could have been achieved even without TOM. A practical solution would attempt to implement steps 1 and 4 of table 4 as a for-loop iterating over all detector positions, each iteration computing a different \mathbf{M}_i and executing the appropriate step. Assuming some practical numbers for LSQR iterations and detector positions, e.g. 30 iterations and 256 positions, this would require computing a single-projection forward matrix $30 \times 256 \times 2$ times and would produce an image every few hours depending on resolution. Implementing TOM as a matrix-matrix multiplication with \mathbf{M}_0 could in this instance reduce execution time by a factor of 2 or 3, yet still potentially require hours per image. By avoiding manipulation of \mathbf{M}_0 and instead applying image transformation to the intermediate images used during the iterative inversion we limited the necessary computations to algorithms well established in computer graphics, namely coordinate transformation and interpolation. As a proof of principle we deployed optimized and CPU parallelized implementations and were thereby able to achieve reconstruction times close to those common when using the full matrix-model. On the available hardware we could not achieve faster reconstruction even when using 12 worker threads for execution of TOM. Three major reasons for this can be stated. First, allocation of CPU time to the worker threads is handled by the operating system, which also has to allow time for many other services. Second, the TOM routine is implemented as a DLL plug-in for Matlab (mexw64) and in our evaluation, depicted in fig. 4.10, is called about 60000 times. This incurs a growing overhead that counteracts improvements gained by parallel computation. Lastly, the demonstrated implementation may not be optimal. While we strived for optimal parallelization, some (weak) race conditions were unavoidable, e.g. reading of the input image during bi-cubic interpolation. A better implementation of parallelizable tasks and a more optimized compiler would certainly help.

Nonetheless, while using the same hardware, we cannot hope to improve performance beyond the original LSQR routine using the full forward matrix, even if the computational overhead induced by TOM was zero. However, we have reduced memory requirements to a minimum. This in turn enables us to change the execution hardware from multi-core CPUs with working memory, nowadays typically DDR3 with a maximum bandwidth of up to 51.2 GB/s, to graphics cards (GPUs) with thousands of stream processors and high-speed GDDR5 memory with up to 288 GB/s of bandwidth. Additionally, the computational overhead introduced by our method fully consists of algorithms that have been heavily optimized for parallel execution on GPUs. Another interesting aspect of the method proposed concerns its regularizing effect for limited view detection geometries. An essential aspect of image transformations is the interpolation of the input image in terms of the output image coordinates. This implies the use of sub-resolution information that is provided by the smooth surface interpolated from the set of discrete image pixels and thus effects the suppression of limited view artifacts. On the other hand, care needs to be taken when setting the image resolution to be reconstructed, i.e. the number of pixels per area unit. If this is chosen to low compared to the information contained in the acoustic data, interpolation errors become too large and may destabilize the inversion or introduce aliasing artifacts. In sum, the method presented herein has the potential to unlock the use of

massive parallelization and GPUs for accurate model-based optoacoustic image reconstruction. The next steps include the careful implementation of the proposed algorithm for 2D imaging in a suitable GPU programming language such as OpenCL; the extension of the algorithm to 3D image reconstruction models, both as a proof of concept and in OpenCL; and modifications with respect to the number and order of transformations necessary to accommodate the use of detector shape correction [86], known as spatial impulse response. Finally, modeling of heterogeneous speed of sound distribution, available in some forward models, should be investigated with respect to the potential for implementation using image operations such as warping. These open challenges notwithstanding, the future of model-based optoacoustic imaging will be dominated by GPU implementations, either on single card machines or, where necessary due to data size, in a multi-card environment.

Appendix

8.1 List of figures

Figure 2-1 – Essential aspects of optoacoustic imaging	16
Figure 2-2 – Scattering at the molecular level. Photons ($h\nu$) undergoing elastic scattering with molecules (M), up to three scattering events are shown.	17
Figure 2-3 – (a) Setup employed to measure the absorption coefficient of chromophores. (b) Simplified analogy employed in the definition of the scattering coefficient.....	18
Figure 2-4 – Effect of increasing density of scattering events (left to right, red arrow indicates source of illumination): directional beam propagating in water with increasing amounts of lipid added.	19
Figure 2-5 – Molar extinction coefficient of major intrinsic tissue chromophores: oxygenated (Hb) and de-oxygenated hemoglobin (HbO_2) data compiled by Scott Prahl (Oregon Medical Laser Center / OMLC), water (inferred from [45]), lipid (from [46] by approximating molecular composition, weight and density of purified pig oil) and eumelanin (from OMLC who deduced data from [47]).	21
Figure 2-6 – Measured signal amplitude versus frequency of a longitudinal acoustic wave after travel through 5mm, 10mm, 20mm and 30mm of (top) distilled water and (bottom) average tissue.	23
Figure 2-7 – Ideal optoacoustic signals from microspheres of different diameters: 150 μ m diameter in blue; 450 μ m diameter in red. The time signals are depicted in (a) and the corresponding absolute frequency domain values in (b). The larger sphere attains a frequency maximum at a lower frequency compared to the smaller sphere. Both spheres have repetitions of decreasing amplitude at higher frequencies. (a.u. = arbitrary units)	26
Figure 2-8 – (a) Exaggerated measurement setup used to acquire the optoacoustic signal from a microsphere, which in reality was small enough to assume homogenous illumination of the full volume of the sphere. (b) The corresponding signal (in arbitrary units, a.u.) measured after de-convolution with the electrical impulse response and placed such as to avoid distortions by a geometrical impulse response of the detector; diameter of sphere approx. 150 μ m.	27

- Figure 2-9 – Directivity of optoacoustic (OA) sources and detectors. Row (a) depicts two ideal detectors (D1, D2) measuring optoacoustic signals (plotted on the right) from an ideal spherical OA source at distance r . Row (b) shows the same detectors measuring signals (plotted right) from multiple ideal sources arranged in a line with distance r to detector 1 (D1). For D2 signals start with the first source viewed from D2. The red dashed lines in (a) and (b) highlight traces of integration as defined in eq. (20), i.e. $v_s t$. In row (c) a line detector (D_{L1}) has the same length as the maximum distance between sources in (b) and measures signal from a single source, as in (a). The red dashed line represents the wave front. Plots show time on the x-axis and pressure on the y-axis, both in arbitrary units.28
- Figure 2-10 – Main stages of laser light generation and transmission. (a) The pump laser beam (green) is generated by optical excitation of a gain medium (crystal) and subsequent resonant amplification. (b) The monochromatic pump beam is tuned to the desired wavelength by unidirectional oscillation through a non-linear crystal. The pump energy is divided into the desired signal beam, the idler and the remainder of the pump. (c) The signal beam is coupled into a fiber bundle for safe and flexible transmission. Each fiber consists of two materials with different refractive indices ($n_1 > n_2$) resulting in total internal reflection. Typical transmission efficiencies of fiber bundles are between 60-70%.29
- Figure 2-11 – Cross-section of individual fiber illustrates coupling in air (n_0), guided transmission within the core of the fiber and emission at the distal end in water (n_0').31
- Figure 2-12 – Ultrasound detection depicting (a) a single element ultrasound transducer layout, (b) the detection system including cabling and data acquisition electronics and (c) the electrical response of the system upon excitation by an impulse. (d) Frequency domain plot of (c).34
- Figure 2-13 – Focused acoustic transducers with sections of respective sensitivity field around the origin: (a) spherically focused, (b) cylindrically focused. Both elements are comparable in their characteristic size, i.e. radius $R=60\text{mm}$, $\vartheta=22^\circ$ ($b=0.7\text{mm}$). Sections in color indicate maximum and minimum receivable amplitude of signals up to 7.5MHz from points within each depicted plane.....36
- Figure 2-14 – Definitions of parameters used to characterize focused ultrasound arrays. (a) Definitions describing individual elements. (b) Structure of piezo-composite material. (c) Definitions describing array geometry.....37
- Figure 2-15 – Focused detection arrays and their sensitivity fields depicted as sections along x-y, x-z and y-z (centered on the origin). Row (a) depicts a full-tomographic view, i.e. the array fully encloses the ROI. Row (b) depicts only half-tomographic detection. Row (c) depicts the view obtainable from a standard linear ultrasound array. All images are on the same colorbar.....39
- Figure 2-16 – Numerical analysis of the optoacoustic signal from an ideal spherical pressure source: (a) ideal conditions, (b) numerical derivative of (a), (c) same as (a) but filtered by the impulse response of a real detector, (d) numerical derivative of (c).....42
- Figure 2-17 – Numerical study comparing backprojection and model-based reconstruction algorithms. (a) Simulated setup where each of 256 detectors measures the signal shown in 2.16(c), i.e. the source is centered within the ring of detectors. (b) Backprojection reconstruction showing strong positive and negative values at the boundary. (c) Model-based reconstruction achieving a smooth boundary.....43
- Figure 2-18 – Multi-spectral unmixing problem illustrated: top box represents the accessible data consisting of 3 images acquired at 600, 700 and 800 nm wavelength. The observed “scene” is composed of a rectangular, a circular and a triangular region. Three chromophores are present

- and distributed within the regions as shown with concentrations c_1 - c_4 . The absorption spectra of each chromophore are given at the bottom.45
- Figure 3-1 – (a) Graphical user interface software implemented for testing and debugging of the custom multi-channel DAQ. (b) Selection of first signals measured by the DAQ prototype in the course of testing and debugging. Simulated optoacoustic signal measured by a DAQ using (c) high impedance ($1M\Omega$, not matched to cabling) and (d) low impedance (50Ω , matched to cabling).49
- Figure 3-2 – Flow charts showing multi-threaded execution of data acquisition (retrieval and error handling) implemented as a C# assembly (part I) and Matlab based data processing (part II).50
- Figure 3-3 – Initialization routine and inter-process data flow is shown in the top half. The bottom half provides a template for acquisition using multiple DAQs in parallel by means of C# multi-threading. Care has to be taken in this scenario to properly synchronize threads and present a single data interface to Matlab.52
- Figure 3-4 – Studies relating to DAQ development. (a) Comparative measurements between the National Instruments (NI) DAQ and the custom developed Falkenstein Mikrosysteme (FM) DAQ. (b) Study of electrical impulse response: 64 simulated OA signals were convolved by 64 impulse responses each slightly phase shifted and frequency distorted (top left), scaled (bottom left) and added on noise measurements taken from the FM-DAQ. Reconstructions on the right (1 shows reconstruction target) were performed from uncorrected signals (2) and signals de-convolved by two impulse response measurements (3 and 4) as described in [77]. (c) Reconstructions from identical data showing improved image quality after impulse response correction (de-convolution).53
- Figure 3-5 – (a)-(c) Phantom types: (a) Type A configuration. (b) Type B configuration. (c) Porcine muscle phantom. (d) Spectra of employed absorbers. Schematic showing construction of (e) linear array and (f) curved arrays. (g) Measurement setup chosen to attain the ideal illumination/detection pattern.55
- Figure 3-6 – Optoacoustic signal of absorber(s) within inner tube(s) from (a) phantom A1, (b) phantom B1. Arrows indicate object boundaries.56
- Figure 3-7 – Linear array reconstructions. The first row shows single wavelength images of (a) phantom A1, (b) phantom A2, (c) phantom A3. The second row shows the distribution of ink from (d) phantom B1, (e) phantom B2, (f) phantom B3. Grayscale represents a single wavelength image, whereby the color overlay shows the resolved ink concentration. The third row shows the distribution of AF750 from (g) phantom B1, (h) phantom B2, (i) phantom B3. Grayscale images are the same as in the second row; however the color overlay shows the AF750 concentration.58
- Figure 3-8 – Curved array reconstructions. The first row shows single wavelength images of (a) phantom A1, (b) phantom A2, (c) phantom A3. The second row shows the distribution of ink from (d) phantom B1, (e) phantom B2, (f) phantom B3. Grayscale represents a single wavelength image, whereby the color overlay shows the resolved ink concentration. The third row shows the distribution of AF750 from (g) phantom B1, (h) phantom B2, (i) phantom B3. Grayscale images are the same as in the second row; however the color overlay shows the AF750 concentration.60
- Figure 3-9 – Phases of development: (a) Top row depicts the developed concept (left) and conclusions for illumination gained from phantom studies. (b) The middle row shows a “free” concept implementation (left) without sealing the array cavity, the intermediate stage

- attempting handheld operation with sealed cavity (middle) and an advanced sealing design (right). (c) The bottom row illustrates the devised “double O-ring” sealing mechanism (left), the final operational prototype (middle) and two experimental applications (right). 63
- Figure 3-10 – Design and implementation of the deployment prototype. (a) 3D-CAD model of the new water coupling concept: array and counter-plates are depicted on the left; the first O-ring is depicted with a cross-section in the middle; a second O-ring is depicted on the right. (b) Novel illumination concept showing light exiting the rectangular fiber output at a 32° angle. (c) Technical drawing of the new detection array with integrated coupling mechanics (left) and the fully assembled implementation (right) coupled with water and featuring a movable carriage (back and forth) to optimize illumination according to the shape of the flexible contact surface (foil). 65
- Figure 3-11 – (a) Schematic illustration of tissue viability assessment in the lower colon. (b) Laboratory setups employed for studying perfusion dynamics. FB: fiber bundle; LA: linear array; ROI: red frame. (c) Experiment simulating the target application: a bolus of highly absorbing ink (external excitation) is injected into a stream of background perfusion liquid (blood or water). The configuration is similar to the one depicted in the rightmost image of (b) but extended by an optical diffuser. 67
- Figure 4-1 – Delay and Sum image reconstruction algorithm: for each image pixel (px_i) and each detection element k (a) the time of propagation (also referred to as delay) is computed and converted by the average speed of sound to an index k_i into signal s_k . (b) The identified value is then added to the appropriate position in the image buffer. All pixels are the sum of multiple input data values. 72
- Figure 4-2 – The full forward model established by stacking matrices and data vectors of all measurement positions. 75
- Figure 4-3 – The tomographic imaging problem in 2D requires detection along the dotted circle, which encloses the solid square that represents the image to be reconstructed. (a) The forward problem modeled by computing a second matrix $M1$ for a new detector position rotated by α . (b) Alternative solution based on $M0$ and rotating the image grid by $-\alpha$. (c) Light blue areas indicate pixels missing in $M0$. (d) $M0$ is extended to include all pixels enclosed by the dashed circle. 76
- Figure 4-4 – (a) Initial pressure distribution used for forward simulation of acoustic data and represents the reconstruction target. (b) Handheld optoacoustic imaging probe employed to obtain data in-vivo. (c) Simulated acoustic data for channel 200 (of 360) at four noise levels: no noise, minimum noise (NL=1), intermediate noise (NL=5) and maximum noise (NL=10). 80
- Figure 4-5 – Reconstruction of the noise free simulated dataset obtained after 80 LSQR iterations by (a) the standard IMMI algorithm and (b) TOM. Both images were normalized to values between 0 and 1 and are shown on the same colorbar. (c) Difference image between (a-b) after minimum subtraction to fit the same colorbar as in (a,b); to improve contrast original 0 values have been rendered bright green. (d) Plot showing the sum of squared differences (SSD) over number of LSQR iterations for IMMI and TOM. For reference values for backprojection (BP) and delay and sum (DS) algorithms are also given. 81
- Figure 4-6 – Additional detection geometries considered in simulation. (a) Spiral tomography covering 360 unique angles over a span of 1080° with radii ranging from 0.03 m to 0.05 m. (b) IMMI and (c) TOM reconstruction of spiral geometry. (d) Rotate-translate tomography covering 18 angles over 360° , each featuring 20 linearly translated detector positions. (e) IMMI

- and (f) TOM reconstruction of rotate-translate geometry. Each reconstruction includes the SSD relative to the reconstruction target in the bottom right corner.82
- Figure 4-7 – (a) Reconstructions for IMMI (top row) and TOM (bottom row) at three noise levels (NL=1,5,10). (b) Sum of squared differences (SSD) for TOM (red) and IMMI (blue) at increasing noise level.83
- Figure 4-8 – Reconstructions of a dataset obtained in-vivo from the lower arm of a human volunteer. The first row shows a frame (40x40mm²) close to the wrist after 25 LSQR iterations for (a) IMMI, (b) TOM and (c) the difference image (a)-(b). The second row shows another frame of the same size a few mm towards the elbow reconstructed by (d) IMMI, (e) TOM and (f) the difference image (d)-(e). Image values in (a) and (d) were restricted to extreme values found in (b) and (e) respectively. Subsequently, images (a,b) and (d,e) were normalized to values between 0 and 1. Furthermore, all images are shown on the same colorbar. ra: radial artery; v: vein.84
- Figure 4-9 – Results from IMMI and TOM after 1, 3, 7, 11, 15 and 25 iterations for frame 1, depicted in Fig. 6(a) and (b). For each iterative step six images are shown: a region dominated by artifacts in the top row and a region containing relevant features in the bottom row. The column order is IMMI, TOM and the difference image. At each iteration full images obtained by IMMI and TOM were processed in the same manner as described in Fig. 6. The colorbar is valid for all images at one iterative step.85
- Figure 4-10 – Execution times over number of CPU threads for parallelized TOM and IMMI with pre-computed matrix. (a) Intel Core i5-2400 (max. 4 threads). (b) Intel Xeon X5650 (max. 12 threads).86
- Figure 4-11 – The first row shows the transducer geometries for (a) MSOT64 and (b) MSOT128/MSOT256. The second row illustrates the two system setups including laser, data acquisition (DAQ) and sample holder with transparent membrane. (c) MSOT64 achieves even in-plane (z=0) illumination by using a ten arm fiber bundle arranged from one side at an angle of 33° relative to the circumference of the sample. (d) MSOT128/256 enables similar illumination by arranging a second ten arm fiber bundle symmetrically from both sides at an angle of 24°. Both fiber bundles cover an angle of 270° in the xy-plane.88
- Figure 4-12 – Numerical estimation of the 2D sensitivity field of detection (0.5-7.5 MHz) within the imaging plane of the array. Black ellipses mark the full-width half-maximum (FWHM) range. The first and last element of each array is noted on the images by a short solid line marked with an arrow and element number. (a) 64 element array covering 172°; diameter at FWHM: 15.5 mm. (b) 128 element array covering 270°; vertical diameter at FWHM: 17.1 mm; horizontal diameter at FWHM: 21.0 mm. (c) 256 element array covering 270°; diameter at FWHM: 32.6 mm. (d) “Visibility region” (gray) for MSOT64 and (e) MSOT128/256 that allows stable reconstruction of feature boundaries (ROI = region of interest).90
- Figure 4-13 – (a) Numerical setup covering a rectangular region of 30x30mm² – 900 microspheres of 187.5µm diameter equally spaced in 1mm steps. (b) Top view photograph of the microsphere-containing phantom showing the sphere distribution and the fluence distribution. The disk diameter was 30 mm; the PE spheres attained diameters of 180-212µm. (c) Schematic of the experimental phantom assembly.91
- Figure 4-14 – Top row shows simulated reconstruction results from (a) MSOT64, (b) MSOT128 and (c) MSOT256. For each image negative values were removed and the remainder normalized to 1. Details at the periphery and the center, framed (4x4mm²) and color-coded by array, were magnified for display at the bottom left and right respectively. Graphs below depict

- diagonal cross-sections (top-left to bottom-right) of the magnified detail images for (d) the periphery and (e) the center.93
- Figure 4-15 – Top row shows experimental phantom reconstruction results from (a) MSOT64, (b) MSOT128 and (c) MSOT256. For each image negative values were set to zero and the remainder normalized to 1. Furthermore, images were segmented based on their local maxima. Details at the periphery and the center, framed (4x4mm²) and color-coded by array, were magnified for display at the bottom left and right respectively. Graphs below depict diagonal cross-sections of individual microspheres (circled blue, red and green) for (d) the periphery (numbered 1-3) and (e) the center (numbered 4-6). Individual cross-sections were artificially spaced to allow sufficient distance for comparison.94
- Figure 4-16 – Single-shot in-vivo mouse images at 850 nm wavelength: the first column shows results obtained from MSOT64; second column MSOT128; third column MSOT256. The last column shows mouse cryoslices at equivalent positions. The mouse head is shown in (a-d): 1. sagittal sinus; 2. temporal artery; 3. extra-cranial blood vessel; 4. deep cerebral vessel. The liver region is shown in (e-h): 5. spinal cord; 6. aorta; 7. vena cava; 8. vena porta; 9. liver; 10. stomach. The kidney region is shown in (i-l): 11. kidney; 12. spleen.....96
- Figure 4-17 – Mouse cross-section at the liver level. (a) MSOT256 result in-vivo at 900 nm wavelength. (b) Equivalent cryoslice obtained from a similar mouse. Corresponding features have been encircled and numbered: 1. Spinal cord; 2-4. Vascular structures within the liver; 5. Stomach.97
- Figure 4-18 – Profiles of spinal cord at liver level. (a) Magnifications for MSOT64, MSOT128 and MSOT256. Cuts in radial (marked r) and transversal (marked t) direction are line-coded by array. (b) Profile of radial trace from top to bottom. (c) Profile of transversal trace from left to right. Prominent features: top and sides of in-plane vascular structure, blood vessel perpendicular to the imaging plane.98
- Figure 5-1 – Cardiovascular atherosclerosis 100
- Figure 5-2 – Stages of atherosclerosis..... 101
- Figure 5-3 – Thyroid anatomy and location relative to the respiratory and cardio-vascular system. 103
- Figure 6-1 – Cross-sections showing lower arm vasculature of a male volunteer 7 cm from the elbow – axes are given in mm. (a) Optoacoustic image using the initial curved array prototype. (b) Directional ultrasonography image, overlaid on standard ultrasonography image in gray, indicating positive flow in yellow/red; negative flow in green/blue. Annotations: 1.Skin surface; 2.Intermediate antebrachial vein; 3.Radial artery. 106
- Figure 6-2 – Cross-sections showing cardio-vascular features of a female volunteer at the lower neck level – axes are given in mm. (a) Optoacoustic image from the initial curved array prototype. (b) Directional ultrasonography image, overlaid on standard ultrasonography image in gray, indicating positive flow in yellow/red; negative flow in green/blue. Annotations: 1.Skin surface; 2.Common carotid; 3.Internal jugular vein; 4.External jugular vein. (c) Screen capture of video sequence showing carotid enlargement due to heartbeat. 107
- Figure 6-3 – (a) Optoacoustic and (b) ultrasound cross-sections of the left thyroid lobe of the first volunteer. The optoacoustic image, leveled and normalized from 0 to 1, shows with high sensitivity vascular features of skin, muscles (1,2) and within the thyroid lobe (3). The corresponding ultrasound image in grayscale also depicts Directional Power Doppler signals superimposed in color (red/blue colormaps indicating opposite flow directions). C: Carotid, T: Thyroid, Tr: Trachea, s: sternocleidomastoid muscle, m: infrahyoid muscle; axes in mm... 108

- Figure 6-4 – Cross-section of right thyroid lobe of the second volunteer. (a) To limit the influence of strong absorbers (large vein marked 3) on available contrast the optoacoustic image was range limited with respect to high intensity values before leveling and normalization from 0 to 1. Besides larger features (e.g. muscles, thyroid) optoacoustic imaging allows identification of prominent vascularization (1, 2) and a fine vascular network (oval highlight) stretching inside the imaging plane and perpendicular to it (fine dots). (b) The corresponding ultrasound image confirms features detected in (a), whereby grayscale represents the pulse-echo and color the Directional Power Doppler signal (red/blue colormaps indicating opposite flow directions). C: Carotid, T: Thyroid, Tr: Trachea, s: sternocleidomastoid muscle, m: infrahyoid muscle; axes in mm.109
- Figure 6-5 – Time series of handheld scans at 850nm wavelength from (a), (b) the arm of a male volunteer (30x30mm²) and (c), (d) the anterior neck region of a female volunteer (30x25mm²). Images show a single wavelength, whereby we chose a red colormap for lower spatial frequencies and superimposed higher spatial frequencies in semi-transparent bright white. The sequence shown in (a) was taken close the wrist where the radial artery (ra) is flanked by two veins. Another sequence, (b), was taken closer to the elbow where the radial artery was located deeper inside the tissue (inside and below a muscle). The sequence in (c) displays the slightly tense sternocleidomastoid muscle whereas (d) shows a sequence under full tension. ca: carotid artery; sm: sternocleidomastoid; ij: internal jugular vein; ej: external jugular vein; s: skin. .111
- Figure 6-6 – Time series showing a controlled occlusion experiment at critical time points. Upon occlusion of the vascular system using a sphygmomanometer the radial artery starts collapsing. Just before the release it has fully disappeared. Re-perfusion increases its size and visibility. All images show the same frame of 40 mm width and 20 mm height, held constant during the experiment. Data were acquired using HOT-256 and 800nm wavelength.112
- Figure 6-7 – Time series showing a manual scan (top-down) of the calf of a female volunteer acquired using HOT-256 and 850nm wavelength (22x25mm²). Vascular features (mostly veins) can be visually tracked on images of 45mm height and 50mm width. The large vein (v1) moves out of focus, while another vein (v2) moves from left to right and then splits, i.e. in 3D it moves diagonally towards the ankle. sf: sub-cutaneous fat; s: skin; mb: muscle boundary; v1, v2: veins; bf: bi-furcation.113
- Figure 6-8 – Identifying the best measurement position. (a) This position results in poor image quality, shown in (c), because most vessels elongate perpendicular to the array axis. (b) The position chosen for subsequent experiments as most vessels are approximately parallel to the array axis.114
- Figure 6-9 – Experimental setup including fiber bundles for illumination, ultrasound array and injection catheter. (a) The excised colon segment with region of interest of 12 mm (x-axis) by 20 mm (y-axis). (b) In-vivo mouse tail (highlighted) with region of interest of 5 mm (x-axis) by 20 mm (y-axis).115
- Figure 6-10 – Artificial perfusion of an excised colon segment. (a) Masked absolute sum of reconstructed region of interest over time: saline perfusion in the blood filled vasculature (dotted line) and blood perfusion in the cleared vasculature (solid line). Injections were performed successively. (b) Optoacoustic images of representative time points: t1 – t4 for saline perfusion, and t5 – t8 for blood perfusion. Images were plotted on a linear scale from 0–1 with 0 and 1 representing the minimum and maximum pixel value over all image frames in the sequence. Axes x and y correspond to the coordinate system displayed in fig. 6.9(a).117

- Figure 6-11 – Saline injection in a mouse tail in-vivo: 3 injections in intervals of 40s. (a) Masked absolute sum of reconstructed region of interest over time. The steady state before injections is marked by t1; t2 and t4 denote beginning and end of the first injection; t5 and t6 mark an intermediate point and the end of the recovery phase. (b) Images obtained at t1-t6 representing the contrast cycle achieved by the first saline injection. Images were plotted on a linear scale from 0–1 with 0 and 1 representing the minimum and maximum pixel value of the first image in the sequence. Axes x and y correspond to the coordinate system displayed in fig. 6.9(b). 118
- Figure 6-12 – ICG injection in a mouse tail in-vivo: 3 injections of 10 μ l ICG in intervals of 40s. (a) Masked absolute sum of reconstructed region of interest over time. The steady state before injections is marked by t1; t2 and t4 denote beginning and end of the first injection; t5 and t6 mark an intermediate point and the end of the recovery phase. (b) Images obtained at t1-t6 representing the contrast cycle achieved by the first ICG injection. Images were plotted on a linear scale from 0–1 with 0 and 1 representing the minimum and maximum pixel value over all image frames in the sequence. Axes x and y correspond to the coordinate system displayed in fig. 6.9(b). 119
- Figure 6-13 – Comparison showing the effect of increasing volume of saline injection on the MAS value. The equilibrium state (eq) is rapidly lowered by the clearing effect of saline on the blood concentration. Higher injection volumes do not seem to influence recovery time but instead just extend the time of minimum blood concentration. 120

8.2 List of tables

Table 1 – Major clinical imaging modalities and Multi-Spectral Optoacoustic Tomography	10
Table 2 – Optical properties of employed phantoms at 750 nm	56
Table 3 – Achieved SNR in this study	57
Table 4 – Summary of LSQR algorithm	76
Table 5 – Summary of modified LSQR algorithm	78

8.3 List of publications

Dima, A. ; Burton, N.C.* ; Ntziachristos, V., “Multispectral optoacoustic tomography at 64, 128, and 256 channels.” J. Biomed. Opt. 19:36021 (2014)

Dima, A. ; Gateau, J. ; Claussen, J.* ; Wilhelm, D.* ; Ntziachristos, V., „Optoacoustic imaging of blood perfusion: Techniques for intraoperative tissue viability assessment.”, J. Biophotonics 6, 485-492 (2013)

Dima, A. ; Ntziachristos, V., “Non-invasive carotid imaging using optoacoustic tomography.”, Opt. Express. 20, 25044-25057 (2012)

Dima, A. ; Ntziachristos V., “Optoacoustic imaging for clinical applications: devices and methods.” Expert Opinion on Medical Diagnostics. 2011;5(3):263-72.

Gateau, J. ; Caballero, M.A.A. ; **Dima, A.** ; Ntziachristos, V., “Three-dimensional optoacoustic tomography using a conventional ultrasound linear detector array: Whole-body tomographic system for small animals.”, Med. Phys. 40:013302 (2013)

Jetzfellner, T. ; Rosenthal, A. ; Englmeier, K.-H. ; **Dima, A.** ; Angel Araque Caballero, M. ; Razansky, D. ; Ntziachristos, V., “Interpolated model-matrix optoacoustic tomography of the mouse brain.”, Appl. Phys. Lett. 98:163701 (2011)

Bühler, A. ; Rosenthal, A. ; Jetzfellner, T. ; **Dima, A.** ; Razansky, D. ; Ntziachristos, V., “Model-based optoacoustic inversions with incomplete projection data.”, Med. Phys. 38, 1694-1704 (2011)

Jetzfellner, T. ; Rosenthal, A. ; Bühler, A. ; **Dima, A.** ; Englmeier, K.-H. ; Ntziachristos, V. ; Razansky, D., “Tomographic optoacoustic inversion in dynamic illumination scenarios.”, Proc. SPIE 7899:78991Y (2011)

Jetzfellner, T. ; Rosenthal, A. ; Englmeier, K.-H. ; **Dima, A.** ; Angel Araque Caballero, M. ; Razansky, D. ; Ntziachristos, V., “Interpolated model-matrix optoacoustic tomography of the mouse brain.”, Appl. Phys. Lett. 98:163701 (2011)

Jetzfellner, T. ; Rosenthal, A. ; Bühler, A. ; **Dima, A.** ; Englmeier, K.H. ; Ntziachristos, V. ; Razansky, D., “Optoacoustic tomography with varying illumination and non-uniform detection patterns.”, J. Opt. Soc. Am. A-Opt. Image Sci. Vis. 27, 2488-2495 (2010)

8.4 References

- [1] N. B. Smith, and A. Webb, *Introduction to Medical Imaging*: Cambridge University Press, 2010.

- [2] T. F. Massoud, and S. S. Gambhir, "Molecular imaging in living subjects: seeing fundamental biological processes in a new light," *Genes & Development*, vol. 17, no. 5, pp. 545-580, March 1, 2003, 2003.
- [3] M. Rudin, and R. Weissleder, "Molecular imaging in drug discovery and development," *Nature Reviews: Drug Discovery*, vol. 2, no. 2, pp. 123-131, 2003.
- [4] A. A. B. Jr., and K. Licha, *Molecular Imaging*, Berlin: Springer, 2005.
- [5] B. Chance, "Optical method," *Annual Review of Biophysics and Biophysical Chemistry*, vol. 20, no. 0883-9182 (Print), 19910919 DCOM-19910919, 1991.
- [6] B. Chance, K. Kang, L. He *et al.*, "Highly sensitive object location in tissue models with linear in-phase and anti-phase multi-element optical arrays in one and two dimensions," *Proceedings of the National Academy of Sciences*, vol. 90, no. 8, pp. 3423-3427, April 15, 1993, 1993.
- [7] V. Ntziachristos, C.-H. Tung, C. Bremer *et al.*, "Fluorescence molecular tomography resolves protease activity in vivo," *Nature Medicine*, vol. 8, no. 7, pp. 757-760, July, 2002.
- [8] C. Balas, "A novel optical imaging method for the early detection, quantitative grading, and mapping of cancerous and precancerous lesions of cervix," *Biomedical Engineering, IEEE Transactions on*, vol. 48, no. 1, pp. 96-104, 2001.
- [9] A. J. Chaudhari, F. Darvas, J. R. Bading *et al.*, "Hyperspectral and multispectral bioluminescence optical tomography for small animal imaging," *Physics in Medicine and Biology*, vol. 50, no. 23, pp. 5421, 2005.
- [10] V. Ntziachristos, and D. Razansky, "Molecular Imaging by Means of Multispectral Optoacoustic Tomography (MSOT)," *Chemical Reviews*, pp. 2783-2794, 2010.
- [11] R. Weissleder, and M. J. Pittet, "Imaging in the era of molecular oncology," *Nature*, vol. 452, no. 7187, pp. 580-589, 2008.
- [12] T. Krucker, and B. S. Sandanaraj, "Optical imaging for the new grammar of drug discovery," *Philosophical Transactions of the Royal Society A: Mathematical, Physical and Engineering Sciences*, vol. 369, no. 1955, pp. 4651-4665, November 28, 2011, 2011.
- [13] A. G. Bell, "On the Production and Reproduction of Sound by Light: the Photophone," *Proceedings of the American Association for the Advancement of Science*, vol. 29, pp. 115-136, 1880.
- [14] A. Rosencwaig, "Photoacoustic Spectroscopy of Biological Materials," *Science*, vol. 181, no. 4100, pp. 657-658, August 17, 1973, 1973.
- [15] G. J. Diebold, and P. J. Westervelt, "The photoacoustic effect generated by a spherical droplet in a fluid," *Journal of the Acoustical Society of America*, vol. 84, no. 6, pp. 2245-2251, 1988.

- [16] A. A. Oraevsky, S. L. Jacques, R. O. Esenaliev *et al.*, "Laser-based optoacoustic imaging in biological tissues," *Proceedings of SPIE*, vol. 2134A, pp. 122-128, 1994.
- [17] R. A. Kruger, "Photoacoustic ultrasound (PAUS)—Reconstruction tomography," *Medical Physics*, vol. 22, no. 10, pp. 1605-9, 1995.
- [18] M. W. Sigrist, "Laser generation of acoustic waves in liquids and gases," *Journal of Applied Physics*, vol. 60, no. 7, pp. R83-R122, 1986.
- [19] X. Wang, Y. Pang, G. Ku *et al.*, "Noninvasive laser-induced photoacoustic tomography for structural and functional in vivo imaging of the brain," *Nature Biotechnology*, vol. 21, no. 7, pp. 803-806, 2003.
- [20] E. Z. Zhang, and *et al.*, "In vivo high-resolution 3D photoacoustic imaging of superficial vascular anatomy," *Physics in Medicine and Biology*, vol. 54, no. 4, pp. 1035, 2009.
- [21] E. Z. Zhang, J. Laufer, and P. Beard, "Three-dimensional photoacoustic imaging of vascular anatomy in small animals using an optical detection system." pp. 64370S-64370S-8.
- [22] R. Ma, A. Taruttis, V. Ntziachristos *et al.*, "Multispectral optoacoustic tomography (MSOT) scanner for whole-body small animal imaging," *Opt. Express*, vol. 17, no. 24, pp. 21414-21426, 2009.
- [23] V. Kozhushko, T. Khokhlova, A. Zharinov *et al.*, "Focused array transducer for two-dimensional optoacoustic tomography," *The Journal of the Acoustical Society of America*, vol. 116, no. 3, pp. 1498-1506, 2004.
- [24] L. Song, K. Maslov, R. Bitton *et al.*, "Fast 3-D dark-field reflection-mode photoacoustic microscopy in vivo with a 30-MHz ultrasound linear array," *Journal of Biomedical Optics*, vol. 13, no. 5, pp. 054028-5, 2008.
- [25] H.-P. Brecht, R. Su, M. Fronheiser *et al.*, "Whole-body three-dimensional optoacoustic tomography system for small animals," *Journal of Biomedical Optics*, vol. 14, no. 6, pp. 064007-8, 2009.
- [26] D. Razansky, A. Buehler, and V. Ntziachristos, "Volumetric real-time multispectral optoacoustic tomography of biomarkers," *Nat. Protocols*, vol. 6, no. 8, pp. 1121-1129, 2011.
- [27] A. Bühler, X. L. Deán-Ben, J. Claussen *et al.*, "Three-dimensional optoacoustic tomography at video rate," *Optics Express*, vol. 20, no. 20, pp. 22712-22719, 2012.
- [28] L. Xiang, B. Wang, L. Ji *et al.*, "4-D Photoacoustic Tomography," *Sci. Rep.*, vol. 3, 2013.
- [29] B. Wang, L. Xiang, M. S. Jiang *et al.*, "Photoacoustic tomography system for noninvasive real-time three-dimensional imaging of epilepsy," *Biomedical Optics Express*, vol. 3, no. 6, pp. 1427-1432, 2012/06/01, 2012.
- [30] A. A. Oraevsky, A. A. Karabutov, S. V. Solomatin *et al.*, "Laser optoacoustic imaging of breast cancer in vivo," *Proceedings of SPIE*. pp. 6-15.

- [31] M. Srirang, K. Alexei, C. G. v. H. Johan *et al.*, "The Twente Photoacoustic Mammoscope: system overview and performance," *Physics in Medicine and Biology*, vol. 50, no. 11, pp. 2543, 2005.
- [32] R. A. Kruger, R. B. Lam, D. R. Reinecke *et al.*, "Photoacoustic angiography of the breast," *Medical Physics*, vol. 37, no. 11, pp. 6096-6100, 2010.
- [33] J. J. Niederhauser, M. Jaeger, R. Lemor *et al.*, "Combined ultrasound and optoacoustic system for real-time high-contrast vascular imaging in vivo," *IEEE Transactions on Medical Imaging*, vol. 24, no. 4, pp. 436-440, 2005.
- [34] R. G. M. Kolkman, P. J. Brands, W. Steenbergen *et al.*, "Real-time in vivo photoacoustic and ultrasound imaging," *Journal of Biomedical Optics*, vol. 13, no. 5, pp. 050510-3, 2008.
- [35] M. Fournelle, H. Hewener, C. Gunther *et al.*, "Free-hand 3d optoacoustic imaging of vasculature." pp. 116-119.
- [36] M. P. Fronheiser, S. A. Ermilov, H.-P. Brecht *et al.*, "Real-time optoacoustic monitoring and three-dimensional mapping of a human arm vasculature," *Journal of Biomedical Optics*, vol. 15, no. 2, pp. 021305-7, 2010.
- [37] C. Haisch, K. Eilert-Zell, M. Vogel *et al.*, "Combined optoacoustic/ultrasound system for tomographic absorption measurements: possibilities and limitations," *Analytical and Bioanalytical Chemistry*, vol. 397, no. 4, pp. 1503-1510, 2010.
- [38] C. Kim, T. N. Erpelding, L. Jankovic *et al.*, "Deeply penetrating in vivo photoacoustic imaging using a clinical ultrasound array system," *Biomed. Opt. Express*, vol. 1, no. 1, pp. 278-284, 2010.
- [39] G. M. Leonardo, O. Ragnar, R. B. Daniel *et al.*, "Real-time photoacoustic and ultrasound imaging: a simple solution for clinical ultrasound systems with linear arrays," *Physics in Medicine and Biology*, vol. 58, no. 1, pp. N1, 2013.
- [40] X. L. Deán-Ben, A. Ozbek, and D. Razansky, "Volumetric real-time tracking of peripheral human vasculature with GPU-accelerated three-dimensional optoacoustic tomography," *IEEE Transactions on Medical Imaging*, pp. 10.1109/TMI.2013.2272079, 2013.
- [41] A. G. Bell, "The Spectrophone," *Bulletin of the Philosophical Society of Washington*, vol. 4, pp. 20, 1881.
- [42] V. Ntziachristos, A. Leroy-Willig, and B. Tavitian, *Textbook of in vivo imaging in vertebrates*: Wiley, 2007.
- [43] V. Ntziachristos, "Going deeper than microscopy: the optical imaging frontier in biology," *Nat Meth*, vol. 7, no. 8, pp. 603-614, 2010.
- [44] S. R. Arridge, "Optical tomography in medical imaging," *Inverse Problems*, vol. 15, no. 2, pp. R41, 1999.

- [45] G. M. Hale, and M. R. Querry, "Optical Constants of Water in the 200-nm to 2000-nm Wavelength Region," *Applied Optics*, vol. 12, no. 3, pp. 555-563, 1973/03/01, 1973.
- [46] R. L. P. van Veen, H. j. c. m. Sterenborg, A. Pifferi *et al.*, "Determination of VIS- NIR absorption coefficients of mammalian fat, with time- and spatially resolved diffuse reflectance and transmission spectroscopy," *OSA Technical Digest*. p. SF4.
- [47] T. Sarna, and H. A. Swartz, "The Physical Properties of Melanins," *The Pigmentary System*, pp. 311-341: Blackwell Publishing Ltd, 2007.
- [48] T. L. Szabo, *Diagnostic Ultrasound Imaging: Inside Out*: Elsevier Academic Press, 2004.
- [49] P. Laugier, and G. Haiat, "Introduction to the Physics of Ultrasound," *Bone Quantitative Ultrasound*: Springer Netherlands, 2011.
- [50] J. M. M. Pinkerton, "The Absorption of Ultrasonic Waves in Liquids and its Relation to Molecular Constitution," *Proceedings of the Physical Society. Section B*, vol. 62, no. 2, pp. 129, 1949.
- [51] L. Wang, *Photoacoustic imaging and spectroscopy*, Boca Raton: CRC Press, 2009.
- [52] E. Zhang, J. Laufer, and P. Beard, "Backward-mode multiwavelength photoacoustic scanner using a planar Fabry-Perot polymer film ultrasound sensor for high-resolution three-dimensional imaging of biological tissues," *Applied Optics*, vol. 47, no. 4, pp. 561-577, 2008.
- [53] Y. Xu, L. V. Wang, G. Ambartsoumian *et al.*, "Reconstructions in limited-view thermoacoustic tomography," *Medical Physics*, vol. 31, no. 4, pp. 724-733, 2004.
- [54] E. Bossy, K. Daoudi, A.-C. Boccara *et al.*, "Time reversal of photoacoustic waves," *Applied Physics Letters*, vol. 89, no. 18, pp. 184108, 2006.
- [55] B. T. Cox, S. Kara, S. R. Arridge *et al.*, "k-space propagation models for acoustically heterogeneous media: Application to biomedical photoacoustics," *The Journal of the Acoustical Society of America*, vol. 121, no. 6, pp. 3453 2007.
- [56] M. Xu, and L. V. Wang, "Universal back-projection algorithm for photoacoustic computed tomography," *Physical Review E*, vol. 71, no. 1, pp. 016706-7, 2005.
- [57] K. P. Köstli, M. Frenz, H. Bebie *et al.*, "Temporal backward projection of optoacoustic pressure transients using Fourier transform methods," *Physics in Medicine and Biology*, vol. 46, no. 7, pp. 1863-1872 2001.
- [58] W. Kun, S. A. Ermilov, R. Su *et al.*, "An Imaging Model Incorporating Ultrasonic Transducer Properties for Three-Dimensional Optoacoustic Tomography," *Medical Imaging, IEEE Transactions on*, vol. 30, no. 2, pp. 203-214, 2011.
- [59] A. Rosenthal, D. Razansky, and V. Ntziachristos, "Fast semi-analytical model-based acoustic inversion for quantitative optoacoustic

- tomography," *IEEE Transactions on Medical Imaging*, vol. 29, no. 6, pp. 1275-1285, 2010.
- [60] S. Park, A. B. Karpouk, S. R. Aglyamov *et al.*, "Adaptive beamforming for photoacoustic imaging," *Opt. Lett.*, vol. 33, no. 12, pp. 1291-1293, 2008.
- [61] D. Queirós, X. L. Deán-Ben, A. Bühler *et al.*, "Modeling the shape of cylindrically focused transducers in three-dimensional optoacoustic tomography," *J Biomed. Opt.*, vol. 18, no. 7, 2013.
- [62] X. L. Deán-Ben, R. Ma, A. Rosenthal *et al.*, "Weighted model-based optoacoustic reconstruction in acoustic scattering media," *Physics in Medicine and Biology*, vol. 58, no. 16, pp. 5555-5566, 2013.
- [63] X. L. Dean-Ben, V. Ntziachristos, and D. Razansky, "Acceleration of Optoacoustic Model-Based Reconstruction Using Angular Image Discretization," *Medical Imaging, IEEE Transactions on*, vol. 31, no. 5, pp. 1154-1162, 2012.
- [64] C. C. Paige, and M. A. Saunders, "LSQR: An Algorithm for Sparse Linear Equations and Sparse Least Squares," *ACM Trans. Math. Softw.*, vol. 8, no. 1, pp. 43-71, 1982.
- [65] C.-I. Chang, *Hyperspectral Imaging - Techniques for Spectral Detection and Classification*, p. 370: Springer US, 2003.
- [66] G. Lu, and B. Fei, "Medical hyperspectral imaging: a review," *Journal of Biomedical Optics*, vol. 19, no. 1, pp. 010901-010901, 2014.
- [67] M. Ferrari, L. Mottola, and V. Quaresima, "Principles, Techniques, and Limitations of Near Infrared Spectroscopy," *Canadian Journal of Applied Physiology*, vol. 29, no. 4, pp. 463-487, 2004/08/01, 2004.
- [68] Y. Hoshi, "Functional near-infrared optical imaging: Utility and limitations in human brain mapping," *Psychophysiology*, vol. 40, no. 4, pp. 511-520, 2003.
- [69] B. Cox, J. G. Laufer, S. R. Arridge *et al.*, "Quantitative spectroscopic photoacoustic imaging: a review," *Journal of Biomedical Optics*, vol. 17, no. 6, pp. 0612021-0612022, 2012.
- [70] S. Tzoumas, N. Deliolanis, S. Morscher *et al.*, "Unmixing Molecular Agents From Absorbing Tissue in Multispectral Optoacoustic Tomography," *Medical Imaging, IEEE Transactions on*, vol. 33, no. 1, pp. 48-60, 2014.
- [71] J. Glatz, N. C. Deliolanis, A. Buehler *et al.*, "Blind source unmixing in multi-spectral optoacoustic tomography," *Opt. Express*, vol. 19, no. 4, pp. 3175-3184, 2011.
- [72] D. Razansky, C. Vinegoni, and V. Ntziachristos, "Multispectral photoacoustic imaging of fluorochromes in small animals," *Optics Letters*, vol. 32, no. 19, pp. 2891-2893, 2007.
- [73] J. Laufer, B. Cox, E. Zhang *et al.*, "Quantitative determination of chromophore concentrations from 2D photoacoustic images using a

- nonlinear model-based inversion scheme," *Applied Optics*, vol. 49, no. 8, pp. 1219-1233, 2010/03/10, 2010.
- [74] A. Rosenthal, D. Razansky, and V. Ntziachristos, "Quantitative Optoacoustic Signal Extraction Using Sparse Signal Representation," *IEEE Transactions on Medical Imaging*, vol. 28, no. 12, pp. 1997-2006, 2009.
- [75] A. Buehler, E. Herzog, D. Razansky *et al.*, "Video rate optoacoustic tomography of mouse kidney perfusion," *Optics Letters*, vol. 35, no. 14, pp. 2475-2477, 2010.
- [76] A. Taruttis, E. Herzog, D. Razansky *et al.*, "Real-time imaging of cardiovascular dynamics and circulating gold nanorods with multispectral optoacoustic tomography," *Optics Express*, vol. 18, no. 19, pp. 19592-19602, 2010/09/13, 2010.
- [77] A. Rosenthal, V. Ntziachristos, and D. Razansky, "Optoacoustic methods for frequency calibration of ultrasonic sensors," *Ultrasonics, Ferroelectrics, and Frequency Control, IEEE Transactions on*, vol. 58, no. 2, pp. 316-326, 2011.
- [78] A. Dima, and V. Ntziachristos, "Non-invasive carotid imaging using optoacoustic tomography," *Optics Express*, vol. 20, no. 22, pp. 25044-25057, 2012.
- [79] A. Buehler, A. Rosenthal, T. Jetzfellner *et al.*, "Model-based optoacoustic inversions with incomplete projection data," *Medical Physics*, vol. 38, no. 3, pp. 1694-1704, 2011.
- [80] A. Dima, N. C. Burton, and V. Ntziachristos, "Multispectral optoacoustic tomography at 64, 128, and 256 channels," *Journal of Biomedical Optics*, vol. 19, no. 3, pp. 036021-036021, 2014.
- [81] J. Gateau, M. A. A. Caballero, A. Dima *et al.*, "Three-dimensional optoacoustic tomography using a conventional ultrasound linear detector array: Whole-body tomographic system for small animals," *Medical Physics*, vol. 40, no. 1, pp. 013302-11, 2013.
- [82] A. Buehler, M. Kacprowicz, A. Taruttis *et al.*, "Real-time handheld multispectral optoacoustic imaging," *Optics Letters*, vol. 38, no. 9, pp. 1404-1406, 2013.
- [83] A. Dima, J. Gateau, J. Claussen *et al.*, "Optoacoustic imaging of blood perfusion: Techniques for intraoperative tissue viability assessment," *Journal of Biophotonics*, vol. 6, no. 6-7, pp. 485-492, 2013.
- [84] W. Kun, S. Richard, A. O. Alexander *et al.*, "Investigation of iterative image reconstruction in three-dimensional optoacoustic tomography," *Physics in Medicine and Biology*, vol. 57, no. 17, pp. 5399, 2012.
- [85] A. Rosenthal, T. Jetzfellner, D. Razansky *et al.*, "Efficient framework for model-based tomographic image reconstruction using wavelet packets," *Medical Imaging, IEEE Transactions on*, vol. PP, no. 99, pp. 1-1, 2012.

- [86] A. Rosenthal, V. Ntziachristos, and D. Razansky, "Model-based optoacoustic inversion with arbitrary-shape detectors," *Medical Physics*, vol. 38, no. 7, pp. 4285-4295, 2011.
- [87] X. L. Dean-Ben, A. Buehler, V. Ntziachristos *et al.*, "Accurate Model-Based Reconstruction Algorithm for Three-Dimensional Optoacoustic Tomography," *Medical Imaging, IEEE Transactions on*, vol. 31, no. 10, pp. 1922-1928, 2012.
- [88] M. A. Anastasio, Z. Jin, P. Xiaochuan *et al.*, "Half-time image reconstruction in thermoacoustic tomography," *Medical Imaging, IEEE Transactions on*, vol. 24, no. 2, pp. 199-210, 2005.
- [89] G. Paltauf, J. A. Viator, S. A. Prahl *et al.*, "Iterative reconstruction algorithm for optoacoustic imaging," *The Journal of the Acoustical Society of America*, vol. 112, no. 4, pp. 1536-1544, 2002.
- [90] R. Goldman, *An Integrated Introduction to Computer Graphics and Geometric Modeling*: CRC Press, Inc., 2009.
- [91] J. Fung, and S. Mann, "Using graphics devices in reverse: GPU-based Image Processing and Computer Vision." pp. 9-12.
- [92] B. Shuhui, L. Zhenbao, T. Shiina *et al.*, "Model-Based Reconstruction Integrated With Fluence Compensation for Photoacoustic Tomography," *Biomedical Engineering, IEEE Transactions on*, vol. 59, no. 5, pp. 1354-1363, 2012.
- [93] B. E. Treeby, and B. T. Cox, "k-Wave: MATLAB toolbox for the simulation and reconstruction of photoacoustic wave fields," *Journal of Biomedical Optics*, vol. 15, no. 2, pp. 021314-021314-12, 2010.
- [94] J.A. Jensen, and N. B. Svendsen, "Calculation of pressure fields from arbitrarily shaped, apodized and excited ultrasound transducers," *IEEE Transactions on Ultrasonics Ferroelectrics and Frequency Control*, vol. 39, no. 2, pp. 262-267, 1992.
- [95] J. A. Jensen, "Field: A Program for Simulating Ultrasound Systems," *Medical & Biological Engineering & Computing*, vol. 34, no. Supplement 1, Part 1, pp. 351-353, 1996.
- [96] N. American Thyroid Association Guidelines Taskforce on Thyroid, C. Differentiated Thyroid, D. S. Cooper *et al.*, "Revised American Thyroid Association management guidelines for patients with thyroid nodules and differentiated thyroid cancer," *Thyroid*, vol. 19, no. 11, pp. 1167-214, Nov, 2009.
- [97] M. P. J. Vanderpump, "The epidemiology of thyroid disease," *British Medical Bulletin*, vol. 99, no. 1, pp. 39-51, September 1, 2011, 2011.
- [98] L. Davies, and H. Welch, "Current thyroid cancer trends in the united states," *JAMA Otolaryngology-Head & Neck Surgery*, vol. 140, no. 4, pp. 317-322, 2014.

- [99] D. L. Segev, D. P. Clark, M. A. Zeiger *et al.*, "Beyond the Suspicious Thyroid Fine Needle Aspirate," *Acta Cytologica*, vol. 47, no. 5, pp. 709-722, 2003.
- [100] P. P. Linas Urbanavičius, Dirk Van de Putte and Donatas Venskutonis, "How to assess intestinal viability during surgery: A review of techniques," *World Journal of Gastrointestinal Surgery*, vol. 3, no. 5, pp. 59-70, 2011.
- [101] M. J. Niedre, R. H. de Kleine, E. Aikawa *et al.*, "Early photon tomography allows fluorescence detection of lung carcinomas and disease progression in mice in vivo," *Proceedings of the National Academy of Sciences of the United States of America*, vol. 105, no. 49, pp. 19126-19131, December 9, 2008, 2008.
- [102] H. Suh, O. A'amar, E. Rodriguez-Diaz *et al.*, "Elastic Light-Scattering Spectroscopy for Discrimination of Benign from Malignant Disease in Thyroid Nodules," *Annals of Surgical Oncology*, vol. 18, no. 5, pp. 1300-1305, 2011/05/01, 2011.
- [103] L. C. Conti de Freitas, E. Phelan, L. Liu *et al.*, "Optical coherence tomography imaging during thyroid and parathyroid surgery: A novel system of tissue identification and differentiation to obviate tissue resection and frozen section," *Head and Neck*, vol. 36, no. 9, pp. 1329-1334, 2014.
- [104] I. Banaka, G. Kaltsas, S. Antoniou *et al.*, "Prognostic value of vascularity index for the diagnosis of autoimmune thyroid disease," *Journal Belge de Radiologie*, vol. 94, no. 4, pp. 185, 2011.
- [105] H. J. Moon, J. Y. Kwak, M. J. Kim *et al.*, "Can Vascularity at Power Doppler US Help Predict Thyroid Malignancy?," *Radiology*, vol. 255, no. 1, pp. 260-269, 2010.
- [106] V. S. Dogra, B. K. Chinni, K. S. Valluru *et al.*, "Preliminary Results of Ex Vivo Multispectral Photoacoustic Imaging in the Management of Thyroid Cancer," *American Journal of Roentgenology*, vol. 202, no. 6, pp. W552-W558, 2014/06/01, 2014.
- [107] J. Levi, S.-R. Kothapalli, S. Bohndiek *et al.*, "Molecular Photoacoustic Imaging of Follicular Thyroid Carcinoma," *Clinical Cancer Research*, vol. 19, no. 6, pp. 1494-1502, March 15, 2013, 2013.
- [108] J. Xia, M. R. Chatni, K. Maslov *et al.*, "Whole-body ring-shaped confocal photoacoustic computed tomography of small animals in vivo," *Journal of Biomedical Optics*, vol. 17, no. 5, pp. 050506-1, 2012.